

Development and application of novel processing tools and methods for cardiac optical mapping

Christopher O'Shea

A thesis submitted to
The University of Birmingham
for the degree of
Doctor of Philosophy

Research and Training Centre in Physical Sciences for Health
School of Chemistry
College of Engineering and Physical Sciences
University of Birmingham
September 2019

UNIVERSITY OF
BIRMINGHAM

University of Birmingham Research Archive

e-theses repository

This unpublished thesis/dissertation is copyright of the author and/or third parties. The intellectual property rights of the author or third parties in respect of this work are as defined by The Copyright Designs and Patents Act 1988 or as modified by any successor legislation.

Any use made of information contained in this thesis/dissertation must be in accordance with that legislation and must be properly acknowledged. Further distribution or reproduction in any format is prohibited without the permission of the copyright holder.

Abstract

Cardiac optical mapping provides unparalleled spatio-temporal resolution information of cardiac electrophysiology. It has hence emerged as an important technology in understanding cardiac electrical behaviour in physiological and pathophysiological states. There is a requirement for effective data analysis tools that are high-throughput, robustly characterised and flexible with regards to a growing array of experimental models.

In this thesis a MATLAB based software, ElectroMap, was developed for analysis of diverse optical mapping datasets. ElectroMap incorporates existing and novel methods to allow quantification and mapping of action potential and calcium transient morphology and activation/repolarisation times. Automated pacing cycle length detection and segmentation were implemented, realising high-throughput analysis of beat-to-beat responses and transient behaviour. Standalone modules dedicated to calculation of conduction velocity and alternans were introduced, allowing thorough integration of key factors in arrhythmogenesis. Semi-automated analysis of temporal variations in wave morphology were developed from previous methodologies for electrogram analysis. Algorithms to use fractional rate of change of fluorescence as a measure of conduction were also introduced to the software. Algorithms were tested in silico datasets, mouse and guinea pig optical mapping datasets and preliminary experiments also showed use for in vivo human electrogram mapping of atrial fibrillation.

Declaration

I hereby declare that the work presented here in this thesis titled, “Development and application of novel processing tools and methods for cardiac optical mapping” is the work of my own, unless otherwise stated. The work here was written and submitted by me to the School of Chemistry, University of Birmingham, United Kingdom as fulfilment of the degree of Doctor of Philosophy. I further declare that this work has not been submitted to any other university for the award of any other degree, diploma or equivalent course.

Christopher O'Shea

Acknowledgements

First and foremost, I want to thank my primary supervisors, Dr Davor Pavlovic and Dr Kashif Rajpoot. I can honestly say I have loved undertaking this work and never once questioned my decision to do a PhD and specifically this project. There has obviously been times of struggle and hard work to get to this point, but thanks to your dedication and guidance, I have been afforded fantastic, life shaping opportunities both professionally and personally and for that I will always be grateful and indebted to you both. One of these opportunities has been to work with numerous brilliant people including Dr Larissa Fabritz, Dr Rob Neely, Dr Joao Correia, Dr Andrew Holmes, Dr James Winter, Prof Paulus Kirchhof and Prof Ming Lei. Thank you all for sharing your knowledge, passion and time with me.

I'd like to acknowledge everyone I have worked with day to day as part of the heart failure and arrhythmias cluster. You have all helped me learn and apply what were, and still are, foreign and difficult concepts for me to grasp, bared with me as I made a mess of both desk and lab spaces, and in general just been fantastic and inspiring people to be around. I particularly would like to thank Simon Wells for his effort, above and beyond his own project, in teaching me the technique.

Undertaking this PhD would not have been possible without the support of numerous friends, some of whom I have met thanks to this project, and others frankly that I am sick of at this point. I especially want to thank Lorraine Curtis, Jack Banting, Andrew 'Pricey' Price, Joshua Finn, Charles Leathem, Adam Lewis, Old Edwardians cricket club, everyone in the 2015 sci-phy cohort, Zoë Schofield, Molly O'Reilly, Daniel Johnson and Alan Hutton.

Finally, I would like to acknowledge my family. To my wonderful grandmothers (Nanny O'Shea and Nanny Clarke), thank you for your lifetime of devotion to your families and me. To Mum, Dad and Emily. It is with your continued and seemingly unconditional support; I've finally finished school (kind of)! Thank you. (Also, as it is December and I am skint, consider this your Christmas present).

Project Outcomes

The following publications constitute this thesis:

Publication 1 (Chapter 3): ElectroMap: High-throughput open-source software for analysis and mapping of cardiac electrophysiology. **C O'Shea**, A P Holmes, T Y Yu, J Winter, S P Wells, J Correia, B J Boukens, J R deGroot, G S Chu, X Li, G.A Ng, P Kirchhof, L Fabritz, K Rajpoot, D Pavlovic. Sci. Rep. 9:1389, 1–13, 2019.

Publication 2 (Chapter 4): Cardiac Optogenetics and Optical Mapping – Overcoming Spectral Congestion in All-Optical Cardiac Electrophysiology (Review). **C O'Shea**, A P Holmes, J Winter, J Correia, X Ou, R Dong, S C He, P Kirchhof, L Fabritz, K Rajpoot, D Pavlovic. Front. Physiol. 10:182, 1-14, 2019

Publication 3 (Chapter 4): A protocol for dual calcium-voltage optical mapping in murine sinoatrial preparation with optogenetic pacing. R Dong*, R Mu-u-min*, A Reith*, **C O'Shea***, S C He, K Duan, K Kou. X Tan, D Pavlovic, X Ou, M Lei. Front. Physiol. 10:954, 1-11, 2019. *These authors share first authorship

Publication 4 (Chapter 5): Transverse cardiac slicing and optical imaging for analysis of transmural gradients in membrane potential and Ca²⁺ transients in murine heart. Q Wen, K Gandhi, R A Capel, G Hao, **C O'Shea**, G Neagu, S Pearcey, D Pavlovic, D A Terrar, J Wu, P Camelliti, M Lei. J. Physiol. 596, 3951–3965. 2018

Publication 5 (Chapter 5): A protocol for transverse cardiac slicing and optical mapping in murine heart. S C He*, Q Wen*, **C O'Shea***, R Mu-u-min*, K Kun, A Grassam-Rowe, Y Liu, Z Fan, X Q Tan, X Ou, P Camelliti, D Pavlovic, M Lei. Front. Physiol. 10:755, 1-8, 2019. *These authors share first authorship

Publication 6 (Chapter 6): Wave morphology similarity mapping of temporal regularity in optical action potentials. **C O'Shea**, J Winter, A P Holmes, D M Johnson, J Correia, P Kirchhof, L Fabritz, K Rajpoot, D Pavlovic. Under Review in Progress in Biophysics and Molecular Biology.

Through work undertaken for this thesis, the following additional outputs have also been produced

Publications

- Examination of the effects of conduction slowing on the upstroke of the optically-recorded action potentials. **C O'Shea**, D Pavlovic, K Rajpoot, J Winter. *Front. Physiol.* 10:1295, 1-11, 2019.
- High-Throughput Analysis of Optical Mapping Data Using ElectroMap. **C O'Shea**, A P Holmes, T Y Yu, J Winter, S P Wells, B A Parker, D Fobian, D M Johnson, J Correia, P Kirchhof, L Fabritz, K Rajpoot, D Pavlovic. *J. Vis. Exp.* (148), e59663, 2019
- Sympathetic nervous regulation of cardiac alternans in the intact heart. J Winter, M J Bishop, C D E Wilder, **C O'Shea**, D Pavlovic, M J Shattock. *Front. Physiol.* 9:16, 1–12. 2018

Publications undergoing peer review

The amplitude-normalised area of a bipolar electrograms as a measure of local conduction delay in the heart, C M Costa, G Anderson, V Meijborg, **C O'Shea**, M J Shattock, P Kirchhof, R Coronel, S A Niederer, D Pavlovic, T Dhanjal, J Winter. Under Review in *Frontiers in Physiology*.

Software

ElectroMap software: <https://github.com/CXO531/ElectroMap>

Published Abstracts

- **O'Shea C**, Winter J, Holmes AP, Yu TY, Correia J, Li X, et al. Arrhythmia analysis of electrogram and optical data in electromap: a novel, opensource software platform. *EP Europace*. 2019;21(Supplement 2):ii765.
- Wells S, **O'Shea C**, Waddell H, Kirchhof P, Pavlovic D, Delbridge L, et al. Acute Oestradiol Slows Conduction in Male, but not Female, Murine Left Atria. *Heart, Lung and Circulation*. 2019;28:S200.
- **O'Shea C**, Wells S, Holmes AP, Winter J, Correia J, Kirchhof P, et al. 135 Development and validation of high-throughput processing and analysis software platform for cardiac optical mapping. *Heart*. 2018 Jun 1;104(Suppl 6):A98 LP-A98.
- Winter J, **O'Shea C**, Pavlovic D, Fabritz L, Kirchhof P. 151 Direct evidence that sympathetic nervous activation accelerates ventricular conduction velocity, but inhibition of responses by DI-8-ANEPPS. *Heart*. 2018 Jun 1;104(Suppl 6):A107 LP-A108.

- **O'Shea C**, Wells S, Holmes AP, Winter J, Correia J, Kirchhof P, et al. 135 Development and validation of high-throughput processing and analysis software platform for cardiac optical mapping. *Heart* . 2018 Jun 1;104(Suppl 6):A98 LP-A98.
- **O'Shea C**, Holmes AP, Yu TY, Winter J, Correia J, Kirchhof P, et al. Development of a novel software package for high-throughput processing and analysis of cardiac optical mapping data. In: *Heart*. 2017. p. 128–9.

Conference presentations: oral talks

- Heart Rhythm Congress, Birmingham, UK, 2019
- 42nd EWGCCE meeting, Essen, Germany, 2018
- International Society for Heart Research European Section Meeting, Hamburg, Germany, 2017

Conference presentations: posters

- BHF accelerator award opening ceremony, Birmingham, UK, 2019. First prize for best research poster
- BSCR Spring meeting, Manchester, UK, 2019
- Institute of Cardiovascular Sciences away day, Birmingham, UK, 2019. Joint winner of best poster prize
- EHRA, Lisbon, Portugal, 2019
- BSCR Spring meeting, Manchester, UK, 2018
- Leducq transatlantic network, Birmingham, UK, 2018
- Dutch-German Cardiovascular research meeting, Amsterdam, The Netherlands, 2019
- Biophysical Society annual meeting, San Francisco, USA, 2018
- BSCR spring meeting, Manchester, UK, 2017

Contents

1	Introduction	1
1.1	Cardiac physiology	2
1.1.1	Heart anatomy and function	2
1.1.2	Cardiac conduction system	4
	The cardiac action potential	7
	Excitation-contraction coupling	12
1.2	Cardiac Arrhythmias	13
1.2.1	Mechanisms of cardiac arrhythmias	14
	Disturbances in action potential generation: ectopic activity	14
	Disturbances in action potential propagation: re-entry . . .	16
1.2.2	Atrial Fibrillation	19
1.3	Measuring cardiac electrical activity	20
1.4	Optical mapping	23
1.4.1	Voltage sensitive dyes	24
1.4.2	Intracellular calcium dyes	26
1.4.3	Optical mapping hardware	27
1.4.4	Optical mapping data processing	28
	Pre-processing	28
	Region of interest selection by image thresholding	28
	Spatial filtering	30
	Temporal filtering	32

Ensemble averaging	34
Baseline correction	34
1.5 Thesis motivation and aims	35
1.6 Thesis structure	36
1.7 Chapter 1 references	37
2 Experimental methods - mouse atrial optical mapping	47
2.1 Experimental and analysis methods: Mouse atrial optical mapping	48
2.2 Animal procedures and models	48
2.3 Buffer solutions	49
2.4 Heart isolation	49
2.5 Langendorff perfusion	50
2.5.1 Di-4-ANEPPS dye loading	51
2.5.2 Rhod-2AM dye loading	52
2.5.3 Rh-237 dye loading	52
2.6 Atrial isolation	53
2.7 Optical mapping	54
2.7.1 Pacing protocols	57
2.7.2 Data analysis	58
2.7.3 Statistical analysis	59
2.8 Chapter summary	59
2.9 Chapter 2 references	60
3 ElectroMap: High-throughput open-source software for analysis and mapping of cardiac electrophysiology	62
3.1 ElectroMap: High-throughput open-source software for analysis and mapping of cardiac electrophysiology	64
3.2 Additional material	78
3.3 Testing the efficacy of ensemble averaging in optical mapping . . .	78

3.3.1	Ensemble averaging for improved optical signal quality in mouse left atria	81
3.4	Comparison of local conduction velocity vector quantification methods	84
3.4.1	Finite difference and polynomial surface comparison in model datasets	87
3.4.2	Finite difference and polynomial surface comparison in experimental datasets	88
3.4.3	Discussion and conclusion on local conduction velocity vector quantification methods	90
3.5	Testing of baseline correction methods	91
3.6	Chapter summary	93
3.7	Chapter 3 References	94
4	Optical mapping of optogenetic models	96
4.1	Cardiac Optogenetics and Optical Mapping – Overcoming Spectral Congestion in All-Optical Cardiac Electrophysiology	98
4.2	A Protocol for Dual Calcium-Voltage Optical Mapping in Murine Sinoatrial Preparation With Optogenetic Pacing	113
5	Optical mapping of transverse mouse ventricular slices	125
5.1	Transverse cardiac slicing and optical imaging for analysis of transmural gradients in membrane potential and Ca ²⁺ transients in murine heart	128
5.2	A protocol for transverse cardiac slicing and optical mapping in murine heart.	144
6	Temporal irregularity quantification and mapping of optical action potentials using wave morphology similarity	153
6.1	Temporal irregularity quantification and mapping of optical action potentials using wave morphology similarity	154
7	Effects of high fat diet and pitx2 deficiency on left atrial electrophysiology	167
7.1	Introduction	168

7.2	Methods	170
7.3	Results	171
7.3.1	High fat diet increases mouse body weight of both WT and pitx2 deficient mice	171
7.3.2	High fat diet prolongs left atrial action potential duration in both wild type and pitx2null mice	172
7.3.3	High fat diet does not alter beat-to-beat variability of repolarisation	174
7.3.4	High fat diet does not alter left atrial optical time to peak or conduction velocity	175
7.4	Discussion	176
7.5	Conclusion	180
7.6	Chapter 7 References	180
8	Conclusions	184
8.1	Thesis Outcomes	184
8.2	Limitations	186
8.2.1	General limitations of optical mapping	186
8.2.2	Mouse models in cardiac electrophysiology research	187
8.2.3	Analysis limitations and future work	188
8.3	Conclusion	190
8.4	Chapter 8 References	191
A	Supplementary Information for ElectroMap: High-throughput open-source software for analysis and mapping of cardiac electrophysiology, Chapter 3	195
A.1	Supplementary Material	195
A.1.1	Detailed Methods	195
	Software Development and Availability	195
	Optical Mapping	196
A.1.2	Processing and Analysis Parameters	198

Activation and duration mapping	199
Conduction Velocity Measurement	199
Calcium decay constant (τ)	201
Cardiac alternans module	202
Dominant frequency and phase mapping	203
A.1.3 Production of model murine datasets	204
Model Pseudocode	206
A.1.4 Supplemental Figures	208
A.2 Supplemental References	217

List of Figures (Excluding those in publications)

1.1	Anatomy and blood flow of the heart	2
1.2	Cardiac intercalated disk	3
1.3	Electrical conduction system of the heart	5
1.4	Example human and mouse action potentials and ionic currents .	8
1.5	Triggered activity examples	15
1.6	Model of re-entry	17
1.7	Spiral wave re-entry	18
1.8	Sinus rhythm echocardiogram	21
1.9	Jablonski diagram and chemical structure of Di-4-ANEPPS	24
1.10	Principle of optically recorded action potentials using voltage sensitive dye	26
1.11	Otsu thresholding of an optical mapping dataset.	29
1.12	Principles of spatial filtering.	31
1.13	Example of convolution temporal filtering methods.	33
2.1	Isolated heart cannulation via the ascending aorta.	50
2.2	Dye loading on Langendorff apparatus.	51
2.3	Dissected atria in optical mapping superfusion chamber.	54
2.4	Optical mapping setup.	56
2.5	Atrial pacing protocols.	58
3.1	Ensemble averaging techniques.	79

3.2	Action potential duration measurement validation and ensemble averaging model testing.	82
3.3	Ensemble averaging to resolve action potential duration changes. .	84
3.4	Polynomial and finite difference conduction velocity measurement in ideal, no noise, datasets.	88
3.5	Polynomial and finite difference conduction velocity measurement accuracy as a function of signal noise.	89
3.6	Comparison of polynomial and finite difference multi-vector conduction velocity quantification methods.	90
3.7	Baseline correction testing.	92
3.8	Baseline correction of simulated data.	93
7.1	Effects of high fat diet on body weight of wild type and pitx2null mice.	172
7.2	Action potential duration 70 mapping of wild type and pitx2null mouse left atria, with and without high fat diet.	173
7.3	Action potential duration 30 and APD50 mapping of wild type and pitx2null mouse left atria, with and without high fat diet.	174
7.4	Beat-to-beat variability of wild type and pitx2null mouse left atria, with and without high fat diet.	175
7.5	Conduction velocity and time to peak mapping of wild type and pitx2null mouse left atria, with and without high fat diet.	176
A.1	Automatic, pacing frequency, based signal segmentation options and validation	208
A.2	Activation and repolarisation definitions	209
A.3	Action potential duration mapping	210
A.4	Conduction velocity module	211
A.5	Model murine action potential example	212
A.6	Calcium mapping	213
A.7	Alternans module	214
A.8	Diastolic interval mapping	215
A.9	Optogenetic pacing peak removal	215

A.10 Software comparison	216
------------------------------------	-----

Chapter 1

Introduction

This chapter provides an overview of the physiology of the heart, focusing on electrical activity, the action potential, cardiac arrhythmias and methodologies used to measure the action potential. In particular, the application, advantages, implementation and processing of cardiac optical mapping are discussed. Current analysis options are summarised, and the aims and structure of this thesis are outlined.

1.1 Cardiac physiology

1.1.1 Heart anatomy and function

The heart acts to pump blood throughout the pulmonary and systemic circulation. Newly oxygenated blood from the lungs enters the left atrium (LA) from the pulmonary veins and is pumped down into the left ventricle (LV). From the LV, it is pumped via the aorta to the rest of the body. After travelling through the systemic circulation, the de-oxygenated blood enters the right atrium via the superior and inferior vena cave (SVC/IVC) and is pumped into the right ventricle (RV). From here, it is directed to the pulmonary circulation via the pulmonary artery for re-oxygenation, Figure 1.1 [1]. This process is repeated for every heartbeat, as the heart fills with (diastole) and expels (systole) blood. The process is collectively known as the cardiac cycle [2].

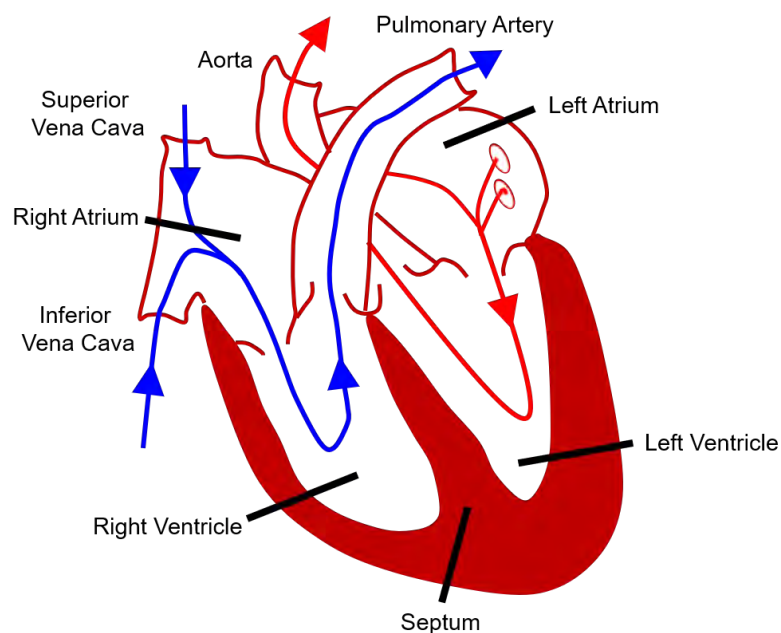


Figure 1.1: Anatomy and blood flow of the heart. Blue denotes deoxygenated blood, red shows oxygenated blood. Dark red denotes the cardiac tissue

Owing to its primary role of pumping blood, the heart is a muscular organ. The cardiac tissue is organised into three layers: the inner endocardium, the middle myocardium and the outer epicardium. The heart is made up primarily (by volume) of cardiac muscle cells, cardiomyocytes (CMs). CMs in the myocardium are electrically and mechanically coupled to each other at junctions known as intercalated discs which contain gap junctional (electrical coupling) and adherence proteins (for dynamic mechanical coupling via the adherence junctions and cell adhesion at the desmosomes), Figure 1.2 [3]–[5]. These junctions exist predominantly at the cell ends, and the connected CMs make up muscle fibres. The coupling of CMs in this way means electrical and mechanical impulses are conducted from cell to cell, meaning the heart forms an

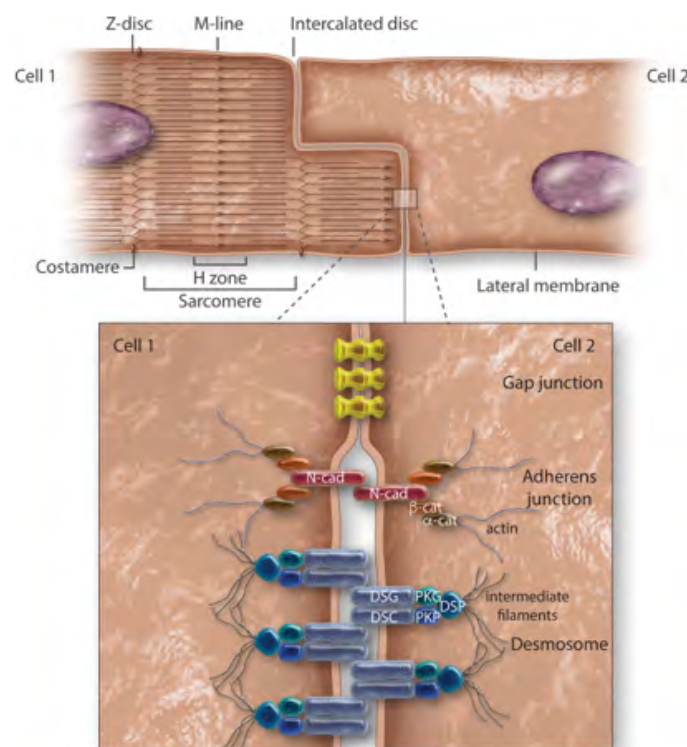


Figure 1.2: Cardiac intercalated disk. Diagram of the connection of neighbouring cardiomyocytes via the intercalated disk. Inset shows the connection of the cell at the gap junctions (electrical coupling), adherence junctions (dynamic mechanical coupling) and desmosomes (strong cell to cell adhesion). Extracted from [5].

electrical/functional syncytium. Fibres are further arranged into sheets (4 to 6 CMs thick) separated by connective tissue. The directionality of these sheets varies throughout the myocardium, giving rise to a complex 3D architecture to ensure multidirectional contraction to maximise cardiac output [6].

Due to the differing functions of the four cardiac chambers, there is substantial heterogeneity in anatomy. The ventricular walls are thicker than the atria for example, and the LV is approximately three times thicker than the RV due to the greater force required for delivery of blood to the systemic compared to pulmonary circulation. There are also regional differences. The inner endocardial layer of the heart contains mainly endothelial cells. Meanwhile, the epicardium connects the heart to the pericardium, the double sac of connective tissue and serous fluid that protects the heart. The epicardium hence is made up primarily of connective tissue [6].

1.1.2 Cardiac conduction system

Efficient pumping of the blood is achieved through the coordinated contraction and relaxation of the cardiac muscle in all four chambers. The contraction of the individual cardiomyocytes, like other muscle cells in the body, is initiated by the electrical excitation of the cell. For the heart to contract, electrical impulses must therefore propagate through the tissue in a coordinated manner. In a healthy heart, rhythmic activity is known as sinus rhythm. During sinus rhythm, electrical impulses, known as cardiac action potentials (AP) begin in the sinoatrial node (SAN), a region located in the RA, near the SVC, which contains pacemaker CMs

[7]. Pacemaker cells are specialised, exhibiting automaticity – they depolarise without an impulse from a neighbouring cell. It is these cells in the SAN therefore that set the heart rate and begin the conduction of electrical impulses through the cardiac tissue. A schematic diagram of the electrical conduction system is shown in Figure 1.3 [1].

From the SAN, electrical impulses must spread throughout the rest of the heart. In the healthy myocardium, CMs are electrically coupled by low resistance gap junctions [8]. Gap junctions are formed of connexins, transmembrane proteins that form a connexon (or connexin hemichannel), an assembly of six connexins with a pore domain. The connection of two connexons from neighbouring cells creates the gap junction, which allows for bi-directional flow of ions (and signalling molecules) between the two cells [9].

Owing to the gap junctions, current from a depolarised cell can flow to its electrically coupled neighbouring cell, assuming that the neighbouring cell is less

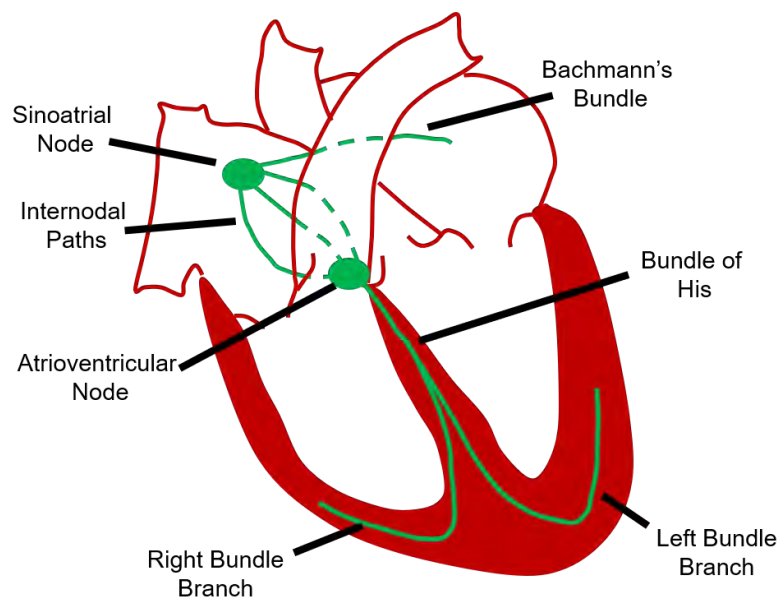


Figure 1.3: Electrical conduction system of the heart. The primary conduction pathways and nodal regions are shown in green.

depolarised. The transmembrane voltage (V_m) of the neighbouring cell will then increase until it reaches threshold potential. At this point, voltage gated Na^+ channels will open, causing a large influx of Na^+ and initiating the AP. This cell-cell communication is the process by which electrical impulses are spread throughout the heart [10].

To facilitate conduction, specialised tracts with very fast conduction speeds connect the SAN to the LA (Bachmann's bundle) and to the atrioventricular node (AVN) which sits at the interatrial septum at the junction between the atria and ventricles. Electrical impulses in the AVN are slowed, travelling at a slower conduction velocity (CV), hence allowing the ventricles to fill following atrial contraction. Following the AVN, the electrical impulses enter the bundle of His, which splits into left and right branches, and are spread throughout the ventricles via the Purkinje fibres [8]. The CV in the fibres is *ca.* 200-400cm/s, ensuring coordinated muscular contraction. Within the ventricular muscle itself, the impulse travels at *ca.* 50cm/s, generally from the endo- to epicardium [10], [11].

Several factors dictate the directionality and speed of impulse transmission in cardiac tissue. CMs are elongated cells that form strands, with the gap junctions forming preferentially at cell ends. The result is larger CVs in the longitudinal direction, parallel to cell alignment, compared to transverse or perpendicular direction [12].

A larger cell size and lower cell-cell resistance will increase CV as it will increase the amount of axial current that flows from one cell to the next [10]. Hence, cells in the specialised conduction fibres described above are larger and contract less

than others in the heart [6]. In contrast, both gap junction uncoupling (reduction of electrical conductivity between the cells) and reduction in fast sodium current (via loss, block or reduced function of sodium channels) are prominent mechanisms by which conduction can slow in cardiac tissue [10], [13], [14]. The causes of conduction slowing can be genetic in origin, for example expression or functional changes in ion channels altering electrical properties, pharmacological or in response to lifestyle or injury [13]–[16]. Understanding slowed cardiac conduction is paramount as it is a key mechanism underlying arrhythmia [17],[18].

The cardiac action potential

The electrical impulse that propagates and causes the contraction of CMs is the cardiac action potential (AP) [19], [20]. The cardiac AP is a transient de- and repolarisation of a CMs transmembrane voltage (V_m). It is initiated and controlled by the movement of ions such as Na^+ , Ca^{2+} , and K^+ , into and out of the intra- and extracellular environment, both through the cell membrane (via ion channels and pumps) and through intracellular stores such as the sarcoplasmic reticulum (SR) [20], [21].

An example human ventricular AP is shown in Figure 1.4A [22], alongside the associated time courses of the various currents which contribute to generation AP. The AP consists of four phases [2], [6] –

Phase 0 (Depolarisation): The AP of a neighbouring myocyte raises the V_m from the resting membrane potential (RMP) to a threshold value (ca. -60mV).

This triggers the opening of voltage gated Na^+ channels, rapidly increasing Na^+ membrane conductivity and hence generating a large depolarising influx of Na^+ ions, I_{Na} . The V_m rapidly depolarises to around +20 to +30mV, and the sodium channels inactivate automatically due to the short-lived time dependence of their open state.

Phase 1 (Initial Repolarisation): The V_m then begins to initially repolarise quickly due to the transient outward current, I_{to} . I_{to} results from voltage gated K^+ channels which open at positive potentials, allowing K^+ ions to flow out of the cell along the electrochemical gradient. Chloride influx (Cl^-) is also known to contribute to I_{to} . The rise in intracellular Na^+ also leads to an increase in

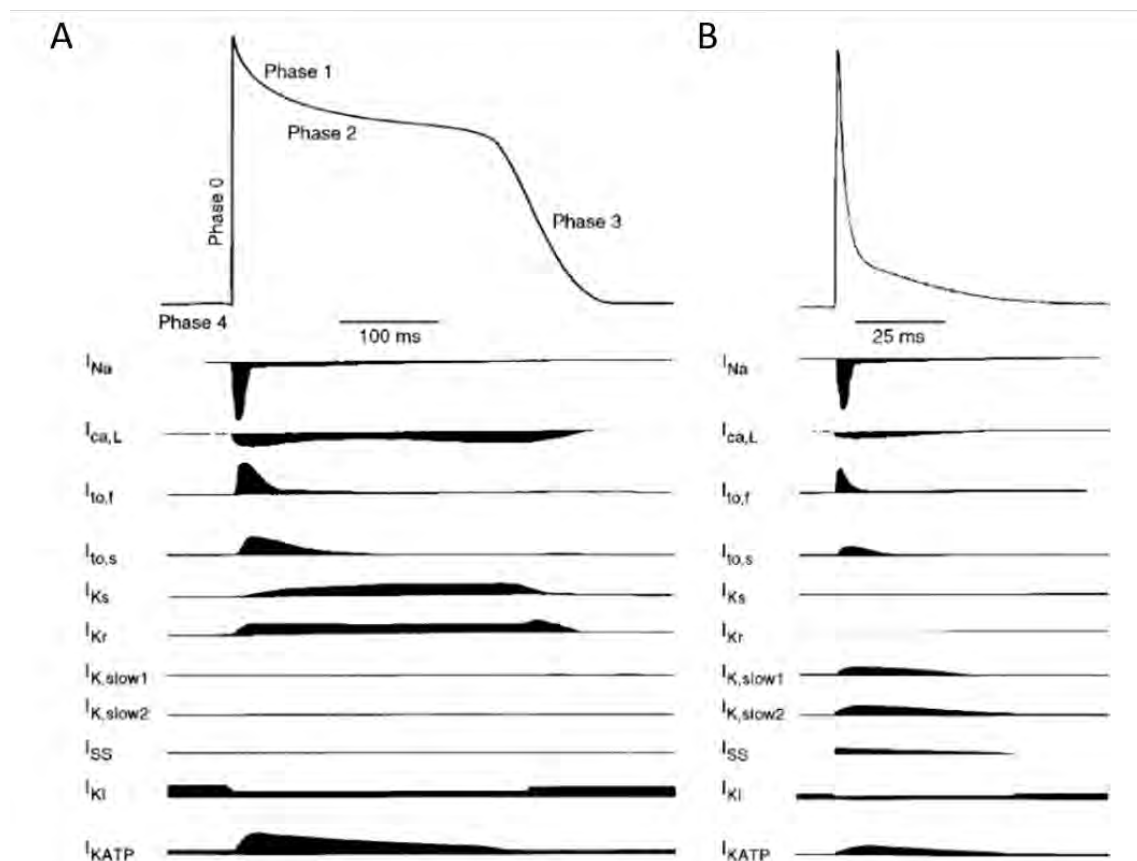


Figure 1.4: Example human and mouse action potentials. A) Example human action potential and ionic currents. B) Example mouse action potential and ionic currents. Inward (depolarising) currents are shown as negative values while outward (repolarising) currents are shown as positive values. Extracted from [22]

sodium-potassium pump activity (I_{NaK}) which expels three Na^+ for two K^+ , increasing the repolarising I_{NaK} current during the AP.

Phase 2 (Plateau): The rapid depolarisation of the cell also initiates voltage gated channels known as long opening (L-type) Ca^{2+} channels. These channels carry a depolarising current, I_{CaL} , bringing Ca^{2+} ions into the cell. These channels open and inactivate more slowly than the fast sodium channels, prolonging the action potential and starting the plateau phase of the human (and other large animal) ventricular AP. Peak I_{CaL} occurs approximately 2-7ms after the AP initiation, and subsequently slowly decreases. I_{CaL} closely matches the outward K^+ current, which is reduced during the plateau phase due to obstruction of inward rectifier channels (I_{Kir} , or also referred to as I_{K1}) at depolarised V_m .

As the time dependent L-type Ca channels begin to close, reducing I_{CaL} , the late plateau phase is maintained by the Na^+ - Ca^{2+} exchanger (NCX). The influx of Ca^{2+} into the sarcoplasm from both the L-type Ca^{2+} channels and calcium induced calcium release from the SR activates NCX. NCX exchanges three Na^+ for one Ca^{2+} , and is hence electrogenic, creating depolarising current I_{NCX} .

Phase 3 (Repolarisation): In the late plateau phase, K^+ conductance begins to rise due to activation of delayed and slow rectifier K^+ channels (I_{Kr} and I_{Ks}). These channels are voltage gated, like the Na^+ and Ca^{2+} channels, but are much more slowly activated, driving repolarisation in the late phase of the AP. Furthermore, the repolarisation of V_m leads to reactivation of I_{Kir} , further driving late repolarisation.

Phase 4 (RMP): In non-pacemaker cells, V_m will then sit at the RMP of *ca.* -90mV

owing to the constant outward flow of K^+ ($I_{K_{ir}}$), the closed state of the Na^+ and Ca^{2+} channels and activity of the NaK pump.

Following phase 1 depolarisation, healthy CMs enter an effective refractory period (ERP). During this period, increased V_m and inactivated Na^+ channels means that the cell is un-excitabile. This mechanism prevents retrograde excitation and ensures the electrical impulse travels throughout the heart as described above. As the cell repolarises and the Na^+ channels reactivate, the cell can be reactivated by a depolarised neighbouring cell, ending the ERP. Changes in the ERP, like CV, are implicated in arrhythmogenesis (see section 1.2) [18].

The AP described above relates to a human ventricular AP. However, just as there is heterogeneity in the anatomical structure of the heart, the same is true for the cellular and EP properties of the heart. For example, CMs can be broadly classified into three classes [6], [23].

(i) Working CMs: These cells form the bulk of the myocardium and are connected as described above to create a mechanical and electrical syncytium. The sarcolemma of most cardiomyocytes contains invaginations known as t-tubules, allowing ion transfer deep into the cells during the AP, vital for excitation-contraction (EC) coupling.

(ii) Pacemaker CMs: These cells make up the SAN and AVN and exhibit automaticity: the ability to spontaneously initiate an action potential without an external stimulus. They achieve this through spontaneous diastolic depolarisation thanks to specialised ion channels, primarily HCN4. These

channels, at negative V_m , slowly conduct Na^+ . The current produced by these channels is the funny current (I_f), and during diastole I_f depolarises the membrane towards AP initiation threshold. These cells are smaller than the working cardiomyocytes, exhibit limited contraction and are highly innervated to realise regulation of cardiac function by the autonomic nervous system. In a healthy heart, cells in the SAN exhibit the fastest rate of spontaneous activity, and hence set the heart rate by overdrive pacing.

(iii) Conduction CMs: These cells are found in fibres such as the bundles of His and Purkinje fibres. They are similar to the working CMs but are larger and contract less to realise increased conduction speeds.

These three cell types show marked differences in AP morphology throughout the heart. However, AP heterogeneity is not simply limited to these three broad cell types. The CMs throughout the heart will differ depending on location and function. The atrial and ventricular APs are morphologically distinct. Furthermore transmural dispersion, alterations in AP morphology in the epicardial, myocardial and endocardial layers, has been reported in human [24] and animal models [25]. Work which forms sections of this thesis (chapter 5) has shown that the mouse, a widely utilised model within cardiac research, also exhibits significant transmural gradients in line with large animal models [26], [27]. Differences are also present between the LA versus RA and LV versus RV [28].

Excitation-contraction coupling

The purpose of the coordinated spread of electrical stimuli throughout the cardiac tissue is to elicit contraction. The process by which an AP causes cellular contraction is known as excitation-contraction (EC) coupling and is mediated by Ca^{2+} . At rest, the intracellular Ca^{2+} concentration ($[\text{Ca}^{2+}]$) is $0.1\mu\text{M}$ [29]. However, as Ca^{2+} enters the cell via L-type Ca^{2+} channels during the AP, $[\text{Ca}^{2+}]$ rises.

The initial rise in $[\text{Ca}^{2+}]$ via the L-type channels initiates a process termed calcium-induced calcium release. The sarcoplasmic reticulum (SR) is an intracellular organelle which is a large store of Ca^{2+} , and within its membrane contains ion channels and pumps. One of these channels is the Ca^{2+} activated release channel, the ryanodine receptor (RyR) [30]. Large amounts of Ca^{2+} is therefore released from the SR. The result is an increase in $[\text{Ca}^{2+}]$ to around $100\mu\text{M}$, although substantial buffering of the Ca^{2+} ions limits the concentration of free Ca^{2+} to *ca.* $1\mu\text{M}$ [21].

The free Ca^{2+} is then able to activate myofibrils within the CM sarcomere, the functional unit responsible for contraction [21]. Within the sarcomere, free Ca^{2+} binds to troponin-C, which forms part of the wider troponin complex. The troponin complex acts to regulate the action of the thin actin and thick myosin filaments. At rest, troponin-I blocks actin binding sites, preventing crossbridge formation with myosin. On Ca^{2+} binding to troponin-C, a conformational change is induced that initiates troponin-I to expose a binding site on the actin molecule [1]. This actin site can then bind to the ATPase head of myosin, forming a crossbridge. Through

ATP hydrolysis, flexion of the myosin head is induced, bringing the thin filament closer to the sarcomere centre, shortening the sarcomere length and contracting the cell [29].

For the cell to subsequently relax, $[Ca^{2+}]$ must be removed from the cytoplasm to allow unbinding from troponin-C, resetting the sarcomere to its resting length. Ca^{2+} removal back into the SR is mediated by the action of the SR Ca^{2+} -ATPase (SERCA). Concurrently, Ca^{2+} is also extruded from the cell via NCX. There is also some minor contribution (<1% in rabbit CMs) from mitochondrial channels (mitochondrial Ca^{2+} uniporter) and the membrane pump Ca^{2+} -ATPase [31]. EC coupling therefore is the basis by which electrical impulses, namely the cardiac AP described above, control and coordinates the contraction of the heart. The rise and fall of $[Ca^{2+}]$ that mediates ECs coupling is known as the calcium transient (CaT) [21].

1.2 Cardiac Arrhythmias

The previous sections describe healthy cardiac rhythm and electrical function and conduction, known as sinus rhythm. However, disturbances in the electrical function of the heart can cause the heart, or specific areas of heart, to develop an irregular rhythm known as an arrhythmia. Disturbances in heart electrical function can arise for several reasons. These include acute periods of ischemia or hypoxia, genetic variants which alter electrical or mechanical function, dysregulation by the autonomic nervous system, tissue remodelling such as cardiac hypertrophy or fibrosis, ionic disturbances and hormonal or

pharmacological influences that alter ion handling properties [13], [15], [20], [32]–[34]. Cardiac arrhythmias present a substantial health burden [35]. The most commonly sustained arrhythmia for example, atrial fibrillation (AF), is diagnosed in between 2-3% of adults in US and Europe [36], with actual occurrence likely to be higher owing to undiagnosed or silent AF [37].

1.2.1 Mechanisms of cardiac arrhythmias

The primary mechanism by which an arrhythmia, such as AF, is sustained is known as the driver and can result from problems in either the generation or propagation of APs.

Disturbances in action potential generation: ectopic activity

In the healthy heart SAN pacemaker cells generate an AP, which then propagates throughout the conduction system [8]. However, the sinus node function can become pathophysiological through influences such as changes in autonomic regulation or injury [7]. Furthermore, electrical stimuli can arise outside of the SAN, a phenomenon known as ectopic activity [32]. Due to injury, genetic factors, aging and other factors, CMs throughout the heart can develop their own pacemaker activity ('latent' pacemakers) [38]. Cells that develop their own pacemaker activity can become uncoupled from the SAN activity, causing new activation sites from which depolarising waves propagate and thus disrupt the normal coordination of the heart, resulting in arrhythmia [39]. This disruption

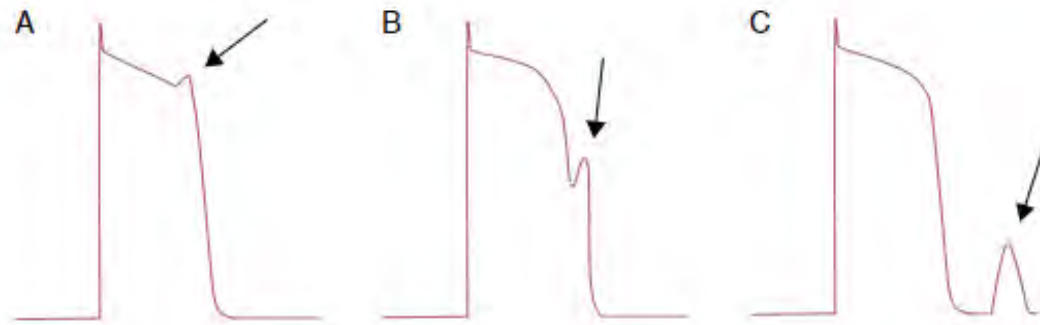


Figure 1.5: Triggered activity examples A) Early afterdepolarisation. B) Phase 3 afterdepolarisation. C) Delayed afterdepolarisation. Extracted from [40].

can result in the initiation of spiral wave activity, see below.

Additionally, cells can exhibit abnormal depolarisation events during or just after the repolarisation phase of the AP, known as afterdepolarisations. If the amplitude of afterdepolarisation is sufficient, it can trigger an AP, which may then activate neighbouring cells, resulting in a triggering site which again decouples cells from SAN activity.

Afterdepolarisations are split into 2 subclasses. Early after depolarisations (EADs, Figure 1.5A-B) occur during phase 2 or 3 of the AP. EADs develop because of a shifting of the normal outward current during repolarisation to a net inward current, and frequently occur with a prolongation of APD. The prolongation of the AP allows recovery of L-type Ca^{2+} , allowing regeneration of depolarising I_{CaL} [41].

Delayed after depolarisations (DADs, Figure 1.5C) occur in phase 4, and can often be linked to alterations in intracellular Ca^{2+} concentrations or malfunctions in the SR Ca^{2+} channels, RyRs [42]. These factors can cause abnormal diastolic levels of $[\text{Ca}^{2+}]$, activating Ca^{2+} extrusion via NCX, increasing

depolarising current I_{NCX} .

Disturbances in action potential propagation: re-entry

Abnormalities in the propagation of APs can also lead to arrhythmias, in particular the initiation of self-sustaining depolarisation wavefronts [10]. An example is the genesis of re-entrant circuits in cardiac tissue. Re-entry can occur when a block within cardiac tissue blocks the activation wavefront. The wavefront hence propagates around the block. If there is an area of unidirectional block, the activation wave will travel around the block in one direction. In certain circumstances, the circular wavefront can become self-sustained and rapidly activated, as shown in Figure 1.6, causing arrhythmia [40], [43], [44]. This phenomenon is described as leading circle re-entry.

The likelihood of a reentrant circuit forming in this manner is described by the cardiac wavelength (WL) which is equal to ERP x CV, and hence describes the distance travelled by a wavefront in one refractory period. With a shorter wavelength (short ERP and/or slow CV), it is more likely that a retrograde wavefront will not collide with its refractory tail, meaning the activity becomes self-sustained. Several pathophysiological mechanisms can alter ERP or CV, including altered ionic handling, cardiomyocyte gap junctional and adherence coupling, and tissue remodelling. Prolongation of cardiac WL, for example by increasing ERP by pharmacological ion channel modulation, is hence a key therapeutic strategy used to treat arrhythmia [45] .

Although the first appreciation of leading-circle re-entry dates back to the late

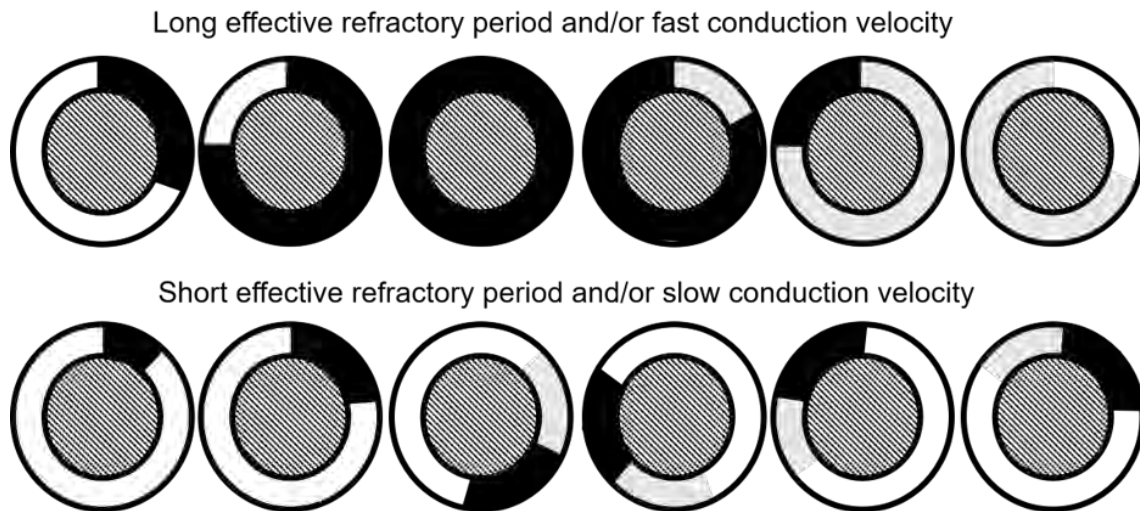


Figure 1.6: Model of re-entry. Example of re-entry around an area of functional or anatomical block. Excited/refractory tissue is shown in black, and relative refractory period is shown in grey. In the top example, a long effective refractory period and/or fast conduction leads to the wave colliding with its own refractory tail, terminating activity. In the bottom panels, short effective refractory period and/or slow conduction means the wavefront does not collide with its refractory tail and continues to propagate indefinitely. Adapted from [44]

1800s [44], [46], [47], the related but distinct concept of spiral-wave re-entry has only more recently been studied [47]–[50]. The chemical Belousov–Zhabotinsky reaction demonstrates that a fundamental property of excitable media, like cardiac tissue, is the potential emergence of complex and dynamic macroscopic activity such as spiral excitation waves [51], [52]. Well before the first experimental observations [50], *in silico* studies had shown the possibility of spiral waves in cardiac tissue [49], [53].

A spiral wave rotates outwards from a centre with a curved activation front, Figure 1.7A. A curved wavefront is a key distinguishing feature of spiral waves. In contrast to a planar wavefront, a cell at the curved wavefront edge is coupled to more than one cell if the spiral wave is convex, and less than one cell if the wavefront is concave, Figure 1.7B. This has important consequences for CV, as it alters the ratio between the excited (source) and excitable (sink) cells. In the

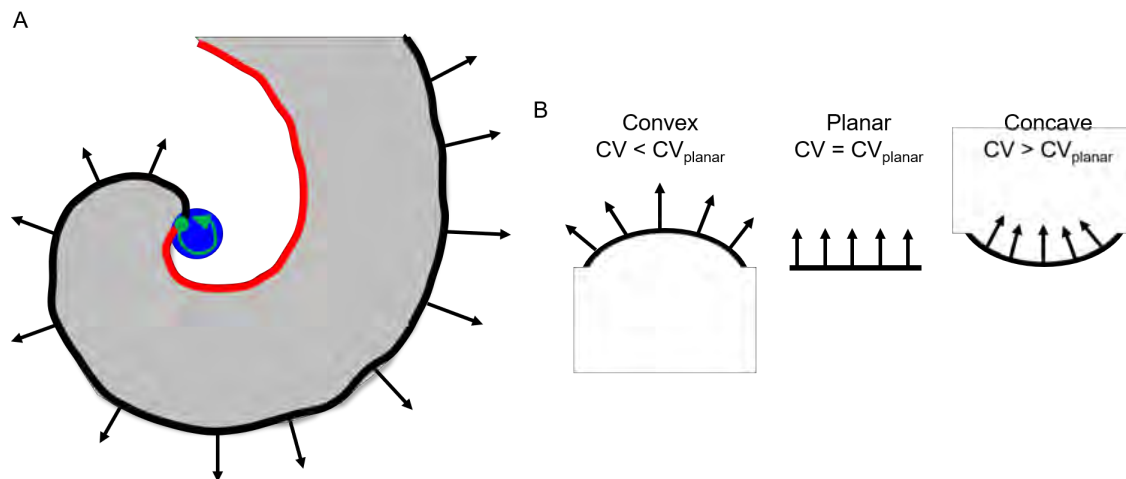


Figure 1.7: Spiral wave re-entry. A) Diagram of a spiral wave. The activation wavefront is shown in black while the repolarisation wavetail is shown in red. The point where the wavefront and tail meet is the phase singularity point which has undefined voltage state, marked in green. The blue area marks a possible region within which the phase singularity point may meander. B) Effects of wavefront curvature on conduction velocity (CV) compare to the CV of planar wave (CV_{planar}). In both panels, black arrows indicate activation direction. Adapted from [47]

case of a convex wavefront, CV is reduced as the current flow from one cell is spread, leading to less current flow into the individual cells and a greater time for activation threshold V_m to be reached. The opposite holds for concave waves, where CV is increased compared to planar waves owing to a larger source-sink ratio [47].

The spiral waves are often anchored to unexcitable tissue, such as small arteries or connective tissue [50]. However, they can also rotate around a normally excitable core where the depolarising wavefront meets the repolarisation wavetail. The meeting of the fronts at this point renders this region unexcited and is known as the phase-singularity point. The core of such a spiral wave can circle a small region or even meander through the cardiac tissue depending on the interaction between the activation wavefront and repolarisation wavetail

(black and red in Figure 1.7A respectively), unlike when a spiral wave is anchored to an anatomical feature [47], [50].

A spiral wave can be initiated by disturbance of a normal, sinus, wavefront by an anatomical feature or by spontaneous activity, such as ectopic activation of a competing wavefront. In the case of an ectopic wavefront, it will propagate until it meets refractory tissue created by the sinus wavefront, where ectopic activation is blocked. However, as the refractory cells recover, the ectopic wavefront will begin to excite cells preferentially in the direction that the sinus recovery wavetail travels, curving the wavefront of the ectopic wave. If the conditions are such that the now curved ectopic wavefront continuously encounters excitable cells, a sustained spiral wave is setup. Again, as with leading circle re-entry, the likelihood of this occurring depends on CV (and therefore wavefront shape for the reasons described above) and ERP. A shorter ERP promotes the re-entrant behaviour by increasing the probability of cells at the wavefront being non-refractory, as does a slowing of CV.

1.2.2 Atrial Fibrillation

Arrhythmogenesis is hence multifaceted, and there are many subtypes of arrhythmias with distinct pathophysiological causes, manifestations and localisations. As already highlighted, Atrial fibrillation (AF) is the most common arrhythmia and increases the risk of stroke, heart failure and sudden death [54], [55]. AF is a supraventricular arrhythmia, characterised by the rapid and disorganised activation of atrial cardiomyocytes at rates of up to 600

depolarisations per minute [56]. Both triggered activity and re-entry have been proposed as mechanisms by which AF is induced and maintained [48], [56], [57]. Current treatment for AF includes pharmacological rate or rhythm therapy [45], and surgical interventions such as electrical isolation through catheter ablation procedures [54]. All treatment options however demonstrate variable results and inconsistent outcomes for patients [15], [37], [58], highlighting the requirement for further study of the causes and mechanisms of AF, alongside other arrhythmias.

1.3 Measuring cardiac electrical activity

The electrical activity of the heart, both in health and disease, has long been studied. The first electrocardiogram (ECG) for example was reported in 1887 [59]. The ECG remains a staple of clinical cardiac electrophysiology to non-invasively study the electrical activity of the heart. By placing electrodes at the body surface, changes in the extracellular potential of the heart during the initiation and propagation of APs can be recorded. A 'normal' ECG waveform in sinus rhythm is shown in Figure 1.8 [1], and its various deflections are split to aid interpretation. The P wave for example is associated with atrial depolarisation, the QRS complex with ventricular depolarisation and the T wave with ventricular repolarisation [60]. Changes in the timing, duration or morphology of these deflections are used to diagnose arrhythmia [61], [62].

Single trace electrograms as in the case of ECG signals give a summative signal of the electrical activity of the heart. However, electrograms can also be mapped

across the heart surface using both invasive and non-invasive techniques. Invasive catheters with electrodes on their surface can record electrograms from the endocardial or epicardial surface [63], [64]. Both single electrode and multielectrode catheters are used, and by manoeuvring the catheter across the cardiac tissue high resolution maps of electrograms can be constructed. Features of these electrograms, for example, activation time, voltage amplitude or fractionation, are often used for monitoring or in guiding interventional procedures such as ablation [65]. Non-invasively, an array of several electrodes (>100) on the body can be used to map the electrical activity at body surface. From this information, the potential at the epicardial surface can be calculated and mapped [66], in a procedure known as body-surface mapping [67]. Electrograms can also be mapped using multi-electrode arrays, which have found use both clinically [63] and pre-clinically [68].

An electrogram is a multiphasic recording of changes in extracellular potential, and not directly of the transmembrane potential, which is the difference between

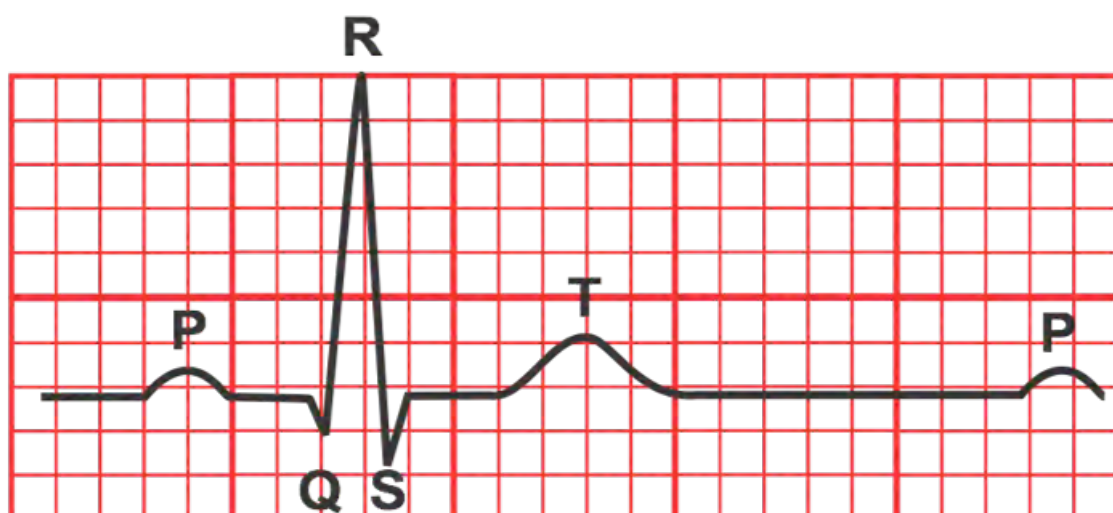


Figure 1.8: Sinus rhythm electrocardiogram. The P wave represents atrial depolarisation, the QRS complex represents ventricular repolarisation, while the T wave represents ventricular repolarisation [1]

the extracellular and intracellular potential, i.e. the potential that changes during the action potential. Action potentials can be directly recorded using microelectrodes, where one electrode records the intracellular potential while another records extracellularly. The difference between the two electrodes then gives the transmembrane AP (TAP) recording from a single cell [32]. Similarly, intracellular potential changes can be measured by patch clamp technique, where suction is used to probe the intracellular space, and current controlled ('current clamp') to record voltage changes compared to an extracellular reference, again from a single cell [69]. Patch clamp can also be operated in 'voltage clamp' mode, to probe specific ionic currents by using intracellular and extracellular solutions to isolate currents of interest [69], [70].

Furthermore, the AP can be measured using electrodes without direct contact with the intracellular space as monophasic APs (MAPs). Compared to microelectrodes used in patch clamp or to record TAPs, MAP electrodes are larger ($>0.1\text{mm}$ diameter), thereby recording from many cells, and consist of a proximal and distal electrode, neither of which crosses the membrane [71], [72]. However, by inactivating one part of the tissue, signals can be recorded with similar morphology to those obtained via microelectrodes. MAP recordings match those of TAPs with extremely high fidelity [73]. The exact mechanisms behind the origin of MAPs however is still under debate [74].

1.4 Optical mapping

Electrode techniques are either indirect recordings of the AP (in the case of electrograms) or inherently low spatial resolution (from single cells/region). Even high-density electrogram arrays and catheters are spatially limited by the physical size of electrodes. These drawbacks have led to the adoption of optical mapping.

Optical mapping is a fluorescence-based technique, where cardiac preparations are 'stained' with dyes sensitive either to transmembrane voltage or intracellular calcium concentration. By appropriate imaging of these preparations, high spatiotemporal resolution mapping of AP and CaT activation and morphology can be achieved, far exceeding the resolutions possible with electrode techniques [69]. As a result, since the first demonstration in cardiac tissue with voltage sensitive dyes in 1976 [75], optical mapping has furthered our understanding of cardiac EP and arrhythmias in several ways. Among others areas, optical mapping has expanded our knowledge of the role of spiral wave and genetic predispositions in AF [15], [48], gap junctional remodelling in sudden cardiac death [76], transmural heterogeneity in cardiac tissue [27], [77] and autonomic regulation in health and disease [34], [78], [79]. Optical mapping has been applied in cardiac preparations including whole hearts [80], isolated atria [32], [81], [82], ventricular wedges [83], cardiac slices [26], [27], [79] and cellular monolayers [84].

1.4.1 Voltage sensitive dyes

Optical mapping relies on the use of fluorescent dyes, i.e. synthetic or biological molecules that emit light with a spectrum that is shifted in wavelength when compared to excitation wavelength [85], [86]. Commonly, the emission wavelength is longer than the excitation wavelength. An electron transitions to a higher energy state when it absorbs a photon of appropriate wavelength. In the excited state several mechanisms mean the excited electron can undergo non-radiative transitions to lower energy levels (but not back to ground state). The result is the energy difference of electron relaxation back to ground state is lower compared to its excitation, and so the photon emitted during relaxation is lower energy and longer wavelength than the excitation/illumination photon, Figure 1.9A [87].

In the case of voltage sensitive dyes (VSDs), the most commonly used for

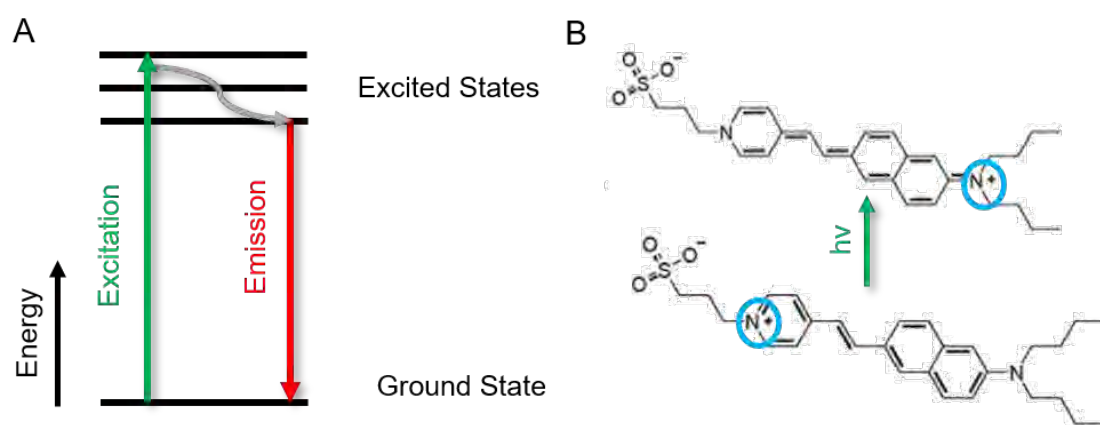


Figure 1.9: Jablonski diagram and chemical structure of di-4-ANEPPS. A) Jablonski diagram of excitation of a dye by absorption of an incoming photon (green), While excited, the molecule undergoes non radiative energy transitions (grey) and emits a photon of lower energy (red). B) Chemical structure of Di-4-ANEPPS in both its ground (bottom) and excited (top) state. Blue circle highlights the shift of charge distribution on excitation

cardiac optical mapping are synthetic styryl dyes, such as Di-4-ANEPPS (di-4-amino-naphthyl-ethylene-pyridinium-propyl-sulfonate, Figure 1.9B). Di-4-ANEPPS imbeds within the cellular membrane. Excitation of Di-4-ANEPPS can shift the molecule from a ground state to an excitation state with an altered charge distribution (Figure 1.9B) [88]. However, the electric dipole of the molecule means the surrounding electric field shifts the energy levels of the electronic field. This phenomenon is known as electrochromic shift [89]. Thus, the wavelength spectra emitted by dyes such as Di-4-ANEPPS is proportional to the surrounding electric field, and hence the transmembrane voltage when the dye is embedded in the cellular membrane. In the case of Di-4-ANEPPS, there is a 'blue shift' in the emission spectra, i.e. at more positive membrane potentials, the peak emission wavelength decreases, Figure 1.10 [88], [90]. Hence, by recording the fluorescence intensity through a long-pass filter, an (inverted) optical recording of the AP is obtained, Figure 1.10 [91].

Several other synthetic VSDs used in optical mapping work on similar principles, such as Di-8-ANEPPS (an analogue of Di-4-ANEPPS with altered chemical structure to avoid dye internalisation) and Rh-237 [34], [43]. Synthetic electrochromic dyes are the mostly widely utilised in optical mapping. However, alternative strategies are available. Some dyes, in particular genetically encoded VSDs, use Förster energy resonance transfer (FRET) to sense voltage [85]. These dyes are thought to overcome some drawbacks of electrochromic dyes with respect to signal quality, phototoxicity and photobleaching [92], although limitations persist with response times and delivery [93]. Newly developed dyes (e.g. FluoVolt) work on the principle of photon-induced electron transfer [92] and

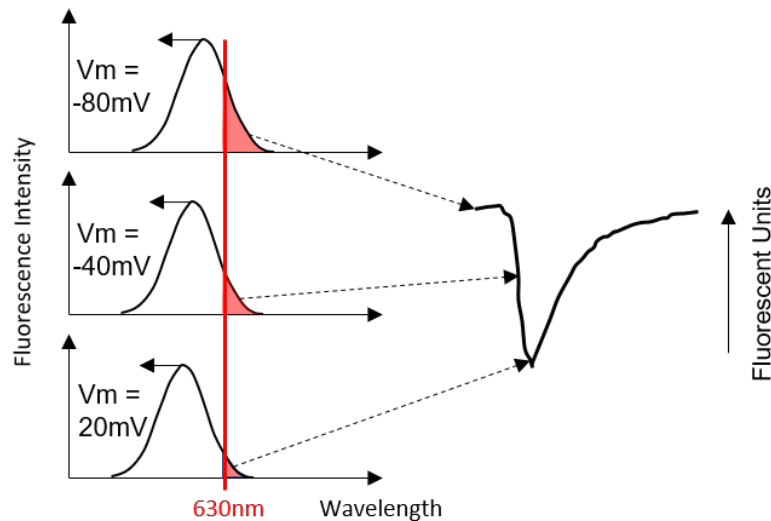


Figure 1.10: Principle of optically recorded action potentials using voltage sensitive dye (VSD). Example spectra of emitted fluorescence of a VSD at different transmembrane potentials (V_m). The red line represents a long pass filter. As the increase in V_m during depolarisation induces spectral shift, the number of photons passing through the filter (red region) decreases. The result is a measured fluorescence intensity that is inversely proportional to V_m , and an inverted optical recording of the action potential as shown on the right. Figure adapted from [91]

have been shown to outperform electrochromic indicators for signal quality and experimental lifetime. However, their use remains sparse [94] and studies have also suggested these dyes may induce side effects on cardiomyocyte properties [95], although the same can be said for other VSDs [85], [96].

1.4.2 Intracellular calcium dyes

A separate class of dyes used in optical mapping are intracellular Ca^{2+} sensors that internalise within the cell. They are commonly esterified to neutralise the charge, aiding intracellular uptake. The ester is then enzymatically cleaved once in the cell, leaving behind a Ca^{2+} chelator and a fluorophore. As Ca^{2+} is chelated, fluorescence output increases, and subsequently decreases upon dissociation,

reporting the changing Ca^{2+} concentration in the intracellular space where the sensor localises, either in the cytosol or sarcoplasmic reticulum [97].

1.4.3 Optical mapping hardware

A full review of optical mapping setups as part of a wider technical review into all-optical electrophysiology through the combination of optical mapping with optogenetic technologies is provided as part of section 4.1 [98]. The specific setup predominantly used in this thesis is described in detail in section 2, while other setups from which data is presented are described where appropriate.

Briefly, an optical mapping setup consists of the following key components. An illumination source is required to excite fluorescent dyes. An ideal illumination source will be spatially and temporally homogeneous in order to reduce non-physiological fluorescent alterations. The most commonly used illumination sources are therefore LEDs, which benefit from narrow wavelength spectra, long operational lifetimes and low heat emission [99], though Tungsten-Halogen lamps, Mercury/Xeon arc lamps and lasers have also been used. Optical filters are then required to separate the excitation light from the emitted fluorescence light. The emitted fluorescence is then imaged by a camera. In modern optical mapping setups, charge-coupled device (CCD) and complementary metal oxide semiconductor (CMOS) cameras are most commonly used. These cameras are utilised as they allow collection of high spatial resolution images ($>10,000$ pixels) at kHz sampling rates to effectively capture the millisecond dynamics of cardiac activity [100].

1.4.4 Optical mapping data processing

The high spatio-temporal imaging of cardiac electrical behaviour afforded by optical mapping results in large raw datasets, commonly composed of thousands of image frames each individually made up of multiple pixels [101]. Each one of these pixels contains one or more optically recorded AP and/or CaT. Therefore, there is a necessity for high throughput and automated analysis of optical mapping datasets. [102], [103]

Pre-processing

Sub millisecond exposure rates, small pixel sizes, inhomogeneous dye loading, sub optimal illumination and small fractional fluorescence changes means optical signals are often characterised by low signal to noise ratios. Hence, several pre-processing steps are required for effective analysis [104]. Key pre-processing steps and methods are described below.

Region of interest selection by image thresholding

As optical mapping images contain both tissue and background, data masking is required to create a binary mask of 1 for areas to be analysed and 0 for background pixels. Ideally, this process should be done automatically as manual selection is time consuming and susceptible to user bias. Automatic thresholding can be applied utilising the Otsu method [105]. The Otsu method calculates a single threshold value to classify foreground and background pixels based on the

image histogram (distribution of intensity values in an image, Figure 1.11). For a given threshold value, T , the amount of the variance between the intensity of the two classes (σ) is calculated as

$$\sigma(T) = \sqrt{\omega_1(T)\sigma_1^2(T) + \omega_2(T)\sigma_2^2(T)} \quad (1.1)$$

where $\sigma_{1,2}$ is the variance of class 1 and 2 respectively, and $\omega_{1,2}$ is the probability of a pixel being in class 1 or 2 respectively. The threshold value is then chosen so that the variance between the intensity of the two classes is maximised (alternatively: so that the variance within each class is minimised).

Figure 1.11 shows an example of applying Otsu thresholding to an optical

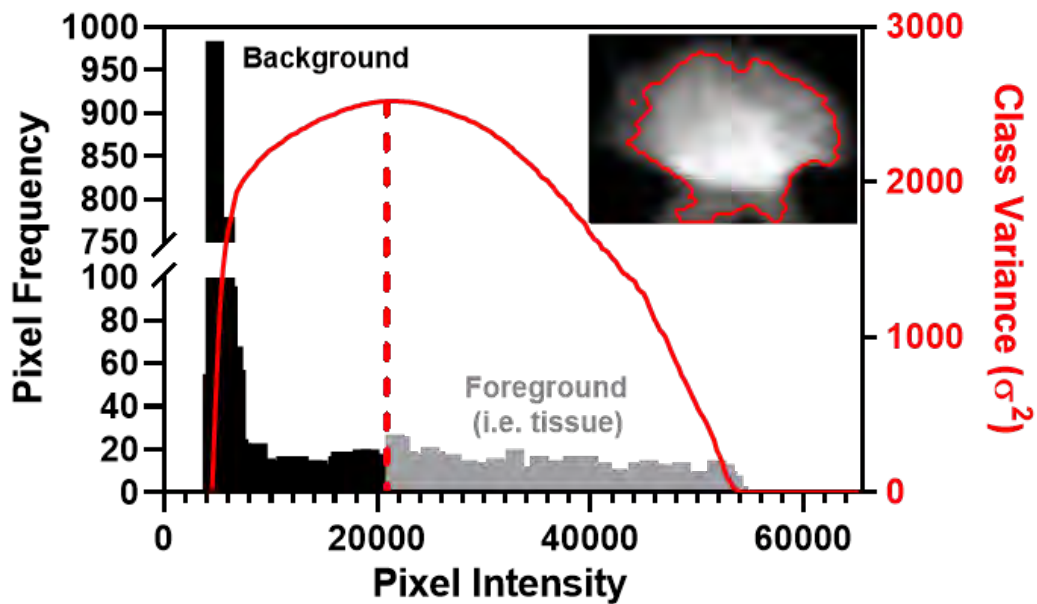


Figure 1.11: Otsu thresholding of an optical mapping dataset. The image histogram of the optical mapping image frame shown in inset is shown on the left y axis. The class variance as a function of a pixel intensity threshold is shown on the right y axis. The result of thresholding using the maximal variance intensity value (dashed red line) is shown in the inset

mapping image. It is observed that the Otsu calculated threshold has successfully removed all background pixels from analysis. However, several tissue pixels have also been incorrectly masked and classified as belonging to the background.

The image histogram shown in Figure 1.11 highlights limitations in using the Otsu method for cardiac optical mapping images. Although a clear peak is observed at lower intensities corresponding to background pixels, the rest of the intensity values are widely and uniformly distributed across a wide intensity range. Non-homogeneous dye loading and/or illumination means baseline intensity can widely vary in optical mapping image sets, resulting in a widespread and non-normal distribution in tissue brightness [101]. In these situations, Otsu method is sub-optimal as the image histogram is not bimodally distributed between background and foreground pixels, making distinction difficult [106]. Initial intensity is also not the only criteria by which pixels may warrant exclusion from analysis. Some tissue areas, despite good dye loading, may exhibit low changes in fluorescence due to physiological or experimental factors, or exhibit motion artefacts. For these reasons, manual region of interest selection, despite being labour intensive, is also commonly used.

Spatial filtering

Spatial filtering or 'binning' is a commonly applied technique to denoise signals recorded from multipixel images. When spatial filtering is applied, the intensity value for a pixel at a given frame number is not an independent value, but rather

an averaged value from neighbouring pixels. This is achieved by convolution of the image frame with a kernel [101]. The main features of a kernel for spatial filtering are size (for example 3x3, 5x5 pixels etc.) and morphology, which dictates the weight of a given pixels location on the final value. For pixel at location x,y , spatial filtering with a $N \times N$ pixel kernel will yield a final intensity $F_{x,y}$ of

$$F_{x,y} = \frac{1}{N^2} \sum_{i=-m}^m \sum_{j=-m}^m f_{x+i,y+j} w_{i,j} \quad (1.2)$$

where $f_{x+i,y+j}$ is the pixel intensity before convolution with the kernel, m is $N/2-0.5$ assuming N is odd and $w_{i,j}$ is the weight at that kernel location, defining the centre of the kernel as $(0,0)$.

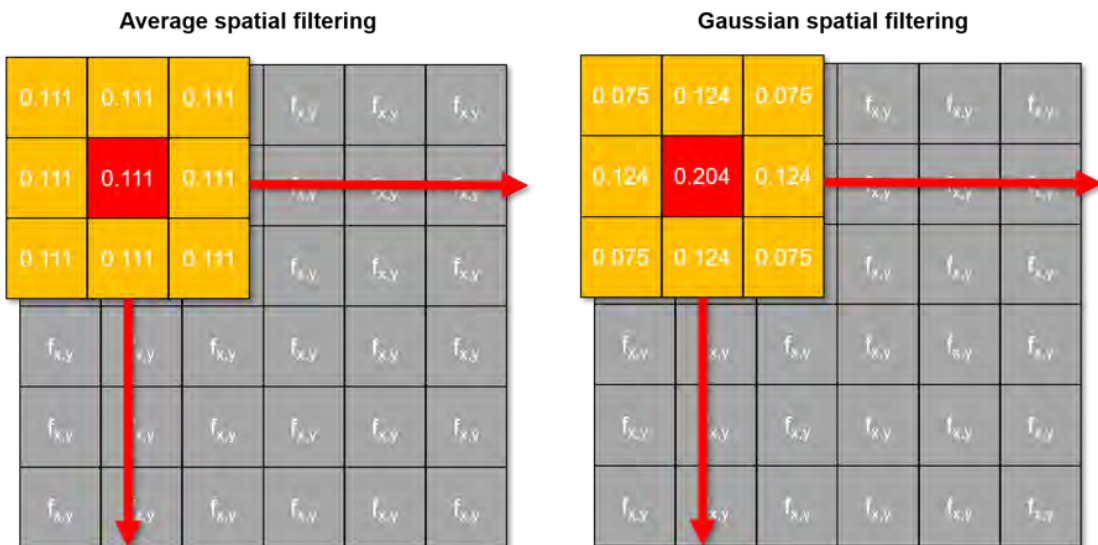


Figure 1.12: Principles of spatial filtering. A) An example of an ‘average’ 3x3 spatial filter (orange/red) applied to an optical mapping image frame (grey) in which each pixel has fluorescent value $f_{x,y}$. The red value is the central pixel to which the convolution will be applied. Following convolution with the average filter, each location will have a fluorescent value $F_{x,y}$ as shown by equation 1.2, where the weights (w) are given by the relevant values in the convolution kernel. B) Similar to (A), but here the convolution kernel weights are described by a Gaussian distribution

If using average or 'boxcar' filtering, then each weight in the convolution kernel will be $1/N^2$. Use of average kernels however may result in spatial broadening and over smoothing of the optically recorded signals, which contain fast alterations for example during depolarisation [101]. An alternative measure therefore is to use a kernel morphology where the pixels closest to the pixel of interest (central pixel) contribute most to the final intensity. Gaussian kernels achieve this by using a Gaussian curve to decide the weight applied to each pixel location based on distance from central pixel. Figure 1.12 for example shows two 3x3 pixel kernels, one average filter (Figure 1.12A) and the other a Gaussian filter with standard deviation of 1 (Figure 1.12B). All weights in the average filter are 0.11, (i.e. $1/3^2$). However, in the Gaussian filter the weight given to the central pixel (0.204) is greater than that of the nearest neighbour pixels (0.124) or next nearest neighbour pixels (0.075). This helps to preserve the underlying morphology of the pixel of interest during spatial filtering denoising.

Temporal filtering

Temporal filtering can be applied in a similar sense to that described above for spatial filtering, but instead with a kernel than spans a certain period in the temporal domain [107]. A simple example of temporal filtering is unweighted moving average filtering, where the value at a given time point is calculated as the average of a set number of points before and after the time point of interest. Unweighted average filtering in this manner can mask/distort impulse-like rapid phenomena in signals, such as the rapidly changing fluorescent values during depolarisation [101]. Savitzky-Golay filtering in contrast fits a low degree

polynomial to datapoints around the point of interest via least-squares fitting [108]. By filtering in this manner, short-lived variations in the signal will be accounted for. Figure 1.13 for example shows the application of 11 point moving average and Savitzky-Golay (3rd order) to a mouse atrial OAP.

An alternative to convolution-based temporal filtering is digital filtering. Frequency spectra analysis of a variety of optically recorded APs from various models shows that the majority of the signal has major frequency components much less than 100Hz, corresponding to physiologically relevant phases of the AP [109]. A well-designed digital filter therefore can directly remove high-frequency ($>100\text{Hz}$) noise while leaving the low-frequency components of the signal (i.e the action potential) unaltered. In practice however, such ideal filtering is not possible as such a filter would be discontinuous and of infinite order. Approximate filters therefore must be designed which can be split into two broad classes: finite impulse response and infinite impulse response. Both filter types contain numerous options including different filter design with varying phase and ripple response, stopband and passband.

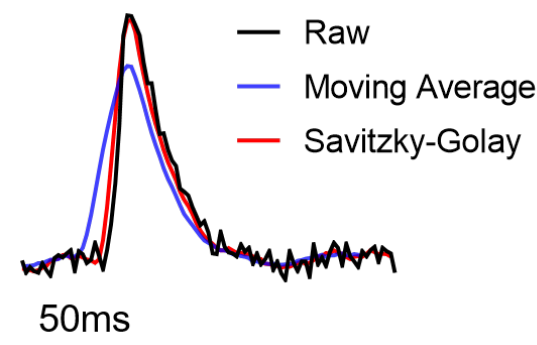


Figure 1.13: Example of convolution temporal filtering methods. Small amplitude, high frequency variations in the raw optical signal (black) are removed by 11 point moving average (blue) and Savitzky-Golay (3rd order, red)

Ensemble averaging

The cyclic nature of cardiac activity means that an alternative to use of spatial or temporal filtering techniques is the use of temporal oversampling and multi-beat (or ensemble) averaging. Here, consecutive APs (or calcium transients) are aligned either by knowledge of pacing cycle length or by signal features such as peak amplitudes [110]. The rationale is that averaging in this manner will reduce the amplitude of signal noise due to its random nature, while preserving the underlying physiological signal. Of course, successful application of ensemble averaging relies on important criteria including accurate signal alignment and temporal stability. The use of ensemble averaging in both model and experimental datasets is explored in chapter 3.

Baseline correction

Factors such as bubbles, photobleaching and fluid motion can cause non-physiological changes in fluorescent signal baselines which require correction. Suggested methods to achieve baseline correction include the application of low degree polynomials, with higher degree polynomials required for more complex variations in baseline values [101]. However, previous studies have suggested that linear top hat filtering may be a more robust method for baseline correction [101]. Here, a structuring element of given length is utilised so that changes with a time period less than the kernel length are removed [101]. Baseline correction is explored in chapter 3.

1.5 Thesis motivation and aims

Once data has been processed using all or a subset of the methods described above, non-consistent techniques and definitions are applied for final analysis. The approaches used are often specific to experimental setup, model, and question. Equally, both processing and analysis requires computational expertise to apply. Several research groups design and utilise custom processing methods [100], [111]–[113], while others use commercial software where the underlying algorithms are difficult to access [114], [115]. Some freely available solutions are present [102], [116], [117], but even basic functionalities such as multi-beat averaging and conduction velocity quantification remain only accessible to a few specialised groups. These limitations prevent further uptake and objective analysis of optical mapping technologies. Therefore, to address these gaps, we pursued the development and utilisation of new tools and software for analysis of optical mapping datasets.

The primary aim of this thesis were:

- To develop processing and analysis tools for optical mapping datasets
- To develop novel analysis approaches to increase automation of optical mapping data analysis
- To use developed tools and techniques for the analysis of unique pre-clinical models using optical mapping, including mouse ventricular slices and genetically altered models
- To study the application and effects of optogenetic pacing on mouse

1.6 Thesis structure

This thesis is an alternative format thesis, whereby following chapter 2, which gives a detailed account to the biological experiments conducted, chapters 3-6 consist of published work.

An introduction is given to each chapter consisting of published articles to explain the contribution of the thesis author and the wider context and significance of the work. Specifically, chapter 3 outlines development and validation of a MATLAB based software platform for analysis of EP mapping datasets [103], [118]. Chapter 4 and 5 focus on the use of this platform to analyse data from optogenetic models (chapter 4) [98], [119] and mouse transverse cardiac slices (chapter 5) [26], [27]. Chapter 6 reports development of a new analysis methodology, termed optical wave similarity, for automated quantification of temporal instability in optical mapping datasets.

Chapter 7 summarises unpublished work using optical mapping to study the effects of high fat diet on left atrial EP on a mouse model with heterozygous deletion of *pitx2*, a transcription factor associated with the development of AF. Chapter 8 is a summary of the work presented and discusses limitations and future work. Due to the inclusion of published works with their own references, individual references are provided for each chapter. All published work is preceded by a short introduction to provide the wider context of the work and to

set out author contributions.

1.7 Chapter 1 references

- [1] R. E. Klabunde, *Cardiovascular Physiology Concepts*, 2nd ed. Baltimore: Lippincot Williams and Wilkins, 2012.
- [2] J. . Levick, *An Introduction to Cardiovascular Physiology*, 5th ed. London: Hodder Arnold, 2010.
- [3] P. Y. Sato et al., "Loss of Plakophilin-2 Expression Leads to Decreased Sodium Current and Slower Conduction Velocity in Cultured Cardiac Myocytes," *Circulation Research*, vol. 105, pp. 523–526, 2009.
- [4] J. R. De Groot et al., "Conduction slowing by the gap junctional uncoupler carbenoxolone," *Cardiovascular Research*, vol. 60, no. 2, pp. 288–297, 2003.
- [5] S. H. Vermij, H. Abriel, and T. A. B. van Veen, "Refining the molecular organization of the cardiac intercalated disc," *Cardiovascular research*, vol. 113, no. 3, pp. 259–275, 2017.
- [6] P. C. Franzone, L. F. Pavarino, and S. Scacchi, *Mathematical Cardiac Electrophysiology*, Volume 13. London: Springer, 2014.
- [7] M. De Marneffe, J.-M. Gregoire, P. Waterschoot, and M. P. Kestemont, "The sinus node function: normal and pathological," *European Heart Journal*, vol. 14, no. 5, pp. 649–654, 1993.
- [8] J. Renwick, C. Kerr, R. McTaggart, and J. Yeung, "Cardiac electrophysiology and conduction pathway ablation," *Canadian Journal of Anaesthesia*, vol. 40, no. 11, pp. 1053–1064, 1993.
- [9] G. Cheung, O. Chever, and N. Rouach, "Connexons and pannexons: Newcomers in neurophysiology," *Frontiers in Cellular Neuroscience*, vol. 8, no. November. pp. 1–19, 2014.
- [10] A. G. Kléber and Y. Rudy, "Basic Mechanisms of Cardiac Impulse Propagation and Associated Arrhythmias," *Physiological Reviews*, vol. 84, no. 2, pp. 431–488, 2004.
- [11] S. Kaese and S. Verheule, "Cardiac electrophysiology in mice: A matter of size," *Frontiers in Physiology*, vol. 3 SEP, no. September, pp. 1–19, 2012.
- [12] M. S. Spach, W. T. Miller, D. B. Geselowitz, R. C. Barr, J. M. Kootsey, and E. A. Johnson, "The discontinuous nature of propagation in normal canine cardiac muscle. Evidence for recurrent discontinuities of intracellular resistance that affect

the membrane currents," *Circulation Research*, vol. 48, no. 1, pp. 39–54, 1981.

[13] C. O'Shea, D. Pavlovic, K. Rajpoot, and J. Winter, "Examination of the effects of conduction slowing on the upstroke of the optically-recorded action potentials," *Frontiers in Physiology*, vol. 10, no. 1295, pp. 1–11, 2019.

[14] M. Entz, S. A. George, M. J. Zeitz, T. Raisch, J. W. Smyth, and S. Poelzing, "Heart rate and extracellular sodium and potassium modulation of gap junction mediated conduction in Guinea pigs," *Frontiers in Physiology*, vol. 7, no. FEB, pp. 1–10, 2016.

[15] F. Syeda et al., "PITX2 Modulates Atrial Membrane Potential and the Antiarrhythmic Effects of Sodium-Channel Blockers," *Journal of the American College of Cardiology*, vol. 68, no. 17, pp. 1881–1894, 2016.

[16] Y. Bao et al., "Scn2b Deletion in Mice Results in Ventricular and Atrial Arrhythmias," *Circulation: Arrhythmia and Electrophysiology*, vol. 9, no. 12, pp. 1–15, 2016.

[17] J. L. R. M. Smeets, M. A. Allesie, W. J. E. P. Lammers, F. I. Bonke, and J. Hollen, "The wavelength of the cardiac impulse and reentrant arrhythmias in isolated rabbit atrium. The role of heart rate, autonomic transmitters, temperature, and potassium," *Circulation Research*, vol. 58, no. 1, pp. 96–108, 1986.

[18] G. D. K. Matthews, L. Guzadhur, I. N. Sabir, A. A. Grace, and C. L.-H. Huang, "Action potential wavelength restitution predicts alternans and arrhythmia in murine *Scn5a*^{+/−} hearts," *The Journal of Physiology*, vol. 591, no. 17, pp. 4167–4188, 2013.

[19] L. F. Santana, E. P. Cheng, and W. J. Lederer, "How does the shape of the cardiac action potential control calcium signaling and contraction in the heart?," *Journal of Molecular and Cellular Cardiology*, vol. 49, no. 6, pp. 901–903, 2010.

[20] E. Marbán, "Cardiac channelopathies," *Nature*, vol. 415, pp. 213–218, 2002.

[21] D. M. Bers, "Cardiac Excitation-Contraction Coupling," *Nature*, vol. 415, no. January, pp. 198–205, 2002.

[22] J. M. Nerbonne, "Studying cardiac arrhythmias in the mouse - A reasonable model for probing mechanisms?," *Trends in Cardiovascular Medicine*, vol. 14, no. 3, pp. 83–93, 2004.

[23] N. J. Severs, "The cardiac muscle cell," *BioEssays*, vol. 22, no. 2, pp. 188–199, 2000.

[24] Q. Lou, V. V. Fedorov, A. V. Glukhov, N. Moazami, V. G. Fast, and I. R. Efimov, "Transmural Heterogeneity and Remodeling of Ventricular Excitation-Contraction Coupling in Human Heart Failure," *Circulation*, vol. 123, pp. 1881–1890, 2011.

[25] C. Antzelevitch and J. Fish, "Electrical heterogeneity within the ventricular wall," *Basic Research in Cardiology*, vol. 527, pp. 517–527, 2001.

- [26] Q. Wen et al., "Transverse cardiac slicing and optical imaging for analysis of transmural gradients in membrane potential and Ca²⁺ transients in murine heart," *The Journal of Physiology*, vol. 596, no. 17, pp. 3951–3965, 2018.
- [27] S. He et al., "A Protocol for Transverse Cardiac Slicing and Optical Mapping in Murine Heart," *Frontiers in Physiology*, vol. 10, no. 775, pp. 1–8, 2019.
- [28] A. Kelly et al., "Normal interventricular differences in tissue architecture underlie right ventricular susceptibility to conduction abnormalities in a mouse model of Brugada syndrome," *Cardiovascular research*, no. December, pp. 790–799, 2017.
- [29] R. E. Klabunde, "Electrical Activity of the Heart," in *Cardiovascular Physiology Concepts*, 2nd ed., Philadelphia, PA: Wolters Kluwer/Lippincott, 2012, pp. 9–35.
- [30] Z. Qu, M. B. Liu, and M. Nivala, "A unified theory of calcium alternans in ventricular myocytes," *Scientific Reports*, vol. 6, no. July, p. 35625, 2016.
- [31] J. W. Bassani, R. A. Bassani, and D. M. Bers, "Relaxation in rabbit and rat cardiac cells: species-dependent differences in cellular mechanisms," *The Journal of Physiology*, vol. 476, no. 2, pp. 279–293, 1994.
- [32] A. P. Holmes et al., "A Regional Reduction in Ito and IK_{ACh} in the Murine Posterior Left Atrial Myocardium Is Associated with Action Potential Prolongation and Increased Ectopic Activity," *Plos One*, vol. 11, no. 5, p. e0154077, 2016.
- [33] S. Wells et al., "Acute Oestradiol Slows Conduction in Male, but not Female, Murine Left Atria," *Heart, Lung and Circulation*, vol. 28, p. S200, 2019.
- [34] J. Winter, M. Bishop, C. Wilder, C. O'Shea, D. Pavlovic, and M. J. Shattock, "Sympathetic nervous regulation of cardiac alternans in the intact heart," *Frontiers in Physiology*, vol. 9, no. January, pp. 1–12, 2018.
- [35] D. Mozaffarian et al., *Heart disease and stroke statistics-2016 update a report from the American Heart Association*, vol. 133, no. 4. 2016.
- [36] A. J. Camm, T. F. Luscher, G. Maurer, and P. W. Serruys, "Epidemiology and global burden of arrhythmias," in *ESC CardioMed*, Oxford: Oxford University Press, 2018, pp. 1–17.
- [37] W. Chua et al., "Data-driven discovery and validation of circulating blood-based biomarkers associated with prevalent atrial fibrillation," *European Heart Journal*, pp. 1–10, 2019.
- [38] J. Hüser, L. A. Blatter, and S. L. Lipsius, "Intracellular Ca²⁺ release contributes to automaticity in cat atrial pacemaker cells," *Journal of Physiology*, vol. 524, no. 2, pp. 415–422, 2000.
- [39] L. Staerk, J. A. Sherer, D. Ko, E. J. Benjamin, and R. H. Helm, "Atrial Fibrillation," *Circulation Research*, vol. 120, no. 9, pp. 1501–1517, 2017.

- [40] L. Gaztanga, F. E. Marchlinski, and Brian P. Betensky, "Mechanisms of Cardiac Arrhythmias," *Rev Esp Cardiol*, vol. 65, no. 2, pp. 174–185, 2012.
- [41] C. Antzelevitch and A. Burashnikov, "Overview of basic mechanism of cardiac arrhythmia," *Card Electrophysiol Clin.*, vol. 3, no. 1, pp. 23–45, 2011.
- [42] M. R. Rosen, H. Gelband, C. Merker, and B. F. Hoffman, "Mechanisms of digitalis toxicity. Effects of ouabain on phase four of canine Purkinje fiber transmembrane potentials," *Circulation*, vol. 47, no. 4, pp. 681–689, 1973.
- [43] V. G. Fast and A. G. Kléber, "Anisotropic conduction in monolayers of neonatal rat heart cells cultured on collagen substrate," *Circulation Research*, vol. 75, no. 3, pp. 591–595, 1994.
- [44] G. R. Mines, "On dynamic equilibrium in the heart," *The Journal of Physiology*, vol. 46, no. 4–5, pp. 349–383, 1913.
- [45] M. Lei, L. Wu, D. A. Terrar, and C. L.-H. Huang, "Modernized Classification of Cardiac Antiarrhythmic Drugs," *Circulation*, vol. 138, no. 17, pp. 1879–1896, 2018.
- [46] J. A. McWilliam, "Fibrillar Contraction of the Heart," *The Journal of Physiology*, vol. 8, no. 5, pp. 296–310, 1887.
- [47] P. Comtois, J. Kneller, and S. Nattel, "Of circles and spirals: Bridging the gap between the leading circle and spiral wave concepts of cardiac reentry," *Europace*, vol. 7, no. SUPPL. 2, pp. 10–20, 2005.
- [48] J. Jalife, "Rotors and spiral waves in atrial fibrillation," *Journal of Cardiovascular Electrophysiology*, vol. 14, no. 7, pp. 776–780, 2003.
- [49] N. Wiener and A. Rosenbleuth, "The mathematical formulation of the problem of conduction of impulses in a network of connected excitable elements, specifically in cardiac muscle," *Arch Inst Cardiol Mex*, vol. 16, no. 3, pp. 205–65, 1946.
- [50] J. M. Davidenko, A. V. Pertsov, R. Salomonsz, W. Baxter, and J. Jalife, "Stationary and drifting spiral waves of excitation in isolated cardiac muscle," *Nature*, vol. 355, pp. 349–351, 1992.
- [51] A. T. Winfree, "Spiral Waves of Chemical Activity," *Science*, vol. 175, pp. 634–635, 1972.
- [52] E. Entcheva and G. Bub, "All-optical control of cardiac excitation: Combined high-resolution optogenetic actuation and optical mapping," *The Journal of physiology*, vol. 9, no. November 2014, pp. 2503–2510, 2016.
- [53] A. Grenadier and A. Panfilov, "Spiral waves in heart," *Biofizika*, vol. 26, no. 6, pp. 1107–8, 1981.
- [54] P. Kirchhof et al., "2016 ESC Guidelines for the management of atrial

fibrillation developed in collaboration with EACTS,” *European Heart Journal*, vol. 37, pp. 2893–2962, 2016.

[55] A. L. Aro and S. S. Chugh, “Epidemiology and global burden of arrhythmias,” in *ESC CardioMed*, 3rd ed., 2018, pp. 1–17.

[56] S. Nattel, B. Burstein, and D. Dobrev, “Atrial remodeling and atrial fibrillation: mechanisms and implications,” *Circulation. Arrhythmia and electrophysiology*, vol. 1, no. 1, pp. 62–73, 2008.

[57] G. K. Moe and J. A. Abildskov, “Atrial fibrillation as a self-sustaining arrhythmia independent of focal discharge,” *American Heart Journal*, vol. 58, pp. 59–70, 1959.

[58] N. F. Marrouche et al., “Catheter Ablation for Atrial Fibrillation with Heart Failure,” *New England Journal of Medicine*, vol. 378, no. 5, pp. 417–427, 2018.

[59] A. D. Waller, “A Demonstration on Man of Electromotive Changes accompanying the Heart’s Beat,” *Journal of Physiology*, vol. 8, no. 5, pp. 229–234, 1887.

[60] M. J. Janse, “Some aspects of cardiac electrophysiology,” in *Einthoven 2002. 100 Years of Electrocardiography.*, Leiden: The Einthoven Foundation, 2002, pp. 1–7.

[61] J. Malmivuo and R. Plonsey, *Bioelectromagnetism*. Oxford: Oxford University Press, 1995.

[62] V. Fuster, R. . Walsh, and R. . Harrington, *Hurst’s the Heart*, 13th ed. New York: MacGraw-Hill, 2011.

[63] N. M. S. de Groot et al., “Electropathological Substrate of Longstanding Persistent Atrial Fibrillation in Patients With Structural Heart Disease,” *Circulation*, vol. 122, no. 17, pp. 1674–1682, 2010.

[64] X. Li et al., “An interactive platform to guide catheter ablation in human persistent atrial fibrillation using dominant frequency, organization and phase mapping,” *Computer Methods and Programs in Biomedicine*, vol. 141, pp. 83–92, 2017.

[65] F. Ravelli and M. Mase, “Computational mapping in atrial fibrillation: How the integration of signal-derived maps may guide the localization of critical sources,” *Europace*, vol. 16, no. 5, pp. 714–723, 2014.

[66] L. R. Bear et al., “Forward Problem of Electrocardiography: Is It Solved?,” *Circulation: Arrhythmia and Electrophysiology*, vol. 8, no. 3, pp. 677–684, 2015.

[67] A. J. Shah et al., “Body Surface Electrocardiographic Mapping for Non-invasive Identification of Arrhythmic Sources,” *Arrhythmia Electrophysiology Review*, vol. 2, no. 1, p. 16, 2013.

- [68] S. P. Wells et al., "Cardiomyocyte functional screening – interrogating comparative electrophysiology of high-throughput model cell systems."
- [69] J. Dunlop, M. Bowlby, R. Peri, D. Vasilyev, and R. Arias, "High-throughput electrophysiology: An emerging paradigm for ion-channel screening and physiology," *Nature Reviews Drug Discovery*, vol. 7, no. 4, pp. 358–368, 2008.
- [70] M. O'Reilly et al., "Design, Synthesis, and Biological Evaluation of a New Series of Carvedilol Derivatives That Protect Sensory Hair Cells from Aminoglycoside-Induced Damage by Blocking the Mechanoelectrical Transducer Channel," *Journal of Medicinal Chemistry*, vol. 62, no. 11, pp. 5312–5329, 2019.
- [71] M. R. Franz, "Current status of monophasic action potential recording: Theories, measurements and interpretations," *Cardiovascular Research*, vol. 41, no. 1, pp. 25–40, 1999.
- [72] P. F. Kirchhof, C. Larissa Fabritz, and M. R. Franz, "Phase angle convergence of multiple monophasic action potential recordings precedes spontaneous termination of ventricular fibrillation," *Basic Research in Cardiology*, vol. 93, no. 5, pp. 412–421, 1998.
- [73] M. R. Franz, "Method and Theory of Monophasic," *Progress in Cardiovascular Diseases*, vol. XXXIII, no. 6, pp. 347–366, 1991.
- [74] G. Tse, S. T. Wong, V. Tse, and J. M. Yeo, "Monophasic action potential recordings: Which is the recording electrode?," *Journal of Basic and Clinical Physiology and Pharmacology*, vol. 27, no. 5, pp. 457–462, 2016.
- [75] G. Salama and M. Morad, "Merocyanine 540 as an optical probe of transmembrane electrical activity in the heart," *Science*, vol. 6, no. 121, pp. 485–487, 1976.
- [76] D. E. Gutstein et al., "Conduction slowing and sudden arrhythmic death in mice with cardiac-restricted inactivation of connexin43," *Circulation Research*, vol. 88, no. 3, pp. 333–339, 2001.
- [77] R. D. Walton et al., "Influence of the Purkinje-muscle junction on transmural repolarization heterogeneity," *Cardiovascular Research*, vol. 103, no. 4, pp. 629–640, 2014.
- [78] L. Wang et al., "Different paths, same destination: divergent action potential responses produce conserved cardiac fight-or-flight response in mouse and rabbit hearts," *Journal of Physiology*, vol. 15, pp. 3867–3883, 2019.
- [79] C. Kang et al., "Human Organotypic Cultured Cardiac Slices: New Platform For High Throughput Preclinical Human Trials," *Scientific Reports*, vol. 6, no. February, pp. 1–13, 2016.
- [80] K. Ihara, K. Sugiyama, K. Takahashi, M. Yamazoe, T. Sasano, and T. Furukawa, "Electrophysiological Assessment of Murine Atria with

High-Resolution Optical Mapping,” *Journal of Visualized Experiments*, vol. 132, no. February, p. e56478, 2018.

[81] A. V. Glukhov, V. V. Fedorov, M. E. Anderson, P. J. Mohler, and I. R. Efimov, “Functional anatomy of the murine sinus node: high-resolution optical mapping of ankyrin-B heterozygous mice,” *AJP: Heart and Circulatory Physiology*, vol. 299, no. 2, pp. H482–H491, 2010.

[82] T. Y. Yu et al., “An automated system using spatial oversampling for optical mapping in murine atria. Development and validation with monophasic and transmembrane action potentials,” *Progress in Biophysics and Molecular Biology*, vol. 115, no. 2–3, pp. 340–348, 2014.

[83] D. Lang et al., “Arrhythmogenic remodeling of 2 versus 1 adrenergic signaling in the human failing heart,” *Circulation: Arrhythmia and Electrophysiology*, vol. 8, no. 2, pp. 409–419, 2015.

[84] C. Houston et al., “Characterisation of re-entrant circuit (or rotational activity) in vitro using the HL1-6 myocyte cell line,” *Journal of Molecular and Cellular Cardiology*, vol. 119, no. April, pp. 155–164, 2018.

[85] C. Broyles, P. Robinson, and M. Daniels, “Fluorescent, Bioluminescent, and Optogenetic Approaches to Study Excitable Physiology in the Single Cardiomyocyte,” *Cells*, vol. 7, no. 6, p. 51, 2018.

[86] L. M. Loew, G. W. Bonneville, and J. Surow, “Charge Shift Optical Probes of Membrane Potential,” *Biochemistry*, vol. 17, no. 19, pp. 4065–4071, 1978.

[87] A. Jablonski, “Efficiency of Anti-Stokes Fluorescence in Dyes,” *Nature*, vol. 131, pp. 839–840, 1933.

[88] M. Tsemperouli and K. Sugihara, “Characterization of di-4-ANEPPS with nano-black lipid membranes,” *Nanoscale*, vol. 10, no. 3, pp. 1090–1098, 2018.

[89] W. Liptay, “Electrochromism and Solvatochromism,” *Angewandte Chemie*, vol. 8, no. 3, pp. 177–188, 1969.

[90] S. Habib-E-Rasul Mullah et al., “Evaluation of voltage-sensitive fluorescence dyes for monitoring neuronal activity in the embryonic central nervous system,” *Journal of Membrane Biology*, vol. 246, no. 9, pp. 679–688, 2013.

[91] T. Y. Yu, “Optical imaging of cardiac atrial activation and repolarisation in genetically altered models.” 2015.

[92] E. W. Miller, J. Y. Lin, E. P. Frady, P. A. Steinbach, W. B. Kristan, and R. Y. Tsien, “Optically monitoring voltage in neurons by photoinduced electron transfer through molecular wires,” *Proceedings of the National Academy of Sciences of the United States of America*, vol. 109, no. 6, pp. 2114–2119, 2012.

[93] R. Shinnawi et al., “Monitoring human-induced pluripotent stem cell-derived cardiomyocytes with genetically encoded calcium and voltage fluorescent

reporters,” *Stem Cell Reports*, vol. 5, no. 4, pp. 582–596, 2015.

[94] M. T. McPheeters, Y. T. Wang, A. A. Werdich, M. W. Jenkins, and K. R. Laurita, “An infrared optical pacing system for screening cardiac electrophysiology in human cardiomyocytes,” *PLoS ONE*, vol. 12, no. 8, pp. 1–19, 2017.

[95] P. Robinson et al., “Measurement of myofilament calcium in living cardiomyocytes using a targeted genetically encoded indicator,” *bioRxiv*, 2018.

[96] A. P. Larsen, K. J. Sciuto, A. P. Moreno, and S. Poelzing, “The voltage-sensitive dye di-4-ANEPPS slows conduction velocity in isolated guinea pig hearts,” *Heart rhythm: the official journal of the Heart Rhythm Society*, vol. 9, no. 9, pp. 1493–500, 2012.

[97] R. 3rd Jaimes, R. D. Walton, P. L. C. P. Pasdois, O. Bernus, I. R. Efimov, and M. W. Kay, “A Technical Review of Optical Mapping of Intracellular Calcium within Myocardial Tissue,” *American Journal of Physiology - Heart and Circulatory Physiology*, vol. 310, no. 11, p. ajpheart.00665.2015, 2016.

[98] C. O’Shea et al., “Cardiac Optogenetics and Optical Mapping – Overcoming Spectral Congestion in All-Optical Cardiac Electrophysiology,” *Frontiers in Physiology*, vol. 10, no. 182, pp. 1–14, 2019.

[99] J. Beacher, “LEDs for fluorescence microscopy,” *Biophotonics International*, 2008.

[100] T. Y. Yu et al., “Optical mapping design for murine atrial electrophysiology,” *Computer Methods in Biomechanics and Biomedical Engineering: Imaging Visualization*, vol. 5, no. 5, pp. 368–378, 2017.

[101] J. I. Laughner, F. S. F. S. Ng, M. S. Sulkin, R. M. Arthur, and I. R. Efimov, “Processing and analysis of cardiac optical mapping data obtained with potentiometric dyes,” *AJP: Heart and Circulatory Physiology*, vol. 303, no. 7, pp. H753–65, 2012.

[102] C. Gloschat et al., “RHYTHM: An Open Source Imaging Toolkit for Cardiac Panoramic Optical Mapping,” *Scientific Reports*, vol. 8, no. 2921, pp. 1–12, 2018.

[103] C. O’Shea et al., “ElectroMap: High-throughput open-source software for analysis and mapping of cardiac electrophysiology,” *Scientific Reports*, vol. 9, no. 1389, pp. 1–13, 2019.

[104] J. I. Laughner, F. S. Ng, M. S. Sulkin, R. M. Arthur, and I. R. Efimov, “Processing and analysis of cardiac optical mapping data obtained with potentiometric dyes,” *AJP: Heart and Circulatory Physiology*, vol. 303, no. 7, pp. H753–H765, 2012.

[105] N. Otsu, “A Threshold Selection Method from Gray-Level Histograms,” *IEEE Transactions on Systems, Man, and Cybernetics*, vol. 9, no. 1, pp. 62–66, 1979.

- [106] J. Kittler and J. Illingworth, "On Threshold Selection Using Clustering Criteria," *IEEE Transactions on Systems, Man and Cybernetics*, vol. SMC-15, no. 5, pp. 652–655, 1985.
- [107] K. L. Venkatachalam, J. E. Herbrandson, and S. J. Asirvatham, "Signals and signal processing for the electrophysiologist: Part I: Electrogram acquisition," *Circulation: Arrhythmia and Electrophysiology*, vol. 4, no. 6, pp. 965–973, 2011.
- [108] A. Savitzky and M. J. E. Golay, "Smoothing and Differentiation of Data by Simplified Least Squares Procedures," *Analytical Chemistry*, vol. 36, no. 8, pp. 1627–1639, 1964.
- [109] H. Asfour, L. M. Swift, N. Sarvazyan, M. Doroslovački, and M. W. Kay, "Signal decomposition of transmembrane voltage-sensitive dye fluorescence using a multiresolution wavelet analysis," *IEEE Transactions on Biomedical Engineering*, vol. 58, no. 7, pp. 2083–2093, 2011.
- [110] I. Uzelac and F. H. Fenton, "Robust framework for quantitative analysis of optical mapping signals without filtering," *Computing in Cardiology*, vol. 42, pp. 461–464, 2015.
- [111] M. Faggioni et al., "Suppression of spontaneous ca elevations prevents atrial fibrillation in calsequestrin 2-null hearts," *Circulation: Arrhythmia and Electrophysiology*, vol. 7, no. 2, pp. 313–320, 2014.
- [112] R. Jaimes, S. Kuzmiak-Glancy, D. M. Brooks, L. M. Swift, N. G. Posnack, and M. W. Kay, "Functional response of the isolated, perfused normoxic heart to pyruvate dehydrogenase activation by dichloroacetate and pyruvate," *Pflugers Arch.*, vol. 468, no. 1, pp. 131–142, 2016.
- [113] K. Wang et al., "Cardiac tissue slices: preparation, handling, and successful optical mapping.," *American journal of physiology. Heart and circulatory physiology*, vol. 308, no. 9, pp. H1112-25, 2015.
- [114] D. C. Parrish et al., "Transient denervation of viable myocardium after myocardial infarction does not alter arrhythmia susceptibility," *American Journal of Physiology - Heart and Circulatory Physiology*, no. lcd, p. ajpheart.00300.2017, 2017.
- [115] R. C. Myles, L. Wang, C. Kang, D. M. Bers, and C. M. Ripplinger, "Local beta-adrenergic stimulation overcomes source-sink mismatch to generate focal arrhythmia," *Circulation Research*, vol. 110, no. 11, pp. 1454–1464, 2012.
- [116] J. Tomek, R. A. B. Burton, and G. Bub, "Ccoffinn: Automated Wave Tracking in Cultured Cardiac Monolayers," *Biophysical Journal*, vol. 111, no. 8, pp. 1595–1599, 2016.
- [117] A. N. Doshi et al., "Feasibility of a semi-automated method for cardiac conduction velocity analysis of high-resolution activation maps," *Computers in Biology and Medicine*, vol. 65, pp. 177–183, 2015.

- [118] C. O'Shea et al., "High-Throughput Analysis of Optical Mapping Data Using ElectroMap," *Journal of Visualized Experiments*, no. 148, pp. 1–10, 2019.
- [119] R. Dong et al., "A Protocol for Dual Calcium-Voltage Optical Mapping in Murine Sinoatrial Preparation With Optogenetic Pacing," *Frontiers in Physiology*, vol. 10, no. 954, pp. 1–11, 2019.

Chapter 2

Experimental methods - mouse atrial optical mapping

This chapter provides detailed experimental methods for optical mapping of isolated mouse atria. Data collected using this protocol by myself is shown in Chapters 3, 6 and 7.

2.1 Experimental and analysis methods: Mouse atrial optical mapping

The following sections detail the experimental methods for mouse atrial optical mapping performed by the author of this thesis at the University of Birmingham. This thesis also contains analysis of raw data obtained in separate experiments conducted by other experimenters, and the relevant methodologies are presented and attributed where appropriate throughout.

2.2 Animal procedures and models

All animal procedures were undertaken in accordance with ethical guidelines set out by the UK Animals (Scientific Procedures) Act 1986 and Directive 2010/63/EU of the European Parliament on the protection of animals used for scientific purposes. Experiments were approved by the home office (PPL 30/2967 and PFDAAF77F) and the institutional review board at University of Birmingham. Mice were housed in individually ventilated cages, with sex-matched littermates, under standard conditions: 12-hour light/dark cycle, 22°C and 55% humidity. Food and water were available ad libitum. The general health status of all mice (bearing, grooming, behaviour, body weight) was monitored daily and immediately prior to surgery.

Experiments outlined below were performed on mice with heterozygous expression of a Pitx2 null allele (pitx2null) [1], bred on a C57/BL6 background, and wild-type (WT) littermates.

2.3 Buffer solutions

A bicarbonate buffered Krebs-Henseleit (KHB) solution was used for mouse atrial optical mapping experiments, containing in mM: NaCl 118; KCl 3.52; MgSO₄ 0.83; KH₂PO₄ 1.18; NaHCO₃ 24.9; Glucose 11.0; CaCl₂ 1.8. The solution was heated to 36°C-37°C and equilibrated with 95%O₂/5%CO₂ to maintain a pH of 7.4. Chemicals were purchased from Sigma-Aldrich.

2.4 Heart isolation

Mice were initially placed in an anaesthetisation chamber filled with 4% isoflurane in O₂ for 2minutes. Flow rate was 2-3L/min and gas continuously scavenged. Mice were then transferred to the surgical bed, placed in the supine positions, and supplied with continuous anaesthetisation by 4% isoflurane in O₂ via a facemask. The pedal reflex was tested to confirm deep anaesthesia. Once deep anaesthesia was confirmed, the limbs were tapped down. An initial incision was made just below the rib cage, and the rib cage bilaterally cut. The diaphragm was then pierced, and the rib cage moved back to reveal the heart and lungs. The heart was then lifted from behind with curve forceps, and the vessels cut to remove the whole heart. Death was via exsanguination.

The isolated heart was then placed in a petri dish containing KHB solution at 4°C to temporally stop contraction (cardioplegia) [2]. The anticoagulant heparin was added to the dish to prevent blood clot in the isolated heart. Excess tissue, for example lungs, connective tissue or adipose tissue, was removed. The heart

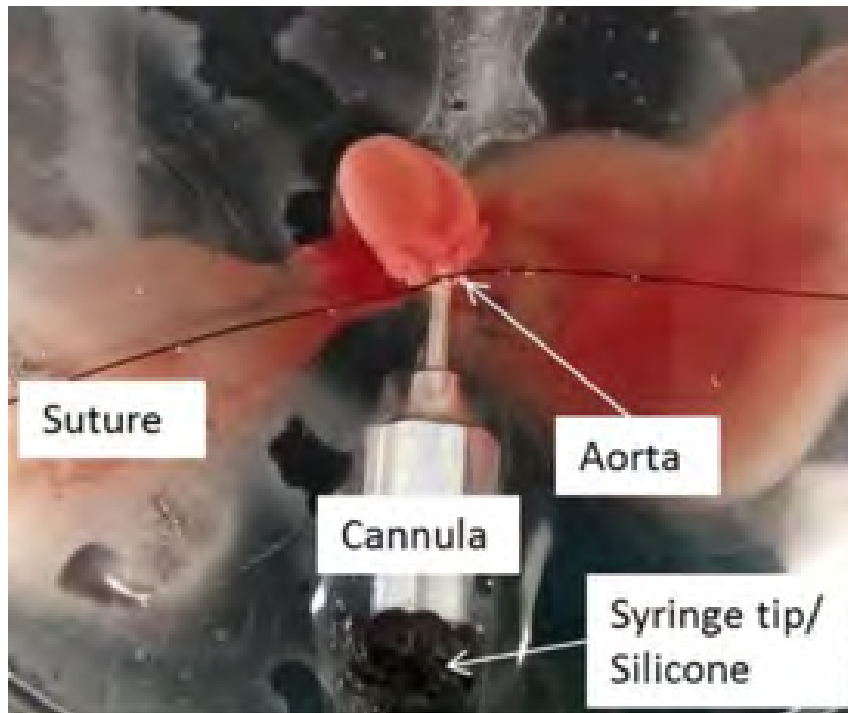


Figure 2.1: Isolated heart cannulation by the ascending aorta. Cannulated heart as described. The syringe is filled with KHB, which was then injected into the heart to remove blood.

was then placed into a petri dish containing clean KHB solution for cannulation of the ascending aorta. The petri dish was placed on a custom stand for a 2ml syringe with a 1mm (outer diameter) cannula attached, Figure 2.1. The syringe contained 2ml of KHB solution. All air bubbles were removed before cannulation. The ascending aorta was then cannulated, above the aortic valve. Sutures were then used to tie the heart to the cannula, and KHB solution retrogradely perfused through the aorta to clear remaining blood.

2.5 Langendorff perfusion

The cannulated heart was transferred to a vertical Langendorff system [3], and the heart was retrogradely perfused with 37°C KHB solution, Figure 2.2. Initial

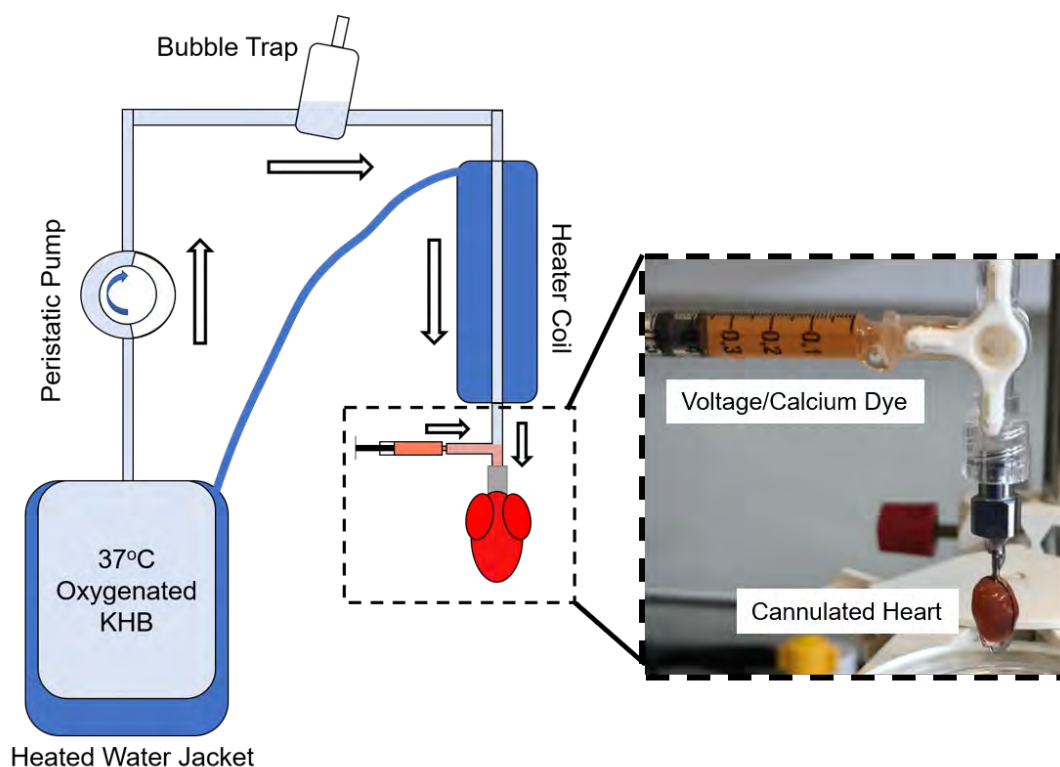


Figure 2.2: Dye loading on Langendorff apparatus Schematic diagram of Langendorff perfusion system used for dye loading showing relative locations of heated water jacket, peristaltic pump, bubble trap, heater coil and cannulated heart. White arrows show the direction of flow for KHB solution. Inset shows dye introduction into the perfusion line via a three-way tap,

flow rate was 4ml/min, although this was reduced to 2ml/min for dye loading (see below). In some studies, a cannula was placed into the left ventricle to allow solution to drain from the heart. This was only done if signs of high pressure were observed, for example poor flow through the heart and solution build up in the bubble trap. Hearts were allowed to equilibrate until beating was again observed.

2.5.1 Di-4-ANEPPS dye loading

Potentiometric dye Di-4-ANEPPS (Invitrogen, UK) was stored at 4°C at a concentration of 5mg/ml in DMSO in 25 μ l aliquots [4]. The dye was removed

from storage and thawed for 5 to 10 minutes. The dye was then dissolved in 1 ml 37°C KHB solution and injected into the perfusion line of the Langendorff apparatus via a three-way tap, immediately before the solution reached the heart. Loading was via bolus injection (Figure 2.2), and the loading time was 3 to 5 minutes. As the dye was loaded, solution that had passed through the heart was collected and reapplied to the epicardial surface to maximise dye loading. Once the heart had been loaded with the fluorescent dye, the heart was removed from the Langendorff apparatus and placed in a petri dish containing 37°C KHB solution.

2.5.2 Rhod-2AM dye loading

In separate experiments intracellular Ca^{2+} dye Rhod-2AM was utilised. Rhod-2AM (Invitrogen, UK) was stored at -20°C in 50 µg aliquots in powder form [5]. The dye was mixed with 60 µl of DMSO containing 10% Pluronic F127, a surfactant used to facilitate solubilisation [6]. The dye was then dissolved in 1 ml 37°C KHB solution and injected into the perfusion line of the Langendorff system as above over 10 to 15 minutes.

2.5.3 Rh-237 dye loading

Some experiments were performed using Rh-237 (Invitrogen, UK) [7]. The isolation and loading protocols differ from that presented above, and were performed by Dr James Winter, and not be the author of this thesis. Mouse

hearts were isolated under terminal anaesthesia (4% isoflurane in 100% O₂), and Langendorff perfused at 70-80mmHg with a buffer solution containing in mM: NaCl 114.0; KCl 4.0; CaCl 1.4; NaHCO₃ 24.0; NaH₂PO₄ 1.1; glucose 11.0 and sodium pyruvate 1.0. Solution was heated to 37°C, equilibrated with 95% O₂/5%CO₂ to maintain a pH of 7.4 and passed through a 5µm nitrocellulose filter. Chemicals were purchased from Sigma-Aldrich. Rh-237 was stored at 4°C at a concentration of 1.25mg/ml in DMSO in 70µl aliquots. The dye was dissolved in 1ml of 37°C buffer solution and injected into the perfusion line over a period of 4 to 5 minutes. As this setup allowed for continuous monitoring of dye loading, 2 to 3 aliquots (140-210µl) of dye were added until sufficient signal was observed.

All subsequent steps, including atrial pinning and optical mapping, were the same for both preparations and performed by the author of this thesis.

2.6 Atrial isolation

The left atrium (LA) was dissected and placed into the optical mapping superfusion chamber, Figure 2.3. In some studies, the right atrium (RA) was also removed. The LA (and RA if applicable) were then pinned to the black silicone surface of the optical mapping chamber using fine entomology pins. The atria were pinned with the anterior surface facing up. Two or three pins were used at the edges of the tissue, ensuring that 1) the pins would not block any part of the atria from the camera and 2) stimulus electrodes could be placed on the LA, near where the LA attached to the septal wall *in vivo*. The RA was not

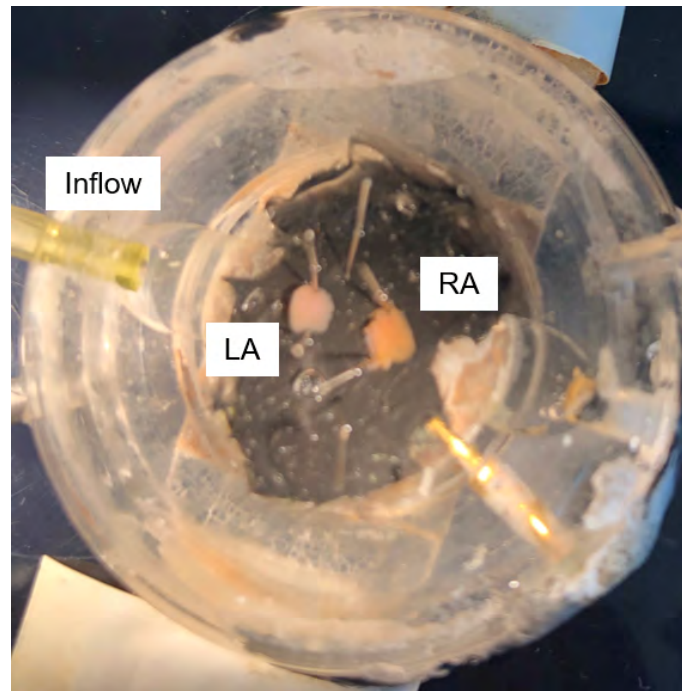


Figure 2.3: Dissected atria in optical mapping superfusion chamber.

paced to study spontaneous activity from the sinoatrial node.

2.7 Optical mapping

The atrial tissue was then placed in the optical mapping setup, Figure 2.4. 100ml oxygenated (95%O₂/5%CO₂) KHB solution was continuously superfused across the atrial surface and recirculated. 50 μ l Blebbistatin (Cayman Chemical, USA) solution (25mg/ml in DMSO) was added into the superfusate. Blebbistatin selectively inhibits myosin by stabilising myosin in a metastable state which occurs before force generation [8], [9], decoupling the electrical and mechanical coupling of the cardiomyocytes. This is vital for optical mapping experiments, as contraction will introduce motion artefacts into the recorded signals, precluding effective analysis [10], [11]. Blebbistatin was used as it has been reported that it achieves uncoupling without alteration of several electrophysiological (EP)

parameters, making it the most widely used excitation-contraction uncoupler in optical experiments [9], [12]. There are however reports of blebbistatin affecting electrically and optically recorded action potential duration, as well as other parameters including restitution and arrhythmia inducibility, in isolated rabbit hearts [12].

The superfusate (KHB and Blebbistatin) was pumped to the optical mapping chamber via a custom-made heating element (Martyn Preston, University of Oxford) and a bubble trap. The heating element was connected to a feedback thermometer to maintain a temperature range of 35°C to 37°C at the optical mapping chamber, checked by a digital thermocouple before and during experiments. Peristaltic pumps were used both to pump the solution to the chamber and remove excess solution, which was pumped back for recirculation.

The optical mapping superfusion chamber containing the atrium/atria was placed in the optical mapping setup directly below the camera lens, Figure 2.4. Bipolar platinum electrodes were then placed on the LA near to where the left atrial appendage (LAA) connects to the posterior wall. Pacing rate was set at a holding frequency of 1 or 3Hz depending on pacing protocol, and voltage increased until optical action potentials (OAP) were seen. This defined the diastolic threshold of the preparation, and the LA was paced at twice the threshold. Pacing was achieved with 2ms pulses, generated using an isolated constant voltage stimulator (Digitimer, UK). Spike2 software (Cambridge Electronic Design, UK) was used to create and deliver pacing protocols. The atria were then left to equilibrate on the system for a minimum of 10minutes.

After 10 minutes, illumination LEDs were switched on. Four LEDs (two twin LEDs) at 530nm were used for illumination and directed towards the atrium/atria. A 630nm longpass filter was used to collect emitted fluorescence from voltage dyes Di-4-ANEPPS or Rh-237. When using Rhod-2AM, a 585/40nm bandpass filter was used. Images were acquired using a 2nd generation, 'scientific' CMOS camera with a single pixel area of $6.5\mu\text{m}^2$ (ORCA flash 4.0, Hamamatsu, Japan). The maximal resolution of the images was 128 x 2048 pixels, and unless stated images were acquired at 0.987kHz. Images were collected using WinFluor (Dr John Dempster, University of Strathclyde, UK). WinFluor allowed continuous monitoring of the OAPs from a selected region of interest. This allowed for confirmation of the cessation of motion artefacts, and for the

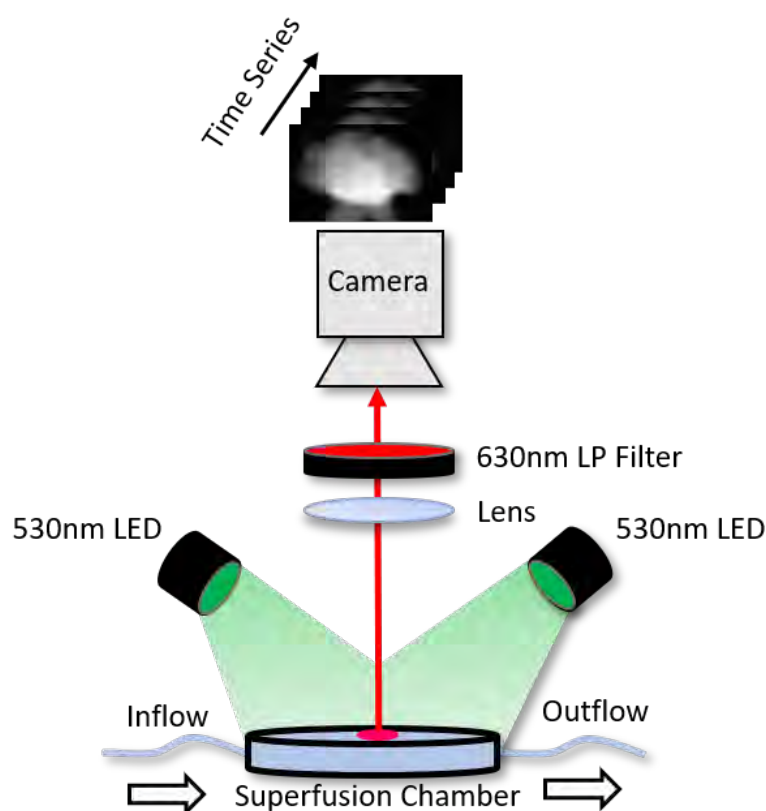


Figure 2.4: Optical mapping setup. A schematic diagram of the optical mapping setup used.

identification of premature atrial activity or missed stimulus captures. Experimental recording time was 60s, and illumination was turned off between recordings to prevent photobleaching or phototoxic side effects [13], [14].

2.7.1 Pacing protocols

Two main pacing protocols were used for the optical mapping experiments. Raw optical voltage signals, before any processing other than signal inversion, are shown from these pacing protocols in Figure 2.5. The first protocol had a holding cycle length (CL) of 1000ms (1Hz). During recordings, the atria were then paced at CLs of 120ms, 100ms and 80ms (8.33Hz, 10Hz and 12.5Hz) respectively for 100 beats. There was a 5 second gap between each CL, Figure 2.5A. This protocol was used so the atria has sufficient time to adapt to each new pacing frequency, and to allow study of both adaptation time and beat to beat variability. This protocol also included a burst of 20 pulses at 50ms CL.

The second protocol ('ramp' protocol) had a holding cycle length (CL) of 333ms (3Hz). On starting the protocol, the pacing CL was reduced to 150 or 120ms (6.67 or 8.33Hz) for 100 beats. The CL was then reduced by 10ms every 20 beats, until the CL was 50ms (20Hz), Figure 2.5B. This protocol allowed investigation into the restitution properties of the atria from one experimental recording, with one 'ramp' lasting 34s or 23.2s, depending on starting CL.

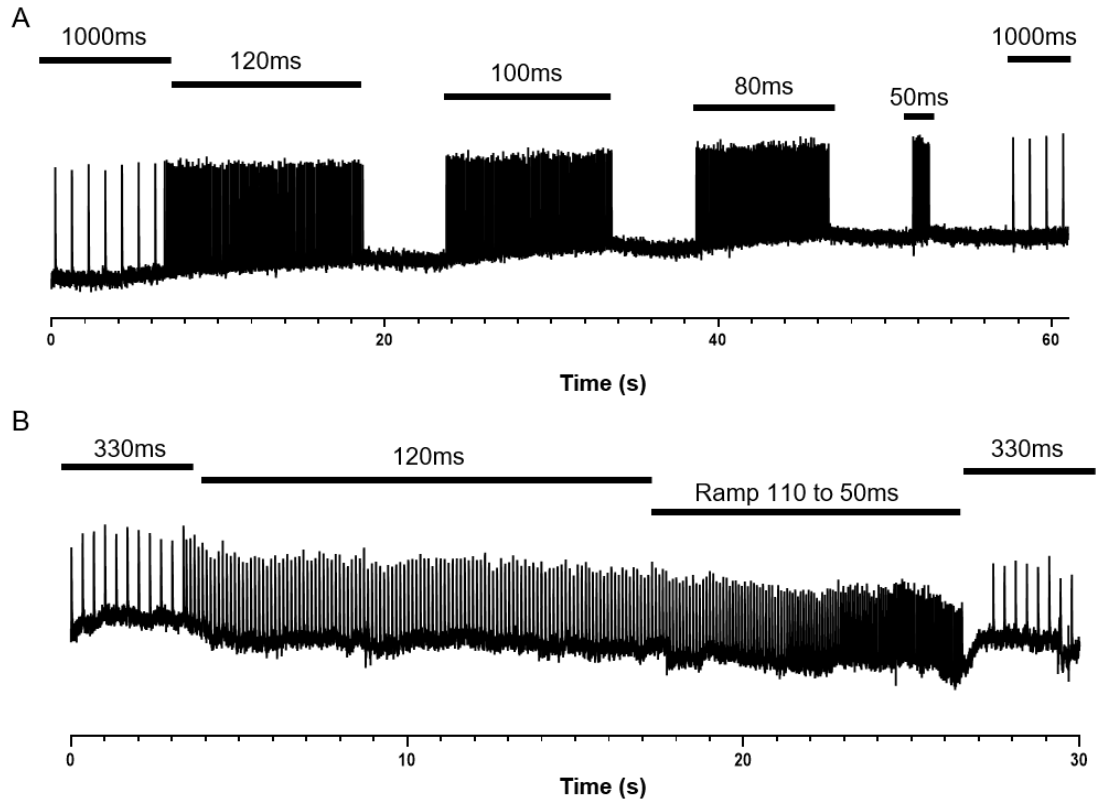


Figure 2.5: Atrial pacing protocols A) Optical action potentials (arbitrary intensity) as recorded when atria paced using 120-100-80ms protocol. B) Optical action potentials as recorded when atria paced using the 'ramp' protocol.

2.7.2 Data analysis

Data was exported from WinFluor in uncompressed Tagged Image File Format (TIFF), and the exported images analysed using a MATLAB built software that was developed as part of this thesis, ElectroMap [11], [15]. See Chapter 3 for a detailed description of the use and development of ElectroMap. ElectroMap allowed application of spatial filtering, baseline correction, temporal filtering and multi-beat (ensemble) averaging. Unless otherwise stated for data presented in this thesis, images were processed using a 3x3 pixel Gaussian spatial filter, standard deviation = 1. Non-physiological changes in baseline (as seen in the raw traces in Figure 2.5) were corrected for with a top-hat filter with kernel length

of 100ms. When analysing data from the first pacing protocol (CL = 120-100-80ms, Figure 2.5A), the final 20 of the 100 stimuli were ensemble averaged.

Unless otherwise stated, the following analysis parameters were used. For conduction velocity (CV), the Bayly multi-vector method was utilised with a 5x5 pixel window [16]. Action potential duration (APD)/calcium transient duration (CaTD) was measured from time of maximum upstroke velocity (i.e. dF/dt_{max}) to time of repolarisation/decay to chosen level from peak [17], [18]. Time to peak (TTP) was defined as time from 10% to 90% rise [19].

2.7.3 Statistical analysis

All data are presented as mean \pm standard error of the mean. Group differences were tested using paired t-tests or one-way analysis of variance as appropriate with Bonferroni test, and were accepted as significant when $P < 0.05$.

2.8 Chapter summary

This chapter has provided detailed experimental methodology for optical mapping of isolated mouse atrial tissue. Due to the small size and high heart rate of the mouse heart, robust protocols to study its cardiac electrophysiological behaviour using high spatiotemporal temporal optical mapping are vital, in particular in the context of the unique advantages of mouse models. These include large litters, short gestation periods, rapid maturation

and, potentially most importantly, established and widely used methods for genetic manipulation. In the current thesis, data obtained using the protocol outlined here is presented in Chapters 3, 6 and 7.

2.9 Chapter 2 references

- [1] M.-F. Lu, C. Pressman, R. Dyer, R. L. Johnson, and J. F. Martin, "Function of Rieger syndrome gene in left-right asymmetry and craniofacial development," *Nature*, vol. 401, no. September, pp. 276–278, 1999.
- [2] P. Nardi et al., "Warm blood cardioplegia versus cold crystalloid cardioplegia for myocardial protection during coronary artery bypass grafting surgery," *Cell Death Discovery*, vol. 4, no. 23, pp. 1-6, 2018.
- [3] R. M. Bell, M. M. Mocanu, and D. M. Yellon, "Retrograde heart perfusion: The Langendorff technique of isolated heart perfusion," *Journal of Molecular and Cellular Cardiology*, vol. 50, no. 6, pp. 940–950, 2011.
- [4] E. Fluhler, V. G. Burnham, and L. M. Loew, "Spectra, Membrane Binding, and Potentiometric Responses of New Charge Shift Probes," *Biochemistry*, vol. 24, no. 21, pp. 5749–5755, 1985.
- [5] A. Minta, J. Kao, and R. Tsien, "Fluorescent indicators for cytosolic calcium based on rhodamine and fluorescein chromophores," *JOURNAL OF BIOLOGICAL CHEMISTRY*, vol. 264, no. 14, pp. 8171–8178, 1989.
- [6] L. B. Cohen et al., "Changes in axon fluorescence during activity: Molecular probes of membrane potential," *The Journal of Membrane Biology*, vol. 19, no. 1, pp. 1–36, 1974.
- [7] A. Grinvald, R. Hildesheim, I. C. Farber, and L. Anglister, "Improved fluorescent probes for the measurement of rapid changes in membrane potential," *Biophysical Journal*, vol. 39, no. 3, pp. 301–308, 1982.
- [8] J. S. Allingham, R. Smith, and I. Rayment, "The structural basis of blebbistatin inhibition and specificity for myosin II," *Nature Structural and Molecular Biology*, vol. 12, no. 4, pp. 378–379, 2005.
- [9] V. V. Fedorov et al., "Application of blebbistatin as an excitation-contraction uncoupler for electrophysiologic study of rat and rabbit hearts," *Heart Rhythm*, vol. 4, no. 5, pp. 619–626, 2007.
- [10] J. Christoph and S. Luther, "Marker-Free Tracking for Motion Artifact Compensation and Deformation Measurements in Optical Mapping Videos of

Contracting Hearts,” *Frontiers in Physiology*, vol. 9, no. November, 2018.

[11] C. O’Shea et al., “High-Throughput Analysis of Optical Mapping Data Using ElectroMap,” *Journal of Visualized Experiments*, no. 148, pp. 1–10, 2019.

[12] K. E. Brack, R. Narang, J. Winter, and G. Andr, “The mechanical uncoupler blebbistatin is associated with significant electrophysiological effects in the isolated rabbit heart,” vol. 5, pp. 1009–1027, 2013.

[13] S. Habib-E-Rasul Mullah et al., “Evaluation of voltage-sensitive fluorescence dyes for monitoring neuronal activity in the embryonic central nervous system,” *Journal of Membrane Biology*, vol. 246, no. 9, pp. 679–688, 2013.

[14] L. Kaestner et al., “Genetically encoded voltage indicators in circulation research,” *International Journal of Molecular Sciences*, vol. 16, no. 9, pp. 21626–21642, 2015.

[15] C. O’Shea et al., “ElectroMap: High-throughput open-source software for analysis and mapping of cardiac electrophysiology,” *Scientific Reports*, vol. 9, no. 1389, pp. 1–13, 2019.

[16] P. V Bayly et al., “Estimation of Conduction Velocity Vector Fields from Epicardial Mapping Data,” vol. 45, no. 5, pp. 563–571, 1998.

[17] R. D. Walton, R. M. Smith, B. G. Mitrea, E. White, O. Bernus, and A. M. Pertsov, “Extracting surface activation time from the optically recorded action potential in three-dimensional myocardium,” *Biophysical Journal*, vol. 102, no. 1, pp. 30–38, 2012.

[18] C. O’Shea, D. Pavlovic, K. Rajpoot, and J. Winter, “Examination of the effects of conduction slowing on the upstroke of the optically-recorded action potentials,” *Frontiers in Physiology*, vol. 10, no. 1295, pp.1-11 2019.

[19] J. I. Laughner, F. S. Ng, M. S. Sulkin, R. M. Arthur, and I. R. Efimov, “Processing and analysis of cardiac optical mapping data obtained with potentiometric dyes,” *AJP: Heart and Circulatory Physiology*, vol. 303, no. 7, pp. H753–H765, 2012.

Chapter 3

ElectroMap: High-throughput open-source software for analysis and mapping of cardiac electrophysiology

This chapter reports the development, validation and application of a MATLAB based software package for analysis of both optical and electrogram mapping datasets, ElectroMap. As outlined in chapter 1, optical mapping datasets require significant processing of raw signals to realise effective analysis of key EP parameters. Furthermore, different experimental models, hardware and questions necessitate distinct processing and analysis pipelines. Commonly, analysis of optical mapping data has hence been undertaken using either commercial software or using custom, in-house algorithms. This prevents uptake of the technique and objective analysis across research groups.

We therefore aimed to create an analysis platform for optical mapping datasets with key features including:

- Easy to use graphical user interface
- Flexibility with regards to experimental model and hardware
- Established and validated novel methodologies for analysis of pro-arrhythmic phenomena

- High throughput, multi-beat analysis across long experimental timescales
- Freely available as both source code or standalone versions

This chapter consists of a publication (Publication 1 and Appendix A) detailing the development, validation and application of a MATLAB based software package for analysis of both optical and electrogram mapping datasets, ElectroMap. Key features, such as conduction velocity quantification and multi-beat analysis across long experimental timescales were validated using *in silico* mouse datasets, experimental datasets from mouse, guinea pig and human optically mapped samples and *in vivo* human electrogram mapping data from a patient undergoing catheter ablation surgery for atrial fibrillation. ElectroMap has been released open source and is available from <https://github.com/CXO531/ElectroMap>.

Furthermore, unpublished work detailing comparisons of processing and analysis techniques is provided in sections 3.2 to 3.5.

3.1 ElectroMap: High-throughput open-source software for analysis and mapping of cardiac electrophysiology

Publication 1.

This research was originally published in Scientific Reports.

C O'Shea, A P Holmes, T Y Yu, J Winter, S P Wells, J Correia, B J Boukens, J R deGroot, G S Chu, X Li, G.A Ng, P Kirchhof, L Fabritz, K Rajpoot, D Pavlovic. *Sci. Rep. 9:1389, 1–13, 2019.*

The supplementary information that accompanied publication 1 can be found in appendix A. Supplementary Figures I-X referred to in the manuscript correspond to Figures A1-A10. Supplementary videos I-III can be found at <https://www.nature.com/articles/s41598-018-38263-2#Sec15>.

Author contributions in publication 1

I designed and wrote the software (building upon some pre-existing MATLAB scripts for basic conduction and duration analysis designed by Ting Yue Yu), designed the graphical user interface, produced model datasets, conducted some experiments, analysed all included data using the software and wrote the manuscript.

Simon Wells conducted the hypoxia experiments. James Winter conducted the guinea pig experiments. Joris deGroot and Bastiaan Boukens conducted human tissue optical mapping experiments. Gavin Chu and G.Angre Ng collected *in-vivo* human electrogram data.

SCIENTIFIC REPORTS

OPEN

ElectroMap: High-throughput open-source software for analysis and mapping of cardiac electrophysiology

Christopher O'Shea^{1,2,3}, Andrew P. Holmes^{1,4}, Ting Y. Yu¹, James Winter¹, Simon P. Wells^{1,11}, Joao Correia⁵, Bastiaan J. Boukens⁶, Joris R. De Groot⁷, Gavin S. Chu^{8,9}, Xin Li⁸, G. Andre Ng^{8,9}, Paulus Kirchhof^{1,10}, Larissa Fabritz^{1,10}, Kashif Rajpoot³ & Davor Pavlovic¹

The ability to record and analyse electrical behaviour across the heart using optical and electrode mapping has revolutionised cardiac research. However, wider uptake of these technologies is constrained by the lack of multi-functional and robustly characterised analysis and mapping software. We present ElectroMap, an adaptable, high-throughput, open-source software for processing, analysis and mapping of complex electrophysiology datasets from diverse experimental models and acquisition modalities. Key innovation is development of standalone module for quantification of conduction velocity, employing multiple methodologies, currently not widely available to researchers. ElectroMap has also been designed to support multiple methodologies for accurate calculation of activation, repolarisation, arrhythmia detection, calcium handling and beat-to-beat heterogeneity. ElectroMap implements automated signal segmentation, ensemble averaging and integrates optogenetic approaches. Here we employ ElectroMap for analysis, mapping and detection of pro-arrhythmic phenomena *in silico*, *in cellulo*, animal model and *in vivo* patient datasets. We anticipate that ElectroMap will accelerate innovative cardiac research and enhance the uptake, application and interpretation of mapping technologies leading to novel approaches for arrhythmia prevention.

The incidence and prevalence of cardiac diseases continues to increase every year^{1,2}. Adequate prevention and treatment requires a better understanding of the mechanistic drivers³. Detailed understanding of spatial and temporal electrical behaviour and ionic handling across the heart is integral to this.

Ability to measure field potentials and conduction from multiple sites can be achieved by contact/non-contact electrodes arrays. More recently, optical mapping has allowed measurement and mapping of action potential and calcium transient morphology and conduction, leading to a broader utilisation of mapping technologies in the cardiovascular sphere. Increasingly, electrode array mapping has made its way from pre-clinical to clinical arena whilst the use of optical mapping continues to expand in experimental research. Optically imaging intact tissue using voltage or calcium sensitive fluorescent dyes has advantages over surface electrodes but the requirement for contraction uncouplers and inability to perform *in vivo* experiments limits clinical utility of optical mapping⁴. Nevertheless, insights from optical mapping experiments have informed our understanding of complex arrhythmias and electrophysiological remodelling in heart disease^{5–8}. Electrode mapping has equally provided

¹Institute of Cardiovascular Sciences, University of Birmingham, Birmingham, UK. ²EPSRC Centre for Doctoral Training in Physical Sciences for Health, School of Chemistry, University of Birmingham, Birmingham, UK. ³School of Computer Science, University of Birmingham, Birmingham, UK. ⁴Institute of Clinical Sciences, University of Birmingham, Birmingham, UK. ⁵Institute of Microbiology and Infection, School of Biosciences, University of Birmingham, Birmingham, UK. ⁶Amsterdam UMC, University of Amsterdam, Department of Anatomy and Physiology, Amsterdam, The Netherlands. ⁷Amsterdam UMC, University of Amsterdam, Heart Center, Department of Cardiology, Amsterdam, The Netherlands. ⁸Department of Cardiovascular Sciences, University of Leicester, Leicester, UK. ⁹NIHR Leicester Biomedical Research Centre, Glenfield Hospital, Leicester, UK. ¹⁰Department of Cardiology, UHB NHS Trust, Birmingham, UK. ¹¹Department of Physiology, University of Melbourne, Melbourne, Australia. Kashif Rajpoot and Davor Pavlovic jointly supervised this work. Correspondence and requests for materials should be addressed to K.R. (email: k.m.rajpoot@bham.ac.uk or d.pavlovic@bham.ac.uk)

vital knowledge^{9,10}, demonstrating that re-entry drives ventricular tachycardia¹¹, actively guiding current clinical ablation strategies. Some arrhythmogenic principles, for example in atrial fibrillation (AF), remain poorly understood from a mechanistic standpoint^{12,13} and thus require further experimentation.

Increased availability of optical mapping hardware in the laboratory has led to expansion of this technology. Further uptake and wider application is hindered by limitations with respect to data processing and analysis. This challenge is intensified as developing camera technology provides ever-increasing spatio-temporal resolution. Furthermore, multiple processing algorithms are employed before the underlying data can be interpreted^{14,15}. These algorithms require computational expertise to implement and are commonly developed and used within individual research groups, utilising techniques specific to camera resolution, file type and animal species. Whilst some software solutions are accessible, even straightforward calculation of conduction velocity (CV) across the heart is currently unavailable, but to a few specialist groups. There is an unmet need for a robustly tested mapping software that allows high-throughput data processing, analysis, and mapping of electrophysiology from different acquisition modalities and diverse datasets with distinct electrophysiological (EP) properties (for example: animal, human tissue and cell monolayers). Therefore, we present novel and robust open-source software, ElectroMap, for analysis of voltage and calcium optical mapping data. This work builds upon our previously published algorithms^{15–17} while integrating analytic approaches developed and validated by others^{6,14,18,19}. ElectroMap provides analysis of key EP parameters including action potential and calcium transient morphology, calcium decay constant (τ), activation and repolarisation times, diastolic interval (DI), time-to-peak, phase mapping and dominant frequency (DF). A key innovation is the introduction of a comprehensive CV module for robust investigation of CV changes. This module integrates established single vector¹⁸ and multi vector²⁰ techniques for CV measurement as well as a novel “activation constant” analysis. Furthermore, semi-automated alternans analysis is enabled through development of a comprehensive alternans detection and quantification module. ElectroMap integrates automated pacing frequency recognition, ensemble (i.e. multi-beat) averaging and beat-to-beat analysis options. Here we employ ElectroMap for analysis, mapping and detection of pro-arrhythmic phenomena *in silico*, *in cellulo*, animal model and *in vivo* patient datasets, and thus demonstrate its utility for cardiac research.

Methods

Expanded details about methods are provided in the Supplementary Material. All animal procedures were undertaken in accordance with ethical guidelines set out by the UK Animals (Scientific Procedures) Act 1986 and Directive 2010/63/EU of the European Parliament on the protection of animals used for scientific purposes. Studies conformed to the Guide for the Care and Use of Laboratory Animals published by the U.S. National Institutes of Health under assurance number A5634-01. Experiments were approved by the home office (mouse: PPL 30/2967 and PFDAAF77F, guinea pig: PPL PF75E5F7F) and the institutional review boards at University of Birmingham (murine) and King's College London (guinea pig). For optical mapping of human tissue, left atrial appendages were obtained from patients with atrial fibrillation (AF) during thoracoscopic surgery, as described before²¹. The study was in accordance with the declaration of Helsinki and approved by the Review Board of the Academic Medical Center, Amsterdam. *In vivo* intracardiac data were obtained in a clinical study approved by local ethics committee for patients undergoing AF ablation at the University Hospitals of Leicester NHS Trust as previously described²². All patients gave written informed consent.

Optical Mapping. Both mouse and guinea pig optical mapping experiments were conducted as previously reported. For experiments in mouse^{7,15,17} fluorescent dye (Voltage: DI-4-ANEPPS, Calcium: Rhod-2AM) was loaded into Langendorff perfused whole hearts. Left atria were isolated, with the posterior atrial surface exposed. Atria were superfused under normoxic (95%O₂/5%CO₂) or hypoxic (95%N₂/5%CO₂) conditions. Pacing was performed via bipolar platinum electrode, and fluorescence captured using ORCA flash 4.0 camera (1 kHz sampling rate, maximum field of view: 200 × 2048 pixels, 71 µm/pixel, Hamamatsu Electronics, Japan). Isolated guinea pig hearts⁸ were loaded with voltage dye Di-8-ANEPPS, paced via silver bipolar electrodes and imaged using Evolve Delta 512 × 512 pixel EMCCD cameras (500 Hz sampling rate, 64 × 64 pixels, 320 µm/pixel, Photometrics, USA) mounted on a Olympus MVX10 stereomicroscope.

Human left atrial appendages²¹ were removed using an endoscopic stapling device (Endo GIA stapler, Tyco Healthcare Group) and transported to the optical mapping setup in 100 mL cooled perfusion fluid. Atrial preparation was submerged in a recording chamber, loaded with Di-4-ANEPPS and paced using an epicardial electrode. MiCAM Ultima camera (2 kHz sampling rate, 100 × 100 pixels, 100 µm/pixel SciMedia, USA) was used to record epicardial images.

***In-vivo* Human Mapping.** A high-density non-contact multi-electrode array catheter (Ensite Array, St. Jude Medical, USA) was positioned in the right atrium. Virtual unipolar electrograms were bandpass filtered from 1–100 Hz with additional noise filtering, then exported from a 2048 node geometry as previously described²².

ElectroMap Design and Development. All data processing and analysis was performed using ElectroMap, Fig. 1a. ElectroMap is developed to run on multiple platforms. It can run either within MATLAB or as a standalone executable (.exe for Windows and .dmg for macOS) with download of the freely available MATLAB runtime (see Supplementary Material). Processing parameters and additional modules are adjustable using custom made graphical user interfaces. Software is designed to handle the widely used TIFF and MAT formats. Custom input of sampling frequency and pixel size makes it compatible with various cameras and acquisition systems. ElectroMap allows automatic or adjusted region selection (Fig. 1b) and multiple filtering options (see Supplementary Material for full details of filtering options). Unless stated otherwise, all the signals in Figs 1–8 underwent spatial (4 × 4 pixel Gaussian, sigma = 1.5) and temporal (3rd order Savitzky-Golay) filtering to allow

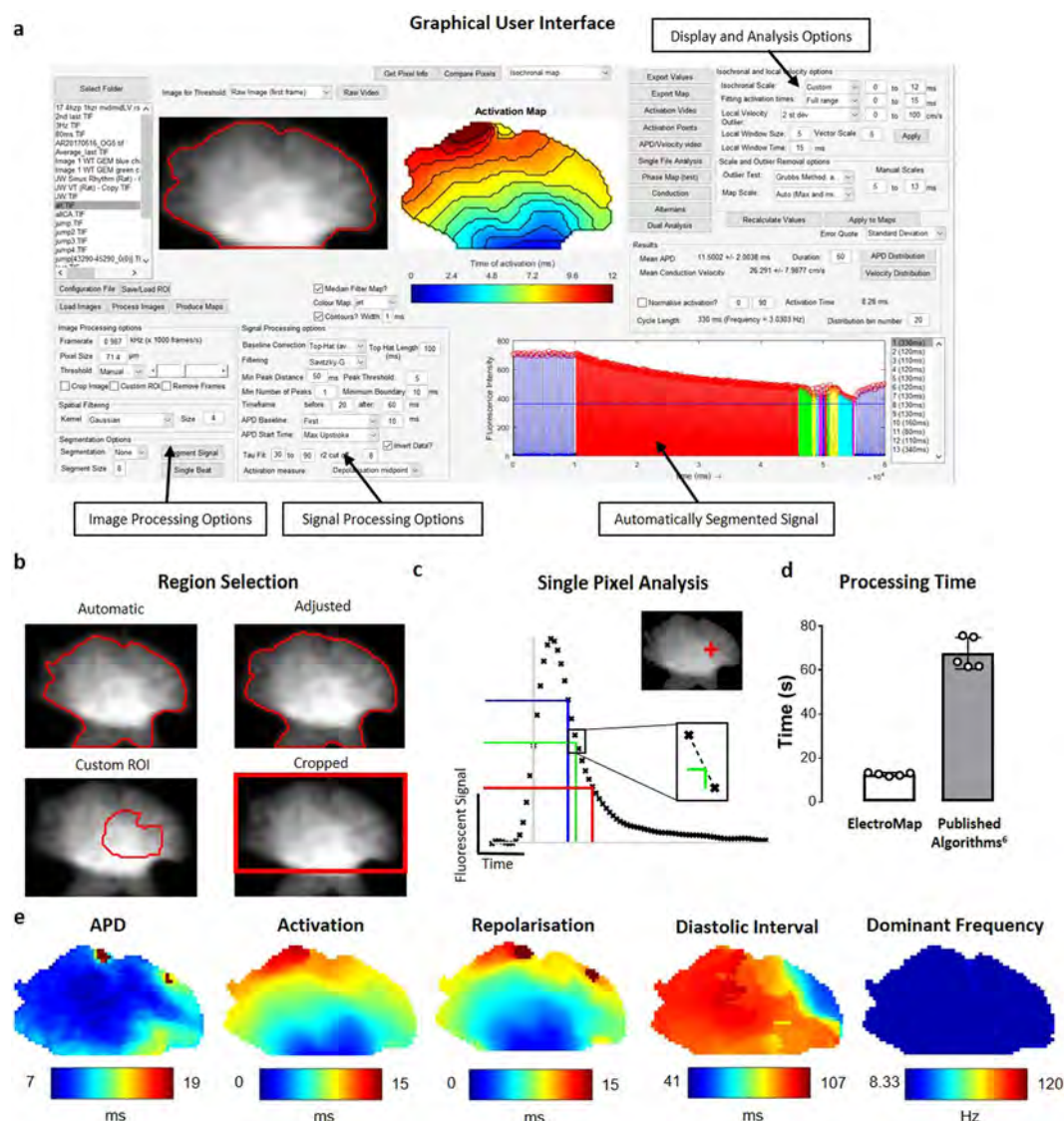


Figure 1. ElectroMap interface and function. **(a)** ElectroMap Graphical User Interface with automatic signal segmentation, image processing, signal processing, display and analysis options highlighted. **(b)** Illustration of 4 different region selection methods available in ElectroMap. **(c)** Example of analysis from one pixel (top inset) within murine atrial images. Action potential duration (APD) 30 (blue), 50 (green) and 70 (red) are calculated from time of maximum upstroke velocity (vertical grey line) to 30%, 50%, 70% repolarisation respectively. Time of repolarisation calculated by linear interpolation (dotted line) between sampling points, as shown for 50% repolarisation in lower inset. **(d)** Time taken to process and analyse 5 image stacks of murine left atria from raw images to conduction velocity calculation, comparison of ElectroMap and our previously published algorithms. **(e)** Selection of pseudo-colour maps denoting some of the electrophysiological parameters measurable using ElectroMap.

effective EP parameter quantification from single image pixels (Fig. 1c). The ElectroMap user interface permits signal inversion via a simple checkbox option. User-defined settings can be stored and recalled for future analysis.

Integration of automated pacing frequency recognition and numerous user-defined segmentation options (Supplementary Fig. I) enables simple and intuitive application of powerful analysis strategies including beat-to-beat analysis of long experimental files and multi-beat (ensemble) averaging to improve signal-to-noise ratio (SNR). Code optimization resulted in increased processing speed of up to five-times, compared to our previously published algorithms¹⁵ (Fig. 1d).

ElectroMap incorporates several definitions for activation (Start – d^2F/dt^2_{max} , Upstroke – dF/dt_{max} , Depolarisation Midpoint, Peak) and repolarisation (Downstroke – dF/dt_{min} , Repolarization Percentage, End – d^2F/dt^2_{max}), Supplementary Fig. II. Repolarisation percentage can be set to any custom value between 0 and 100% repolarisation/decay from peak for both repolarization and duration mapping (Supplementary Fig. III). Unless stated otherwise, depolarization midpoint was used to create activation maps, action potential duration (APD) was defined from upstroke to 50% repolarization and calcium transient duration (CaT) was defined from upstroke

to 50% repolarization/decay. For calcium transient analysis, τ was calculated by fitting a mono-exponential model to a user defined region of decay from peak cytosolic calcium. Cardiac alternans were measured as change in duration or peak amplitude from one calcium transient to the previous. Additionally, effects of cytosolic calcium load were investigated by comparing 'load' and 'release' alternans amplitude, as in Wang *et al.*²³. Analysis results can be exported from ElectroMap's interface as TIFF files for individual maps, AVI/GIF files for multi-image analyses such as beat-to-beat (see Supplementary Video I), and comma separated value (.csv) files for parameter distribution and beat-to-beat analysis.

Statistical analysis. Data are presented as mean \pm standard error. Differences between group means were examined using two-tailed, paired Student's t-test or using One Way Analysis of Variance (ANOVA) with Bonferroni test, and were accepted as significant when $P < 0.05$.

Results

We have developed a novel, user-adaptable, semi-automated, robust, open-source software ElectroMap using MATLAB, see Fig. 1a for graphical user interface. The software is freely downloadable from <https://github.com/CXO531/ElectroMap>, and is available as a standalone executable file or as source code which can be run and edited in MATLAB. Algorithms implemented within ElectroMap have previously been validated against monophasic and transmembrane potentials in murine atria¹⁵. Here, we present the application and further validation of ElectroMap for the analysis and mapping of basic and complex cardiac electrophysiology from optical mapping datasets (Figs 1–8) and endocardial electrograms (Fig. 8).

Conduction Velocity Module. Analysis of the spread of electrical activation in cardiac tissue at high spatiotemporal resolution is one of the most powerful applications of optical mapping. We have developed a comprehensive CV analysis module within ElectroMap (Supplementary Fig. IV), to overcome a multitude of complexities and potential user-bias associated with CV calculations^{18,24}. The module incorporates two established methods that rely on superimposing a vector field upon the activation map: (i) multi-vector and (ii) single vector method (see Fig. 2a,b). Additionally, we have developed a novel method that quantifies time taken to activate a percentage of the tissue. This approach allows calculation of 'activation constant' (see Fig. 2c,d), thereby providing a measure of activation spread across the whole tissue.

To validate the three CV calculation methods, we generated computationally simulated model data (Fig. 3a and Supplementary Fig. V; for algorithms, see Supplementary Material). All three methods accurately measured conduction velocities ranging from 10 to 100 cm/s in isotropic model data (Fig. 3a(i)). As shown in Fig. 3b,c, single vector and multi-vector methods demonstrate a linear increase in CV with faster model conduction speed. Activation curve method accurately detected a change in CV (Fig. 3d), increase in model CV led to a reduction in the time taken to activate 50% (act_{50}) of the tissue. We also validated CV analysis methods using models of anisotropic activation (Fig. 3a(ii)) and regional conduction block (Fig. 3a(iii)). Single vector analysis correctly detected slower CV along the transverse ($180^\circ/360^\circ$) compared to longitudinal ($0^\circ/270^\circ$) direction in anisotropic waves, and conduction slowing adjacent to the region of conduction block (Fig. 3e). Similarly, multi-vector method successfully identified regions of reduced CV in anisotropic waves and severe conduction slowing around the area of conduction block (Fig. 3f). Activation curve analysis was able to detect the slowing of conduction in the anisotropic wave, as evident by a prolongation of the activation curve, and a delay in activation caused by conduction block (Fig. 3g). Additionally, Gaussian noise with incrementally increasing standard deviation (defined as percentage of action potential amplitude, Supplementary Fig. VII) was introduced to isotropic simulated data with CV of 50 cm/s, Fig. 3h. As expected, increased noise in single beat data decreases the ability to accurately calculate CV, with noise levels above 20% resulting in erroneous CV measurements (Fig. 3i). However, SNR can be improved using temporal and spatial filtering or multi-beat ensemble averaging within ElectroMap. Temporal filtering (Savitzky-Golay filter) did not improve CV measurement, whereas both spatial filtering (3×3 Gaussian filter) and ensemble averaging of 10 beats substantially improved CV measurement accuracy.

Further validation was performed using experimental datasets acquired from murine left atrial tissue. We focused on two physiologically relevant stimuli known to reduce CV: an increase in pacing frequency²⁵ and acute hypoxia²⁶ (Fig. 4a). Indeed, significant slowing of CV, due to increased pacing frequency, was detected by multi-vector method (Fig. 4b, $P = 0.0335$) and activation curve method, as shown by an increase in the act_{50} (Fig. 4c and d, $P = 0.0119$). Both methods also accurately detected a more severe slowing of CV caused by exposure to acute hypoxia (Fig. 4e–g, $P < 0.0001$ and $P = 0.0051$ respectively).

High-Throughput Beat-to-Beat Analysis. Studies of beat-to-beat variation can provide important information about short periods of regional or whole tissue electrical instability, e.g. in response to pacing frequency change, pharmacological agents or disease states. Therefore, we developed and tested algorithms to allow high-throughput analysis of beat-to-beat alterations in long experimental files. Guinea pig hearts were paced over 70 seconds with a 5–8–5 Hz pacing protocol²⁷ and beat-to-beat changes in APD₅₀ examined (Fig. 5a and Supplementary Videos I and II). Increasing the pacing frequency (from 5 Hz to 8 Hz) induced reversible shortening of mean ventricular APD (Fig. 5b). Furthermore, significant APD heterogeneity was detected in the first 4 beats, immediately after transition from 5 Hz to 8 Hz (Fig. 5b,c). Switching back from 8 Hz to 5 Hz (at 40 s) also induced some APD heterogeneity while highlighting a slow return to the steady state APD (Fig. 5b,d).

Calcium Decay Mapping. Optical mapping is increasingly utilised to study calcium release patterns across myocardial tissue or cellular monolayers, in response to disease, genetic factors or drug administration¹⁹. The estimation of calcium decay constant (τ) is common in single cell studies. However, τ is not commonly mapped

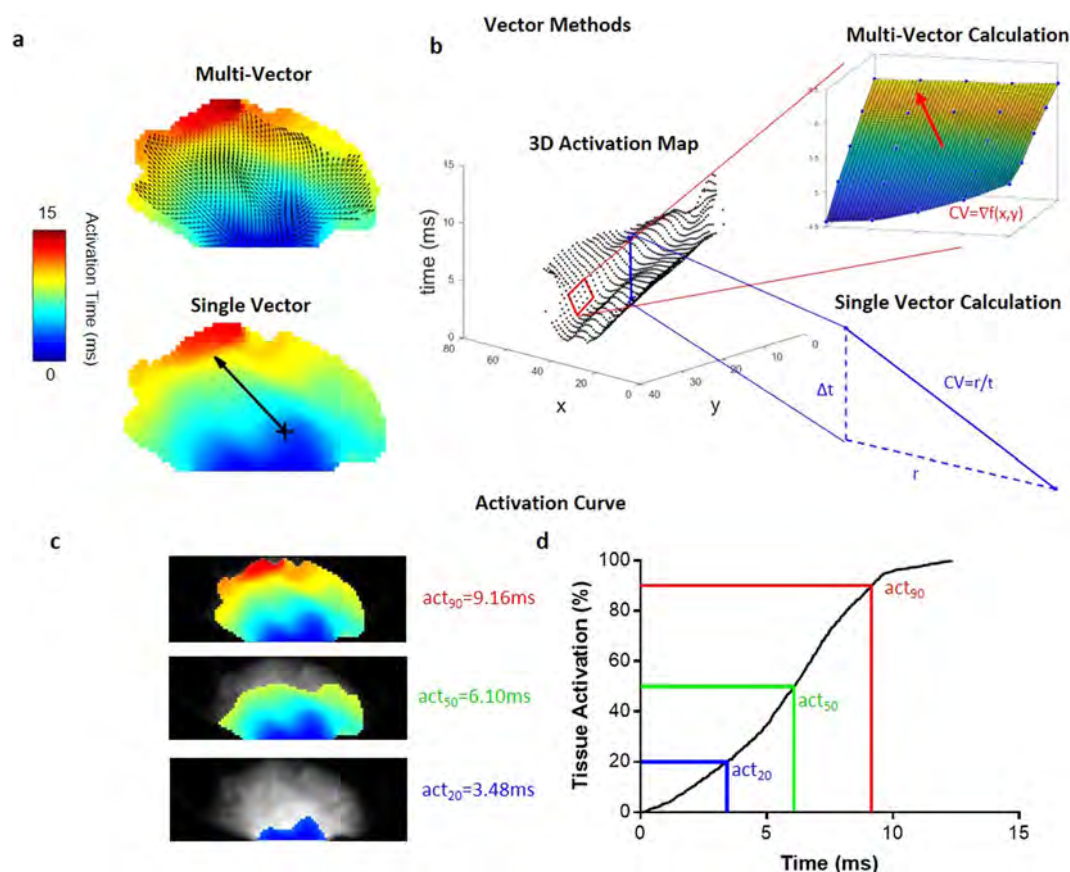


Figure 2. ElectroMap conduction velocity module quantification methods. (a) Vector methods applied to murine atria. Top panel: multi-vector method, with local conduction vectors (arrows) calculated across the tissue. Lower panel: single velocity method, where conduction speed is measured along the vector (arrow) connecting two points. (b) Activation map represented in 3D with x,y pixel positions and activation time on z-axis. Upper inset demonstrates calculation of one local vector from a 5×5 pixel region by fitting of a polynomial surface ($f(x,y)$) to measured activation times ($t(x,y)$). Lower inset shows calculation of single vector velocity from activation time difference (Δt) and distance (r) between two selected points. (c) Activation of the murine atria at 20% (act_{20}), 50% (act_{50}), and 90% (act_{90}), total activation. (d) The associated activation curve, with act_{20} , act_{50} and act_{90} highlighted.

across multicellular preparations²⁸, likely due to lack of support for this function in available software platforms. We developed algorithms for calculation of CaT and τ maps, as shown in Fig. 6a,b. Importantly, CaT can be measured from various ‘activation times’ during upstroke (Supplementary Figs II and VI), allowing for assessment of both calcium release and uptake (Fig. 6a inset). Moreover, τ can be fitted from any user-defined value (Fig. 6b inset). To test and validate algorithms developed for calculation of τ , mouse atria were loaded with Rhod-2AM and paced at incremental frequencies (3–8.33–10–12.5 Hz). Software accurately calculated progressively shorter τ values at higher pacing frequencies (Fig. 6c,d, $P < 0.0001$ for all pacing frequencies compared to 3 Hz). Interestingly, higher pacing frequencies were associated with a reduction in τ heterogeneity (Fig. 6e, $P = 0.0286$ and $P = 0.0168$ for 10 Hz and 12.5 Hz pacing respectively).

Alternans Analysis Module. Alternans are beat-to-beat 2-period oscillations in ion handling, electrical activity and hence mechanical contraction of the myocardium that can act as a precursor to conduction block and lethal arrhythmias^{29,30}. We have developed a module within ElectroMap to detect and quantify alternans across tissue and cellular monolayers. Alternans module is capable of quantifying peak, duration, and release or load alternans (see Supplementary Fig. VIII for alternans definitions).

In Fig. 7 we demonstrate utility of the alternans module in detection and quantification of calcium alternans in a murine left atrium loaded with Rhod-2AM. The atrium was subjected to high frequency pacing of 12.5 Hz, initially leading to moderate alternans (Fig. 7a, blue CaTs) and then transitioning to more pronounced alternans (Fig. 7a, red CaTs). ElectroMap was used to generate maps allowing visualization and alternans quantification across the atrium (Fig. 7b,c). Alternans displayed clear spatial heterogeneity (Fig. 7b,c) with increased ‘CaT Peak Alternans’ correlating with changes in diastolic calcium load (‘Load Alternans’), see Fig. 7c.

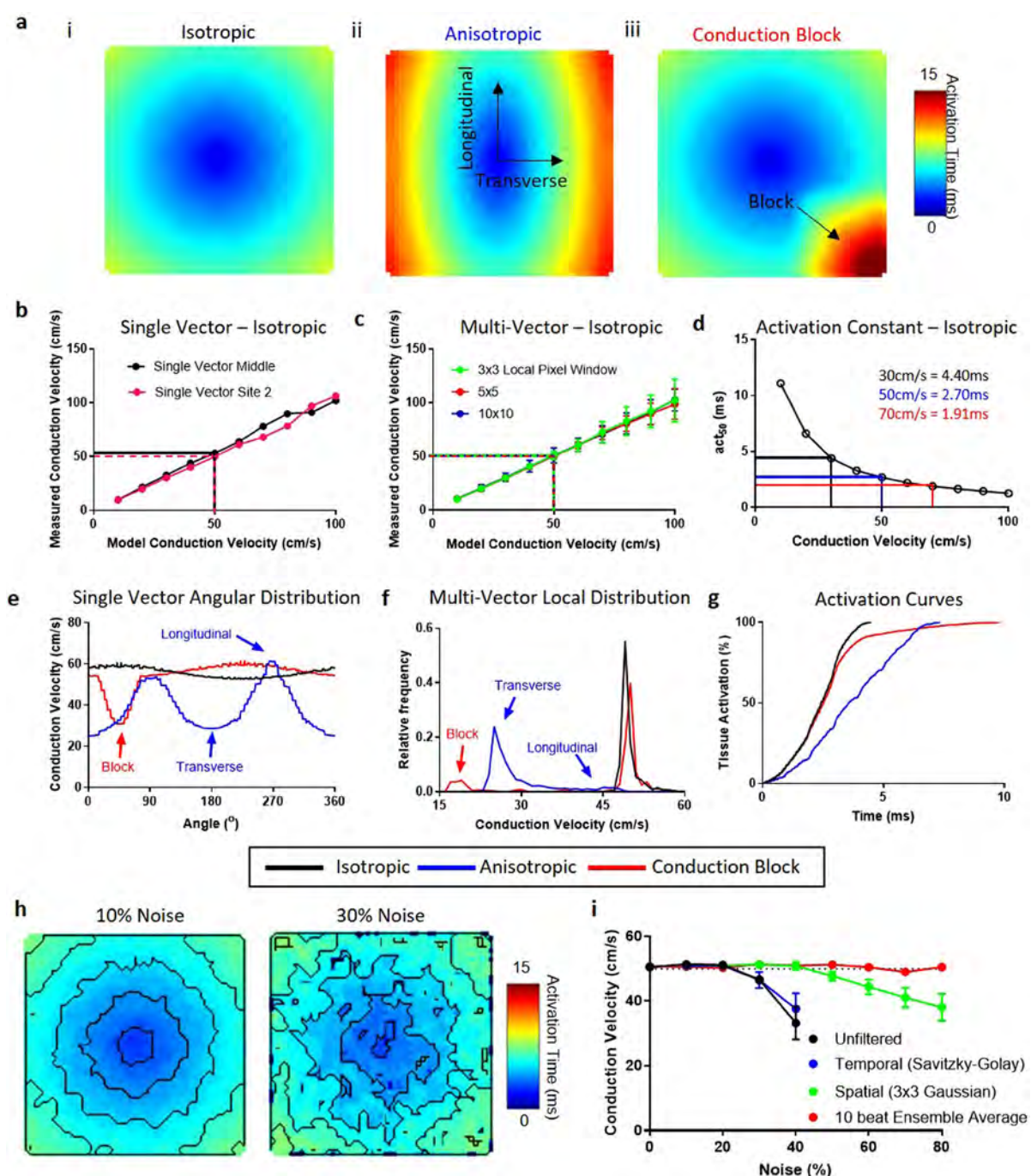


Figure 3. Validation of conduction velocity quantification methods using model datasets. **(a)** Model conduction datasets exhibiting isotropic conduction (i), anisotropic conduction (ii) and isotropic conduction with a 2:1 conduction block in lower right region (iii). **(b–d)** Measured conduction velocities (CV) from isotropic conduction model datasets spanning 10 to 100 cm/s using ElectroMap. **(b)** CV is measured using a single vector from centre of sample (black) and from edge of sample (pink). **(c)** multi-vector method is used with window sizes of 3×3 (green), 5×5 (red) and 10×10 (blue) pixels. CV is then measured as mean of the magnitude of all local vectors calculated, with error bars representing the standard deviation of the mean. **(d)** Activation curve method with act_{50} (time to 50% activation) used to quantify conduction. **(e–g)** Three CV quantification methods applied to model datasets with isotropic, anisotropic and conduction block present conduction. In all three cases, fastest model conduction was 50 cm/s. **(e)** Change in measured CV as a function of angle using single vector method from centre of tissue. **(f)** Distribution of local vector magnitude measured by multi-vector method (5×5 pixel window) in the three model datasets. **(g)** Activation curves from the model datasets. **(h)** Example activation maps from unfiltered model datasets with isotropic conduction of 50 cm/s, but with 10% and 30% signal noise. **(i)** Measured CV using multi-vector method (5×5 pixel window) from unfiltered (Black), temporally filtered (Savitzky-Golay, Blue), Spatially filtered (3×3 Gaussian, Green) and 10 beat ensemble averaged (Red) model datasets at increasing noise levels, $n = 5$ at each noise level.

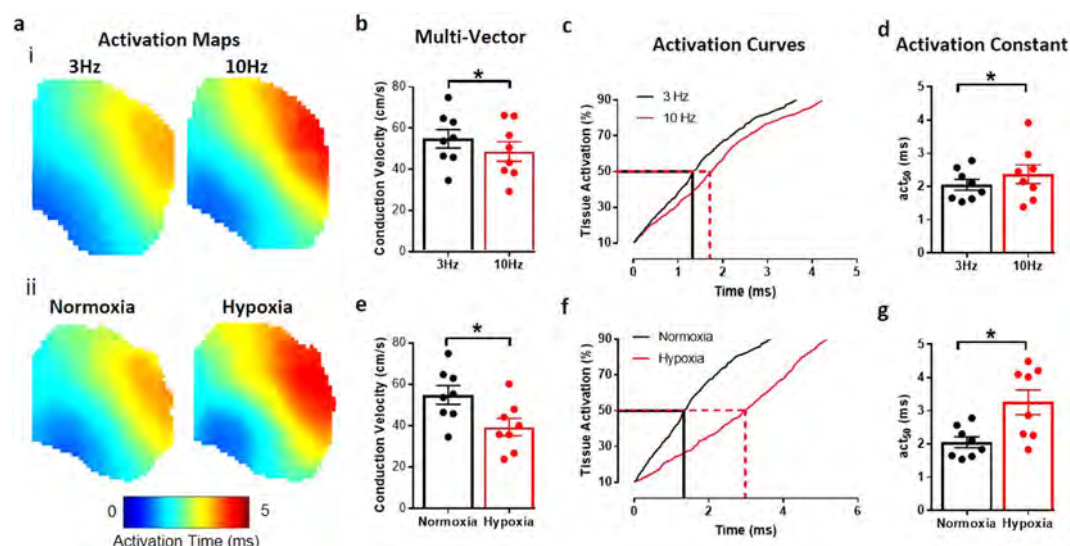


Figure 4. Validation of conduction velocity quantification methods in murine atria. **(a)** Activation maps from murine atria at 3 Hz and 10 Hz pacing (i), and during normoxia and hypoxia (ii). **(b)** Pacing at 10 Hz slows CV, measured using multi-vector method. **(c)** Representative activation curve showing prolongation of activation at 10 Hz vs 3 Hz pacing. **(d)** Pacing at 10 Hz slows CV, measured by time to 50% activation (act_{50}). **(e)** CV slowing induced by hypoxia, measured using multi-vector method. **(f)** Representative activation curve showing prolongation of activation curve by hypoxia. **(g)** Hypoxia slows CV, measured by time to 50% activation (act_{50}). Grouped data displayed as mean \pm standard error, $n = 8$, * $P < 0.05$ by paired t-test.

Human Optical Mapping and Electrogram Recordings. ElectroMap's utility extends to human tissue, see Fig. 8a for optical mapping of human atrial appendages. We also looked to test whether ElectroMap can be applied to analysis of clinically relevant mapping technologies. Right atrial virtual electrograms from a patient during sinus rhythm and AF were recorded and analysed after QRST subtraction²². During sinus rhythm, the spread of activation was calculated from the timing of dV/dt_{min} in each electrogram, generating an activation map (Fig. 8b). ElectroMap clearly identified higher DF components (Fig. 8c) during AF in the physiological range of 4–10 Hz (DF range can be set within ElectroMap's interface). Additionally, marked phase discontinuities (Fig. 8d and Supplementary Video III) are observed in the electrogram recordings during AF. These findings are confirmed using previously published algorithms²² with similar areas of high dominant frequency and discontinuous phase behaviour identified (Fig. 8e,f).

Additional Features. ElectroMap analysis options further extend to measure diastolic interval (DI) and time to peak. DI is measured from APD90 to the following activation time, which can be difficult to quantify in low SNR samples on a single beat. To validate the DI function, guinea pig hearts were loaded with Di-8-ANEPPS and pacing cycle length was decreased in 10 ms intervals from 170 ms to 110 ms. Ensemble averaging of 10 beat segments was used to produce an 'average beat diastolic interval', with improved SNR, and DI mapping function was validated by plotting DI-APD restitution curves (Supplementary Fig. VIII). Both APD50 and DI decrease more rapidly at higher pacing frequencies as previously demonstrated³¹.

Optogenetic excitation and pacing via light pulses in cardiac tissue expressing light sensitive ion channels is a novel research tool^{32,33} and may even be used for cardiac pacing in patients³⁴. However, introduction of large amplitude light pulses will distort optical mapping images and thus preclude processing and analysis of such data. To this end, ElectroMap integrates a mapping artefact removal algorithm (Supplementary Fig. IX), which can identify and correct for light-pacing peaks, thereby allowing processing and analysis of previously obscured data.

Discussion

This work presents the development and validation of a novel open-source software for analysing and mapping optical and electrical signals. We demonstrate the compatibility of ElectroMap with a variety of camera types, species and experimental models. Key features include comprehensive measurement, analysis and mapping of global and regional conduction, versatile signal segmentation and semi-automated high-throughput analysis of action potential and its spatial and temporal (beat-to-beat) variations, calcium transients, and cardiac alternans. Using model and real data, we demonstrate the application of ElectroMap for analysis, measurement and mapping of basic and complex electrophysiology and its utility in dissecting pro-arrhythmic mechanisms *in vitro* and *in vivo*.

ElectroMap is built on years of international research and development in optical mapping processing and analysis, described in many excellent papers and reviews^{6,14,15,18,35,36}. Algorithms that ElectroMap relies on have previously been validated against monophasic and transmembrane potentials in murine atria¹⁵. Further validation performed against established open-source (Rhythm¹⁴) and commercially available software (Optiq, Cairn Research, UK) yielded similar APD values and activation maps (Supplementary Fig. X). To the best of our knowledge, this is the first such comparison of commonly used analysis algorithms, which should help instil confidence

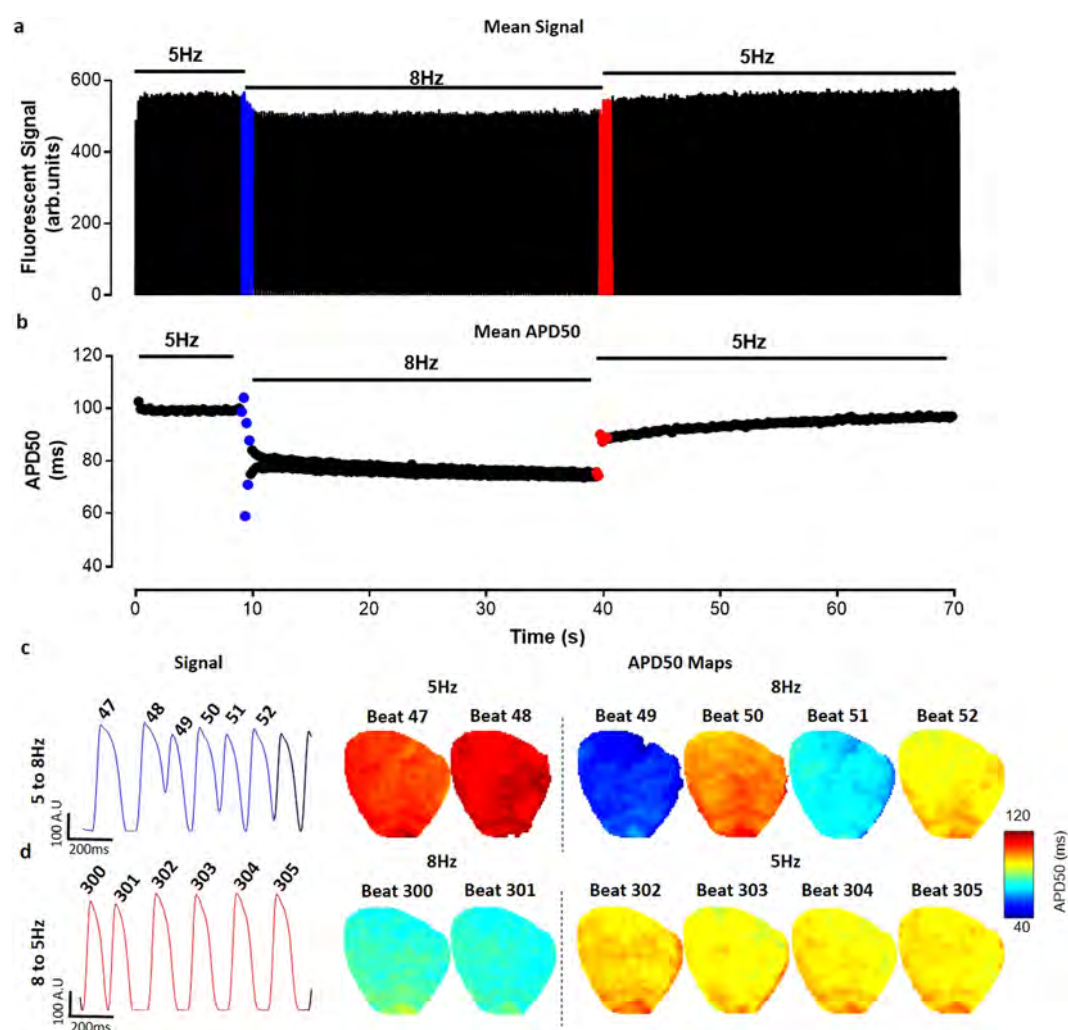


Figure 5. Beat to beat analysis of whole guinea pig heart. (a) Tissue averaged fluorescent signal from voltage dye loaded guinea pig heart across 70 s experiment. (b) Graph of whole heart beat-to-beat changes in mean APD50. (c) Raw trace and whole heart APD50 maps prior to (beats 47 & 48) and immediately after (beats 49–52) pacing frequency increase from 5 Hz to 8 Hz (blue in A and B). (d) Raw trace and whole heart APD50 maps prior to (beats 300 & 301) and immediately after (beats 302–305) pacing frequency return to 5 Hz.

in interpretation of data generated thus far. Importantly, ElectroMap provides further functionalities and outputs, not widely available currently, including ensemble averaging, multiple CV methodologies, automatic frequency detection, signal segmentation, alternans analysis and decay constant mapping. The use of ElectroMap extends beyond optical mapping, allowing for its application in clinical settings with electrogram array data.

Robust validation studies performed using both model and experimental data demonstrate ElectroMap's utility for accurately quantifying key parameters of electrical function and calcium release across cardiac tissue. CV quantification in model data with noise verified that processing using ElectroMap allows accurate parameter quantification. In this case, ensemble averaging proved the most effective processing strategy due to the randomness of the noise and the underlying identical morphology of all simulated action potentials. In other circumstances, (e.g. beat-to-beat variations) ensemble averaging of signals should be avoided, necessitating distinct processing strategies such as spatial filtering, temporal filtering and baseline correction which are all employable using ElectroMap.

Additionally, we demonstrate that improved processing speeds with automatic or user defined signal segmentation enable more complex and computationally challenging analyses; e.g. beat-to-beat variations in APD or regional differences in calcium decay. Indeed, we demonstrate that using ElectroMap, rapid and straightforward analysis of long experimental datasets can reveal acute periods of pro-arrhythmic EP behaviour throughout the entire guinea pig myocardium (Fig. 5). Such analysis would otherwise be missed by ensemble averaging of multiple beats or analysis of a single beat. ElectroMap, in contrast, provides rapid analysis of these complex EP parameters and exports to video and spreadsheet formats that facilitate interpretation of the observed patterns. This may be of particular importance when examining the pathophysiological effects of rapid changes in heart rate and/or immediate and prolonged responses to stimuli such as adrenaline or acute ischaemia. With improving SNR through better cameras and dyes, there is an increasing demand for beat-to-beat analysis of mapping data^{37,38}. We

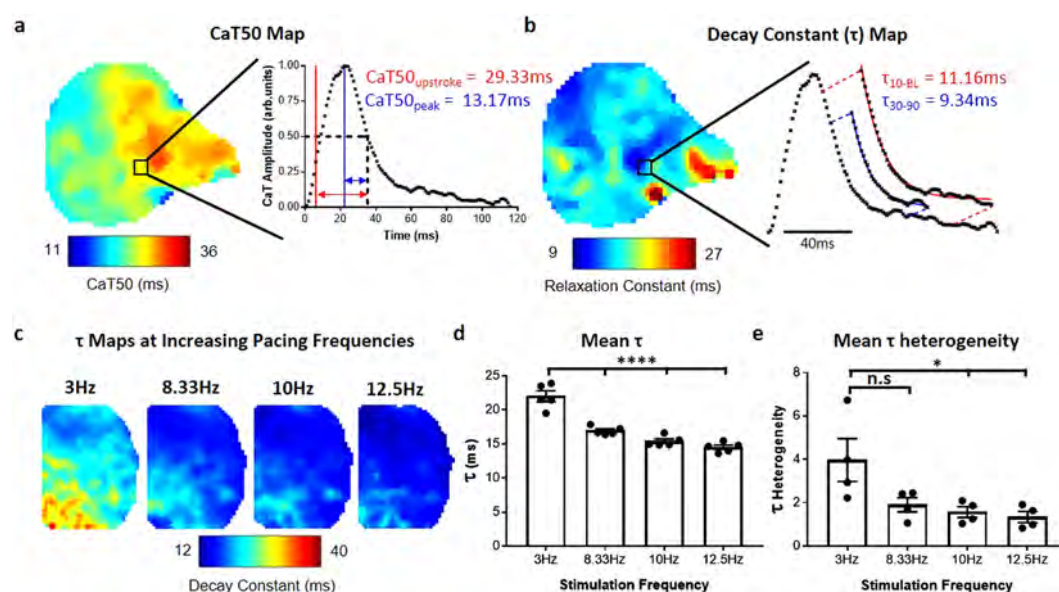


Figure 6. Calcium analysis and decay constant validation. (a) CaT50 map from murine atrium as measured from time of maximum upstroke velocity to 50% decay, illustrated in red in region of interest signal ($\text{CaT50}_{\text{upstroke}}$). Also shown is the measurement of CaT50 from peak amplitude in region of interest (blue, $\text{CaT50}_{\text{peak}}$ map in Supplementary Fig. VA). (b) Map of decay constant, τ , from the same atrium. Map shows calculation of τ by fitting of exponential decay points between 30% and 90% decay from peak (τ_{30-90}), illustrated for the regional signal in blue. Also shown is calculation of τ between 10% decay and baseline (red, τ_{10-BL} map in Supplementary Fig. VD). (c) Representative τ maps (τ_{30-90}) from murine left atria as pacing frequency is increased. (d) Data showing shortening of mean τ across the atria with increased pacing frequency. (e) Data showing decrease of τ heterogeneity (measured as standard deviation of mean τ across individual atria) across the atria with increased pacing frequency. Data displayed as mean \pm standard error, $n = 5$. $P < 0.05$, One-Way ANOVA followed by Bonferroni multiple comparison test against 3 Hz pacing.

anticipate that ElectroMap's ability to achieve such analysis in a high-throughput semi-automated manner will prove valuable for preclinical and clinical researchers.

The ability to simultaneously use three CV quantification methods is a key feature of ElectroMap. This is essential due to inherent limitations of each individual methodology for analysis of cardiac CV^{18,24}. Here, we demonstrate that single vector method can suffer from significant user-generated overestimation of CV (see Supplementary Fig. IVA). More automated approaches have been proposed, such as that of Doshi *et al.*³⁹ whereby single vector quantification is limited to areas where activation time linearly increases. Within ElectroMap's conduction module, we have looked to overcome and highlight difficulties with the single vector method via an automatic angular sweep of measured CV from a user chosen point, as in Fig. 3e and Supplementary Fig. IVA. This approach reveals inherent variability that stems from user-defined propagation direction. ElectroMap automatically identifies the slowest conduction direction, which, in normal circumstances, will be parallel to wavefront propagation. The angular sweep additionally allows straightforward identification of longitudinal and transverse CVs^{40,41}.

Application of multi-vector method reduces the likelihood of user-introduced errors but does not eliminate them completely. Simulation studies by Linnenbank *et al.*¹⁸ for instance demonstrate that despite increased automation, multi-vector methods can introduce systematic errors in CV quantification. The successful use of the method requires minimum criteria to be met in terms of grid size, local region size and angular binning for identification of propagation directions. Another problem can stem from inability to fit local vectors to some areas of the tissue. For example, activation definitions that are intrinsically limited to sampling rate (such as upstroke) can result in local regions where measured activation time is the same throughout. In such circumstances, meaningful surface fit (e.g. Fig. 2b) or other methods for describing local activation such as finite difference analysis⁴², are not achievable²⁴. This can be particularly problematic in small tissue samples, like isolated murine left atria, or in tissues exhibiting fast conduction and/or wavebreak. Viable solutions to this issue include interpolation of data between sampling points or use of alternative activation definitions such as depolarisation midpoint (see Supplementary Fig. II and IV). However, this relies on accurate signal interpolation, not always achievable in practice⁴³. Epicardial conduction velocity quantification can also be complicated by multiple breakthroughs in the endocardium leading to inaccurate CV estimation during complex arrhythmias⁴⁴ or in the absence of epicardial pacing. In conclusion, there is no universally applicable activation measure suited for every optical mapping experiment, further validating the need for integration of multiple activation and CV quantification methodologies within ElectroMap.

ElectroMap incorporates a novel activation curve method of conduction analysis. This method allows users to quantify the time taken to activate a defined tissue percentage or study the whole activation curve. The

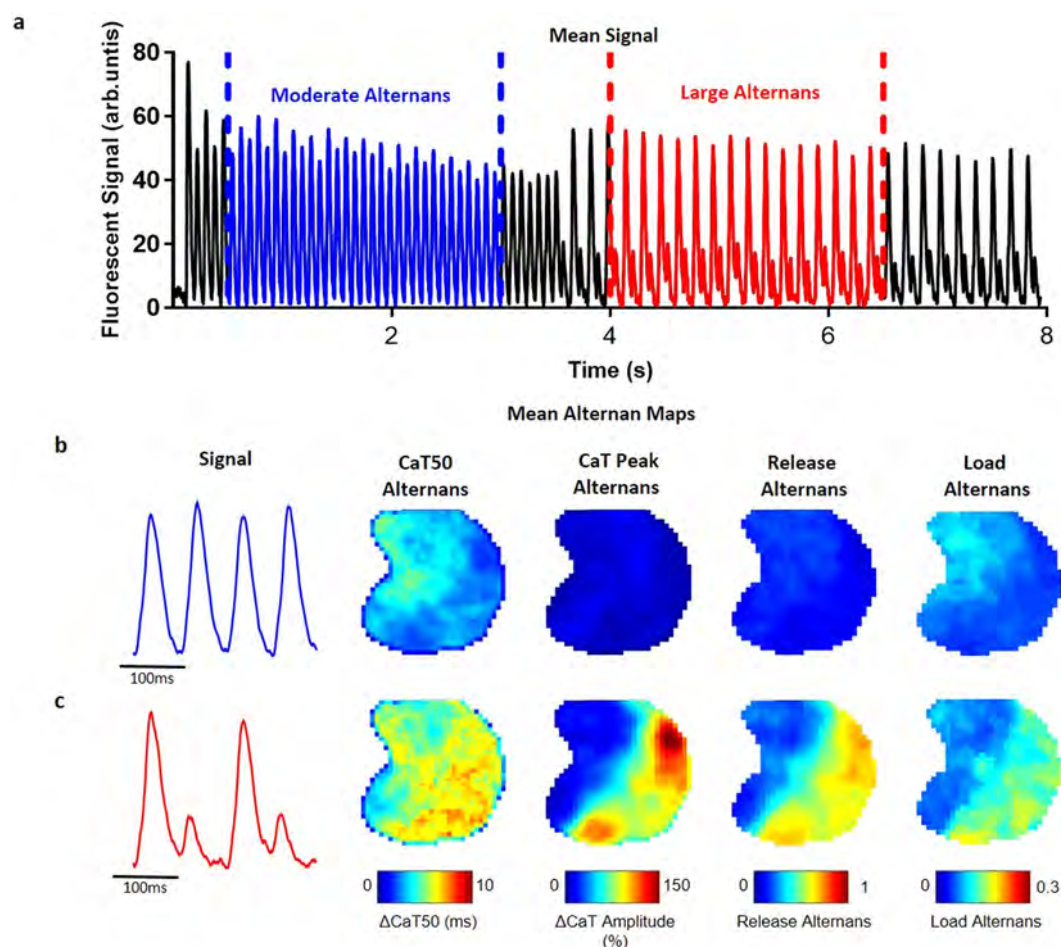


Figure 7. Alternans module. (a) Tissue averaged fluorescent signal from calcium dye loaded mouse atrium paced at 12.5 Hz, showing distinct alternans behaviour at 0.5–3 s (blue, moderate alternans), and 4–6.5 s (red, large alternans). (b) Representative signals and time averaged alternans maps from tissue during moderate alternans behaviour. Four maps shown correspond to the four measures of alternans available in ElectroMap (see methods and Supplementary Fig. VI). (c) Maps during period of large alternans (4–6.5 s) show increase in alternans amplitude, and clear spatial discordance.

methodology is less susceptible to user bias or to sparsity of local vectors in areas of rapid conduction as it does not rely on user input or vector calculation. Furthermore, activation time can be normalized to tissue size, yielding an activation constant in units such as ms/mm². This extends the use of the activation constant to studies where tissue morphology may be altered, such as in hypertrophy or genotype dependent differences in cardiac structure. However, activation constant only provides a summarised measure of activation, thus a combination of analysis methods may be required for robust interrogation of cardiac conduction. Additionally, despite the various CV methods within ElectroMap, conduction analysis can remain challenging if the underlying activation pattern is heterogeneous, often observed in arrhythmic tissue and cultured cardiac monolayers⁴⁵. The ‘Ccoffinn’ method of Tomek *et al.*²⁴ combines sophisticated image processing techniques with novel wavefront tracking algorithms and can potentially overcome heterogeneity issues²⁴.

Defining activation times for APD and CaT duration mapping is an important but complex and often poorly understood analysis option. Different studies utilize distinct features of the upstroke to define activation, including dF/dt_{\max} (upstroke)⁴⁴, d^2F/dt^2_{\max} (start)⁴⁶, depolarization midpoint⁴⁷ and peak⁸. Similarly, time of repolarisation/decay can be measured at a defined repolarisation percentage^{15,48}, dF/dt_{\min} (downstroke) or d^2F/dt^2_{\max} ³⁶. The parameters best suited for duration measurement will depend on experimental model, signal quality and experimental question. We have integrated all of these user-selectable definitions within ElectroMap for both APD (Supplementary Fig. II) and CaT mapping (Fig. 6a and Supplementary Fig. VI).

Similarly, τ calculations can be customised in ElectroMap’s interface to calculate decay constant for any user-defined segment of the calcium reuptake. This permits analysis of cytosolic or SR²³ calcium handling kinetics in different animal species and cells. For example, note the regional discrepancy between CaT50 and τ atrial maps in Fig. 6a,b. This contrast results from the definition in CaT50 used, i.e. time from upstroke to 50% decay (CaT50_{upstroke}). CaT50_{upstroke} is a measure of both the release and reuptake of the cytosolic calcium. In contrast, τ depends only on reuptake kinetics, and so is unaffected by the changes in calcium release. By measuring CaT

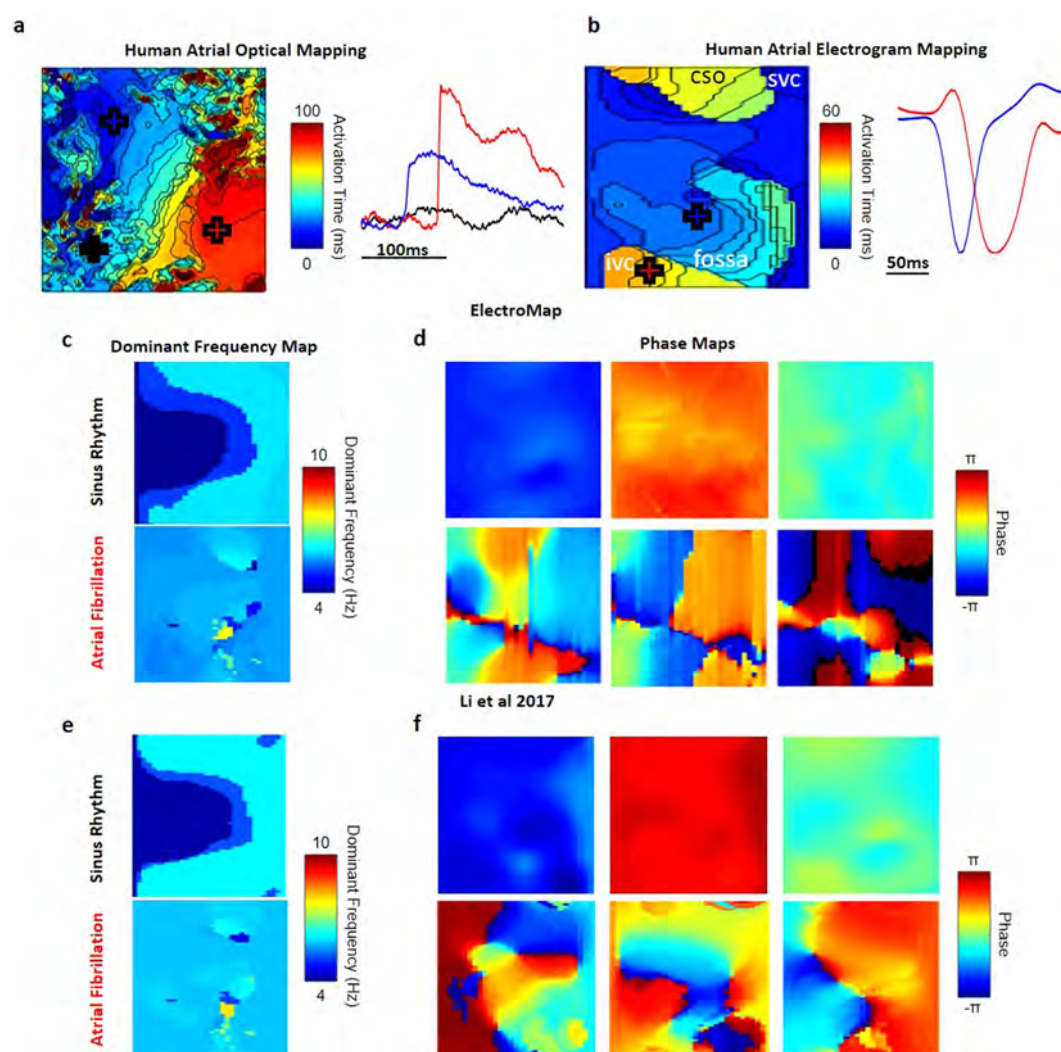


Figure 8. Human atrial optical and electrogram mapping analysis. (a) Activation map and example signals generated from human left atrial appendage stained with voltage sensitive dye. (b) Activation map and example signals generated from human right atrial *in vivo* electrogram array recordings. Labels refer to closest anatomical structure on 2D map - IVC and SVC: Inferior and Superior Vena Cava, CSO – Coronary Sinus Ostium, Fossa - Fossa Ovalis. (c) Dominant Frequency analysis between 4 and 10 Hz, showing localized area of increased frequency during AF. (d) Phase maps at 3 time points during sinus rhythm and AF. Synchronised phase behaviour during sinus rhythm is not replicated during AF. The displayed frames are taken from phase mapping over 30 s, Supplementary Video II. (e) Dominant Frequency analysis and (f) Phase maps at 3 time points during sinus rhythm and AF performed using previously published algorithms of similar datasets²².

from peak ($\text{CaT50}_{\text{peak}}$), the CaT50 and τ values become more similar across the atria (Supplementary Fig. VI). Deciphering pathophysiological relevance of these observations is not within the remit of this manuscript. However, we predict the user-defined tools for comprehensive measurement of vital duration and relaxation parameters that ElectroMap provides will aid understanding of cardiac pathophysiology.

The utility of processing and analysis algorithms in ElectroMap can extend beyond optical mapping. Here, we show analysis of *in vivo* virtual unipolar electrogram recordings from human right atrium (Fig. 8b–d). Despite the contrasting waveforms compared to optical mapping, by analysing the timing of dV/dt_{min} in electrogram recordings, ElectroMap is able to accurately calculate local activation times. Beyond its clinical utility, access to analyses such as dominant frequency and phase mapping, allowing mapping the site of triggered activity during arrhythmia (Fig. 8c,d), can aid the translation of experimental data^{10,49}. These capabilities of ElectroMap require further systematic validation against a range of clinically used platforms, however current outputs are comparable to previous published analysis of similar datasets²², see Fig. 8c–f. Implementation of other analysis options available within ElectroMap such as beat-to-beat segmentation, CV quantification and alternans detection and quantification hold immense potential for the analysis of electrogram data.

ElectroMap provides a robustly validated open-source flexible tool for processing and analysis of optical mapping data. We anticipate ElectroMap to facilitate increased uptake of optical mapping in cardiac electrophysiology. Furthermore, application of novel data analysis strategies developed here will further our understanding of

the mechanisms underpinning lethal arrhythmia. The application of ElectroMap extends beyond optical mapping. Here, we have demonstrated that ElectroMap can also be used in the analysis of clinical electrogram-based mapping data. Moreover, application of high-throughput CV quantification methodologies can be applied to drug-screening pipelines for cardiotoxic effects in cell monolayers. There is scope to broaden the existing functions of ElectroMap, for example, by introducing dual-analysis of simultaneous voltage and calcium recordings and implementing computational approaches to overcome motion artefacts⁵⁰. Furthermore, increases in computational efficiency through more sophisticated computational techniques, such as parallel processing, would allow for faster data processing and could eventually facilitate in-acquisition analysis.

References

1. Mozaffarian, D. *et al.* Heart disease and stroke statistics-2016 update a report from the American Heart Association. *Circulation* **133** (2016).
2. Kirchhof, P. *et al.* The continuum of personalized cardiovascular medicine: A position paper of the European Society of Cardiology. *Eur. Heart J.* **35**, 3250–3257 (2014).
3. Atienza, F., Martins, R. P. & Jalife, J. Translational research in atrial fibrillation: A quest for mechanistically based diagnosis and therapy. *Circ. Arrhythmia Electrophysiol.* **5**, 1207–1215 (2012).
4. Herron, T. J., Lee, P. & Jalife, J. Optical imaging of voltage and calcium in cardiac cells & tissues. *Circ. Res.* **110**, 609–623 (2012).
5. Jalife, J. Rotors and spiral waves in atrial fibrillation. *J. Cardiovasc. Electrophysiol.* **14**, 776–780 (2003).
6. Myles, R. C., Wang, L., Kang, C., Bers, D. M. & Ripplinger, C. M. Local β -adrenergic stimulation overcomes source-sink mismatch to generate focal arrhythmia. *Circ. Res.* **110**, 1454–1464 (2012).
7. Syeda, F. *et al.* PITX2 Modulates Atrial Membrane Potential and the Antiarrhythmic Effects of Sodium-Channel Blockers (2016).
8. Winter, J. *et al.* Sympathetic nervous regulation of cardiac alternans in the intact heart. *Front. Physiol.* **9**, 1–12 (2018).
9. Desk, R., Williams, L. & Health, W. K. Total Excitation of the Isolated Human Heart Total Excitation of the Isolated Human Heart. *Circulation* **41**, 899–912 (1970).
10. de Groot, N. M. S. *et al.* Electropathological Substrate of Longstanding Persistent Atrial Fibrillation in Patients With Structural Heart Disease. *Circulation* **122**, 1674–1682 (2010).
11. Allesie, M. A., Bonke, F. I. M. & Schopman, F. J. G. Circus movement in rabbit atrial muscle as a mechanism of tachycardia. III. The 'leading circle' concept: a new model of circus movement in cardiac tissue without the involvement of an anatomical obstacle. *Circ. Res.* **41**, 9–18 (1977).
12. Schotten, U., Verheule, S., Kirchhof, P. & Goette, A. Pathophysiological Mechanisms of Atrial Fibrillation: A Translational Appraisal. *Physiol. Rev.* **91**, 265–325 (2011).
13. Heijman, J., Guichard, J.-B., Dobrev, D. & Nattel, S. Translational Challenges in Atrial Fibrillation. *Circ. Res.* **122**, 752–773 (2018).
14. Laughner, J. I., Ng, F. S., Sulkin, M. S., Arthur, R. M. & Efimov, I. R. Processing and analysis of cardiac optical mapping data obtained with potentiometric dyes. *AJP Hear. Circ. Physiol.* **303**, H753–H765 (2012).
15. Yu, T. Y. *et al.* An automated system using spatial oversampling for optical mapping in murine atria. Development and validation with monophasic and transmembrane action potentials. *Prog. Biophys. Mol. Biol.* **115**, 340–348 (2014).
16. Yu, T. Y. *et al.* Optical mapping design for murine atrial electrophysiology. *Comput. Methods Biomech. Biomed. Eng. Imaging Vis.* **5**, 368–378 (2017).
17. Holmes, A. P. *et al.* A Regional Reduction in Ito and IKACH in the Murine Posterior Left Atrial Myocardium Is Associated with Action Potential Prolongation and Increased Ectopic Activity. *PLoS One* **11**, e0154077 (2016).
18. Linnenbank, A. C., de Bakker, J. M. T. & Coronel, R. How to measure propagation velocity in cardiac tissue: A simulation study. *Front. Physiol.* **5**(JUL), 1–7 (2014).
19. Jaimes, R. 3rd. *et al.* A Technical Review of Optical Mapping of Intracellular Calcium within Myocardial Tissue. *Am. J. Physiol. Heart Circ. Physiol.* 2015 (2016).
20. Bayly, P. V. *et al.* Estimation of Conduction Velocity Vector Fields from Epicardial Mapping. *Data.* **45**, 563–571 (1998).
21. Krul, S. P. J. *et al.* Treatment of Atrial and Ventricular Arrhythmias Through Autonomic Modulation. *JACC Clin. Electrophysiol.* **1**, 496–508 (2015).
22. Li, X. *et al.* An interactive platform to guide catheter ablation in human persistent atrial fibrillation using dominant frequency, organization and phase mapping. *Comput. Methods Programs Biomed.* **141**, 83–92 (2017).
23. Wang, L. *et al.* Optical mapping of sarcoplasmic reticulum Ca²⁺ in the intact heart: Ryanodine receptor refractoriness during alternans and fibrillation. *Circ. Res.* **114**, 1410–1421 (2014).
24. Tomek, J., Burton, R. A. B. & Bub, G. Ccoffinn: Automated Wave Tracking in Cultured Cardiac Monolayers. *Biophys. J.* **111**, 1595–1599 (2016).
25. Weber, F. M. *et al.* Conduction velocity restitution of the human atrium—An efficient measurement protocol for clinical electrophysiological studies. *IEEE Trans. Biomed. Eng.* **58**, 2648–2655 (2011).
26. Zeevi-Levin, N. *et al.* Gap junctional remodeling by hypoxia in cultured neonatal rat ventricular myocytes. *Cardiovasc. Res.* **66**, 64–73 (2005).
27. Fabritz, L. *et al.* Effect of pacing and mexiletine on dispersion of repolarisation and arrhythmias in Δ KPQ SCN5A (long QT3) mice. *Cardiovasc. Res.* **57**, 1085–1093 (2003).
28. Cheng, Y.-J. *et al.* Focal but reversible diastolic sheet dysfunction reflects regional calcium mishandling in dystrophic mdx mouse hearts. *AJP Hear. Circ. Physiol.* **303**, H559–H568 (2012).
29. Ng, G. A. Feasibility of selection of antiarrhythmic drug treatment on the basis of arrhythmogenic mechanism — Relevance of electrical restitution, wavebreak and rotors. *Pharmacol. Ther.* **176**, 1–12 (2017).
30. Weiss, J. N., Nivala, M., Garfinkel, A. & Qu, Z. Alternans and arrhythmias: From cell to heart. *Circ. Res.* **108**, 98–112 (2011).
31. Clayton, R. H. *et al.* Models of cardiac tissue electrophysiology: Progress, challenges and open questions. *Prog. Biophys. Mol. Biol.* **104**, 22–48 (2011).
32. Entcheva, E. & Bub, G. All-optical control of cardiac excitation: Combined high-resolution optogenetic actuation and optical mapping. *J. Physiol.* **9**, 2503–2510 (2016).
33. Feola, I. *et al.* Localized Optogenetic Targeting of Rotors in Atrial Cardiomyocyte Monolayers. *Circ. Arrhythmia Electrophysiol.* **10** (2017).
34. Nussinovitch, U. & Gepstein, L. Optogenetics for *in vivo* cardiac pacing and resynchronization therapies. *Nat. Biotechnol.* **33**, 750–754 (2015).
35. Jaimes, R. *et al.* A technical review of optical mapping of intracellular calcium within myocardial tissue. *Am. J. Physiol. - Hear. Circ. Physiol.* **310**, H1388–H1401 (2016).
36. Efimov, I. R., Huang, D. T., Rendt, J. M. & Salama, G. Optical mapping of repolarization and refractoriness from intact hearts. *Circulation* **90**, 1469–1480 (1994).
37. Kelly, A. *et al.* Normal interventricular differences in tissue architecture underlie right ventricular susceptibility to conduction abnormalities in a mouse model of Brugada syndrome. *Cardiovasc. Res.* 790–799 (2017).

38. Roney, C. H. *et al.* Rotor Tracking Using Phase of Electrograms Recorded During Atrial Fibrillation. *Ann. Biomed. Eng.* **45**, 910–923 (2017).
39. Doshi, A. N. *et al.* Feasibility of a semi-automated method for cardiac conduction velocity analysis of high-resolution activation maps. *Comput. Biol. Med.* **65**, 177–183 (2015).
40. Thompson, S. A. *et al.* Acute slowing of cardiac conduction in response to myofibroblast coupling to cardiomyocytes through N-cadherin. *J. Mol. Cell. Cardiol.* **68**, 29–37 (2014).
41. Egorov, Y. V., Glukhov, A. V., Efimov, I. R. & Rosenshtraukh, L. V. Hypothermia-induced spatially discordant action potential duration alternans and arrhythmogenesis in nonhibernating versus hibernating mammals. *Am J Physiol Heart Circ Physiol* **303**, H1035–H1046 (2012).
42. Salama, G., Kanai, A. & Efimov, I. R. Subthreshold stimulation of Purkinje fibers interrupts ventricular tachycardia in intact hearts: Experimental study with voltage-sensitive dyes and imaging techniques. *Circ. Res.* **74**, 604–619 (1994).
43. Walton, R. D. *et al.* Extracting surface activation time from the optically recorded action potential in three-dimensional myocardium. *Biophys. J.* **102**, 30–38 (2012).
44. Glukhov, A. V. *et al.* Transmural dispersion of repolarization in failing and nonfailing human ventricle. *Circ. Res.* **106**, 981–991 (2010).
45. Tung, L. & Zhang, Y. Optical imaging of arrhythmias in tissue culture. *J. Electrocardiol.* **39**, 2–6 (2006).
46. Jaimes, R. *et al.* Functional response of the isolated, perfused normoxic heart to pyruvate dehydrogenase activation by dichloroacetate and pyruvate. *Pflugers Arch.* **468**, 131–142 (2016).
47. Kong, W., Ideker, R. E. & Fast, V. G. Transmural optical measurements of Vm dynamics during long-duration ventricular fibrillation in canine hearts. *Heart Rhythm* **6**, 796–802 (2009).
48. Wang, K. *et al.* Cardiac tissue slices: preparation, handling, and successful optical mapping. *Am. J. Physiol. Heart Circ. Physiol.* **308**, H1112–25 (2015).
49. Salinet, J. *et al.* Propagation of meandering rotors surrounded by areas of high dominant frequency in persistent atrial fibrillation. *Heart Rhythm* **14**, 1269–1278 (2017).
50. Christoph, J., Schröder-Schotelig, J. & Luther, S. Electromechanical optical mapping. *Prog. Biophys. Mol. Biol.* **130**, 150–169 (2017).

Acknowledgements

This work was funded by the EPSRC studentship (Sci-Phy-4-Health Centre for Doctoral Training L016346) to D.P., K.R. and L.F., Wellcome Trust Seed Award Grant (109604/Z/15/Z) to D.P., British Heart Foundation Grants (PG/17/55/33087, RG/17/15/33106) to D.P., European Union (grant agreement No 633196 [CATCH ME] to P.K. and L.F.), British Heart Foundation (FS/13/43/30324 to P.K. and L.F.; PG/17/30/32961 to P.K. and A.H.), and Leducq Foundation to P.K. J.W. is supported by the British Heart Foundation (FS/16/35/31952).

Author Contributions

C.O., A.H., T.Y., J.W., J.C., P.K., L.F., K.R. and D.P., designed the research. C.O., A.H., T.Y., J.W., S.W., B.B., J.d.G., G.C., X.L., G.N. and D.P., designed and conducted the experiments. C.O. and T.Y., designed and wrote the software. C.O. analysed the data. C.O., A.H., J.W., P.K., L.F., K.R., and D.P., wrote the paper.

Additional Information

Supplementary information accompanies this paper at <https://doi.org/10.1038/s41598-018-38263-2>.

Competing Interests: PK receives research support from several drug and device companies active in atrial fibrillation and has received honoraria from several such companies. LF has received institutional research grants from EU, BHF, MRC, DFG and Gilead. PK and LF are listed as inventors on two patents held by University of Birmingham (Atrial Fibrillation Therapy WO 2015140571, Markers for Atrial Fibrillation WO 2016012783). All other authors declare no potential conflict of interest.

Publisher's note: Springer Nature remains neutral with regard to jurisdictional claims in published maps and institutional affiliations.



Open Access This article is licensed under a Creative Commons Attribution 4.0 International License, which permits use, sharing, adaptation, distribution and reproduction in any medium or format, as long as you give appropriate credit to the original author(s) and the source, provide a link to the Creative Commons license, and indicate if changes were made. The images or other third party material in this article are included in the article's Creative Commons license, unless indicated otherwise in a credit line to the material. If material is not included in the article's Creative Commons license and your intended use is not permitted by statutory regulation or exceeds the permitted use, you will need to obtain permission directly from the copyright holder. To view a copy of this license, visit <http://creativecommons.org/licenses/by/4.0/>.

© The Author(s) 2019

3.2 Additional material

The following sections detail investigations into ensemble averaging, baseline correction and local vector calculation that were conducted as part of developing the software.

3.3 Testing the efficacy of ensemble averaging in optical mapping

Misapplication of spatial or temporal filtering methods can unphysiologically alter optical recorded cardiac signals. An alternative solution to direct filtering is the use of ensemble or multi-beat averaging, where the cyclic nature of cardiac rhythm is utilised to create an 'average' waveform from several successive action potentials or calcium transients, Figure 3.1A. As pacing cycle length is known, signals can be time matched by stacking fluorescent values at time points separated by the cycle length [1]. This methodology however relies on pacing frequency being known. Methods based on the measured signals, such as the tissue averaged optical signal, are advantageous as they do not rely on prior knowledge of the pacing protocol, can to some extent adapt to physiological pacing and imaging changes, and can be combined with automatic frequency detection algorithms.

The successful use of ensemble averaging relies on accurate signal alignment and temporal stability of the signal. Therefore, to verify the efficacy of ensemble averaging and test different alignment methods, two methods of ensemble

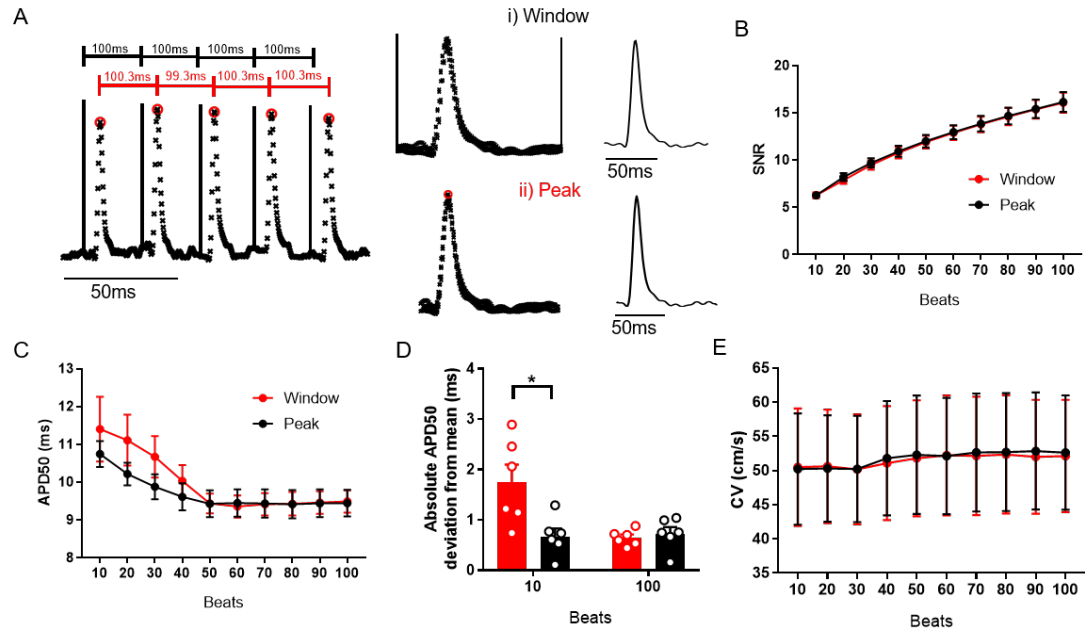


Figure 3.1: Ensemble averaging techniques. A) Example application of the i) Window and ii) Peak techniques for multi-beat averaging. B) Signal to noise ratio (measured as ratio peak amplitude and root mean square of baseline fluorescence) as a function of number of beats averaged. C) Mean APD50 as a function of ensemble averaging technique and number of beats averaged. D) Comparison of inter-sample variability compared to the mean in measured APD50 at 10 and 100 averaged beats. E) Mean CV as a function of ensemble averaging technique and number of beats averaged.

averaging were compared both in effectiveness of reducing noise in optical signals and recovering important EP parameters such as APD in isolated mouse left atria loaded with Di-4-ANEPPS (see section 2). The two methods were (Figure 3.1A) ‘Window’: known pacing frequency used to calculate time point to be averaged which are separated by constant cycle lengths [1], and ‘Peak’: peaks in the tissue averaged optical voltage signal were automatically identified and used for reference to calculate pacing frequency and time points to be matched. No pre- or post-processing was applied other than ensemble averaging. APD50 was calculated as time between maximum upstroke velocity and 50% repolarisation. CV was calculated using the Bayly multi-vector method from activation maps generated using the depolarisation midpoint [2], [3].

Figure 3.1B demonstrates that both methods similarly increased peak SNR to the same extent dependent on number of beats averaged in mouse atria ($n=6$). However, when calculating APD50, there was some evidence of differences between the two methods at lower numbers of averaged beats, but no significant difference in the measured APD50 are present as the number of beats averaged increases, Figure 3.1C. For example, when 10 beats were averaged by the window method, AP50 was 11.4 ± 0.86 ms compared with 10.75 ± 0.34 ms using the automatic peak method ($P=0.50$). At 50 beat averaging, APD50 is 9.44 ± 0.26 ms and 9.43 ± 0.35 ms respectively ($P=0.97$).

Notably however, there is a greater divergence in inter-sample measurements (as measured as deviation from the mean) of APD50 when using the window compared to the peak method at low numbers of averaged beats, Figure 3.1D, which is not the case as more beats are averaged. With 10 beat averaging, the window method results in an inter-sample variability of 1.75 ± 0.35 ms, compared to 0.68 ± 0.16 ms with the peak method ($P=0.043$). This suggests a greater number of action potentials need to be averaged using the window method to accurately recover the waveform. CV measurements are the same by both methods irrespective of number of beats averaged, Figure 3.1E. These results suggest that peak alignment was a more effective method, and was hence decided as the default method of alignment for ensemble averaging. Of course, an important constraint of ensemble averaging will be a loss of beat-to-beat heterogeneity, which can preclude analysis of important phenomena such as alternans.

3.3.1 Ensemble averaging for improved optical signal quality in mouse left atria

To further test the utility of ensemble averaging for use in optically mapped mouse atria, a simple model of the mouse atrial action potential and conduction (see appendix A.1.3) was used to produce model datasets with progressively longer APD₅₀ values (6-14ms), Figure 3.2A, and confirm the accuracy of APD measurement algorithms, Figure 3.2B. APD₅₀ was then set to 10ms and Gaussian noise introduced to these datasets. As expected, increasing Gaussian noise decreased the ability to accurately measure APD from a single beat (Figure 3.2Ci), and increased measurement heterogeneity (Figure 3.2Cii).

Ensemble averaging of 10 beats was then applied to the model dataset, while also independently applying spatial filtering (3x3 Gaussian filter, standard deviation = 1.5) and temporal filtering (3rd order Savitzky-Golay filter, 11ms length). Temporal filtering did not improve ability to measure APD but did reduce measurement heterogeneity within the sample (Figure 3.2C). Both spatial filtering and 10 beat ensemble averaging substantially improved APD measurement accuracy (Figure 3.2C).

In independent experiments, regional action potential morphology heterogeneity was introduced to simulated datasets as an area of prolonged APD (Figure 3.2D) and APD gradient (Figure 3.2E). In the ideal, no noise case, regional differences are accurately identified, which are masked at 30% noise. However, by 10 beat ensemble averaging, these differences can still be clearly identified (Figure 3.2D and E).

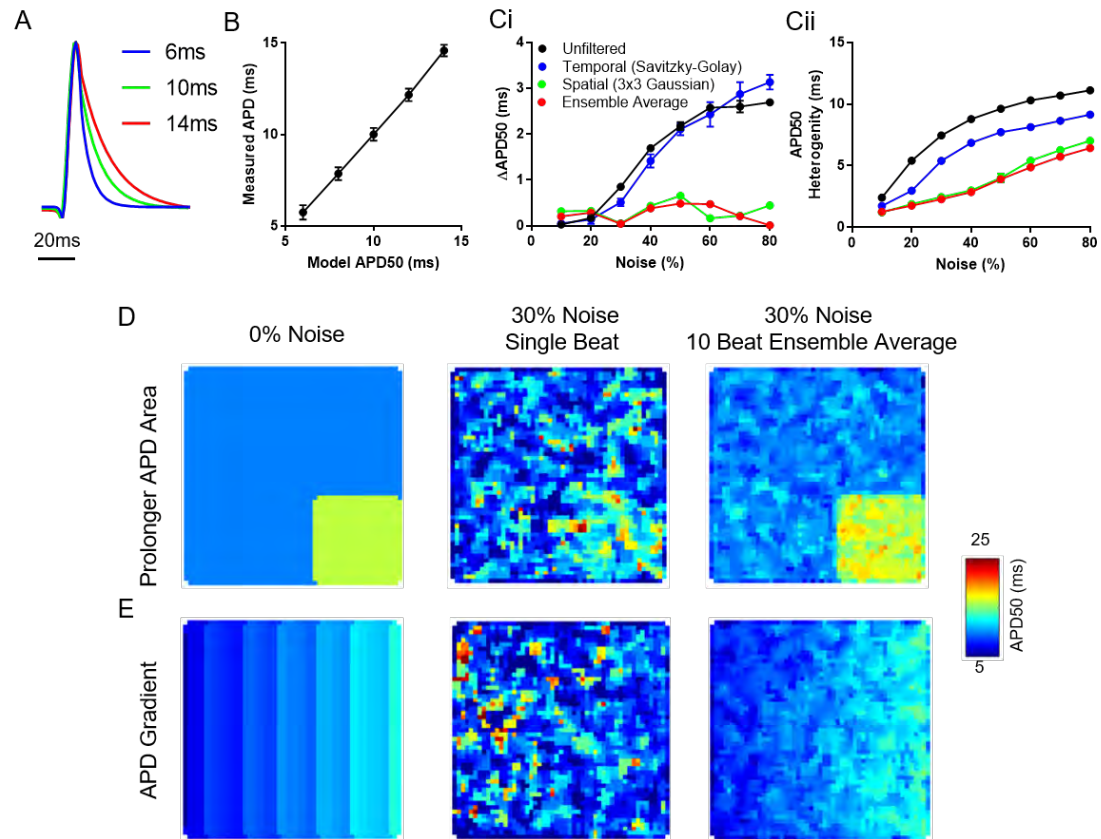


Figure 3.2: Action potential duration (APD) measurement validation and ensemble averaging model testing A) Model action potentials with varying duration. B) ElectroMap measured APD50 from model data with set APD50 spanning 6 to 14ms. C) Absolute change in APD50 measurement compared to 0% noise (i) and APD50 heterogeneity (ii) at increase noise levels for unfiltered (Black), temporally filtered (Savitzky-Golay, Blue), Spatially filtered (3x3 Gaussian, Green) and 10 beat ensemble averaged (Red) data, $n=5$ at all noise levels. D) Model dataset with area of prolonged APD measured at 0% noise, 30% noise from a single beat and 30% noise with 10 beat ensemble average. E) Similar to D), but with a model dataset exhibiting an APD gradient across the tissue.

To further test the utility of ensemble averaging in real optical mapping datasets, mouse left atria ($n=13$) were paced at 3Hz and 10Hz pacing frequency. An increase in pacing frequency is expected to shorten action potential due to cardiac restitution dynamics [4], [5]. As with the model data, ensemble averaging of 10 beats is observed to improve signal quality, here quantified as signal to noise ratio (SNR), Figure 3.3A-C. Noise was defined as the standard deviation of the baseline signal and compared to the amplitude. The increase in SNR

correlates to a reduction in measurement heterogeneity across the tissue, and simultaneously a reduction in the number of pixels in which analysis of APD was not possible (Figure 3.3D). Furthermore, when analysing a single beat, there is no difference between measured APD50 values at the respective pacing frequencies Figure 3.3E. In contrast, when ensemble averaging is applied, an expected decrease in APD50 at 10Hz pacing is observed, Figure 3.3E.

These results suggest ensemble averaging is an effective denoising technique in this experimental setup. It is important to note however that multi-beat averaging relies on the assumption that action potential (AP) morphology is consistent across several cardiac cycles. There are however a number of physiological and pathophysiological conditions in which action potentials morphology is known to alter between beats, for example alternans [6] and other forms of beat-to-beat heterogeneity [7]. In these situations, ensemble averaging may mask important and potentially pro-arrhythmic periods of temporal heterogeneity. It was observed in model studies that spatial filtering is as efficacious for denoising as ensemble averaging. It therefore may be more appropriate for certain studies, although it also has limitations with respect to possibly masking of local spatial heterogeneity [8].

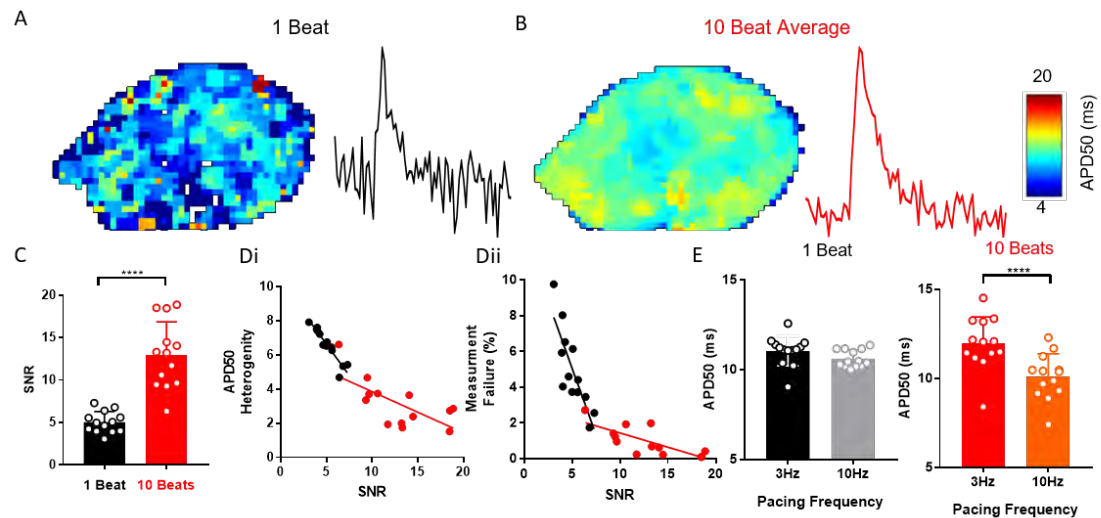


Figure 3.3: Ensemble averaging to resolve action potential duration (APD) changes. A) APD50 map and example single pixel signal from single beat optical action potentials. B) APD50 map and example single pixel signal from optical action potentials generated by ensemble averaging of 10 successive beats (peak method). C) SNR of single beat compared to 10 beat averaged signals. D) APD50 heterogeneity (i) and number of measurement failures (ii) as a function of SNR for single beat and 10 beat averaged APD50 maps. E) APD50 at 3 and 10 Hz pacing frequency, as measured from single beat and 10 beat maps. **** $P < 0.0001$

3.4 Comparison of local conduction velocity vector quantification methods

There are multiple methodologies to compute cardiac CV from optical mapping derived activation maps. The multi-vector method, where conduction is quantified and averaged across an activation map, is widely used as it analyses conduction across whole tissues, rather than along single paths as occurs with single vector methods [9]. This makes multi-vector methods less susceptible to user bias than single vector methods and allows analysis of conduction heterogeneity. There however can persist systematic errors in CV quantification [10].

To perform multi-vector conduction analysis, local CV vectors (CV_{local}), need to be quantified across activation maps. To achieve this, the activation maps are

segmented into local areas of $n \times n$ pixels, and conduction speed and direction quantified as CV_{local} .

A method to quantify CV_{local} is the polynomial surface method developed by Bayly et al, originally proposed for use in epicardial electrode mapping [3]. For each of the local regions, a polynomial surface, $T(x,y)$, is fitted using least squares fitting that describes the relationship between activation time, t , and spatial position (x,y) , where $T(x,y)$ is of the form,

$$T(x,y) = ax^2 + by^2 + cxy + dx + ey + f. \quad (3.1)$$

The local conduction velocity can then be calculated as

$$CV_{local} = \frac{T_x}{T_x^2 + T_y^2} \mathbf{i} + \frac{T_y}{T_x^2 + T_y^2} \mathbf{j} \quad (3.2)$$

where $T_x = \partial x / \partial T$ and $T_y = \partial y / \partial T$ are the 'conduction gradients' in the x and y direction respectively, and \mathbf{i} and \mathbf{j} are unit vector directions. This procedure therefore computes both a magnitude and direction of conduction in each local region.

However, the need to fit polynomial surfaces across whole tissue activation maps can make this a computationally intensive procedure. Additionally, several factors may influence results, including the method for surface approximation. In contrast, the finite difference method represents a simpler technique to approximate local conduction [11], [12]. Here, the activation time difference between the pixel of

interest ($t(x,y)$), and the difference between that and its nearest neighbour pixels ($t(x\pm 1,y)$ and $t(x,y\pm 1)$) can be used to measure the conduction gradients as

$$T_x = \frac{t(x+1,y) - t(x-1,y)}{2d} \mathbf{i}, T_y = \frac{t(x,y+1) - t(x,y-1)}{2d} \mathbf{j} \quad (3.3)$$

where d is the interpixel distance, \mathbf{i} is the unit vector in x direction and \mathbf{j} is the unit vector in y direction. The local conduction can then be quantified as in equation 3.2. Additionally, the underlying formulae underpinning the finite difference method (equation 3.2 and 3.3) can be extended to calculate local conduction gradients from more pixel sites than simply nearest neighbours considered here, resulting in similar versatility in 'local' area size as possible with the polynomial method. This was achieved by modification of equation 3.3 for n^{th} nearest neighbours in the \mathbf{i} and \mathbf{j} direction, equation 3.4.

$$T_x = \frac{1}{n} \sum_1^n \frac{t(x+n,y) - t(x-n,y)}{2nd} \mathbf{i}, T_y = \frac{1}{n} \sum_1^n \frac{t(x,y+n) - t(x,y-n)}{2nd} \mathbf{j} \quad (3.4)$$

The two methods for calculating CV_{local} were then compared using model datasets to test their accuracy in ideal, no noise, cases and robustness to increasing levels of noise. Polynomial and finite difference methodologies were additionally utilised to analyse experimental datasets of voltage dye optically mapped mouse left atria subjected to hypoxic conditions, expected to slow conduction [13]. Magnitude and directionality of conduction, alongside computation time, were compared. Model datasets underwent no pre-processing, while mouse atrial datasets were pre-processed as previously described (3x3 gaussian spatial filter, ensemble averaging of final 20 beats).

3.4.1 Finite difference and polynomial surface comparison in model datasets

To first confirm the efficacy of the two methods, model datasets of isotropic conduction spanning CVs of 10 to 100cm/s were produced (see Appendix A.1.3). Note: As these comparisons focused on local velocity measurement, analysis was restricted to isotropic conduction for simplicity as macroscopic variations (such as anisotropy) are less likely to influence calculations from small activation regions. Both methods were applied with window sizes of 3x3, 5x5 and 7x7 pixels. Figure 3.4A demonstrates that in the ideal no noise case, both methods can accurately quantify conduction, with a linear relationship between model and measured CV. However, the finite difference method does report more heterogeneity in CV measurements compared to the polynomial method, Figure 3.4B. In these models, conduction is homogenous across the tissue, suggesting that the finite difference methodology is more susceptible to errors induced due to imprecise activation times which arise from finite sampling rates and pixel sizes in optical mapped datasets.

To investigate the effects of noise, CV was set at 50cm/s and increasing levels of Gaussian noise, with standard deviation of up to 75% of the signal amplitude, was added to the datasets. Due to the pseudorandom nature of the noise addition, this procedure was repeated five times at each CV ($n=5$). As expected, both methods become less accurate as noise is increased to very large levels ($>40\%$), Figure 3.5. Noise levels in experimental datasets were also quantified by comparing the maximum of the signal amplitude to the standard deviation of the baseline

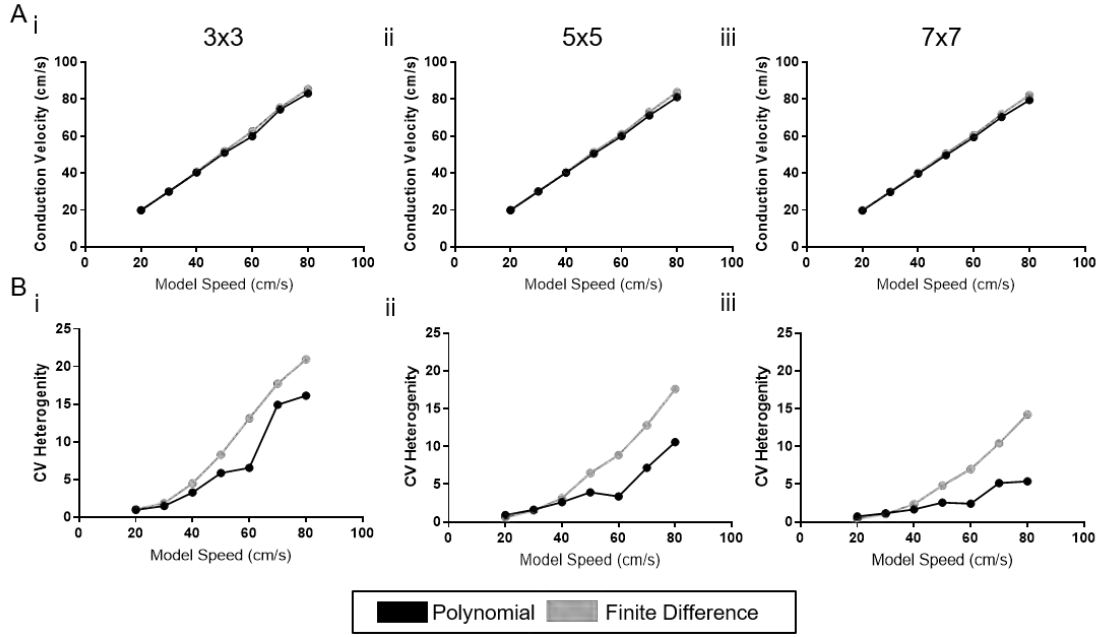


Figure 3.4: Polynomial and finite difference conduction velocity (CV) measurement in ideal, no noise, datasets A) Measured CV as a function of model conduction velocity using the polynomial (black) and finite difference (grey) methods for calculating local CV at window size of i)3x3, ii)5x5 and iii)7x7 pixels. B) Measured CV heterogeneity as a function of model conduction velocity using the polynomial (black) and finite difference (grey) methods for calculating local CV at window size of i)3x3, ii)5x5 and iii)7x7 pixels

(i.e. in an analogous manner to how noise was simulated in the model datasets).

Experimental noise levels ranged from 9 to 19%, as shown in the blue shaded areas in Figure 3.5. At these noise levels, the polynomial method is more accurate than the finite difference method across the window sizes tested.

3.4.2 Finite difference and polynomial surface comparison in experimental datasets

To compare the two methods for measuring local vectors, conduction was quantified from Di-4-ANEPPS loaded mouse left atria (n=14). These experiments were performed using the methods described in section 2 by Simon

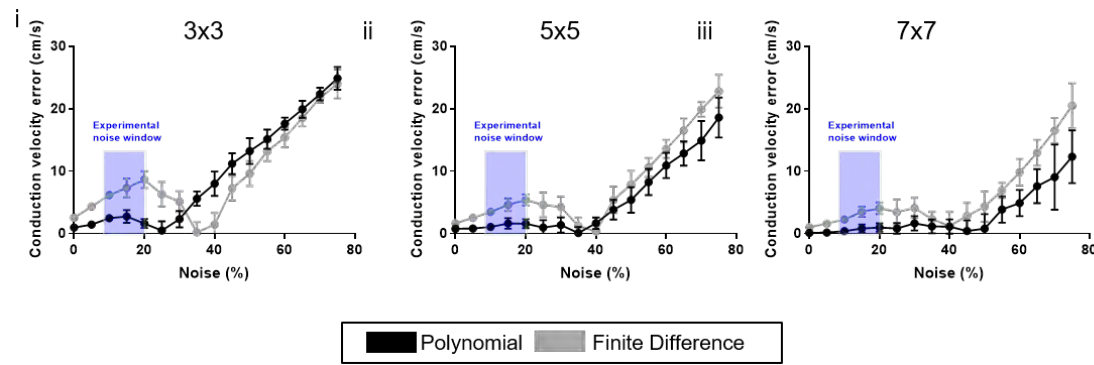


Figure 3.5: Polynomial and finite difference conduction velocity measurement accuracy as a function of signal noise A) Measured CV as a function of signal noise in model of isotropic conduction with conduction velocity 50cm/s using the polynomial (black) and finite difference (grey) methods for calculating local CV at window size of i)3x3, ii)5x5 and iii)7x7 pixels.

Wells, and not by the author of this thesis. Activation maps were generated for each atrium by measuring the time of depolarisation midpoint at 10Hz pacing under normoxic (95%O₂/5%CO₂) and hypoxic (95%N₂/5%CO₂) conditions. CV was then quantified from ‘local’ regions of 3x3 pixels of allow direct comparison between the polynomial and finite difference methods. Mean measurements showed a small difference in measured CV (Figure 3.6A Polynomial = 51.8 ± 2.8 cm/s, finite difference = 54.25 ± 2.8 cm/s, $P=0.027$) between the two methods. Additionally, the finite difference method resulted in greater CV heterogeneity, measured as standard deviation from the mean in each atria (Figure 3.6B, polynomial = 21.3 ± 1.6 cm/s, finite difference = 32.9 ± 2.4 cm/s, $P<0.0001$).

One of the benefits of the multi-vector methods is the automatic directional information that can be simultaneously quantified alongside CV from the angular direction of the local vectors. Here, it is observed there is no difference between the methods in terms of mean direction of conduction (Figure 3.6C) or angular heterogeneity (Figure 3.6D). The finite difference method is less computationally

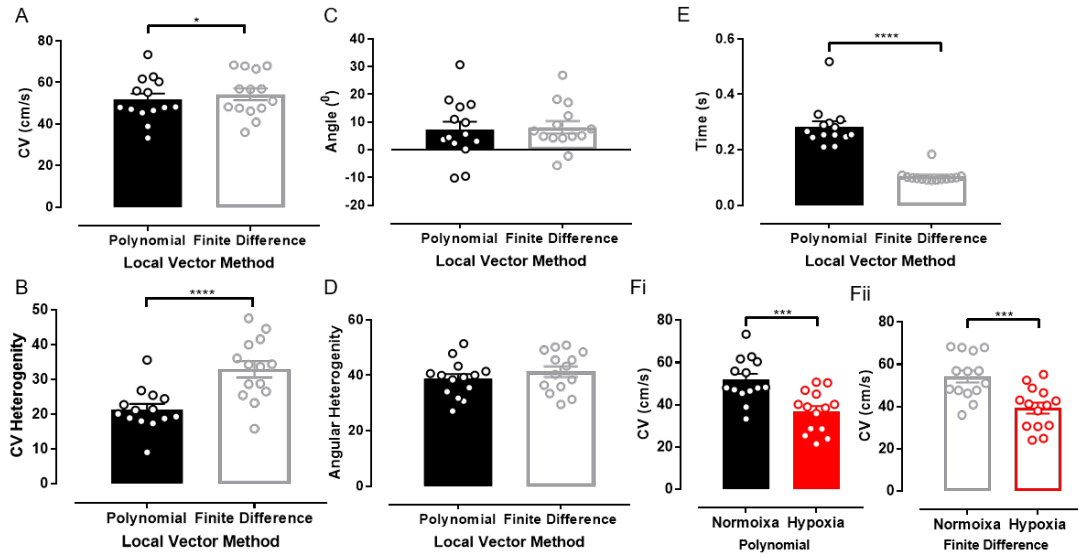


Figure 3.6: Comparison of polynomial and finite difference multi-vector conduction velocity (CV) quantification methods A) Mouse left atrial mean CV as measured using polynomial and finite difference method. B) CV heterogeneity (measured as standard deviation of the mean) as quantified by the two methods. C) Mean propagation direction as quantified using polynomial and finite difference method. D) Angular heterogeneity (measured as standard deviation of the mean) as quantified by the two methods. E) Computation time to quantify CV by the two methods. F) Mean CV under normoxic and hypoxic conditions at 3Hz pacing as quantified by the polynomial (i) and finite difference methods (ii). $n=14$, * $p<0.05$, *** $p<0.01$, **** $p<0.0001$.

intensive than the polynomial method, calculating the same number of local vectors across the activation maps in $31.6 \pm 1.8\%$ of time taken using the polynomial method (Figure 3.6E) and importantly, both methods successfully measured CV slowing induced by hypoxia (Figure 3.6F).

3.4.3 Discussion and conclusion on local conduction velocity vector quantification methods

As shown in Figure 3.5A, the polynomial method is more accurate in quantifying conduction from activation maps generated from signals with similar noise levels as observed in experimental recordings. Hence, it is used as the default

conduction analysis method in the ElectroMap software and for CV quantification in this thesis. Despite this, and the discrepancies in mean CV and increased heterogeneity, the simpler implementation of the finite difference method makes it an attractive alternative to the polynomial method. Automatically calculated conduction directionality (Figure 3.6C-D) remains consistent between the two methods and changes in CV are successfully resolved (Figure 3.6F). Crucially, this is achieved at much shorter timescales (Figure 3.6E) than when using the polynomial method, showing the finite difference method could be applicable to studies such as single beat investigation of conduction over long experimental timescales.

3.5 Testing of baseline correction methods

Polynomial approaches have been suggested as methods to reduce non-physiological changes in fluorescent signal baselines from optical signals [14]. However, previous studies have suggested that linear top hat filtering may be a more robust method for baseline correction [15]. Here, a structuring element of given length is utilised so that changes with a time period less than the kernel length are removed [15].

To test the efficacy of top-hat baseline correction compared to polynomial methods, 17 signals from voltage optical mapping datasets of mouse left atria were baseline corrected by both methods (including 4th and 11th degree polynomials). Top hat filter length was 100ms. Successful baseline correction was quantified as root mean square error (RMSE) compared to an 'ideal' flat

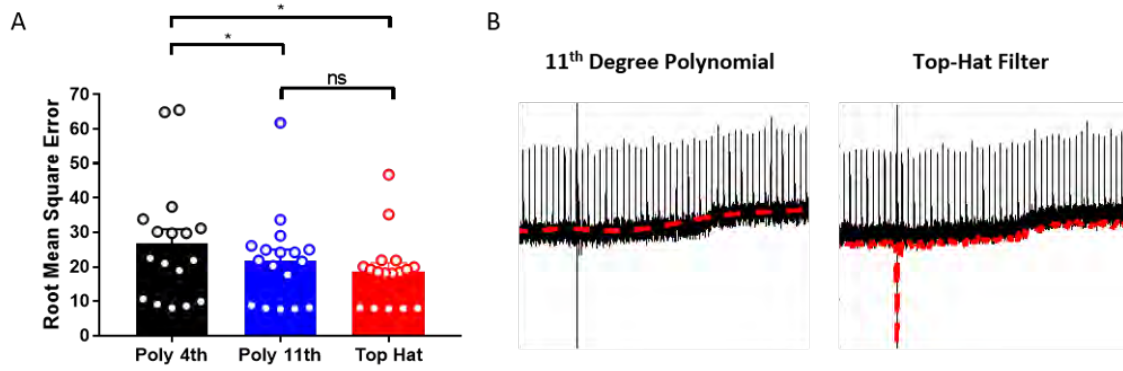


Figure 3.7: Baseline correction testing. A) Root mean square error of optical voltage signal baselines ($n=17$) against an ideal flat baseline after 4th degree and 11th degree polynomial and top-hat filtering baseline correction. B) Example of baseline detection (red) using 11th degree polynomial and top-hat filtering in an optical voltage signal with a varying baseline (long timescale) and a short timescale artefact.

baseline during diastolic periods, with lower RMSE representing better baseline correction. This demonstrated that top-hat filtering outperformed 4th degree polynomial filters ($P=0.0472$, Figure 3.7A) and, although not significantly outperforming the 11th degree polynomial method on RMSE measure ($P=0.1688$, Figure 3.7A), was more adept in detecting sharp events such as bubble artefacts (Figure 3.7B).

To further test efficacy of top-hat method, baseline decay was introduced to simulated data with a sinusoidally changing function with period of 1000 frames (1013ms) and compared to a similar dataset on a flat baseline. 10% noise was also added to both datasets, to match noise levels observed in experimental data. Application of a top-hat filter with a length of 100 frames (101.3ms) accurately identified and corrected for the baseline shift (Figure 3.8A), resulting in similar activation patterns and action potential morphologies values (Figure 3.8B-C).

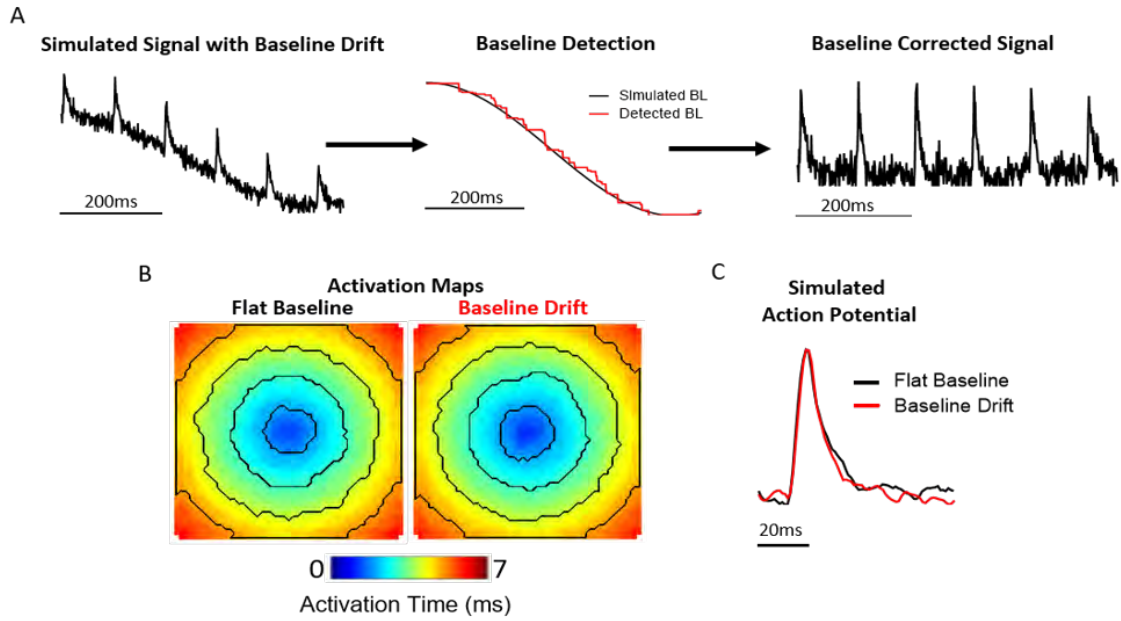


Figure 3.8: Baseline correction of simulated data. A) Example trace from dataset where baseline drift has been artificially added. The baseline has then been detected and then corrected for using top-hat correction method within ElectroMap. B) Activation maps generated from simulated data with flat baseline (black) and baseline corrected data (red) as shown in A. C) Example simulated action potentials from the two datasets, post baseline removal.

3.6 Chapter summary

In this chapter, the development, application and use of an MATLAB based software, ElectroMap, for analysis of optical mapping data has been presented. Key developments within the software included automated pacing cycle length detection and standalone modules for analysis of pro arrhythmic phenomena including conduction changes and alternans. Algorithms were tested *in silico* datasets, mouse and guinea pig optical mapping datasets.

This software package has been used for all analysis of optical mapping data presented in this thesis, unless stated otherwise.

3.7 Chapter 3 References

- [1] I. Uzelac and F. H. Fenton, "Robust framework for quantitative analysis of optical mapping signals without filtering," *Computing in Cardiology*, vol. 42, pp. 461–464, 2015.
- [2] C. O'Shea et al., "High-Throughput Analysis of Optical Mapping Data Using ElectroMap," *Journal of Visualized Experiments*, no. 148, pp. 1–10, 2019.
- [3] P. V Bayly et al., "Estimation of Conduction Velocity Vector Fields from Epicardial Mapping Data," vol. 45, no. 5, pp. 563–571, 1998.
- [4] F. M. Weber et al., "Conduction velocity restitution of the human atrium—An efficient measurement protocol for clinical electrophysiological studies," *IEEE Transactions on Biomedical Engineering*, vol. 58, no. 9, pp. 2648–2655, 2011.
- [5] B. C. Knollmann, T. Schober, A. O. Petersen, S. G. Sirenko, and M. R. Franz, "Action potential characterization in intact mouse heart: Steady-state cycle length dependence and electrical restitution," *American Journal of Physiology - Heart and Circulatory Physiology*, vol. 292, no. 1, pp. 614–621, 2007.
- [6] J. Winter, M. Bishop, C. Wilder, C. O'Shea, D. Pavlovic, and M. J. Shattock, "Sympathetic nervous regulation of cardiac alternans in the intact heart," *Frontiers in Physiology*, vol. 9, no. January, pp. 1–12, 2018.
- [7] D. M. Johnson et al., "IKs restricts excessive beat-to-beat variability of repolarization during beta-adrenergic receptor stimulation," *Journal of Molecular and Cellular Cardiology*, vol. 48, no. 1, pp. 122–130, 2010.
- [8] J. I. Laughner, F. S. F. S. Ng, M. S. Sulkin, R. M. Arthur, and I. R. Efimov, "Processing and analysis of cardiac optical mapping data obtained with potentiometric dyes," *AJP: Heart and Circulatory Physiology*, vol. 303, no. 7, pp. H753–65, 2012.
- [9] A. N. Doshi et al., "Feasibility of a semi-automated method for cardiac conduction velocity analysis of high-resolution activation maps," *Computers in Biology and Medicine*, vol. 65, pp. 177–183, 2015.
- [10] A. C. Linnenbank, J. M. T. de Bakker, and R. Coronel, "How to measure propagation velocity in cardiac tissue: A simulation study," *Frontiers in Physiology*, vol. 5 JUL, no. July, pp. 1–7, 2014.
- [11] I. R. Efimov, D. T. Huang, J. M. Rendt, and G. Salama, "Optical mapping of repolarization and refractoriness from intact hearts," *Circulation*, vol. 90, no. 3, pp. 1469–1480, 1994.
- [12] C. D. Cantwell, C. H. Roney, F. S. Ng, J. H. Siggers, S. J. Sherwin, and N. S. Peters, "Techniques for automated local activation time annotation and conduction velocity estimation in cardiac mapping," *Computers in Biology and*

Medicine, vol. 65, 2015.

[13] N. Zeevi-Levin et al., "Gap junctional remodeling by hypoxia in cultured neonatal rat ventricular myocytes," *Cardiovascular Research*, vol. 66, no. 1, pp. 64–73, 2005.

[14] Laughner JI, Ng FS, Sulkin MS, Arthur RM, Efimov IR. Processing and analysis of cardiac optical mapping data obtained with potentiometric dyes. *AJP: Heart and Circulatory Physiology*. 2012;303(7):H753–65.

[15] Yu TY, Syeda F, Holmes AP, Osborne B, Dehghani H, Brain KL, et al. An automated system using spatial oversampling for optical mapping in murine atria. Development and validation with monophasic and transmembrane action potentials. *Progress in Biophysics and Molecular Biology*. 2014;115(2–3):340–8.

Chapter 4

Optical mapping of optogenetic models

This chapter describes work undertaken on combination of optical mapping of cardiac samples with optogenetic manipulation. Optogenetics refers to the use of genetically encoded photosensitive ion channels or pumps to allow optical control of tissue excitability, including initiation, suppression and modulation of electrical activity of cardiac tissue. Likewise, fluorescent indicators can also be genetically encoded. Combination of optogenetic techniques with optical mapping gives rise to 'all-optical' electrophysiology, allowing precise optogenetic actuation of cardiac tissue with high spatio-temporal resolution imaging of action potential and calcium transient morphology and conduction patterns. This makes all-optical experiments a unique and powerful research platform.

The presented work consists of two published articles. The first (section 4.1) is a technical review of combined optogenetic and optical mapping systems. With the necessity of multiple light paths in all-optical setups, the combination of optical mapping and optogenetics is not straightforward. Therefore, a thorough review of current techniques to achieve such a setup was undertaken.

The second article (section 4.2) presents optical mapping analysis of mouse

sinoatrial nodal preparations which cell specifically express channelrhodopsin2, a light sensitive cation channel. These preparations are shown to be robustly paced by blue light. Using optical mapping of voltage and calcium sensitive dyes, we were able to thoroughly analyse the electrical behaviour of these preparations both in intrinsic and optical pacing conditions, including activation dynamics and calcium transient morphology.

Analysis was conducted using the ElectroMap software (Chapter 3) making use of several of the features in the software. Conduction module was utilised to thoroughly probe the effects of optical pacing on the activation dynamics within the sinoatrial nodal preparations, including identification of earliest activation time, tissue activation curve analysis, conduction velocity quantification, and directionality analysis. Waveform morphology was applied to study calcium transient rise times and duration, while frame removal options were employed to remove optical pacing artefacts. Hence, development of the software made previously difficult to apply analyses routinely employable.

4.1 Cardiac Optogenetics and Optical Mapping – Overcoming Spectral Congestion in All-Optical Cardiac Electrophysiology

Publication 2.

This review article was originally published in Frontiers in Physiology.

Cardiac Optogenetics and Optical Mapping – Overcoming Spectral Congestion in All-Optical Cardiac Electrophysiology (Review). **C O'Shea**, A P Holmes, J Winter, J Correia, X Ou, R Dong, S C He, P Kirchhof, L Fabritz, K Rajpoot, D Pavlovic. *Front. Physiol. 10:182, 1-14, 2019*

Author contributions in publication 2

I conducted the literature review, wrote the manuscript and produced the figures. The primary manuscript was then reviewed and edited by all authors.



Cardiac Optogenetics and Optical Mapping – Overcoming Spectral Congestion in All-Optical Cardiac Electrophysiology

OPEN ACCESS

Edited by:

Christopher Huang,
University of Cambridge,
United Kingdom

Reviewed by:

Gil Bub,
McGill University, Canada
Arkady M. Pertsov,
Upstate Medical University,
United States
Crystal M. Ripplinger,
University of California, Davis,
United States

*Correspondence:

Kashif Rajpoot
k.m.rajpoot@bham.ac.uk
Davor Pavlovic
d.pavlovic@bham.ac.uk

[†]These authors share senior
authorship

Specialty section:

This article was submitted to
Cardiac Electrophysiology,
a section of the journal
Frontiers in Physiology

Received: 14 October 2018

Accepted: 14 February 2019

Published: 07 March 2019

Citation:

O'Shea C, Holmes AP, Winter J,
Correia J, Ou X, Dong R, He S,
Kirchhof P, Fabritz L, Rajpoot K and
Pavlovic D (2019) Cardiac
Optogenetics and Optical Mapping –
Overcoming Spectral Congestion
in All-Optical Cardiac
Electrophysiology.
Front. Physiol. 10:182.
doi: 10.3389/fphys.2019.00182

Christopher O'Shea^{1,2,3}, Andrew P. Holmes^{1,4}, James Winter¹, Joao Correia⁵,
Xianhong Ou⁶, Ruirui Dong⁶, Shicheng He⁶, Paulus Kirchhof^{1,7}, Larissa Fabritz^{1,7},
Kashif Rajpoot^{2*†} and Davor Pavlovic^{1*†}

¹ Institute of Cardiovascular Sciences, University of Birmingham, Birmingham, United Kingdom, ² School of Computer Science, University of Birmingham, Birmingham, United Kingdom, ³ EPSRC Centre for Doctoral Training in Physical Sciences for Health, School of Chemistry, University of Birmingham, Birmingham, United Kingdom, ⁴ Institute of Clinical Sciences, University of Birmingham, Birmingham, United Kingdom, ⁵ Institute of Microbiology and Infection, School of Biosciences, University of Birmingham, Birmingham, United Kingdom, ⁶ Key Laboratory of Medical Electrophysiology of Ministry of Education, Collaborative Innovation Center for Prevention and Treatment of Cardiovascular Disease/Institute of Cardiovascular Research, Southwest Medical University, Luzhou, China, ⁷ Department of Cardiology, UHB NHS Trust, Birmingham, United Kingdom

Optogenetic control of the heart is an emergent technology that offers unparalleled spatio-temporal control of cardiac dynamics via light-sensitive ion pumps and channels (opsins). This fast-evolving technique holds broad scope in both clinical and basic research setting. Combination of optogenetics with optical mapping of voltage or calcium fluorescent probes facilitates 'all-optical' electrophysiology, allowing precise optogenetic actuation of cardiac tissue with high spatio-temporal resolution imaging of action potential and calcium transient morphology and conduction patterns. In this review, we provide a synopsis of optogenetics and discuss in detail its use and compatibility with optical interrogation of cardiac electrophysiology. We briefly discuss the benefits of all-optical cardiac control and electrophysiological interrogation compared to traditional techniques, and describe mechanisms, unique features and limitations of optically induced cardiac control. In particular, we focus on state-of-the-art setup design, challenges in light delivery and filtering, and compatibility of opsins with fluorescent reporters used in optical mapping. The interaction of cardiac tissue with light, and physical and computational approaches to overcome the 'spectral congestion' that arises from the combination of optogenetics and optical mapping are discussed. Finally, we summarize recent preclinical work applications of combined cardiac optogenetics and optical mapping approach.

Keywords: optogenetic, optical mapping, fluorescence, cardiac, action potential, calcium, conduction (action potential), arrhythmias

INTRODUCTION

Over the past 30 years high resolution camera technologies and development of several potentiometric and intracellular calcium sensors has led to optical mapping becoming a valuable tool in cardiac research (Salama et al., 1987; Boukens and Efimov, 2014). Electrical conduction, action potential and calcium transient morphology can be directly measured, quantified, and tracked across multicellular cardiac preparations in high spatio-temporal resolution, unparalleled by traditional electrode techniques (Herron et al., 2012; Yu et al., 2014). Optical mapping has hence played a pivotal role in cardiac research, providing several insights into physiology and pathophysiology of the heart (Jalife, 2003; Myles et al., 2012; Syeda et al., 2016; Winter et al., 2018).

Conversely, optogenetics shifts light to an actuator role to control and tune EP behavior through genetically introducing photosensitive ion channels and pumps (opsins), able to depolarize and hyperpolarize excitable cells. This emergent technology, with its foundations in neuroscience, is now increasingly exploited by heart researchers. Optogenetic pacing of cardiac preparations has now been reported in several experimental models (Park et al., 2014; Vogt et al., 2015; Zhu et al., 2016; Nyns et al., 2017). Beyond rhythm control, optogenetics has been used to terminate arrhythmias in both *ex vivo* and *in vivo* rodent hearts (Bruegmann et al., 2016, 2018; Nyns et al., 2017), suppress and manipulate rotors in cardiomyocyte monolayers (Feola et al., 2017; Watanabe et al., 2017) and elucidate the function of both cardiomyocyte (Wang et al., 2017) and non-cardiomyocyte (Hulsmans et al., 2017) cellular subpopulations in the heart. Hence, optogenetics presents a pivotal emergent technology for basic research, while some of its unique features make it a potentially transformative clinical tool for both pacing and arrhythmia termination.

Combination of optogenetics with optical imaging of cellular monolayers and whole hearts allows 'all-optical' cardiac EP investigation (Figure 1); an approach that has seen growing application in cardiac research (Entcheva, 2013; Nussinovitch and Gepstein, 2015b; Entcheva and Bub, 2016). Owing to contactless operation and high spatio-temporal resolution, all-optical systems are uniquely capable of high throughput control and study of complex phenomena that can arise in excitable media. High spatio-temporal understanding of cardiac behavior in response to optical actuation, aside from providing an invaluable research tool, is also vital if optogenetics is to transition to clinical utility.

The requirement and employment of all-optical approach has been expansively presented in recent reviews (Entcheva and Bub, 2016; Crocini et al., 2017). In the present article, we discuss the basic tools of optogenetics (opsins), and optical mapping (voltage and calcium sensors). We focus on their dual use in all-optical setups, including their mechanisms of action, delivery to cardiac tissue, spectral compatibility and highlight technical considerations and advances that have made all-optical systems practical. Additionally, benefits of all-optical cardiac control and EP interrogation when compared to traditional contact techniques are discussed, and we highlight recent applications of combined cardiac optogenetics and optical mapping approaches.

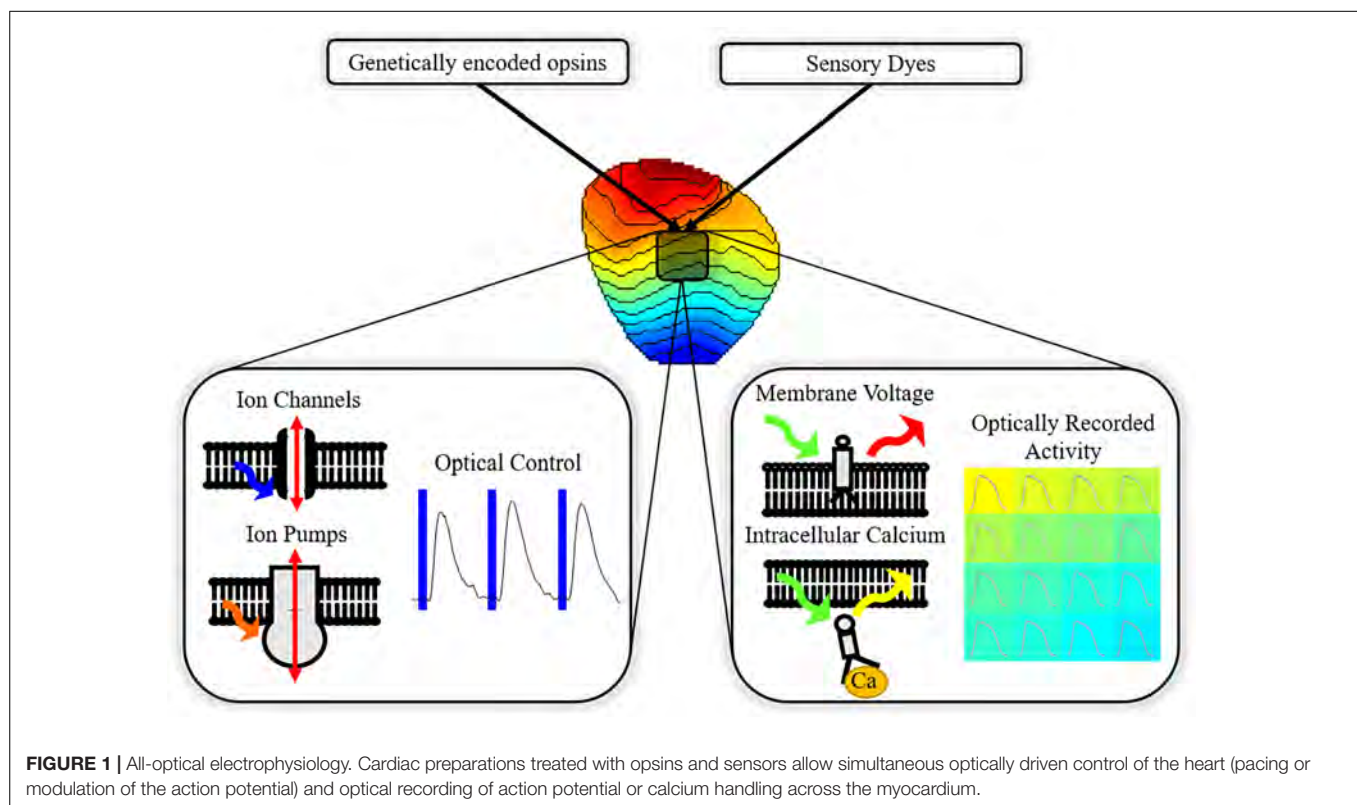
TOOLS OF OPTOGENETICS – OPSINS

The development of optogenetics as a valuable research tool stems from the discovery and cloning of microbial opsins that behave as light-gated ionic channels in the early to mid-2000s – Channelrhodopsins (Nagel et al., 2003, 2005; Boyden et al., 2005). In particular Channelrhodopsin2 (ChR2), and variants thereof, is by far the most utilized opsin in optogenetics. On excitation by blue light (~470 nm) of threshold irradiance, ChR2 opens as its covalently bound photosensitive chromophore, all-trans retinal, isomerizes (Nagel et al., 2003). The opening of the channel allows ions, including Na⁺, to cross the cellular membrane, as occurs in phase 0 of the action potential, initiating depolarization. Hence, cells expressing ChR2 can be effectively stimulated with blue light, initiating and/or prolonging the action potential (Figure 2A). As well as being light sensitive, ChR2 also acts in a voltage dependent manner, with decreasing conductance at more positive membrane potentials and a reversal potential near 0mV (Lin, 2010; Park et al., 2014).

Enhancement of the native properties of ChR2 is vital for the future use of optogenetics in cardiac tissue, due to relatively small currents generated by wild type ChR2 (steady state current ~0.25 nA) and large absorption and scattering of visible light by biological chromophores. This limits optical penetration depth, preventing transmural opsin activation from deep tissue. Deep activation would be advantageous for synchronous cardiac activation and has been demonstrated as an important factor in successful re-entry termination (Karathanos et al., 2016; Watanabe et al., 2017). One possible method to realize deep tissue activation is red-shifting of the excitation window toward the 'biological window' of 650–1350 nm, where the extinction coefficient of biological tissue is greatly reduced (Smith et al., 2009). Light in this wavelength range can penetrate a few centimeters into the cardiac tissue and thus more light can reach and activate deep tissue opsins. Furthermore, decreasing the threshold irradiance required for photocurrent activation and/or increasing channel conductance or opening times, can aid deep tissue activation and reduce energy requirements in optogenetic applications.

Hence, since its isolation and cloning, ChR2 has undergone several alterations including variants with enhanced conductance [ChR2-H134R (Nagel et al., 2005), ChR2-T159C (Berndt et al., 2011), ChR2-XXL (Dawydow et al., 2014)], Ca²⁺ permeability [CatCh (Kleinlogel et al., 2011)] and red shifted spectral properties [ReaChR (Lin et al., 2013)]. Additionally, channelrhodopsins separate from ChR2 have been cloned from distinct algae species and subsequently optimized [CheRiff (Hochbaum et al., 2014)], while chimeras of ChR1 and ChR2 have also demonstrated enhanced photocurrents [ChIEF (Lin et al., 2009)]. These developments have led to a plethora of available depolarizing opsins with diverse spectral and kinetic properties (Schneider et al., 2015). Equally, it has been shown how exogenously supplemented all-trans retinal can significantly increase light sensitivity of ChR2, although concentration dependent cytotoxic effects were also observed (Yu et al., 2015).

An important factor in enhancing the photocurrent of native Channelrhodopsins is the effects mutagenesis can have on the

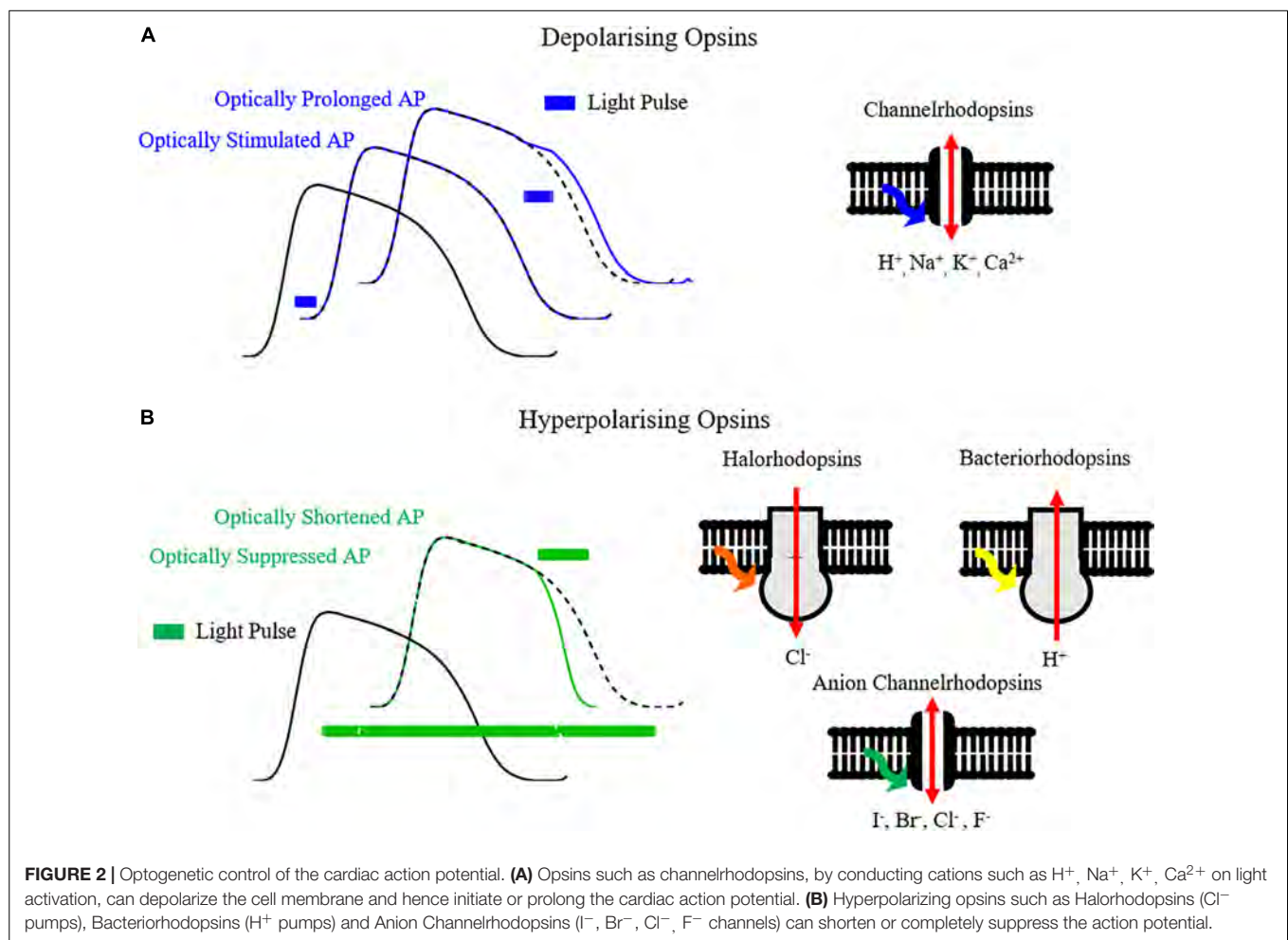


photocycle kinetics. By prolonging channel opening times after the cessation of light activation, light sensitivity can be improved by a short pulse leading to a long-lasting photocurrent, e.g., ChR2-D156A which exhibits a dark off time of > 150 s (Bamann et al., 2010). However, significant slowing of the channel kinetics is detrimental to dynamic initiation and control of membrane perturbation. Therefore, the channelrhodopsins that have found most use in all optical setups (ChR2-H134R, CatCh, ReaChR, and ChRiff) are those whose enhanced photocurrents have been achieved with only moderate prolongation compared to wild type ChR2, which exhibits on and off time constants of ~ 0.2 and ~ 10 ms respectively (Nagel et al., 2003).

Aside from depolarizing Channelrhodopsins, hyperpolarizing opsin pumps include halorhodopsin Cl^- pumps (e.g., eNpHR3.0) and bacteriorhodopsin proton pumps (e.g., Arch and ArchT) (Kandori, 2015). Hyperpolarizing opsins allow selective suppression and shortening of action potentials (Figure 2B), and have been utilized for applications such as suppressing *in vivo* cardiac motion for high resolution imaging in zebrafish (Mickleit et al., 2014). Thanks to distinct absorption characteristics in comparison with ChR2, a cardiac preparation expressing both depolarizing and hyperpolarizing opsins can be selectively stimulated and silenced simply by tuning illumination wavelength, thereby allowing comprehensive control of the action potential. While opsins can be expressed independently, gene-fusion enables formation of protein complexes such as ChR2-ArchT, allowing co-localization and bi-directional control of membrane voltage with one protein complex (Nussinovitch et al., 2014; Streit and Kleinlogel, 2018).

Hyperpolarizing pumps suffer from restricted photocurrent as one ion is transported per absorbed photon (Berndt et al., 2011). Anion channelrhodopsins (ACRs), with the potential for enhanced conductance driven instead by electrochemical gradients, were first realized by mutation of channelrhodopsins to infer Cl^- conductance, although with some remaining cationic conductance and slowing of the channel kinetics (Berndt et al., 2014; Wietek et al., 2014). Subsequently, naturally occurring ACRs with reduced cationic conductance have been discovered and cloned (Govorunova et al., 2015). Preliminary studies indicate that reduced light intensities are required to optically induce hyper- and repolarizing currents in cardiomyocytes using these novel ACRs, compared to pumps (Govorunova et al., 2016). Greater structural and functional understanding of both natural (Kim et al., 2018) and designed (Kato et al., 2018) ACRs promises further optimization of inhibitory channels.

Prolonged use and activation of inhibitory pumps or channels based on conductance of H^+ or Cl^- can detrimentally alter intracellular ionic concentrations (Alfonso et al., 2015; Bernal Sierra et al., 2018). One promising avenue to potentially circumvent this limitation is the development of tools which more closely mimic the resting and repolarization mechanisms of excitable cells via light activated K^+ conductance. Several approaches have now been tested, including recently published PAC-K constructs which combine a cAMP-gated K^+ channel with photo-activated nucleotidyl cyclase, allowing optical silencing of cardiomyocyte (and neuron) activity (Bernal Sierra et al., 2018). These constructs, however, do not currently allow for fast responsive control of membrane potential, eliciting



hyperpolarization lasting minimally for 100 ms, preventing dynamic control during the action potential.

Delivery of Opsins in Cardiac Tissue

Optogenetic control requires reliable, rapidly responsive, and reversible generation of depolarizing and hyperpolarizing currents by the expression of the light gated ionic transport proteins. The first barrier to achieving cardiac optogenetic perturbation therefore is effective delivery and expression of desired opsins in cardiac preparations. Pioneering cardiac optogenetic studies in 2010 transgenically expressed ChR2 in zebrafish (Arrenberg et al., 2010) and mouse (Bruegmann et al., 2010). ChR2 expressing mouse lines remain prevalent (Quiñonez Uribe et al., 2018) and interventions such as Cre recombinase allow powerful research strategies (Wang et al., 2017).

However, requirement for transgenic expression of opsins is costly, time-consuming and limits clinical application of optogenetics (Knollmann, 2010). Therefore, other techniques have been explored exploiting tandem-cell-unit (Jia et al., 2011) and viral (Abilez et al., 2011; Vogt et al., 2015) delivery of ChR2 and other opsins. Tandem-cell-unit delivery centers on the concept where previously non-excitable cells, transfected to express ChR2, are grafted into cardiomyocyte preparations.

The cells couple to the cardiomyocytes via gap junctional proteins and act as 'sparks,' initiating depolarization of coupled cardiomyocytes on light stimulation (Jia et al., 2011).

In viral delivery, opsin genes are encoded in lentiviruses, adenoviruses, or adeno-associated viruses (AAV). Viral methods allow for tissue or cell selectivity, depending on the promoter used, and can be directly injected to realize light excitability. Importantly for future clinical utility of optogenetics, there is increasing evidence that AAVs can be safely and efficaciously used in the heart (Bera and Sen, 2017) and systemic viral delivery can be used to promote cardiac specific ChR2 expression *in vivo* (Ambrosi et al., 2019). In wild type mice for example, AAV injection has shown to result in stable and long lasting ventricular (Vogt et al., 2015; Bruegmann et al., 2016) and atrial (Bruegmann et al., 2018) expression of ChR2. However, transfection rates and consequently optical sensitivity remain variable between treated hearts, and there is some evidence of chamber discrepancies with atrial transfection rates lower than ventricular (Vogt et al., 2015; Bruegmann et al., 2016, 2018). Hence, extensive effort is ongoing to realize the most effective method to introduce optical excitability to cardiac tissue (Ambrosi et al., 2015).

Reports that high-level expression of lentiviral-delivered ChR2 in NRVMs is associated with cytotoxicity also need to be carefully

considered if translational potential of this technology is to be fully realized. The mechanisms underpinning cytotoxicity are unclear, with Ca^{2+} overload and membrane damage being implicated (Li et al., 2017). Further work on mechanistic insight into cytotoxicity is required to ensure safe use of ChR2 and other opsins in cardiac optogenetics.

OPTICAL VOLTAGE AND CALCIUM SENSORS

Synthetic Sensors

A range of sensors are utilized in optical mapping to image transmembrane voltage, as well fluctuations in cytosolic and sarcoplasmic reticulum Ca^{2+} concentrations (Broyles et al., 2018). Synthetic sensors are small molecules that are most commonly introduced to *ex vivo* hearts via Langendorff perfusion, or via superfusion to both *in vitro* and *ex vivo* preparations.

The most popular voltage sensors are 'fast' synthetic styryl sensors, such as di-4-ANEPPS and rh-237, which embed within the plasma membrane, **Figure 1**. As the transmembrane voltage changes, for example during the cardiac action potential, these sensors exhibit fast responding (femto- to picosecond) spectrally shifted fluorescent output due to shifts in charge state and hence dipole energy levels (electrochromism) (Loew et al., 1978; Miller, 2016). Longpass filtering the emitted fluorescence beyond the emission spectra maximum therefore allows recording of optical signals exhibiting fluorescence intensity proportional to cellular membrane voltage changes, i.e., optical action potentials (OAP) (Herron et al., 2012).

On the other hand, intracellular Ca^{2+} sensors such as rhod-2AM are designed to internalize within the cell, **Figure 1**. They are commonly esterified to neutralize the charge, aiding intracellular uptake. The ester is then enzymatically cleaved once in the cell, leaving behind a Ca^{2+} chelator and a fluorophore. As Ca^{2+} is chelated, fluorescence output increases, and subsequently decreases upon dissociation, reporting the changing $[\text{Ca}^{2+}]$ in the intracellular space where the sensor localizes, either in the cytosol or sarcoplasmic reticulum (Jaimes et al., 2016).

Genetically Encoded Sensors

Alternatively to small molecule synthetic sensors, voltage and calcium responsive protein sensors can be genetically encoded to achieve cell specific indicator expression (Liao et al., 2015; Quinn et al., 2016). These are collectively termed genetically encoded voltages/calcium indicators (GEVIs/GECIs), constructed by the fusion of voltage/ Ca^{2+} sensitive and fluorescent proteins (Scanziani and Häusser, 2009). Genetic indicators can be used to independently measure voltage or Ca^{2+} , but can also be fused to create dual voltage-calcium constructs such as CaViar (Hou et al., 2014) which combines QuasAr2 (GEVI) with GCaMP6f (GECI). Furthermore, co-expressed indicator and actuator pairs offer a unique ability to provide all-genetic, all-optical electrophysiological study (Chang et al., 2017). The "Optopatch" platform for example combines genetic indicators with CheRiff and has been utilized both in establishing all-optical

mouse lines and as a high throughput cardiotoxicity screening platform for all-optical pacing with simultaneous voltage and intracellular calcium measurement (Hochbaum et al., 2014; Dempsey et al., 2016; Björk et al., 2017).

Synthetic vs. Genetically Encoded Sensors

Genetic indicators rely on conformational changes to directly alter their fluorescence response or via eliciting processes such as Förster resonance energy transfer (FRET). Consequently, compared to the 'fast' small-molecule sensors, an important limiting factor of current genetically encoded indicators is their response times which are typically in the order of milliseconds (Kaestner et al., 2015). This can prove problematic when measuring the sub millisecond phenomena involved in cardiac depolarization, repolarization and calcium handling (Koopman et al., 2017). Indeed, OAPs recorded by genetic indicators exhibit a significantly altered morphology compared to simultaneously measured OAPs using syntenic sensors (Shinnawi et al., 2015). Coupled to this, the relatively straightforward application to *ex vivo* and *in vitro* preparations makes synthetic sensors more commonly utilized in optical mapping studies (Herron et al., 2012), and to date the pioneering all-optical setups (**Table 1**).

Synthetic sensors will non-specifically stain all the cell subpopulations in cardiac preparations. In contrast, genetic sensors can be successfully utilized *in vivo* and *in vitro* to cell specifically stain cardiomyocytes (or other cell types) (Hou et al., 2014; Dempsey et al., 2016). They hence allow long-term, cell specific, imaging of electrical and calcium activity, currently not possible with synthetic sensors. Furthermore, synthetic sensors suffer from internalization, phototoxicity and cytotoxicity making them only suitable for short-term imaging of cardiac preparations (Kaestner et al., 2015). The extent to which synthetic sensors exhibit toxicity is dependent on study specific parameters including experimental model, sensors concentration and illumination protocols. For example, di-4-ANBDQBS has been shown to exhibit little phototoxicity even at high illumination intensities (Kanaporis, 2012). In this case, the sensor was loaded into guinea pig ventricular preparations and illumination time was restricted to 1 min. In other studies, continuous illumination of di-4-ANBDQBS for 10 min showed significant phototoxic effects compared to a genetic sensor in both human induced pluripotent stem cell cardiomyocyte monolayers (Shaheen et al., 2018), and single cells (Streit and Kleinlogel, 2018). Thus, both of these studies suggest that despite their slower response kinetics, GEVIs and GECIs are valuable tools not only for *in vivo* study but also in situations where phototoxic effects are prominent, such as cellular monolayers and single cells (Fast and Kléber, 1994; Broyles et al., 2018; Streit and Kleinlogel, 2018).

DESIGNING AN ALL-OPTICAL SETUP

The development of a successful all-optical system relies on a number of key features, unique when compared to single purpose, single cell, optical mapping or optogenetic setups.

TABLE 1 | Opsin and sensor combinations used in all-optical setups, with opsin excitation, sensor excitation, and sensor emission spectral characteristics from a specific study.

Opsin	Opsin Excitation λ (nm)	Type	Excitation source	Sensor Excitation λ (nm)	Sensor Emission λ (nm)	Reference	Other studies using specified Opsin/Sensor combination
<u>Voltage Sensors</u>							
ChR2 variants: ChR2-H134R, CatCh, ChRiff (Depolarizing)	470	Synthetic	LED	660 (655/40)	LP700	Klimas et al., 2016	Nussinovitch and Gapstein, 2015a; Yu et al., 2015; Feola et al., 2017; Majumder et al., 2018
		Synthetic	LED	625 (640/40)	774/140	Crocini et al., 2016	Scardigli et al., 2018; Streit and Kleinlogel, 2018; Quiñonez Uribe et al., 2018
		Synthetic	LED	655(690/60)	LP760	Park et al., 2014	Wang et al., 2017
		Synthetic	Hg/Xe arc lamp	(560/55)	LP650	Li et al., 2017	
		Synthetic	Halogen lamp	(565/24)	630/69	Streit and Kleinlogel, 2018	
		Synthetic	—	—	—	Zaglia et al., 2015	Bingen et al., 2014
		Synthetic	LED	635(630/30)	LP665	Streit and Kleinlogel, 2018	
		Synthetic GEVI	Halogen lamp	(525/50)	LP600	Watanabe et al., 2017	
			Laser	593.5	LP665	Streit and Kleinlogel, 2018	
			Laser	640	660-760	Dempsey et al., 2016	Björk et al., 2017
		Laser	647		Björk et al., 2017		
<u>Calcium Sensors</u>							
		Synthetic	LED	530(535/50)	570-625	Klimas et al., 2016	Jia et al., 2011
		Synthetic	LED	530	LP565	Wang et al., 2017	
		GEC1	Laser	488		Björk et al., 2017	
		GEC1	Laser	488		Dempsey et al., 2016	
<u>Voltage Sensors</u>							
ArchT (Hyperpolarizing)	566	GEVI	Laser	593.5	LP665	Streit and Kleinlogel, 2018	
<u>Voltage Sensors</u>							
eNpHR3.0 (Hyperpolarizing)	590	Synthetic	LED	655(690/60)	LP760	Park et al., 2014	

Opsin excitation wavelengths specified in the table are actual excitation wavelengths used in referenced studies. Sensor excitation wavelengths are shown as light source maxima with filtering shown in brackets. Bandpass filters shown as CWL/FWHM. LP, longpass.

Light must be delivered to both the opsins and the voltage or calcium sensors, demanding distinct illumination characteristics. The possibility of illumination crossover necessitates careful consideration of sensors, actuators and filtering requirements. **Table 1** summarizes opsin-sensors combinations that allow stimulation of optical actuation, control and imaging in pivotal all-optical studies.

Opsin and Sensor Compatibility

For an all-optical system, the compatibility of opsins with voltage and Ca^{2+} sensors is paramount, as spectral overlap will result in unwanted crosstalk and perturbation of the cellular membrane. For example, the absorption spectra of the most commonly used synthetic voltage sensor di-4-ANEPPS (excitation peak = 475nm) overlaps with that of ChR2, **Figure 3**. Therefore, excitation of di-4-ANEPPS to optically measure voltage can also excite ChR2, perturbing the membrane potential (Park et al., 2014). With this spectral congestion in mind, it is not surprising that the pioneering all-optical setups imaging Ca^{2+} routinely used rhod-4AM (Jia et al., 2011), which exhibit less spectral overlap with ChR2.

The use of opsins or sensors with red-shifted absorption profiles is the most common solution to spectral congestion. In general, it is easier for an all-optical system to utilize a red-shifted sensor, as the further red-shift of fluorescence emission can then be simply long-pass or band-pass filtered before imaging. Pittsburgh I (PGH1) is a potentiometric sensor whose absorption and emission spectra are far red shifted in comparison to di-4-ANEPPS, with an excitation and emission peak of 608 and 880 nm respectively (in EtOH) (Salama et al., 2005). It was hence the first sensor used in an all-optical manner with concurrent opsin excitation and voltage mapping (Park et al., 2014). By allowing opsin excitation with simultaneous voltage mapping, this system demonstrated how optogenetics can be used to not only pace cardiac tissue but crucially also prolong the action potential by ChR2 excitation during repolarization, a potential

therapeutic approach (Karathanos et al., 2014), or silence activity by eNpHR3.0 driven hyperpolarization (Park et al., 2014).

Alongside PGH1, there are red-shifted variants of di-4-ANEPPS. They include di-4-ANBDQPQ and di-4-ANBDQBS, which share the same basic structure as di-4-ANEPPS but with a distinct chromophore and longer linker sizes. The result is red-shifted absorption and emission spectra, both effectively excited between 500 and 700 nm (**Figure 3**) and imaged from 700 to 900 nm (Matiukas et al., 2007). They are hence spectrally distinct from ChR2. Additionally, 'blue-shifted' opsins are being developed (Lam et al., 2017) which may help avoid spectral overlap, however, their use may be limited by tissue damage and penetration depth.

PGH1, di-4-ANBDQPQ, di-4-ANBDQBS and rh-1691 have all been successfully used in all-optical setups due to their favorable spectral properties. **Table 1** lists potentiometric and calcium sensors used concurrently with optogenetic control and gives examples of illumination and filter setups (discussed in more detail later) that have been employed to minimize actuator-sensor crosstalk. Despite spectral overlap, sensors such as di-4-ANEPPS and GCaMP based calcium indicators have also been used in all-optical setups. However, dual-excitation, and fluorescence baseline shifts on pulse excitation, result in the requirement for spatial separation between excitation and emission areas, or need for extensive pre- and post-acquisition filtering (Dempsey et al., 2016; Li et al., 2017; Wang et al., 2017).

Illumination Sources

For optical mapping, sensor excitation is most commonly achieved using LEDs which benefit from narrow wavelength spectra, long operational lifetimes and low heat emission (Beacher, 2008), though Tungsten-Halogen lamps, Mercury/Xeon arc lamps and lasers are also used. Illumination source is chosen based on a number of characteristics, including wavelength and power. However, illumination of the sample in terms of spatial and temporal homogeneity is of paramount importance for successful optical mapping. In contrast, optical actuation in optogenetics routinely requires impulse-like signals (temporal inhomogeneity) delivered to a specific area of the sample (spatial inhomogeneity). Additionally, a number of studies have demonstrated the importance of patterned light delivery to drive conduction dynamics and realize effective arrhythmia termination (Burton et al., 2015; Crocini et al., 2016; Feola et al., 2017). Therefore liquid crystal (Schmieder et al., 2017) and digital micromirror device (DMD) spatial light modulation coupled to an illumination source such as an LED, able to uniquely deliver synchronous patterned illumination, have been extensively used in cardiac optogenetics from its infancy (Arrenberg et al., 2010). DMDs utilize several hundred thousand or millions of hinged micrometer sized mirrors to deliver illumination patterns with high spatial resolution, an ability that has been key to several optogenetic based discoveries (Scardigli et al., 2018).

Furthermore, fiber-optic coupled LED (Prando et al., 2018) and laser-based approaches have been utilized. This has partially been driven by the potential to incorporate illuminating fibers in clinically used tools for precise spatial illumination *in vivo*

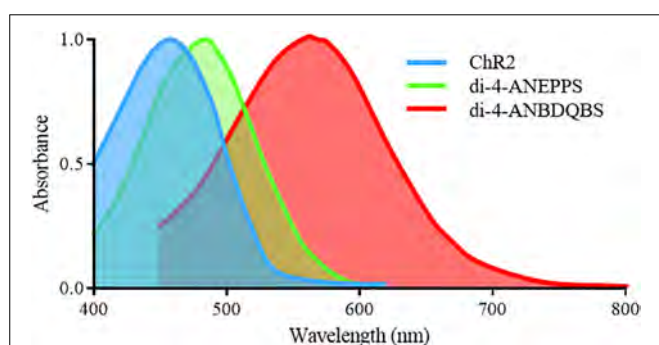


FIGURE 3 | Excitation spectra of the depolarizing opsin ChR2-H134 and voltage sensitive sensors di-4-ANEPPS and di-4-ANBDQBS. Significant overlap exists between the excitation spectra of ChR2 and di-4-ANEPPS, preventing imaging of di-4-ANEPPS without perturbing the membrane potential of ChR2 expressing cells. However, the red-shifted spectra of di-4-ANBDQBS does allow for excitation without simultaneous activation of ChR2.

(Klimas and Entcheva, 2014). Devices incorporating micro LED illumination with photodetectors have also been developed (Xu et al., 2014), and further optimization of such unique light delivery strategies is crucial if latent clinical benefits of optogenetics are to be realized.

Optical Filtering

The use of compatible opsins and sensors to avoid spectral overlap has already been discussed. However, optical filtering is still crucial in effective excitation and imaging of samples, especially when considering the multiple light paths necessary in the majority of all-optical setups. Single wavelength filters utilized in all-optical setups can be broadly characterized as (i) Bandpass filters (ii) Long- or shortpass filters, and (iii) Dichroic mirrors/beam splitters (**Figure 4**). An idealized single wavelength bandpass filter (**Figure 4A**) absorbs wavelengths outside a defined window, characterized by a central wavelength (CWL) and full width half maximum (FWHM). A common use of bandpass filters in all optical setups is excitation filtering, where illumination light is filtered before reaching a sample to narrow spectral bandwidth with a relatively small FWHM filter. This helps avoid interference with other sensors or actuators (Jaimes et al., 2016). For example, an effective excitation filter for red shifted voltage sensor di-4-ANBDQPP may be a 640/40 nm (CWL/FWHM) bandpass filter (Scardigli et al., 2018), placed between the illumination source and sample.

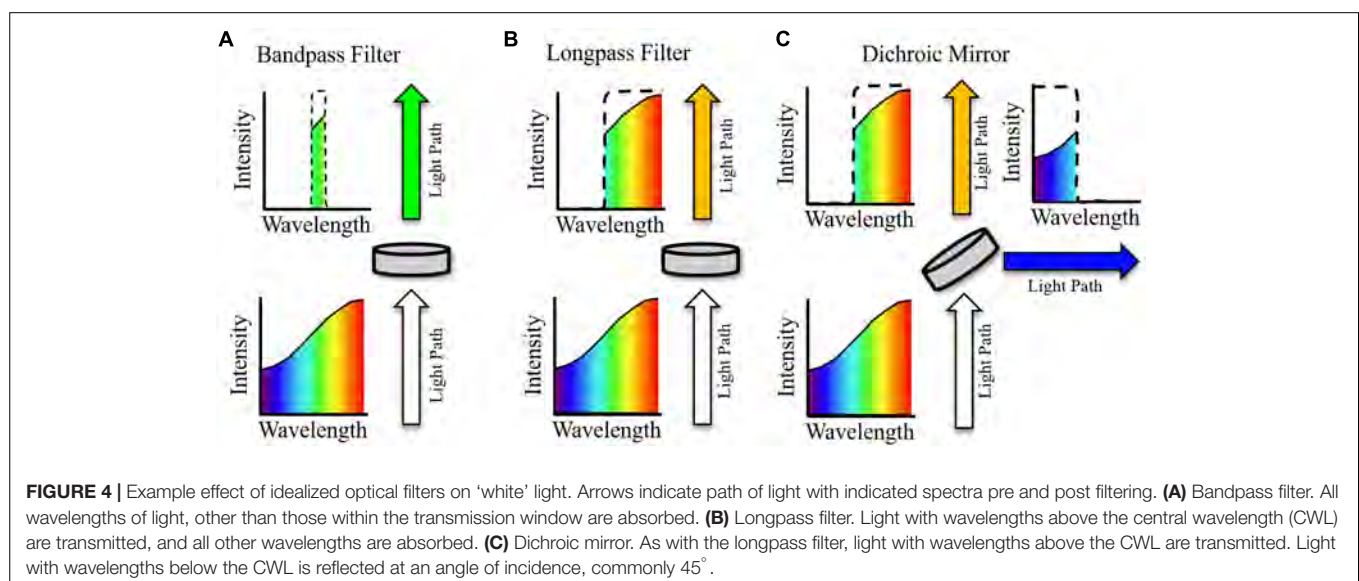
Longpass filters (**Figure 4B**) will absorb light with a wavelength below the CWL but will transmit light above this threshold (with the opposite holding for a shortpass filter with the same CWL). They therefore do not have an associated FWHM and are most used as emission filters, absorbing excitation light wavelengths while conserving the red-shifted fluorescence emission (Park et al., 2014). In conjunction with removing excitation light, longpass filtering is also necessary to effectively measure voltage dependent signals that arise from spectral shift, e.g., the electrochromic based indicators previously discussed,

as the fluorescence must be imaged away from the emission maxima. Bandpass filters with red-shifted CWL compared to excitation wavelengths (and emission maxima if required) can also be used for emission filtering, i.e., between the sample and imaging device. For an effective emission bandpass filter, however, a large FWHM is often desirable to maximize the photon count at the imaging device, assuming absorbance of excitation light is maintained (Scardigli et al., 2018). **Table 1** summarizes excitation and emission filtering setups that have been implemented in all-optical setups encompassing both voltage and calcium indicators.

Bandpass and longpass filters interact with light by either absorbing or transmitting depending on wavelength. Dichroic mirrors (or beam splitters), however, reflect certain wavelengths of light. An idealized longpass dichroic mirror for example (**Figure 4C**) transmits light with wavelength above the CWL and reflects (often at an angle of incidence of 45°) wavelengths below this cut off. Therefore, aside from basic filtering that is also possible to achieve with longpass and bandpass filters, dichroic mirrors can be used for important functions such as directing light paths (Scardigli et al., 2018) and splitting emission in dual sensor setups to either separate cameras or sections of a single imaging chip (Dempsey et al., 2016; Wang et al., 2017). The filters outlined in **Figure 4** are known as single wavelength or single band filters, with one characterizing CWL. In contrast, multiband filters are characterized by multiple transmission wavelength regions. They have hence found particular utility in dual optical mapping setups to simultaneously filter voltage and calcium emission signals (Wang et al., 2015).

Removing Spectral Deconvolution Requirement

Problems with spectral overlap can be circumvented by utilizing optical imaging techniques that are not reliant on fluorescent sensors, i.e., do not require illumination. On initiation of the action potential, excitable cells exhibit changing light



scattering properties, changing contrast (Cohen et al., 1972). However, with well-thought out setup design such as contrast enhancing off-axis illumination, the optical changes of the cell have shown to be a useful (although limited) substitute to direct sensor imaging of transmembrane voltage (Burton et al., 2015). Although parameters such as action potential morphology cannot be accurately recovered, sensor free imaging allows non-invasive tracking of excitation waves through cellular monolayers, and simple integration with optogenetic actuators (Burton et al., 2015). More recently, there has been development of bioluminescent, rather than fluorescent GEVIs such as the FRET based LOTUS-V (Inagaki et al., 2017). As bioluminescent output is stimulated chemically by treatment with a substrate such as Furimazine rather than optically, no illumination is required. This avoids the need for spectral separation between any excitation light and actuators present and facilitates long-term voltage imaging. When expressed in human induced pluripotent stem cell cardiomyocytes, LOTUS-V has been shown to deliver comparable, action potential signals to the synthetic sensor di-8-ANEPPS, although values such as action potential duration were prolonged due to the slower response kinetics (milliseconds) of the FRET response compared to the 'fast' synthetic sensors (Inagaki et al., 2017). The use of bioluminescent sensors in all-optical setups may therefore provide an attractive alternative to fluorescent GEVIs.

Additionally, novel non-genetic techniques for optical cardiac excitation based on graphene substrates (Savchenko et al., 2018), x-ray and ultrasound activated nanoparticles (Berry et al., 2015), or infrared induced temperature gradients (McPheeters et al., 2017) can act as a solution to spectral overlap and to realize deep tissue activation. These optical pacing strategies, however, do not share some of the unique advantages that genetically induced optical de- and hyperpolarization allows, most prominently precise control over wave dynamics or cell-specific activation.

Imaging

As with many other areas of the life sciences, cardiac optical mapping has benefitted from continued advancement of camera technology. Photodiode arrays (PDAs) were utilized in the early optical mapping experiments that moved beyond single photomultiplier tubes (Salama et al., 1987). PDAs benefit from a large dynamic range (as the PDA is made up of large individual diodes) and enhanced sampling rates. Low fractional changes in sensor fluorescence and the sub millisecond dynamics of cardiac electrical activity make these invaluable features for successful optical mapping (Efimov and Salama, 2012).

However, due to the physical arrangement of individual diodes, the maximal spatial resolution of a PDA is more limited compared to charge-coupled device (CCD) and complementary metal oxide semiconductor (CMOS) cameras. In modern setups therefore, CCD and CMOS cameras dominate (Gloschat et al., 2018; Wen et al., 2018). Developments such as electron-multiplication in CCD cameras, and 2nd generation back illuminated 'scientific' CMOS cameras have helped improve dynamic ranges and noise levels of these cameras, while enhanced compatibility with standard computer interfaces such as USB-3 help alleviate previously prohibitive costs (Boukens

and Efimov, 2014). Crucially, these cameras offer much higher spatial resolutions than possible with PDAs, capable of capturing > 10,000 pixel images at kHz sampling rates (Yu et al., 2017). The choice of imaging device for an all-optical setup does not differ considerably from a traditional optical mapping setup, and PDAs, CCD cameras and CMOS cameras have all been successfully utilized. Another important consideration is quantum efficiency of imaging devices in the far-red to near infrared wavelengths, if using red-shifted sensors.

Dual Voltage–Calcium All Optical Setups

Optical mapping of preparations dual loaded with both voltage and calcium sensors offers unique insights into the interplay between the cardiac action potential and Ca^{2+} handling (Myles et al., 2012). Achieving dual voltage-calcium optical mapping requires careful consideration of sensors spectra and filtering requirements. Addition of optical actuation, with its unique spectral, spatial, and temporal illumination requirements, further complicates the setup. Therefore to date, optical setups utilizing both voltage and calcium sensors have been shown to image the two indicators separately or sequentially (Klimas et al., 2016). In all-optical setups with simultaneous voltage-calcium imaging and optical pacing, spatial separation was necessary between pacing site and imaged area (Dempsey et al., 2016).

Computational Post-processing

In lieu of physical methods, computational methods can be used to overcome the spectral congestion that arises from optogenetic manipulation of optically mapped samples. However, it is important to note that these do not overcome undesired modulation of the membrane potential. A simple example is automatic identification and removal of optical pacing peaks by the application of several filters (Feola et al., 2017) or image frame removal (O'Shea et al., 2019). This is an effective strategy providing filtering/frame removal does not alter the fluorescence signal properties at pertinent times, and so ideally requires either temporal or spatial separation between pulsing peaks and fluorescence output.

Light pulses, however, can be more prohibitive to optical mapping analysis if pulses are applied during relevant phases of the cardiac cycle. For example, when pulses of light are delivered during the plateau and repolarization of the action potential, despite optical filtering attempts to avoid crosstalk, blue and green pulses can cause baseline shift in OAPs. As demonstrated by Park et al. (2014), to compensate for this, 'gap compensation' modeling procedures can be implemented. Briefly, this involves construction of a perturbation model of the optical emission ($F_{bluepulse}$) like shown in Equation 1

$$F_{bluepulse} = F_{fit} + A \cdot \left[e^{-\frac{(t-t_{pulse})}{\tau_{slow}}} - e^{-\frac{(t-t_{pulse})}{\tau_{fast}}} \right]^2 \quad (1)$$

where F_{fit} is the model of a control action potential without blue light illumination, A is a constant, t is time, t_{pulse} is start time of the light pulse, and τ_{slow} and τ_{fast} are decay constants. The repolarization phase of the perturbed OAP

therefore is modeled by least square fitting a bi-exponential decay from the start of the blue light pulse allowing recovery of the OAP during optogenetically induced action potential prolongation (Park et al., 2014).

CONTACTLESS ACTUATION AND ELECTROPHYSIOLOGY

Both in basic research and clinically, electrode-based techniques for pacing and stimulation require direct or close contact to cardiac tissue. Although extensively exploited and effective, these actuation methods are not without limitation. The direct contact between electrodes and tissue can promote electrochemical reactions and reactive oxygen species formation. Conversely in some situations, for example in cardioversion strategies (Nyns et al., 2017) or in cardiomyocyte monolayers to improve signal quality (Lapp et al., 2017), simultaneous activation of the large areas is desired rather than at a single site. If the activation region needs to be changed then electrodes must be physically moved, limiting spatial flexibility and throughput. From a clinical perspective, implantable pacemaker and defibrillation devices are highly energy consuming, tissue damaging, prone to post-implantation complications and can cause psychological distress and reduced quality of life (Bruegmann et al., 2016; Israelsson et al., 2018).

Optogenetic pacing therefore is one of a few biological strategies being explored as a replacement for traditional pacemaker devices (Rosen et al., 2011) but undoubtedly its most immediate beneficial quality is the ability realize unique basic research possibilities. Optogenetic opsins can be delivered to specific cell types (Hulsmans et al., 2017; Wang et al., 2017), providing novel research strategies, and promoting precise, repeatable and coordinated activation patterns. Conversely, by changing illumination conditions or the spatial arrangement of opsins expression, simultaneous excitation/suppression of large areas can be achieved. This can be applied in cellular monolayers, where concurrent activation can enhance signal quality, or in cardioversion strategies to terminate arrhythmias (Bruegmann et al., 2018). Contactless actuation avoids tissue damage due to the lack of tissue-electrode interface and can be realized in high-throughput applications such as multi-well cellular assays, discussed in more detail later (Klimas et al., 2016).

Optical mapping offers several clear advantages compared to electrode recording techniques. The spatial resolution achievable with optical mapping systems greatly outperforms multi-electrode array mapping systems. Furthermore, optical imaging can allow detailed, direct and multi-parameter investigation of voltage and calcium dynamics, whereas electrode techniques often make indirect measurements such as field potentials, where signals can be corrupted by noise and can alter significantly over time due to changes in electrode positioning or the maintenance of contact. Therefore, despite some notable disadvantages of optical study including requirement of contraction uncouplers and inability to perform *in vivo* experiments (Boukens and Efimov, 2014), optical mapping

techniques have seen growing use, even prior to transformative capabilities of optical stimulation was made available. The recent combination of actuation and measurement in all-optical setups has therefore, in a relatively short timeframe, delivered remarkable insights into optogenetic pacing (Nussinovitch and Gepstein, 2015a), cell targeting (Wang et al., 2017) and arrhythmia termination (Feola et al., 2017); advancing basic understand and enhancing the prospect of future clinically relevant optical therapies.

EFFECTS OF LIGHT PACING ON ACTION POTENTIAL MORPHOLOGY AND PROPAGATION

For further implementation of optogenetic technologies, detailed understanding of whether optogenetic actuation affects cardiac electrical signal morphology is required. All-optical systems are uniquely advantageous for such investigations, as they are able to report key EP signal parameters for comparison against established techniques, while also providing high spatio-temporal recording of cardiac activation (Entcheva and Bub, 2016).

Recent work using human stem cell-derived cardiomyocytes expressing commercial optogenetic constructs OptoPatch and CaViar have demonstrated that optogenetic modulation does not significantly alter single cell electrophysiological properties (Björk et al., 2017). Furthermore, optogenetic manipulation of neonatal rat ventricular myocyte monolayers expressing ChR2 indicate unaltered conduction velocity, action potential duration and upstroke velocity compared to control cells, using either optogenetic or electrical actuation (Li et al., 2017). Computational insights have for the most part agreed with experimental findings by showing similar action potential morphologies and cell type dependent variability (Williams and Entcheva, 2015). Nevertheless, fundamental differences in electrical and optogenetic stimulation exist. Electrical current injection is traditionally achieved with a rectangular pulse delivered at short pulse widths of 2–10 ms (Myles et al., 2012; Holmes et al., 2016). ChR2 photocurrent exhibits slower onset kinetics, meaning longer pulse timescales can be required to reach excitation threshold (Williams and Entcheva, 2015). The effects of these stimulation differences on *in vitro* and *in vivo* cardiac electrophysiology require further examination.

APPLICATIONS OF ALL OPTICAL CARDIAC ELECTROPHYSIOLOGY

All-optical systems, in their relatively short period of existence, have expanded our understanding of cardiac pathophysiology thanks to their high spatio-temporal resolution and unique ability for targeted tissue excitation. Indeed, by optically mapping voltage in transgenic mice expressing ChR2, threshold excitation and vulnerable areas for proarrhythmic focal ectopic activity has been determined (Zaglia et al., 2015). All-optical setups have allowed demonstration and potential for utility of ChR2 mediated resynchronization

(Nussinovitch and Gepstein, 2015a) and have crucially informed the production of local rather than global areas of conduction block using patterned illumination. The patterned illumination shows similar success in arrhythmia termination but at lower energy costs than global activation (Crocini et al., 2016; Feola et al., 2017). However, whether optogenetic approaches confer energy reduction benefits, over established and effective electrode technologies requires detailed assessment in future studies.

Previously, optical mapping of arrhythmia dynamics in whole hearts has allowed mechanistically driven choice of patterned illumination in an 'open-loop' fashion - information based on previous recordings being used to dictate illumination patterns. Although this proved similarly effective as global illumination, there is reliance on consentient arrhythmia dynamics between hearts (Crocini et al., 2016). However, recent advancements including utilization of DMD illumination technology and high-speed data recording have demonstrated the potential of 'closed-loop' all-optical EP. Here, conduction disorders such as atrioventricular block can be detected by optical mapping and corrected by optical stimulation of ChR2 in real time. Real-time intervention can also conversely be used to setup and then study conduction abnormalities such as re-entry. These abilities make 'closed-loop' systems potentially vital going forward, allowing all-optical research in experimental models that is tunable in a manner hitherto only afforded by computational modeling, and at much reduced timescales (Scardigli et al., 2018). Similarly, all-optical control and output has shown the feasibility of engineering bioelectric tissues capable of complex information processing and in which all constituent parts are fully characterized (McNamara et al., 2016).

A major avenue for use of all-optical setups is the delivery of high-throughput platforms for cardiotoxicity screenings of candidate drug compounds (Klimas et al., 2016; Streit and Kleinlogel, 2018). These platforms are crucial in the context of the comprehensive *in vitro* pro-arrhythmia assay (CiPA) initiative - the recognition that cardiotoxicity screening should not focus solely on hERG channel interactions and must use experimental as well as computational methods (Fermini et al., 2016). All-optical methods are distinctly suited to the changing requirements of cardiotoxicity drug screening. As highlighted, the lack of requirement for direct contact makes optical actuation and optical recording much easier to scale to high-throughput parallelized applications, crucial for screening multiple drugs. As the reported voltage signals result from the sum of all ionic currents, significant alterations in any channel or pump function (not just hERG/I_{Kr}) in response to a drug will be evident, while Ca²⁺ handling abnormalities can also be screened with the use of appropriate sensors (Dempsey et al., 2016; Klimas et al., 2016). If specific channels warrant further investigation, all-optical methods can still be utilized by expression of channels in cells otherwise void of the ionic channels of interest (Streit and Kleinlogel, 2018), and the scalability of optical methods means analysis of other models apart from cell cultures may be achievable in the near future.

CONCLUSION AND FUTURE DIRECTIONS

Optogenetics is a technique that has developed into an immensely useful tool in basic cardiac research with clear, though as of yet unrealized, clinical potential (Entcheva, 2013). Fusion of optogenetics with optical mapping has been made possible by the substantial technical considerations and advances summarized in this review. All-optical electrophysiology, and indeed the field of cardiac optogenetics in general, however, remains a relatively new technique with several opportunities to further advance our understanding of electrical function in the heart.

Recent demonstration of 'closed-loop' all-optical investigation opens up a plethora of exciting opportunities for application of this exciting technology to key research questions, relevant in health and disease. 'Closed-loop' all-optical investigation studies could deliver faster, more physiologically relevant tools than even the most sophisticated computational cardiac models.

In contrast to cardiac research, optogenetics is widespread in neuroscience (Adamantidis, 2015). Effects on heart function and coupling of neurons and cardiac cells are often measured outcomes of neuromodulation. However, cardiac effects of optical neuromodulation are potentially limited to simply beating rate measurements (Nussinovitch and Gepstein, 2015b) or monitored using traditional techniques, with only isolated examples of optical mapping neuronal-cardiac effects (Dong et al., 2016). The combination of optical neuromodulation with all-optical cardiac electrophysiology could deliver unique insights into control of the heart by the nervous system (Wengrowski et al., 2015).

For optogenetic-based therapy to ever be realized in clinical practice, several technological and biological advances need to be implemented. These include novel methods for light and gene delivery to *in vivo* cardiac tissue, wireless control of implantable devices (Gagnon et al., 2017), and advanced materials uniquely designed for use in bio-integrated electronic circuits (Fang et al., 2016). However, regardless of future clinical utility, implementation of optogenetics in all-optical imaging systems has already proved a unique and transformative tool for cardiac research and will continue to be used in the study of the physiology and pathophysiology of the heart.

AUTHOR CONTRIBUTIONS

CO prepared the primary manuscript. AH, JW, JC, PK, LF, KR, and DP critically revised the manuscript. XO, RD, and SH provided intellectual content and technical insights. CO, JW, and DP produced the figures.

FUNDING

This work was funded by the EPSRC studentship (Sci-Phy-4-Health Centre for Doctoral Training L016346) to DP, KR, and LF, Wellcome Trust Seed Award Grant (109604/Z/15/Z) to DP, British Heart Foundation Grants

(PG/17/55/33087 and RG/17/15/33106) to DP, European Union [Grant Agreement No. 633196 (CATCH ME) to PK and LF], British Heart Foundation (FS/13/43/30324 to PK and

LF; PG/17/30/32961 to PK and AH), and Leducq Foundation to PK. JW is supported by the British Heart Foundation (FS/16/35/31952).

REFERENCES

- Abilez, O. J., Wong, J., Prakash, R., Deisseroth, K., Zarins, C. K., and Kuhl, E. (2011). Multiscale computational models for optogenetic control of cardiac function. *Biophys. J.* 101, 1326–1334. doi: 10.1016/j.bpj.2011.08.004
- Adamantidis, A. (2015). Optogenetics: 10 years after ChR2 in neurons—views from the community. *Nat. Neurosci.* 18, 1213–1225. doi: 10.1038/nn.4091
- Alfonsa, H., Merricks, E. M., Codadu, N. K., Cunningham, M. O., Deisseroth, K., Racca, C., et al. (2015). The contribution of raised intraneuronal chloride to epileptic network activity. *J. Neurosci.* 35, 7715–7726. doi: 10.1523/JNEUROSCI.4105-14.2015
- Ambrosi, C. M., Boyle, P. M., Chen, K., Trayanova, N. A., and Entcheva, E. (2015). Optogenetics-enabled assessment of viral gene and cell therapy for restoration of cardiac excitability. *Sci. Rep.* 5:17350. doi: 10.1038/srep17350
- Ambrosi, C. M., Sadananda, G., Klimas, A., and Entcheva, E. (2019). Adeno-associated virus mediated gene delivery: implications for scalable in vitro and in vivo cardiac optogenetic models. (in press). doi: 10.3389/fphys.2019.00168
- Arrenberg, A. B., Stainier, D. Y. R., Baier, H., and Huiskens, J. (2010). Optogenetic control of cardiac function. *Science* 330, 971–974. doi: 10.1126/science.1195929
- Bamann, C., Gueta, R., Kleinlogel, S., Nagel, G., and Bamberg, E. (2010). Structural guidance of the photocycle of channelrhodopsin-2 by an interhelical hydrogen bond. *Biochemistry* 49, 267–278. doi: 10.1021/bi901634p
- Beacher, J. (2008). LEDs for fluorescence microscopy. *Biophotonics Int.* 5324, 208–215. doi: 10.1117/12.525932
- Bera, A., and Sen, D. (2017). Promise of adeno-associated virus as a gene therapy vector for cardiovascular diseases. *Heart Fail. Rev.* 22, 795–823. doi: 10.1007/s10741-017-9622-7
- Bernal Sierra, Y. A., Rost, B. R., Pohfahl, M., Fernandes, A. M., Kopton, R. A., Moser, S., et al. (2018). Potassium channel-based optogenetic silencing. *Nat. Commun.* 9:4611. doi: 10.1038/s41467-018-07038-8
- Berndt, A., Lee, S. Y., Ramakrishnan, C., and Deisseroth, K. (2014). Structure-guided transformation of channelrhodopsin into a light-activated chloride channel. *Science* 344, 420–424. doi: 10.5061/dryad.9r0p6
- Berndt, A., Schoenenberger, P., Mattis, J., Tye, K. M., Deisseroth, K., Hegemann, P., et al. (2011). High-efficiency channelrhodopsins for fast neuronal stimulation at low light levels. *Proc. Natl. Acad. Sci. U.S.A.* 108, 7595–7600. doi: 10.1073/pnas.1017210108
- Berry, R., Getzin, M., Gjestebj, L., and Wang, G. (2015). X-optogenetics and U-optogenetics: feasibility and possibilities. *Photonics* 2, 23–39. doi: 10.3390/photonics2010023
- Bingen, B. O., Engels, M. C., Schali, M. J., Jangsanthong, W., Neshati, Z., Feola, I., et al. (2014). Light-induced termination of spiral wave arrhythmias by optogenetic engineering of atrial cardiomyocytes. *Cardiovasc. Res.* 104, 194–205. doi: 10.1093/cvr/cvu179
- Björk, S., Ojala, E. A., Nordström, T., Ahola, A., Liljeström, M., Hyttinen, J., et al. (2017). Evaluation of optogenetic electrophysiology tools in human stem cell-derived cardiomyocytes. *Front. Physiol.* 8:884. doi: 10.3389/fphys.2017.00884
- Boukens, B. J., and Efimov, I. R. (2014). A century of optocardiography. *IEEE Rev. Biomed. Eng.* 7, 115–125. doi: 10.1109/RBME.2013.2286296
- Boyden, E. S., Zhang, F., Bamberg, E., Nagel, G., and Deisseroth, K. (2005). Millisecond-timescale, genetically targeted optical control of neural activity. *Nat. Neurosci.* 8, 1263–1268. doi: 10.1038/nn1525
- Broyles, C., Robinson, P., and Daniels, M. (2018). Fluorescent, bioluminescent, and optogenetic approaches to study excitable physiology in the single cardiomyocyte. *Cells* 7:E51. doi: 10.3390/cells7060051
- Bruegmann, T., Bei, T., Vogt, C. C., Schrickel, J. W., and Sasse, P. (2018). Optogenetic termination of atrial fibrillation in mice. *Cardiovasc. Res.* 114, 713–723. doi: 10.1093/cvr/cvx250
- Bruegmann, T., Boyle, P. M., Vogt, C. C., Karathanos, T. V., Arevalo, H. J., Fleischmann, B. K., et al. (2016). Optogenetic defibrillation terminates ventricular arrhythmia in mouse hearts and human simulations. *J. Clin. Invest.* 126, 3894–3904. doi: 10.1172/JCI88950
- Bruegmann, T., Malan, D., Hesse, M., Bei, T., Fuegmann, C. J., Fleischmann, B. K., et al. (2010). Optogenetic control of heart muscle in vitro and in vivo. *Nat. Methods* 7, 897–900. doi: 10.1038/nmeth.1512
- Burton, R. A. B., Klimas, A., Ambrosi, C. M., Tomek, J., Corbett, A., Entcheva, E., et al. (2015). Optical control of excitation waves in cardiac tissue. *Nat. Photonics* 9, 813–816. doi: 10.1038/nphoton.2015.196
- Chang, Y. F., Broyles, C. N., Brook, F. A., Davies, M. J., Turtle, C. W., Nagai, T., et al. (2017). Non-invasive phenotyping and drug testing in single cardiomyocytes or beta-cells by calcium imaging and optogenetics. *PLoS One* 12:e0174181. doi: 10.1371/journal.pone.0174181
- Cohen, L. B., Keynes, R. D., and Landowne, D. (1972). Changes in axon light scattering that accompany the action potential: current-dependent components. *J. Physiol.* 224, 727–752. doi: 10.1113/jphysiol.1972.sp009920
- Crocini, C., Ferrantini, C., Coppini, R., Scardigli, M., Yan, P., Loew, L. M., et al. (2016). Optogenetics design of mechanistically-based stimulation patterns for cardiac defibrillation. *Sci. Rep.* 6:35628. doi: 10.1038/srep35628
- Crocini, C., Ferrantini, C., Pavone, F. S., and Sacconi, L. (2017). Optogenetics gets to the heart: a guiding light beyond defibrillation. *Prog. Biophys. Mol. Biol.* 130, 132–139. doi: 10.1016/j.pbiomolbio.2017.05.002
- Dawydow, A., Gueta, R., Ljaschenko, D., Ullrich, S., Hermann, M., Ehmann, N., et al. (2014). Channelrhodopsin-2-XXL, a powerful optogenetic tool for low-light applications. *Proc. Natl. Acad. Sci. U.S.A.* 111, 13972–13977. doi: 10.1073/pnas.1408269111
- Dempsey, G. T., Chaudhary, K. W., Atwater, N., Nguyen, C., Brown, B. S., McNeish, J. D., et al. (2016). Cardiotoxicity screening with simultaneous optogenetic pacing, voltage imaging and calcium imaging. *J. Pharmacol. Toxicol. Methods* 81, 240–250. doi: 10.1016/j.vascn.2016.05.003
- Dong, X., Tung, L., Haganir, R., Dong, X., Lee, G., and Lee, G. (2016). Functional coupling with cardiac muscle promotes maturation of hPSC-derived sympathetic neurons. *Cell Stem Cell* 19, 95–106. doi: 10.1016/j.stem.2016.05.002
- Efimov, I. R., and Salama, G. (2012). The future of optical mapping is bright RE?: review on: “Optical imaging of voltage and calcium in cardiac cells and tissues” by Herron, Lee, and Jalife. *Circ. Res.* 10, e70–e71. doi: 10.1161/CIRCRESAHA.112.270033
- Entcheva, E. (2013). Cardiac optogenetics. *AJP Heart Circ. Physiol.* 304, H1179–H1191. doi: 10.1152/ajpheart.00432.2012
- Entcheva, E., and Bub, G. (2016). All-optical control of cardiac excitation: combined high-resolution optogenetic actuation and optical mapping. *J. Physiol.* 9, 2503–2510. doi: 10.1113/jp271559
- Fang, H., Zhao, J., Yu, K. J., Song, E., Farimani, A. B., Chiang, C.-H., et al. (2016). Ultrathin, transferred layers of thermally grown silicon dioxide as biofluid barriers for biointegrated flexible electronic systems. *Proc. Natl. Acad. Sci. U.S.A.* 113, 11682–11687. doi: 10.1073/pnas.1605269113
- Fast, V. G., and Kléber, A. G. (1994). Anisotropic conduction in monolayers of neonatal rat heart cells cultured on collagen substrate. *Circ. Res.* 75, 591–595. doi: 10.1161/01.RES.75.3.591
- Feola, I., Volkens, L., Majumder, R., Teplenin, A., Schali, M. J., Panfilov, A. V., et al. (2017). Localized optogenetic targeting of rotors in atrial cardiomyocyte monolayers. *Circ. Arrhythm. Electrophysiol.* 10:e005591. doi: 10.1161/CIRCEP.117.005591
- Fermini, B., Hancox, J. C., Abi-Gerges, N., Bridgland-Taylor, M., Chaudhary, K. W., Colatsky, T., et al. (2016). A new perspective in the field of cardiac safety testing through the comprehensive in vitro proarrhythmia assay paradigm. *J. Biomol. Screen.* 21, 1–11. doi: 10.1177/1087057115594589
- Gagnon, L. L., Gagnon-Turcotte, G., Popek, A., Chatelier, A., Chahine, M., and Gosselin, B. (2017). “A wireless system for combined heart optogenetics and electrocardiography recording,” in *Proceedings of the IEEE International Symposium on Circuits and Systems (ISCAS)*, (Piscataway, NJ: IEEE), 1–4. doi: 10.1109/ISCAS.2017.8050365
- Gloschat, C., Aras, K., Gupta, S., Faye, N. R., Zhang, H., Syunyaev, R. A., et al. (2018). RHYTHM: an open source imaging toolkit for cardiac panoramic optical mapping. *Sci. Rep.* 8:2921. doi: 10.1038/s41598-018-21333-w

- Govorunova, E. G., Cunha, S. R., Sineshchekov, O. A., and Spudich, J. L. (2016). Anion channelrhodopsins for inhibitory cardiac optogenetics. *Sci. Rep.* 6:33530. doi: 10.1038/srep33530
- Govorunova, E. G., Sineshchekov, O. A., Janz, R., Liu, X., and Spudich, J. L. (2015). Natural light-gated anion channels: a family of microbial rhodopsins for advanced optogenetics. *Science* 349, 647–650. doi: 10.1126/science.aaa7484
- Herron, T. J., Lee, P., and Jalife, J. (2012). Optical imaging of voltage and calcium in cardiac cells & tissues. *Circ. Res.* 110, 609–623. doi: 10.1161/CIRCRESAHA.111.247494
- Hochbaum, D. R., Zhao, Y., Farhi, S. L., Klapoetke, N., Werley, C. A., Kapoor, V., et al. (2014). All-optical electrophysiology in mammalian neurons using engineered microbial rhodopsins. *Nat. Methods* 11, 825–833. doi: 10.1038/NMETH.3000
- Holmes, A. P., Yu, T. Y., Tull, S., Syeda, F., Kuhlmann, S. M., O'Brien, S.-M., et al. (2016). A regional reduction in Ito and IKACH in the Murine posterior left atrial myocardium is associated with action potential prolongation and increased Ectopic activity. *PLoS One* 11:e0154077. doi: 10.1371/journal.pone.0154077
- Hou, J. H., Kralj, J. M., Douglass, A. D., Engert, F., and Cohen, A. E. (2014). Simultaneous mapping of membrane voltage and calcium in zebrafish heart *in vivo* reveals chamber-specific developmental transitions in ionic currents. *Front. Physiol.* 5:344. doi: 10.3389/fphys.2014.00344
- Hulsmans, M., Clauss, S., Xiao, L., Aguirre, A. D., King, K. R., Hanley, A., et al. (2017). Macrophages facilitate electrical conduction in the heart. *Cell* 169, 510–522.e20. doi: 10.1016/j.cell.2017.03.050
- Inagaki, S., Tsutsui, H., Suzuki, K., Agetsuma, M., Arai, Y., Jinno, Y., et al. (2017). Genetically encoded bioluminescent voltage indicator for multi-purpose use in wide range of bioimaging. *Sci. Rep.* 7:42398. doi: 10.1038/srep42398
- Israelsson, J., Thylén, I., Strömberg, A., Bremer, A., and Årestedt, K. (2018). Factors associated with health-related quality of life among cardiac arrest survivors treated with an implantable cardioverter-defibrillator. *Resuscitation* 132, 78–84. doi: 10.1016/j.resuscitation.2018.09.002
- Jaimes, R., Walton, R. D., Pasdois, P., Bernus, O., Efimov, I. R., and Kay, M. W. (2016). A technical review of optical mapping of intracellular calcium within myocardial tissue. *Am. J. Physiol. Heart Circ. Physiol.* 310, H1388–H1401. doi: 10.1152/ajpheart.00665.2015
- Jalife, J. (2003). Rotors and spiral waves in atrial fibrillation. *J. Cardiovasc. Electrophysiol.* 14, 776–780. doi: 10.1046/j.1540-8167.2003.03136.x
- Jia, Z., Valiunas, V., Lu, Z., Bien, H., Liu, H., Wang, H. Z., et al. (2011). Stimulating cardiac muscle by light cardiac optogenetics by cell delivery. *Circ. Arrhythmia Electrophysiol.* 4, 753–760. doi: 10.1161/CIRCEP.111.964247
- Kaestner, L., Tian, Q., Kaiser, E., Xian, W., Müller, A., Oberhofer, M., et al. (2015). Genetically encoded voltage indicators in circulation research. *Int. J. Mol. Sci.* 16, 21626–21642. doi: 10.3390/ijms160921626
- Kanaporis, G. (2012). Optical mapping at increased illumination intensities. *J. Biomed. Opt.* 17:096007. doi: 10.1117/1.JBO.17.9.096007
- Kandori, H. (2015). Ion-pumping microbial rhodopsins. *Front. Mol. Biosci.* 2:52. doi: 10.3389/fmolb.2015.00052
- Karathanos, T. V., Bayer, J. D., Wang, D., Boyle, P. M., and Trayanova, N. A. (2016). Opsin spectral sensitivity determines the effectiveness of optogenetic termination of ventricular fibrillation in the human heart: a simulation study. *J. Physiol.* 594, 6879–6891. doi: 10.1113/JP271739
- Karathanos, T. V., Boyle, P. M., and Trayanova, N. A. (2014). Optogenetics-enabled dynamic modulation of action potential duration in atrial tissue: feasibility of a novel therapeutic approach. *Europace* 16, iv69–iv76. doi: 10.1093/europace/euu250
- Kato, H. E., Kim, Y. S., Paggi, J. M., Evans, K. E., Allen, W. E., Richardson, C., et al. (2018). Structural mechanisms of selectivity and gating in anion channelrhodopsins. *Nature* 561, 349–354. doi: 10.1038/s41586-018-0504-5
- Kim, Y. S., Kato, H. E., Yamashita, K., Ito, S., Inoue, K., Ramakrishnan, C., et al. (2018). Crystal structure of the natural anion-conducting channelrhodopsin GtACR1. *Nature* 561, 343–348. doi: 10.1038/s41586-018-0511-6
- Kleinlogel, S., Feldbauer, K., Dempfski, R. E., Fotis, H., Wood, P. G., Bamann, C., et al. (2011). Ultra light-sensitive and fast neuronal activation with the Ca2+-permeable channelrhodopsin CatCh. *Nat. Neurosci.* 14, 513–518. doi: 10.1038/nn.2776
- Klimas, A., Ambrosi, C. M., Yu, J., Williams, J. C., Bien, H., and Entcheva, E. (2016). OptoDyCE as an automated system for high-throughput all-optical dynamic cardiac electrophysiology. *Nat. Commun.* 7:11542. doi: 10.1038/ncomms11542
- Klimas, A., and Entcheva, E. (2014). Toward microendoscopy-inspired cardiac optogenetics *in vivo*?: technical overview and perspective. *J. Biomed. Opt.* 19:080701. doi: 10.1117/1.JBO.19.8.080701
- Knollmann, B. C. (2010). Pacing lightly: optogenetics gets to the heart. *Nat. Methods* 7, 889–891. doi: 10.1038/nmeth1110-889
- Koopman, C. D., Zimmermann, W. H., Knöpfel, T., and de Boer, T. P. (2017). Cardiac optogenetics: using light to monitor cardiac physiology. *Basic Res. Cardiol.* 112:56. doi: 10.1007/s00395-017-0645-y
- Lam, P. Y., Mendu, S. K., Mills, R. W., Zheng, B., Padilla, H., Milan, D. J., et al. (2017). A high-conductance chemo-optogenetic system based on the vertebrate channel Trpa1b. *Sci. Rep.* 7:11839. doi: 10.1038/s41598-017-11791-z
- Lapp, H., Bruegmann, T., Malan, D., Friedrichs, S., Kilgus, C., Heidsieck, A., et al. (2017). Frequency-dependent drug screening using optogenetic stimulation of human iPSC-derived cardiomyocytes. *Sci. Rep.* 7:9629. doi: 10.1038/s41598-017-09760-7
- Li, Q., Ni, R. R., Hong, H., Goh, K. Y., Rossi, M., Fast, V. G., et al. (2017). Electrophysiological properties and viability of neonatal rat ventricular myocyte cultures with inducible ChR2 expression. *Sci. Rep.* 7:1531. doi: 10.1038/s41598-017-01723-2
- Liao, M. L. C., De Boer, T. P., Mutoh, H., Raad, N., Richter, C., Wagner, E., et al. (2015). Sensing cardiac electrical activity with a cardiac myocyte-targeted optogenetic voltage indicator. *Circ. Res.* 117, 401–412. doi: 10.1161/CIRCRESAHA.117.306143
- Lin, J. Y. (2010). A user's guide to channelrhodopsin variants: features, limitations and future developments. *Exp. Physiol.* 96, 19–25. doi: 10.1113/expphysiol.2009.051961
- Lin, J. Y., Knutsen, P. M., Muller, A., Kleinfeld, D., and Tsien, R. Y. (2013). ReaChR: a red-shifted variant of channelrhodopsin enables deep transcranial optogenetic excitation. *Nat. Neurosci.* 16, 1499–1508. doi: 10.1038/nn.3502
- Lin, J. Y., Lin, M. Z., Steinbach, P., and Tsien, R. Y. (2009). Characterization of engineered channelrhodopsin variants with improved properties and kinetics. *Biophys. J.* 96, 1803–1814. doi: 10.1016/j.bpj.2008.11.034
- Loew, L. M., Bonneville, G. W., and Surow, J. (1978). Charge shift optical probes of membrane potential. *Biochemistry* 17, 4065–4071. doi: 10.1021/bi00612a030
- Majumder, R., Feola, I., Teplenin, A. S., Antoine, A. F., Vries, D., Pan, A. V., et al. (2018). Optogenetics enables real-time spatiotemporal control over spiral wave dynamics in an excitable cardiac system. *eLife* 7:e41076. doi: 10.7554/eLife.41076
- Matiukas, A., Mitrea, B. G., Qin, M., Pertsov, A. M., Shvedko, A. G., Warren, M. D., et al. (2007). Near infrared voltage sensitive fluorescent dyes optimized for optical mapping in blood-perfused myocardium. *Heart Rhythm* 4, 1441–1451. doi: 10.1037/a0018493. Understanding
- McNamara, H. M., Zhang, H., Werley, C. A., and Cohen, A. E. (2016). Optically controlled oscillators in an engineered bioelectric tissue. *Phys. Rev. X* 6:031001. doi: 10.1103/PhysRevX.6.031001
- McPheeters, M. T., Wang, Y. T., Werdich, A. A., Jenkins, M. W., and Laurita, K. R. (2017). An infrared optical pacing system for screening cardiac electrophysiology in human cardiomyocytes. *PLoS One* 12:e0183761. doi: 10.1371/journal.pone.0183761
- Mickoleit, M., Schmid, B., Weber, M., Fährbach, F. O., Hombach, S., Reischauer, S., et al. (2014). High-resolution reconstruction of the beating zebrafish heart. *Nat. Methods* 11, 919–922. doi: 10.1038/nmeth.3037
- Miller, E. W. (2016). Small molecule fluorescent voltage indicators for studying membrane potential. *Curr. Opin. Chem. Biol.* 33, 74–80. doi: 10.1016/j.cbpa.2016.06.003
- Myles, R. C., Wang, L., Kang, C., Bers, D. M., and Ripplinger, C. M. (2012). Local β -adrenergic stimulation overcomes source-sink mismatch to generate focal arrhythmia. *Circ. Res.* 110, 1454–1464. doi: 10.1161/CIRCRESAHA.111.262345
- Nagel, G., Brauner, M., Liewald, J. F., Adeishvili, N., Bamberg, E., and Gottschalk, A. (2005). Light activation of channelrhodopsin-2 in excitable cells of *Caenorhabditis elegans* triggers rapid behavioral responses. *Curr. Biol.* 15, 2279–2284. doi: 10.1016/j.cub.2005.11.032
- Nagel, G., Szellas, T., Huhn, W., Kateriya, S., Adeishvili, N., Berthold, P., et al. (2003). Channelrhodopsin-2, a directly light-gated cation-selective membrane channel. *Proc. Natl. Acad. Sci. U.S.A.* 100, 13940–13945. doi: 10.1073/pnas.1936192100

- Nussinovitch, U., and Gepstein, L. (2015a). Optogenetics for in vivo cardiac pacing and resynchronization therapies. *Nat. Biotechnol.* 33, 750–754. doi: 10.1038/nbt.3268
- Nussinovitch, U., and Gepstein, L. (2015b). Optogenetics for suppression of cardiac electrical activity in human and rat cardiomyocyte cultures. *Neurophotonics* 2:031204. doi: 10.1117/1.NPh.2.3.031204
- Nussinovitch, U., Shinnawi, R., and Gepstein, L. (2014). Modulation of cardiac tissue electrophysiological properties with light-sensitive proteins. *Cardiovasc. Res.* 102, 176–187. doi: 10.1093/cvr/cvu037
- Nyns, E. C. A., Kip, A., Bart, C. I., Plomp, J. J., Zeppenfeld, K., Schalij, M. J., et al. (2017). Optogenetic termination of ventricular arrhythmias in the whole heart: towards biological cardiac rhythm management. *Eur. Heart J.* 38, 2132–2136. doi: 10.1093/eurheartj/ehw574
- O'Shea, C., Holmes, A. P., Yu, T. Y., Winter, J., Wells, S. P., Correia, J., et al. (2019). ElectroMap: High-throughput open-source software for analysis and mapping of cardiac electrophysiology. *Sci. Rep.* 9:1389. doi: 10.1038/s41598-018-38263-2
- Park, S. A., Lee, S.-R., Tung, L., and Yue, D. T. (2014). Optical mapping of optogenetically shaped cardiac action potentials. *Sci. Rep.* 4:6125. doi: 10.1038/srep06125
- Prando, V., Da Broi, F., Franzoso, M., Plazzo, A. P., Pianca, N., Francolini, M., et al. (2018). Dynamics of neuroeffector coupling at cardiac sympathetic synapses. *J. Physiol.* 11, 2055–2075. doi: 10.1113/jp275693
- Quinn, T. A., Camelliti, P., Rog-Zielinska, E. A., Siedlecka, U., Poggioli, T., O'Toole, E. T., et al. (2016). Electrotonic coupling of excitable and nonexcitable cells in the heart revealed by optogenetics. *Proc. Natl. Acad. Sci. U.S.A.* 113, 14852–14857. doi: 10.1073/pnas.1611184114
- Quiñonez Uribe, R. A., Luther, S., Diaz-maue, L., and Richter, C. (2018). Energy-reduced arrhythmia termination using global photostimulation in optogenetic murine hearts. *Front. Physiol.* 9:1651. doi: 10.3389/fphys.2018.01651
- Rosen, M. R., Robinson, R. B., Brink, P. R., and Cohen, I. S. (2011). The road to biological pacing. *Nat. Rev. Cardiol.* 8, 656–666. doi: 10.1038/nrcardio.2011.120
- Salama, G., Choi, B. R., Azour, G., Lavasani, M., Tumbey, V., Salzberg, B. M., et al. (2005). Properties of new, long-wavelength, voltage-sensitive dyes in the heart. *J. Membr. Biol.* 208, 125–140. doi: 10.1007/s00232-005-0826-8
- Salama, G., Lombardi, R., and Elson, J. (1987). Maps of optical action potentials and NADH fluorescence in intact working hearts. *Am. J. Physiol. Circ. Physiol.* 252, H384–H394. doi: 10.1152/ajpheart.1987.252.2.H384
- Savchenko, A., Cherkas, V., Liu, C., Braun, G. B., Kleschevnikov, A., Miller, Y. I., et al. (2018). Graphene biointerfaces for optical stimulation of cells. *Sci. Adv.* 4:eaat0351. doi: 10.1126/sciadv.aat0351
- Scanziani, M., and Häusser, M. (2009). Electrophysiology in the age of light. *Nature* 461, 930–939. doi: 10.1038/nature08540
- Scardigli, M., Müllenbroich, C., Margoni, E., Cannazzaro, S., Crocini, C., Ferrantini, C., et al. (2018). Real-time optical manipulation of cardiac conduction in intact hearts. *J. Physiol.* 596, 3841–3858. doi: 10.1113/jp276283
- Schmieder, F., Büttner, L., Czarske, J., Torres, M. L., Heisterkamp, A., Klapper, et al. (2017). "Holographically generated structured illumination for cell stimulation in optogenetics," in *Proceedings of the International Society for Optical Engineering* (Amsterdam: Elsevier).
- Schneider, F., Grimm, C., and Hegemann, P. (2015). Biophysics of channelrhodopsin. *Annu. Rev. Biophys.* 44, 167–186. doi: 10.1146/annurev-biophys-060414-034014
- Shaheen, N., Shiti, A., Huber, I., Shinnawi, R., Arbel, G., Gepstein, A., et al. (2018). Human induced pluripotent stem cell-derived cardiac cell sheets expressing genetically encoded voltage indicator for pharmacological and arrhythmia studies. *Stem Cell Reports* 10, 1879–1894. doi: 10.1016/j.stemcr.2018.04.006
- Shinnawi, R., Huber, I., Maizels, L., Shaheen, N., Gepstein, A., Arbel, G., et al. (2015). Monitoring human-induced pluripotent stem cell-derived cardiomyocytes with genetically encoded calcium and voltage fluorescent reporters. *Stem Cell Reports* 5, 582–596. doi: 10.1016/j.stemcr.2015.08.009
- Smith, A. M., Mancini, M. C., and Nie, S. (2009). Bioimaging: second window for in vivo imaging. *Nat. Nanotechnol.* 4, 710–711. doi: 10.1038/nnano.2009.326
- Streit, J., and Kleinlogel, S. (2018). Dynamic all-optical drug screening on cardiac voltage-gated ion channels. *Sci. Rep.* 8:1153. doi: 10.1038/s41598-018-19412-z
- Syeda, F., Holmes, A. P., Yu, T. Y., Tull, S., Kuhlmann, S. M., Pavlovic, D., et al. (2016). PITX2 modulates atrial membrane potential and the antiarrhythmic effects of sodium-channel blockers. *J. Am. Coll. Cardiol.* 68, 1881–1894. doi: 10.1016/j.jacc.2016.07.766
- Vogt, C. C., Bruegmann, T., Malan, D., Ottersbach, A., Roell, W., Fleischmann, B. K., et al. (2015). Systemic gene transfer enables optogenetic pacing of mouse hearts. *Cardiovasc. Res.* 106, 338–343. doi: 10.1093/cvr/cvv004
- Wang, K., Lee, P., Mirams, G. R., Sarathchandra, P., Borg, T. K., Gavaghan, D. J., et al. (2015). Cardiac tissue slices: preparation, handling, and successful optical mapping. *Am. J. Physiol. Heart Circ. Physiol.* 308, H1112–H1125. doi: 10.1152/ajpheart.00556.2014
- Wang, Y., Lin, W. K., Crawford, W., Ni, H., Bolton, E. L., Khan, H., et al. (2017). Optogenetic control of heart rhythm by selective stimulation of cardiomyocytes derived from Pnmt + cells in Murine heart. *Sci. Rep.* 7:40687. doi: 10.1038/srep40687
- Watanabe, M., Feola, I., Majumder, R., Jangsangthong, W., Teplinen, A. S., Ypey, D. L., et al. (2017). Optogenetic manipulation of anatomical re-entry by light-guided generation of a reversible local conduction block. *Cardiovasc. Res.* 113, 354–366. doi: 10.1093/cvr/cvx003
- Wen, Q., Gandhi, K., Capel, R. A., Hao, G., O'Shea, C., Neagu, G., et al. (2018). Transverse cardiac slicing and optical imaging for analysis of transmural gradients in membrane potential and Ca²⁺ transients in murine heart. *J. Physiol.* 596, 3951–3965. doi: 10.1113/jp276239
- Wengrowski, A. M., Wang, X., Tapa, S., Posnack, N. G., Mendelowitz, D., and Kay, M. W. (2015). Optogenetic release of norepinephrine from cardiac sympathetic neurons alters mechanical and electrical function. *Cardiovasc. Res.* 105, 143–150. doi: 10.1093/cvr/cvu258
- Wietek, J., Wiegert, J. S., Adeishvili, N., Schneider, F., Watanabe, H., Tsunoda, S. P., et al. (2014). Conversion of channelrhodopsin into a light-gated chloride channel. *Science* 344, 409–412. doi: 10.1126/science.1249375
- Williams, J. C., and Entcheva, E. (2015). Optogenetic versus electrical stimulation of human cardiomyocytes: modeling insights. *Biophys. J.* 108, 1934–1945. doi: 10.1016/j.bpj.2015.03.032
- Winter, J., Bishop, M., Wilder, C., O'Shea, C., Pavlovic, D., and Shattock, M. J. (2018). Sympathetic nervous regulation of cardiac alternans in the intact heart. *Front. Physiol.* 9:16. doi: 10.3389/fphys.2018.00016
- Xu, L., Gutbrod, S. R., Bonifas, A. P., Su, Y., Sulkin, M. S., Lu, N., et al. (2014). 3D multifunctional integumentary membranes for spatiotemporal cardiac measurements and stimulation across the entire epicardium. *Nat. Commun.* 5:3329. doi: 10.1038/ncomms4329
- Yu, J., Chen, K., Lucero, R. V., Ambrosi, C. M., and Entcheva, E. (2015). Cardiac optogenetics: enhancement by all-trans-retinal. *Sci. Rep.* 5:16542. doi: 10.1038/srep16542
- Yu, T. Y., Dehghani, H., Brain, K. L., Syeda, F., Holmes, A. P., Kirchhof, P., et al. (2017). Optical mapping design for murine atrial electrophysiology. *Comput. Methods Biomech. Biomed. Eng. Imaging Vis.* 5, 368–378. doi: 10.1080/21681163.2015.1081079
- Yu, T. Y., Syeda, F., Holmes, A. P., Osborne, B., Dehghani, H., Brain, K. L., et al. (2014). An automated system using spatial oversampling for optical mapping in murine atria. Development and validation with monophasic and transmembrane action potentials. *Prog. Biophys. Mol. Biol.* 115, 340–348. doi: 10.1016/j.pbiomolbio.2014.07.012
- Zaglia, T., Pianca, N., Borile, G., Da Broi, F., Richter, C., Campione, M., et al. (2015). Optogenetic determination of the myocardial requirements for extrasystoles by cell type-specific targeting of ChannelRhodopsin-2. *Proc. Natl. Acad. Sci. U.S.A.* 112, E4495–E4504. doi: 10.1073/pnas.1509380112
- Zhu, Y. C., Uradu, H., Majeed, Z. R., and Cooper, R. L. (2016). Optogenetic stimulation of *Drosophila* heart rate at different temperatures and Ca²⁺ concentrations. *Physiol. Rep.* 4:e12695. doi: 10.14814/phy2.12695

Conflict of Interest Statement: The authors declare that the research was conducted in the absence of any commercial or financial relationships that could be construed as a potential conflict of interest.

Copyright © 2019 O'Shea, Holmes, Winter, Correia, Ou, Dong, He, Kirchhof, Fabritz, Rajpoot and Pavlovic. This is an open-access article distributed under the terms of the Creative Commons Attribution License (CC BY). The use, distribution or reproduction in other forums is permitted, provided the original author(s) and the copyright owner(s) are credited and that the original publication in this journal is cited, in accordance with accepted academic practice. No use, distribution or reproduction is permitted which does not comply with these terms.

4.2 A Protocol for Dual Calcium-Voltage Optical Mapping in Murine Sinoatrial Preparation With Optogenetic Pacing

Publication 3. This research was originally published in *Frontiers in Physiology*.

A protocol for dual calcium-voltage optical mapping in murine sinoatrial preparation with optogenetic pacing. R Dong*, R Mu-u-min*, A Reith*, **C O'Shea***, S C He, K Duan, K Kou. X Tan, D Pavlovic, X Ou, M Lei. *Front. Physiol.* 10:954, 1-11, 2019. *These authors share first authorship

Author contributions in publication 3

I, alongside Alastair Reith (University of Oxford, UK), conducted all data analysis presented using the ElectroMap software (Chapter 3) and helped to write the manuscript. Experiments described were conducted by Ruirui Dong (Southwest Medical University, China), Alastair Reith and Razik Mu-u-min (University of Oxford, UK), and not by myself.



A Protocol for Dual Calcium-Voltage Optical Mapping in Murine Sinoatrial Preparation With Optogenetic Pacing

Ruirui Dong^{1†}, Razik Mu-u-min^{2†}, Alastair J. M. Reith^{2†}, Christopher O'Shea^{3†}, Shicheng He¹, Kaizhong Duan², Kun Kou¹, Alexander Grassam-Rowe², Xiaoqiu Tan¹, Davor Pavlovic^{3‡}, Xianhong Ou^{1*‡} and Ming Lei^{1,2*‡}

¹Key Laboratory of Medical Electrophysiology of Ministry of Education and Medical Electrophysiological Key Laboratory of Sichuan Province, Institute of Cardiovascular Research, Southwest Medical University, Luzhou, China, ²Department of Pharmacology, University of Oxford, Oxford, United Kingdom, ³Institute for Cardiovascular Sciences, University of Birmingham, Birmingham, United Kingdom

OPEN ACCESS

Edited by:

Bas J. Boukens,
University of Amsterdam,
Netherlands

Reviewed by:

Robert Alan Rose,
University of Calgary, Canada
Vincent Portero,
Academic Medical Center,
Netherlands

*Correspondence:

Xianhong Ou
oxh8081@swmu.edu.cn
Ming Lei
ming.lei@pharm.ox.ac.uk

[†]Joint first authors

[‡]Joint senior authors

Specialty section:

This article was submitted to
Cardiac Electrophysiology,
a section of the journal
Frontiers in Physiology

Received: 15 December 2018

Accepted: 09 July 2019

Published: 06 August 2019

Citation:

Dong R, Mu-u-min R, Reith AJM, O'Shea C, He S, Duan K, Kou K, Grassam-Rowe A, Tan X, Pavlovic D, Ou X and Lei M (2019) A Protocol for Dual Calcium-Voltage Optical Mapping in Murine Sinoatrial Preparation With Optogenetic Pacing. *Front. Physiol.* 10:954. doi: 10.3389/fphys.2019.00954

Among the animal models for studying the molecular basis of atrial and sinoatrial node (SAN) biology and disease, the mouse is a widely used species due to its feasibility for genetic modifications in genes encoding ion channels or calcium handling and signaling proteins in the heart. It is therefore highly valuable to develop robust methodologies for studying SAN and atrial electrophysiological function in this species. Here, we describe a protocol for performing dual calcium-voltage optical mapping on mouse sinoatrial preparation (SAP), in combination with an optogenetic approach, for studying SAP membrane potential, intracellular Ca^{2+} transients, and pacemaker activity. The protocol includes the details for preparing the intact SAP, robust tissue dual-dye loading, light-programmed pacing, and high-resolution optical mapping. Our protocol provides an example of use of the combination of optogenetic and optical mapping techniques for investigating SAP membrane potential and intracellular Ca^{2+} transients and pacemaker activity with high temporal and spatial resolution in specific cardiac tissues. Thus, our protocol provides a useful tool for studying SAP physiology and pathophysiology in mice.

Keywords: sinoatrial preparation, optogenetic pacing, optical mapping, murine heart, Ca^{2+} transient

INTRODUCTION

The heartbeat begins in the sinoatrial node (SAN) arising in a subset of nodal cells that display a spontaneous diastolic depolarization (Bleeker et al., 1980). Unique to such automaticity of the SAN, pacemaker cells possess “membrane clock” contributions by several membrane currents including the funny current, I_f , carried by hyperpolarization-activated cyclic nucleotide-gated (HCN) channels. I_f is initiated specifically at the initial phase of the diastolic depolarization, following the deactivation of outward delayed rectifier K^+ current, and triggering the activation of inward currents. Inward currents include Na^+ -dependent background current; the T- and L-type Ca^{2+} currents, I_{CaT} and I_{CaL} ; and possibly, sustained inward current, I_{st} (Lei et al., 2018). However, more recently, intracellular signaling involving the sarcoplasmic reticulum (SR) Ca^{2+} stores and the cellular cAMP levels and consequent phosphorylation of their signaling proteins have also been implicated in a “ Ca^{2+} clock” contributing to diastolic depolarization (Lei et al., 2018). Whereby, spontaneous RyR2 -mediated Ca^{2+} release may enhance electrogenic effects of the Na^+ - Ca^{2+} exchanger

in late diastolic depolarization (Lei et al., 2018). These SR calcium release events may be triggered by calcium-induced calcium release following the activation of $\text{Ca}_{v1.3}$ calcium channels (Torrente et al., 2016). The relative importance of both the “membrane clock” and “ Ca^{2+} clock” in pacemaker function remains controversial.

On the other hand, sinus node dysfunction (SND) associated with abnormal impulse formation or propagation in the SAN affects ≈ 1 in 600 cardiac patients aged >65 years and is responsible for $\approx 50\%$ of the 1 million permanent pacemaker implants per year worldwide (de Marneffe et al., 1993). Although SND occurs most commonly in elderly patients in the absence of clinically apparent accompanying cardiac disease (de Marneffe et al., 1993), its pathogenesis is unclear. The development of novel pharmacological therapies to cure these patients relies on the thorough understanding of both normal physiology and pathophysiology of the SAN and atria.

Among the animal models for studying the basic molecular mechanisms of the SAN and atrial biology and disease, mice are widely used due to their feasibility for modifications in the expression of different genes that encode ion channels or calcium handling proteins. It is therefore highly valuable to develop robust methodologies and techniques for studying SAN and atrial electrophysiological properties.

Recent advances in the technique of optogenetics provide an unprecedented opportunity for defining specific cell-type function in a highly complex multicellular system. The technique has enabled control over the activity of one specific cell type while leaving others unaltered, with high temporal resolution and cellular precision. Since the first demonstrations of utility in mammalian neurons in 2005 (Boyden et al., 2005), optogenetics has spurred immense research activity in neuroscience and has extended to the cardiac field over the past few years (Entcheva, 2013; Nussinovitch and Gepstein, 2015; Boyle et al., 2018). We recently deployed a cell-type specific optogenetic approach to study the properties of Pnmt^+ cell-derived cardiomyocytes in the murine heart (Wang et al., 2017). Additionally, optical mapping using fluorescent dyes provides exciting opportunities for high spatio-temporal study of cellular electrophysiological events, including Ca^{2+} dynamics of the heart (Wang et al., 2017; Wen et al., 2018). The combination of these two technologies therefore allows development of unprecedented platforms for studying physiological events (e.g., voltage and Ca^{2+} signals) in a selective manner at high spatio-temporal resolution (O'Shea et al., 2019b).

In this manuscript, we describe a detailed protocol for the use of optogenetic and optical mapping techniques for investigating membrane potential and intracellular Ca^{2+} transients and pacemaker activity with high temporal and spatial resolution in sinoatrial preparations (SAPs). The protocol can be a powerful tool for studying SAP physiology and pathophysiology using the mouse as a model system.

METHODS AND MATERIALS

Animals

Pnmt -cre mice used in this study are as described previously (Wang et al., 2017). Animals used were <6 months old.

Pnmt -cre/ChR2 mice exhibit cell-type specific expression of ChR2 by crossing B6.Cg-Gt (*ROSA*)26Sor^{tm27.1(CAG-COP4H134R/tdTomato)Hze/J} strain (Stock no. 012567, Jackson Labs) with a Cre transgenic strain under the control of a *Pnmt* promoter (Wang et al., 2017). Channelrhodopsin 2 (ChR2) was specifically introduced into murine cells expressing the *Phenylethanolamine n-methyltransferase* (*Pnmt*) gene, which encodes for the enzyme responsible for conversion of noradrenaline to adrenaline. The murine model led to the identification of a distinctive class of Pnmt^+ cell-derived neuroendocrine cells and their descendants (i.e., Pnmt^+ cell-derived cardiomyocytes) within the heart (Wang et al., 2017).

All procedures have been approved by Institutional Animals Ethics Committees at Southwest Medical University, Luzhou, China or Department of Pharmacology at University of Oxford, UK and the national guidelines under which the institution operates. All mice used in this study were maintained in a pathogen-free facility at Southwest Medical University or University of Oxford. Mice were given *ad libitum* access to food and water. The authors confirm that they have taken all steps to minimize the animals' pain and suffering.

Materials and Equipment

Table 1 shows the details of materials and buffers.

Figure 1 shows the optical imaging system for light stimulation of ChR2 light-sensitive channels and optical recording.

The tissues were paced through the activation of ChR2 light-sensitive channels. This was achieved by the delivery of 470 nm blue light pulses (13–14 ms pulse width) generated by OptoFlash (Cairn Research, Faversham, UK). Pulses were triggered by a 1,401 digitizer and Spike 2 software (Cambridge Electronic Design). Approximate blue light intensity was measured with a 818-ST2 Wand Detector connected to a 843-R power meter (both Newport Corporation, CA, USA), and we estimate an average irradiance in our experiments of 0.1–0.3 mW/mm² based on an approximate distance of 1–2 cm between Sylgard and liquid light guide (Oriel instruments Model No. 77525).

TABLE 1 | Details of materials and buffers.

Chemical and catalogue reference	Supplier
NaCl (SLBS2340V)	Sigma-Aldrich, St Louis, MO, USA
NaHCO_3 (SLBX3605)	Sigma-Aldrich
NaH_2PO_4 (BCBW9042)	Sigma-Aldrich
KCl (SLBS5003)	Sigma-Aldrich
MgCl_2 (BCBS6841V)	Sigma-Aldrich
CaCl_2 (SLBK1794V)	Sigma-Aldrich
Glucose (SLBT4811V)	Sigma-Aldrich
HEPES (W1122DO10)	Sangon biological Shanghai, China
2,3-butanedione monoxime (BDM) (29297)	Sigma-Aldrich
Blebbistatin (SLBV5564)	Tocris Bioscience Minneapolis, MN, USA
Voltage-sensitive dye RH237 (1971387)	Thermo Fisher Scientific, Waltham, MA, USA
Calcium indicator Rhod-2 AM (1890519)	Invitrogen, Carlsbad, CA, USA
Dimethyl sulfoxide (DMSO) (RNBT7442)	Sigma-Aldrich
Heparin Sodium (H51021209)	Chengdu Haitong Pharmaceutical Co. Ltd. Chengdu, China
Avertin (2,2,2-tribromoethanol)	Sigma-Aldrich Poole, Dorset, UK
Pluronic F127 (1899021)	Invitrogen, Carlsbad, CA, USA

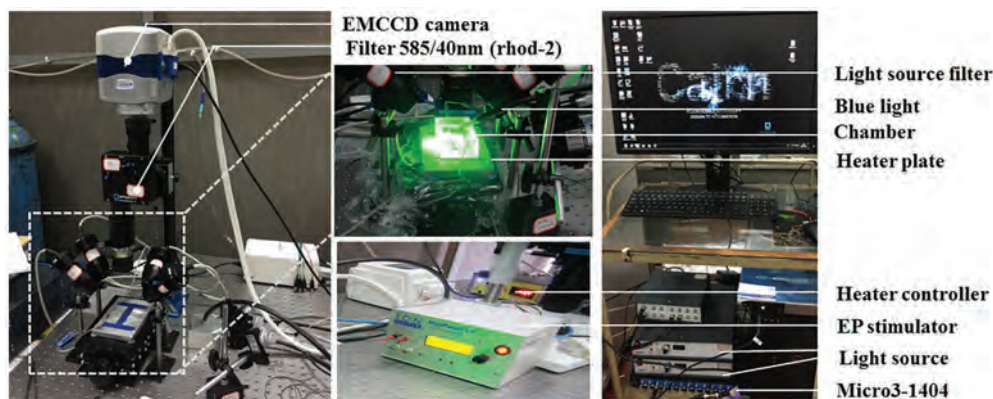


FIGURE 1 | The optical imaging system. Two green (a peak wavelength of 530 nm) and two red (a peak wavelength of 627 nm) LED lights (Cairn Research, Faversham, Kent, UK) were placed around the chamber so as to uniformly illuminate the SAP. The green LEDs were fitted with excitation bandpass filters (S555/25X, Chroma Technology GmbH, Germany), and the red LEDs were fitted with excitation bandpass filters (HQ640/50, Chroma Technology GmbH, Germany) to efficiently select the best excitation wavelength range for Rhod-2 AM and Di-4-ANBDQPPQ, respectively. A multi-bandpass emission filter (ET595/50 + 700LP, Chroma Technology GmbH, Germany) was placed in front of the camera lens to avoid bleed-through of the excitation light and to selectively let the fluorescence emission pass through. A multi-stream light switcher (Cairn Research, Faversham, Kent, UK) was set up to automatically switch between the red and green LED lights in accordance with the frame rate of the camera. Signal recording using this setup is in such a way that one frame data recorded will have only the red light turned on (thereby recording voltage signal alone) and the next frame data recorded will have only the green light turned on (thereby recording CaT signal alone), and the process is repeated until the desired number of frames are recorded.

Buffer Compositions

Physiological Salt Solution

Freshly prepared physiological salt solution (PSS) containing in mM: NaCl 119, NaHCO₃ 25, NaH₂PO₄ 1.0, KCl 4.7, MgCl₂ 1.2, CaCl₂ 1.35, and glucose 10; equilibrated with 95% O₂/5% CO₂ at 37°C, pH = 7.35.

Dye Loading Solution

Calcium indicator Rhod-2 AM (Invitrogen, Carlsbad, CA, USA) was dissolved in dimethyl sulfoxide (DMSO, Sigma-Aldrich, St. Louis, MO, USA) to prepare a stock concentration of 10 mg/ml (8.9 mM). The voltage indicator stock was prepared by dissolving Di-4-ANBDQPPQ (University of Connecticut Health Center) in ethanol to obtain a stock concentration of 29 mM. To avoid repeated freezing and thawing, both stocks were stored in 50 µl aliquots at -20°C. For working concentrations of Rhod-2 AM dye loading solution, 15 µl Rhod-2 AM stock solution was mixed with 15 µl Pluronic F-127 (20% solution in DMSO, Invitrogen, Carlsbad, CA, USA) and then dissolved in 15 ml PSS (10 µM final concentration). Similarly, 5.2 µl of Di-4-ANBDQPPQ stock was mixed with 15 µl Pluronic F-127 and then dissolved in 15 ml PSS to form a working concentration of Di-4-ANBDQPPQ dye loading solution (10 µM final concentration). The working dye loading solutions were prepared on the day of the experiment.

Blebbistatin Physiological Salt Solution

Excitation-contraction uncoupler blebbistatin (Invitrogen, Carlsbad, CA, USA) was dissolved in DMSO (Sigma-Aldrich, St. Louis, MO, USA) to make up 10 mM stock solution. To avoid repeated freezing and thawing, aliquots of 15 µl were

stored at -20°C. A 10 µl of 10 mM stock blebbistatin solution was added to 15 ml PSS to make blebbistatin PSS solution (10 µM final concentration).

Preparation and Equipment

1. Dissection set-up includes stereomicroscope, dissection chamber filled with Sylgard gel, oxygenation device, LED light source, and surgical instruments.
2. The optical mapping system was set up as detailed below:

A custom-designed system equipped with an EMCCD camera (Evolve 128, Photometrics, Tucson, AZ, USA) was used (see **Figure 1**). Two green (to excite Ca²⁺ sensitive dye Rhod-2 AM; a peak wavelength of 530 nm) and two red (to excite the voltage sensitive dye Di-4-ANBDQPPQ; a peak wavelength of 627 nm) LED lights (Cairn Research, Faversham, UK) were placed around the imaging chamber so as to uniformly illuminate the SAP. The green LEDs (peak wavelength = 530 nm) were fitted with excitation bandpass filters (S555/25X, Chroma Technology GmbH, Germany), and the red LEDs (peak wavelength = 627 nm) were fitted with excitation bandpass filters (HQ640/50, Chroma Technology GmbH, Germany) to efficiently select optimal excitation wavelength range for Rhod-2 AM and Di-4-ANBDQPPQ, respectively. A multi-bandpass emission filter (ET595/50 + 700LP, Chroma Technology GmbH, Germany) was placed in front of the camera lens to avoid bleed-through of the excitation light and to selectively let the fluorescence emission to pass through. CaT (calcium transient) and transmembrane potential (V_m) measurements were taken at high resolution (128 × 128 pixels; pixel size 66 × 66 µm) at a rate of 520 frames/s.

PROTOCOL

Harvest the Mouse Heart and Prepare the Sinoatrial Preparation (30 min)

The steps for preparation of the SAP are outlined in **Figure 2** and as described previously (Liu et al., 2007; Hao et al., 2011; Sharpe et al., 2016). The details are as follows:

1. Non-recovery terminal general anesthesia was induced by injection of an overdose of 1.2% Avertin solution (0.5–0.8 ml i.p., 2,2,2-tribromoethanol, Sigma-Aldrich, Poole, Dorset, UK), followed by intraperitoneal injection with heparin (200 units).
2. Following sacrifice *via* cervical dislocation, the heart was rapidly excised and placed in warmed (37°C) and oxygenated (95% O₂ + 5% CO₂ gas) PSS solution in a dissection chamber.
3. The heart was gently pressed with the tips of fingers to push the blood out of heart. Fresh oxygenated PSS was then added for further dissection.
4. SAP containing two atria and the SAN region was dissected after clearing off the lung, thymus, ventricles, and connective tissues (**Figure 2B**).
5. The right atrium was opened from atrioventricular (AV) junction to expose the intercaval region containing the SAN, following which left atrium was opened to expose the left atrial endocardium. As the pacemaker cells are widely distributed throughout the entire region located between the superior (SVC) and inferior vena cava (IVC) and between the crista terminalis and intra-atrial septum (Glukhov et al., 2010), the SAP contains the SAN and the two atria intact.
6. The SAP was pinned onto a small rectangular piece of Sylgard gel by using fine insect pins. All dissection steps were performed in a dissection chamber with oxygenated PSS solution under a stereomicroscope.

Dual Dye Loading of the Sinoatrial Preparation (25 min)

7. A 50 ml falcon tube was filled with 15 ml of the Rhod-2 AM dye loading solution.
8. The Sylgard gel (with SAP attached) was then dropped into the falcon tube.
9. The SAP-containing falcon tube was placed in a 36°C water bath. The solution was oxygenated constantly by gently bubbling with 95% O₂/5% CO₂ (Note: heavy bubbling can lead to the formation of foam due to the presence of Pluronic F-127 in the solution. This can lead to the suboptimal dye loading). The SAP was incubated in the dye loading solution for 15 min.
10. Dual dye loading of the SAP was performed by incubating the SAP in Rhod-2 AM dye loading solution as detailed above (points 7–9), following which the Sylgard gel with SAP attached was transferred into a new 50 ml falcon tube containing 10 μM Di-4-ANBDQPP dye loading solution. Incubation with Di-4-ANBDQPP was performed for 10 min at 36°C and constantly bubbled with 95% O₂/5% CO₂.

Optical Mapping (30 min)

11. The imaging chamber was filled with 15 ml of blebbistatin PSS solution and was placed directly under the camera. The recording chamber was heated up to 36°C by a heating plate.
12. The Sylgard (with SAP attached) was removed from the falcon tube and pinned down in the imaging chamber. The sample was placed between the two field-stimulation electrodes. (Note: Removing the SAP from the Sylgard and pinning down directly in the chamber cause further damage to the SAP. Therefore, pinning down the Sylgard with the intact

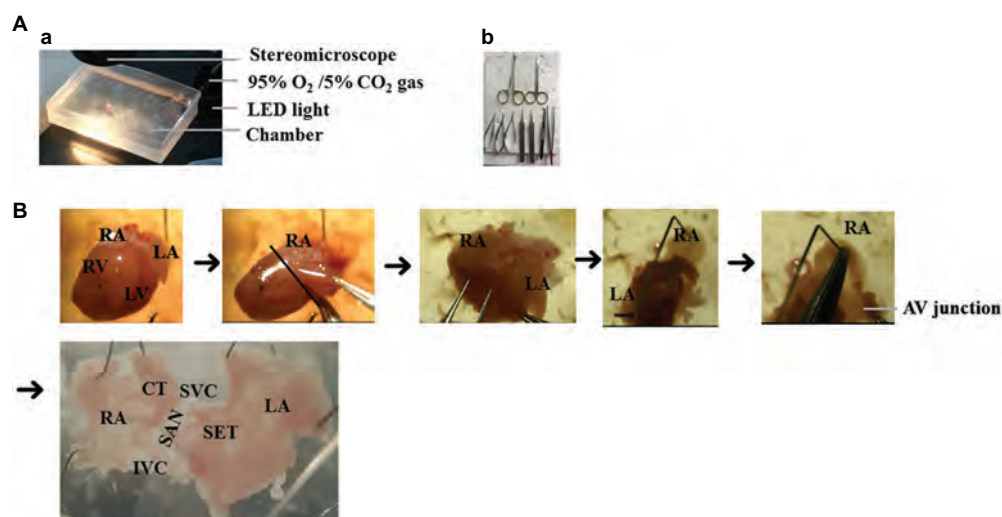
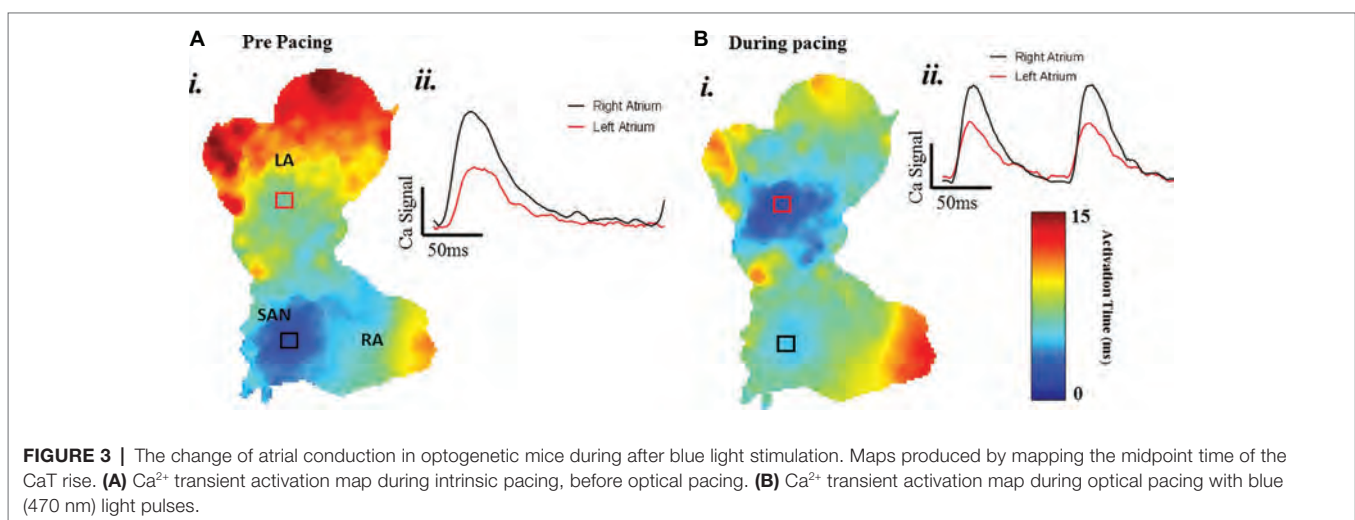


FIGURE 2 | The isolation of mouse SAP. **(A)** The setup of dissection. **(a)** The dissection was performed under the stereomicroscope and oxygenated PSS solution. **(b)** Surgical instruments. **(B)** The preparation of SAP. RA, right atrium; LA, left atrium; RV, right ventricle; LV, left ventricle; SAN, sinoatrial node; AV junction, atrioventricular junction, SET = septum, SVC = superior vena cava, IVC = inferior vena cava, CT = crista terminalis.

- tissue is recommended). The blebbistatin PSS solution was bubbled in the imaging chamber with 95% O₂/5% CO₂ gas.
13. Imaging was performed after cessation of motion by blebbistatin. Imaging used the EMCCD camera controlled by the acquisition software Metamorph (Molecular Devices). During image recordings, the excitation lights were turned on, and bubbling was temporarily stopped (to avoid distortion of the signals due to bubbles and motion of the solution). Since Pnmt⁺ cell-derived cardiomyocytes (PdCMs) express channelrhodopsin-2 (ChR2), they can be excited by exposure to 470 nm blue light. The stimulation protocol was then run, and baseline calcium transient or action potential recordings were taken. Recordings were taken again after stimulating the left atrium using blue light (pacing intervals: 150–160 ms, pulse duration: 13–14 ms, intensity: 1,992 mA). The frame rate of these recordings was 0.52 kHz.
 14. For dual dye imaging, a multistream light switcher (Cairn Research, Faversham, Kent, UK) was set up to automatically switch between the red (627 nm) and green (530 nm) LED lights according to the frame rate of the camera. Signal recording using this setup was performed, so that one frame of the data was recorded under red light illumination (thereby recording V_m signal alone), and the next frame was recorded under green light illumination (thereby recording CaT signal alone) and so forth until the desired number of frames was recorded. This resulted in an interlaced signal containing alternate frames of CaT and V_m signals. The interlaced signal was separated into CaT and voltage signal using ImageJ and saved as separate files. Due to the signals being interposed, the frame rate recording was 0.26 kHz.
 15. The saved image files were loaded, processed, and analyzed using the optical mapping analysis software ElectroMap (developed by Dr. Pavlovic's group, <https://github.com/CXO531/ElectroMap>; O'Shea et al., 2019a).
 16. Images were pre-processed by applying a 4×4 pixel Gaussian spatial filter (standard deviation = 1.5), a Top-Hat baseline correction (kernel size = 100 ms), and a third order Savitzky-Golay temporal filter. A window size of 40 ms before transient peak to 100 ms after transient peak was used. Action potential duration (APD) and CaT duration (CaD) were measured at the desired repolarization/decay percentage at each pixel across the tissue, as measured from time of maximum upstroke velocity (maximum dF/dt).
 17. For assessment of local conduction velocities, activation maps were generated using time of depolarization midpoint. Conduction velocity across the SAP was then quantified using a multi-vector polynomial method (Bayly et al., 1998) with a local window size of 5×5 pixels.
 18. To further assess conduction across the entire SAP, we used activation curve analysis, where the percentage of tissue activated was plotted as a function of time (O'Shea et al., 2019a).

Representative Results

A typical example of an SAP Ca²⁺ transient activation map reconstructed from spontaneous sinus rhythmic Ca²⁺ transients (by Rhod-2 AM) recorded with the optical mapping system is shown in **Figure 3A** for a SAP. The early activation point is located within the intercaval region near to where the SAN is located. However, as shown in **Figure 3B**, the calcium activation pattern and atrial conduction changed after stimulating with blue light (interval: 150 ms; duration: 13 ms; intensity: 1,992 mA; pulses per train: 50). The leading pacemaker site was shifted to the location of left atrium, suggesting that PdCMs were activated earlier than the SAN pacemaker cells. This is consistent with our previous report that PdCM cells predominantly localized to the left atrium and left ventricle, and the heart rate was controlled by stimulating PdCMs selectively with blue light (Wang et al., 2017). We hypothesize that PdCM cells overexpressing ChR2 may be a viable site for spatially-targeted optical pacing when sinus node pacemaker cells are dysfunctional. Further



investigation is required. **Figure 4** shows representative V_m and CaT maps and voltage and calcium traces from different regions of the SAP, illustrating the robustness of this preparation for murine research. We monitored the “rundown” of the V_m and CaT signals for up to 4 h – the average signal “rundown” is less than 25%. Our experiment usually finished within 3 h from the beginning of Langendorff perfusion of the heart. We again observe augmentation of the activation pattern induced by optical pacing, shown by both the voltage (**Figure 4**, upper panel) and calcium (**Figure 4**, lower panel) activation maps. Activation maps were produced by mapping the midpoint time of the AP/CaT rise.

We found that optogenetic pacing of a SAP can shift the activation point to the left, creating a new leading pacemaker site or “neonode.” Activation patterns in the SAP were plotted using ElectroMap (O’Shea et al., 2019a), with the midpoint of the upstroke of the calcium transient used as a pixel-by-pixel readout of tissue activation. The earliest-activating pixel—discarding outliers—was designated the activation point for that tissue. The earliest activation point before pacing was always in the nodal region. Optogenetic pacing of PdCMs can move this activation point to the left (**Figure 5**), establishing a new leading pacemaker site toward the left atrium. This change in the location of the leading pacemaker is reversible upon cessation of pacing (**Figures 5A,E**). Left shift of the leading pacemaker occurred in four of seven SAPs (**Figure 5D**). One leftward

deviation appears more upward relative to the SVC-IVC axis—this is due to contortion of the tissue. Although no leading pacemaker shift occurred in three SAPs, all seven SAPs were successfully paced by blue light: with a decrease in mean cycle length from 264.3 ± 42.7 ms before optogenetic pacing to 159.2 ± 1.4 ms during ($p < 0.02$). Mean cycle length after pacing was 281.9 ± 48.9 ms—not significantly different from before ($p = 0.63$). Therefore, we can always successfully and reversibly pace PdCMs using selective ChR2 overexpression. The variability in pacemaker shift observed (**Figure 5D**) is consistent with the variable distribution of murine PdCMs across both the SAN region and the left atrium (Ni et al., 2017; Wang et al., 2017). In summary, we report the possibility of using optogenetic pacing of PdCMs to establish novel left-shifted leading pacemaker sites in the murine heart.

To study the effects of optogenetic pacing on overall conduction, we utilized activation curve analysis where the percentage of tissue activated is plotted as a function of time (O’Shea et al., 2019a). Optogenetic pacing of PdCMs augments conduction in the SAP—producing a left shift of the activation curve (**Figure 6A**). This is most noticeable in the first few milliseconds of tissue activation (**Figure 6A**, inset). During optogenetic pacing, the rate of tissue activation is initially very rapid (**Figure 6B**, inset), otherwise, there are no major alterations to tissue activation rate (**Figure 6B**). Optogenetic pacing reduces the time to 5% tissue activation from 1.59 ± 0.24 to 0.88 ± 0.17 ms ($p = 0.03$),

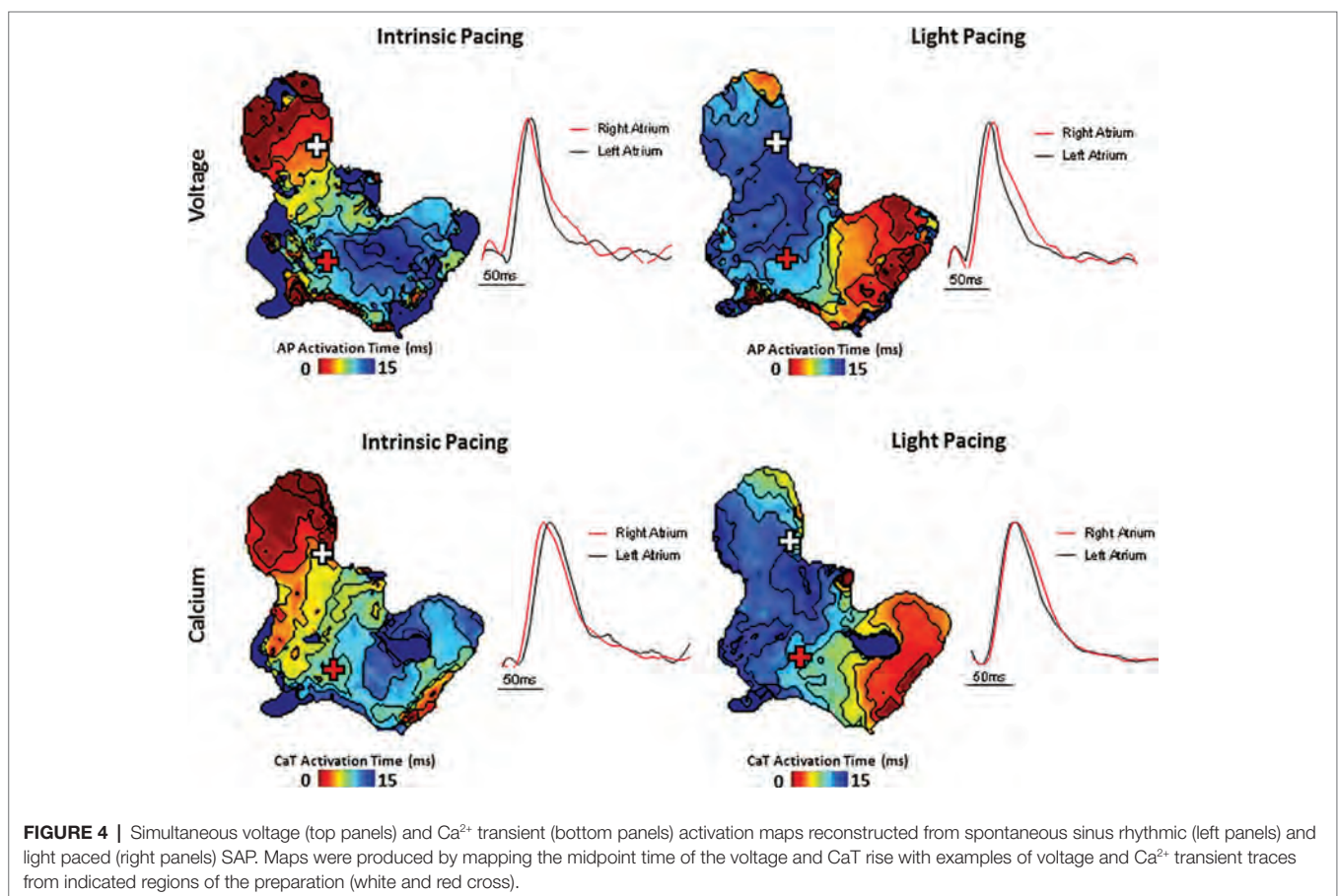


FIGURE 4 | Simultaneous voltage (top panels) and Ca^{2+} transient (bottom panels) activation maps reconstructed from spontaneous sinus rhythmic (left panels) and light paced (right panels) SAP. Maps were produced by mapping the midpoint time of the voltage and CaT rise with examples of voltage and Ca^{2+} transient traces from indicated regions of the preparation (white and red cross).

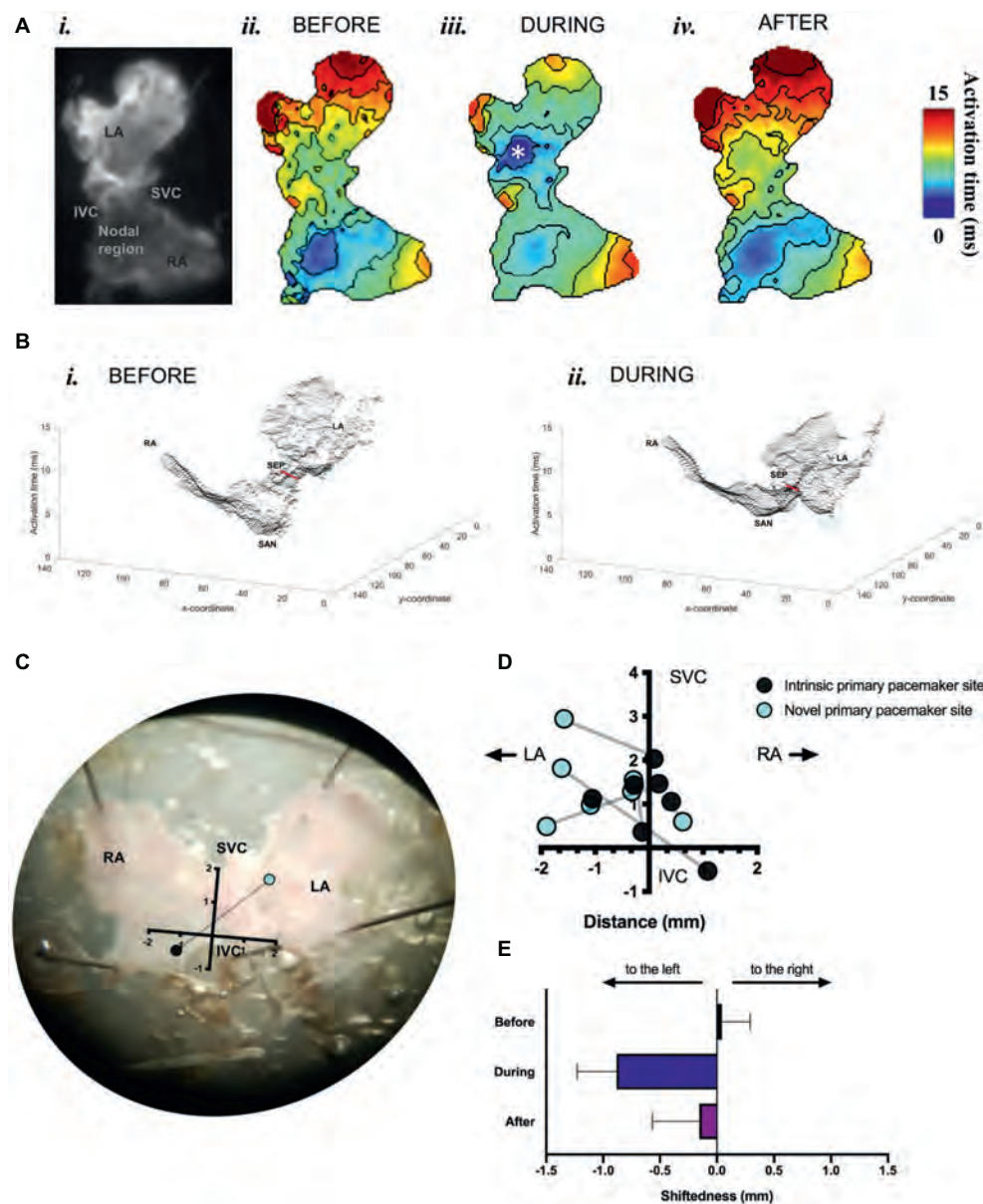


FIGURE 5 | Mapping of activation in SAPs under sinus rhythm and under optogenetic pacing. **(A)** (i) Representative SAP—camera view. (ii) Activation map for this SAP before optogenetic pacing. (iii) Activation map during pacing (note formation of "neonode", white asterisk). (iv) Activation map after pacing. Activation maps are calculated from Ca^{2+} transients. Fifty pacing spikes given, at 6.67 Hz. Contours drawn at 1/frame rate of the EMCCD. Scale bar, right. **(B)** 3-D graphical rendering of activation maps (i) before pacing, (ii) during pacing. SVC-IVC axis in red. Activation time on z-axis. **(C)** Representative SAP—microscope view. Pacemaker shift overlaid. SVC-IVC axis shown. Distances in mm. **(D)** SVC-IVC axis with relative pacemaker shifts plotted (n = 7). **(E)** Mean change in "shiftedness." LA, left atrium; RA, right atrium; SAN, sinoatrial node; SVC, superior vena cava; IVC, inferior vena cava; SEP, septum; NeoN, neonode.

the time to 10% tissue activation from 2.40 ± 0.25 to 1.46 ± 0.26 ms ($p = 0.02$), and the time to 20% tissue activation from 3.91 ± 0.52 to 2.27 ± 0.33 ms ($p = 0.02$) (Figure 6C), but at all points $\geq 30\%$ tissue activation, there is no significant difference in activation time (Figures 6A,B).

We also wanted to explore whether the normal conduction pathways in the tissue remained intact during optogenetic pacing. Using ElectroMap, we computed local conduction velocities using the multi-vector method (Bayly et al., 1998) with a 5×5 -pixel

grid size. The magnitude of conduction velocity vectors (Figure 6D) did not change significantly with optogenetic pacing from 26.9 ± 3.3 before to 28.6 ± 2.5 cm/s during pacing ($p = 0.34$), and there were no major changes in the directionality of conduction vectors either (Figure 6E). In summary, we report the possibility of establishing a novel left-shifted leading pacemaker site, with only minimal, controlled disturbance to normal tissue activation rate, and little or no disturbance to the pathways along which conduction normally propagates.

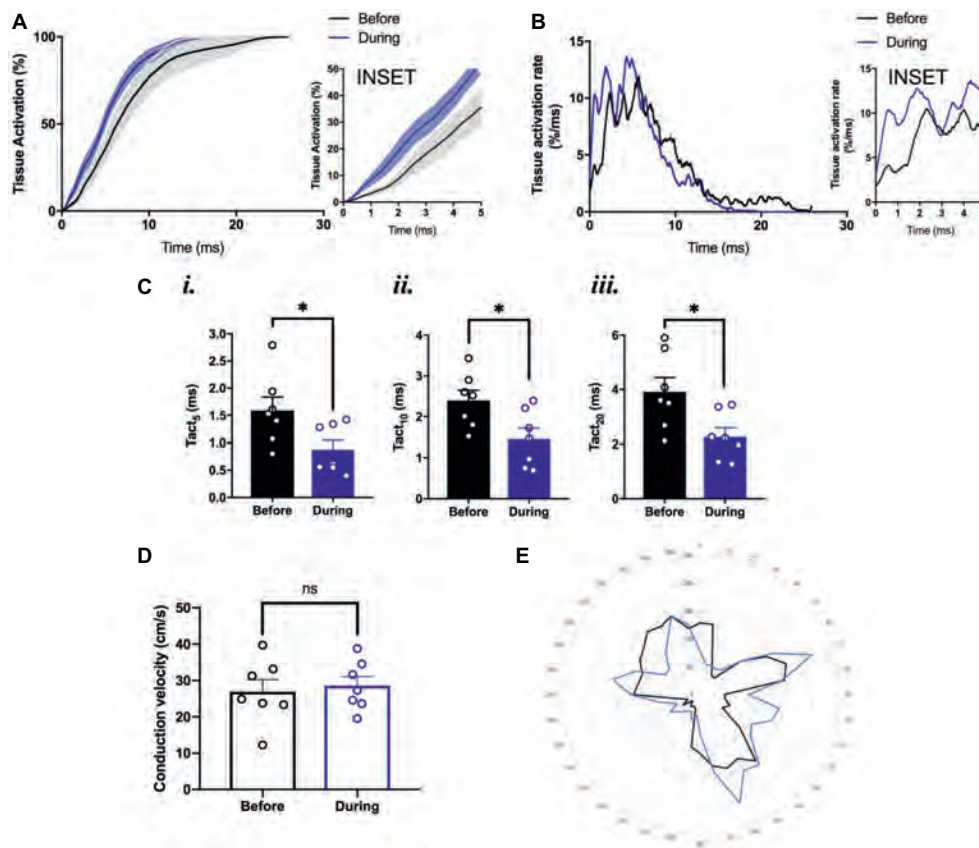


FIGURE 6 | Conduction pattern in the tissue under sinus rhythm and during optogenetic pacing. **(A)** Grouped activation curve showing mean % tissue activated over the time elapsed during a Ca^{2+} transient. SEM denoted by shading. Inset: zoomed section of first 5 ms. **(B)** Rate of change of % tissue activation plotted against time. Inset as above. **(C)** (i) Time to 5% tissue activation. (ii) Time to 10% tissue activation. (iii) Time to 20% tissue activation. **(D)** Mean magnitude of local conduction vectors. **(A–D)** $n = 7$ throughout. **(E)** Representative radar plot, showing local conduction vector directionalities. Angles binned into groups of 10° —so $0^\circ \leq x < 10^\circ$ becomes 5° , $10^\circ \leq x < 20^\circ$ becomes 15° , and so on. Concentric circles represent increasing frequency of vectors at that angle.

We found small alterations to calcium cycling in our tissues, but for the most part, there was no significant change in the characteristics of calcium transient rise time, calcium transient duration to 50% of the decay (CaD50), and calcium transient duration to 75% of the decay (CaD75) with optogenetic pacing. We measured the rise time, calcium transient duration to 50% of the decay (CaD50), and calcium transient duration to 75% of the decay (CaD75) as illustrated in **Figure 7A**. Rise time is a measure of upstroke duration, calculated between 10 and 90% of time to peak, which minimizes analytical uncertainty (Choi and Salama, 2000; Jaimes et al., 2016). We used a mixed-effects model, with Tukey's *post hoc* tests where required, to examine whether there were any significant effects of optogenetic pacing. For rise time, there was a significant overall effect of optogenetic pacing ($p < 0.0001$). *Post hoc* testing revealed that there was no significant effect of pacing on rise time in the right atrium or in the neonodal regions—but in the left atrium, rise time fell from 17.21 ± 0.94 ms before pacing to 15.24 ± 1.14 ms during pacing ($p < 0.002$) and rose again after pacing to 18.60 ± 1.00 ms ($p < 0.05$, during vs. after) and in the nodal region, rise time fell from 17.48 ± 1.03 to 15.24 ± 1.14 ms ($p < 0.03$) and rose again after pacing to 18.44 ± 0.95 ms ($p = 0.02$, during vs. after).

In both regions, there was no significant difference between the before and after conditions (left atrium: $p = 0.39$; nodal region: $p = 0.61$)—so the reduction in rise time with optogenetic pacing is reversible upon cessation of pacing (**Figure 7B**). There was no overall significant effect of optogenetic pacing on either CaD50 ($p = 0.15$) or CaD75 ($p = 0.34$; **Figures 7C,D**). In summary, rise time is shorter in the left atrium and in the SAN region during optogenetic pacing, and this is a reversible change. Otherwise, calcium handling in the murine SAP appears to be only marginally affected.

DISCUSSION

The success in obtaining high quality V_m and Ca^{2+} mapping results in SAPs requires several important technical considerations, including high consumption of oxygen and high sensitivity to temperature and pH of the nodal tissue. Furthermore, the dense arrangement of nodal cells combined with the significant presence of connective tissue makes it hard for a Ca^{2+} dye to reach to the nodal and atrial cells. The critical steps include as follows:

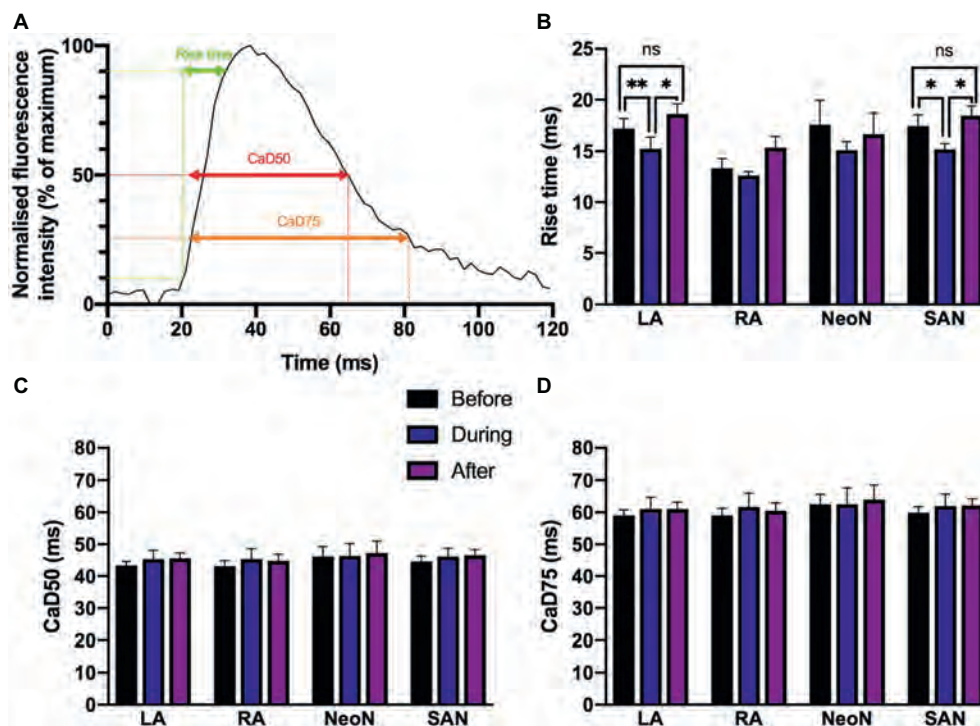


FIGURE 7 | (A) Characteristics of Ca^{2+} transients recorded from different regions under sinus rhythm and optogenetic pacing. Representative Ca^{2+} transient illustrating rise time; CaD50 (Ca^{2+} transient duration to 50% of the decay); and CaD75 (Ca^{2+} transient duration to 75% of the decay). CaD50 and CaD75 are calculated from max. dF/dt (max. upstroke) as detailed in the protocol. **(B)** Mean rise time, before ($n = 7$), during ($n = 7$), and after ($n = 6$) optogenetic pacing. Key at center. Grouping is by region: LA, left atrium; RA, right atrium; NeoN, neonodal region ($n = 4$); SAN, nodal region. **(C)** Mean CaD50 values, no overall significant effect of optogenetic pacing. **(D)** Mean CaD75 values, no overall significant effect of optogenetic pacing.

Tissue Preparation

Intact SAPs were micro-dissected as described previously (Ju et al., 2015). The SAN region was identified from anatomical landmarks, including the superior vena cava, the crista terminalis, and the interatrial septum. The tissue needs to be oxygenated constantly. At this point, temperature is not critical.

Dye Loading

The Ca^{2+} -sensitive dye used to load the SAP tissue was Rhod-2 AM, a dye in the acetoxymethyl ester form. Esterification of the fluorescent molecule (Rhod-2 AM) results in an uncharged molecule that can permeate cell membranes and chelate cytosolic Ca^{2+} . A 100-fold increase in the molecule's fluorescence intensity results from Ca^{2+} chelation (Choi and Salama, 2000). The voltage sensitive dye used was Di-4-ANBDQPPQ, due to its favorable spectral properties for use with Rhod-2 AM. In our experiments, dye loading was carried out by incubating the tissue in a solution consisting of Pluronic F-127 dissolved in DMSO. Pluronic F-127 was incorporated into the dye loading solution to better disperse the dye into the physiological solution. Dye loading was observed to be generally better in younger mice than old, which may be related to connective tissue making up a smaller volume of the node.

The SAP's repetitive contractions may have disrupted dye loading and/or aided the leaking of the dye out from the

tissue, making it a challenge to optimize dye loading conditions. A fluorescent dye that diffuses across the cell membrane well can also exit from the cytoplasm at a high rate. Reagents like probenecid help prevent this to an extent. Combining these with optimized temperatures, timings and oxygen supply are necessary for effective loading of the tissue with dye.

Optical Imaging

During imaging, motion artifacts caused disruption in the measurement of optical signals. Hence, to reduce contraction of the tissue, blebbistatin was used. Blebbistatin is an inhibitor of the adenosine triphosphatases associated with class II isoforms of myosin (Allingham et al., 2005). This compound has been identified as an effective excitation-contraction uncoupler, and previous investigators have used it at several different concentrations (Fedorov et al., 2007). The use of blebbistatin at 10 μM appeared to effectively abolish any motion artifact due to contraction of the SAP without harming SAP.

Pnmt⁺ Cell-Derived Cardiomyocytes (PdCMs) and Biopacemaking Strategies

The advent of cardiac optogenetics has facilitated the identification of a new cardiomyocyte subpopulation in the murine heart, phenylethanolamine-N-methyl transferase Pnmt⁺-derived cardiomyocytes (PdCMs; Wang et al., 2017). Through selective

manipulation of these cells using optogenetics, our study demonstrated how optogenetics can be used to target specific cardiomyocyte subpopulations, overcoming many of the issues associated with traditional electrophysiological techniques. Selectively stimulating PdCMs with rhythmic blue (470 nm) light pulses was sufficient to maintain sinus rhythm in murine atria, supporting previous observations from whole heart studies (Wang et al., 2017). It has also been found previously that the left atrium alone – dissected out – can be paced by light (Wang et al., 2017), but a capacity to optogenetically control the SAP has not been tested before.

The observation that a “neonode” is typically set up toward the left is consistent with previous findings that PdCMs occupy a left-sided distribution in murine heart (Wang et al., 2017). We therefore assessed the effect of pacing on left atrial activation. Optogenetic pacing of PdCMs leads to alterations in the conduction pattern across murine atria. We found (Figure 5) that optogenetic pacing of Pnmt-cre/Ai27D SAPs can often set up new sites of earliest activation (“neonodes”) toward the left of the tissue. Our proof-of-principle studies clearly demonstrate feasibility of optogenetic control of heart rate *via* the specific cell population. Indeed, in four of seven SAPs, we observed “neonode” formation, with the leading pacemaker shifting toward the left atrium. Lack of leftward shift in three of seven preparations may be due to the heterogeneity in cell numbers and clustering of the Pnmt cells in the SAPs, thus altering sink-source properties of the myocardium. While the physiological consequences of the studies presented here (specifically using Pnmt cells) are not immediately clear, application of such approaches is of interest to the community and may lead to important findings on the consequences of the spatial shift in the leading pacemaker.

As recently reviewed by Boyle et al. (2018), initial work in this area assessed possibility to override the intrinsic pacing frequency of a beating heart using optical stimuli. Bruegmann et al. (2010) explored this question in a preclinical model by generating ChR2⁺ transgenic mice. They showed in an open-chest configuration that pulses of light from a focused light source could be used to maintain ventricular activation at rates faster than intrinsic sinus rhythm. Light-induced wavefronts were initiated from different parts of the heart (e.g., atrial or ventricular sites). Remarkably, the authors found that 1:1 capture could be maintained when the illuminated area was small (0.05 mm², ~50 myocytes), suggesting that optogenetic pacing *via* a small population of cells is possible and robust. Several recent studies also provided evidence for the development of optogenetic defibrillating device for termination of tachyarrhythmias (Nyns et al., 2016; Bruegmann et al., 2017). Bruegmann et al. (2017) reported optogenetic termination of atrial tachyarrhythmia in intact hearts from transgenic as well as wild-type mice *ex* and *in vivo*. Thus, they suggested that their report could lay the foundation for the development of implantable devices for pain-free termination of AF. Nyns et al. (2016) demonstrated that forced expression of a light-gated depolarizing ion channel (ReaChR) in the adult rat heart allows contact- and shock-free termination of VTs through brief local illumination of the ventricular surface, i.e., without relying on conventional drugs,

tissue ablation, or electroshocks. Both mono- and polymorphic VTs could be terminated in an effective and repetitive manner by a light-induced electrical current driven by natural electrochemical gradients, providing proof-of-concept for biological arrhythmia termination. Our study also provides proof-of-concept evidence supporting the development of light-based pacing devices targeted to a particular cellular population.

Limitations of the Protocol

There are a number of possible limitations in this protocol including: (1) possibility of injury during the dissection of the preparation; (2) effectiveness of dye loading may vary between preparations, thereby affecting the results; and (3) partial uncoupling (reduction in conductance) due to the use of blebbistatin, which could increase the regional differences in Ca²⁺ dynamics in SAPs.

Conclusions and Future Directions

Here, we have described a detailed protocol for dual optical mapping of murine SAPs with optogenetic pacing. Combination of high-resolution optical imaging with cell-specific optogenetic stimulation allows unique spatial control and study of electrophysiology of the SAP, not possible with traditional direct or field electrode techniques. In the present protocol, we have demonstrated this principle with PdCMs; however, the protocol can be valuable for any mouse models that cell specifically express opsins such as ChR2 within the sinoatrial region of the heart. Therefore, such an approach represents a powerful tool for enhanced electrophysiological understanding of supraventricular physiology and pathophysiology.

Future improvements may focus on exploring dual dye imaging and improved image processing software. Higher resolution and novel optical imaging modalities for 3D optical mapping are also important future directions of optical mapping.

ETHICS STATEMENT

Pnmt-Cre mice used in this study are as described in our previous paper (Wang et al., 2017). Animals used were <6 months old, 20–25 g. All procedures including animal subjects have been approved by Institutional Animals Ethics Committees at Southwest Medical University, Luzhou, China or Department of Pharmacology at University of Oxford and the national guidelines under which the institution operates. All mice used in this study were maintained in a pathogen-free facility at Southwest Medical University or University of Oxford. Mice were given *ad libitum* access to food and water. The authors confirm that they have taken all steps to minimize the animals' pain and suffering. Our work complies with the journal policy and regulations.

AUTHOR CONTRIBUTIONS

RD, RM, AR, and SH performed the experiments and produced the data. CO'S, AR, and DP analysed the results.

AG-R, KD, XT, and KK assisted with data processing and manuscript preparation. ML and XO drafted the manuscript with the assistance of RM, DP, and AR. ML revised the manuscript with the assistance of CO'S, DP, RM, AR, and AG-R.

FUNDING

This study was supported by Medical Research Council (G10002647, G1002082, ML), British Heart Foundation

(PG/14/80/31106, PG/16/67/32340, PG/12/21/29473, PG/11/59/29004 ML; PG/17/55/33087, RG/17/15/33106, FS/19/16/34169, FS/19/12/34204 DP), BHF Centre of Research Excellence, Oxford (ML) grants, EPSRC (L016346 DP), National Natural Science Foundation of China (Nos. 81700308 and 31871181).

ACKNOWLEDGMENTS

We thank Dr. Leslie M. Loew at University of Connecticut for providing Di-4-ANBDQPQ.

REFERENCES

- Allingham, J. S., Smith, R., and Rayment, I. (2005). The structural basis of blebbistatin inhibition and specificity for myosin II. *Nat. Struct. Mol. Biol.* 12, 378–379. doi: 10.1038/nsmb908
- Bayly, P. V., KenKnight, B. H., Rogers, J. M., Hillsley, R. E., Ideker, R. E., and Smith, W. M. (1998). Estimation of conduction velocity vector fields from epicardial mapping data. *IEEE Trans. Biomed. Eng.* 45, 563–571. doi: 10.1109/10.668746
- Bleeker, W. K., Mackaay, A. J., Masson Pevet, M., Bouman, L. N., and Becker, A. E. (1980). Functional and morphological organization of the rabbit sinus node. *Circ. Res.* 46, 11–22. doi: 10.1161/01.RES.46.1.11
- Boyden, E. S., Zhang, F., Bamberg, E., Nagel, G., and Deisseroth, K. (2005). Millisecond-timescale, genetically targeted optical control of neural activity. *Nat. Neurosci.* 8, 1263–1268. doi: 10.1038/nn1525
- Boyle, P. M., Karathanos, T. V., and Trayanova, N. A. (2018). Cardiac optogenetics: 2018. *JACC Clin. Electrophysiol.* 4, 155–167. doi: 10.1016/j.jacep.2017.12.006
- Bruegmann, T., Beiert, T., Vogt, C. C., Schrickel, J. W., and Sasse, P. (2017). Optogenetic termination of atrial fibrillation in mice. *Cardiovasc. Res.* 114, 713–723. doi: 10.1093/cvr/cvx250
- Bruegmann, T., Malan, D., Hesse, M., Beiert, T., Fuegmann, C. J., Fleischmann, B. K., et al. (2010). Optogenetic control of heart muscle in vitro and in vivo. *Nat. Methods* 7, 897–900. doi: 10.1038/nmeth.1512
- Choi, B. R., and Salama, G. (2000). Simultaneous maps of optical action potentials and calcium transients in Guinea-pig hearts: mechanisms underlying concordant alternans. *J. Physiol.* 529, 171–188. doi: 10.1111/j.1469-7793.2000.00171.x
- de Marneffe, M., Gregoire, J. M., Waterschoot, P., and Kestemont, M. P. (1993). The sinus node function: normal and pathological. *Eur. Heart J.* 14, 649–654. doi: 10.1093/eurheartj/14.5.649
- Entcheva, E. (2013). Cardiac optogenetics. *Am. J. Physiol. Heart Circ. Physiol.* 304, H1179–H1191. doi: 10.1152/ajpheart.00432.2012
- Fedorov, V. V., Lozinsky, I. T., Sosunov, E. A., Anyukhovskiy, E. P., Rosen, M. R., Balke, C. W., et al. (2007). Application of blebbistatin as an excitation-contraction uncoupler for electrophysiologic study of rat and rabbit hearts. *Heart Rhythm* 4, 619–626. doi: 10.1016/j.hrthm.2006.12.047
- Glukhov, A. V., Fedorov, V. V., Anderson, M. E., Mohler, P. J., and Efimov, I. R. (2010). Functional anatomy of the murine sinus node: high-resolution optical mapping of ankyrin-B heterozygous mice. *Am. J. Physiol. Heart Circ. Physiol.* 299, H482–H491. doi: 10.1152/ajpheart.00756.2009
- Hao, X., Zhang, Y., Zhang, X., Nirmalan, M., Davis, L., Dobrzynski, H., et al. (2011). TGF- β 1 mediated fibrosis and ion channel remodeling are key mechanisms producing the sinus node dysfunction associated with SCN5A deficiency and aging. *Circ. Arrhythm. Electrophysiol.* 4, 397–406. doi: 10.1161/CIRCEP.110.960807
- Jaimes, R. 3rd, Walton, R. D., Pasdois, P., Bernus, O., Efimov, I. R., and Kay, M. W. (2016). A technical review of optical mapping of intracellular calcium within myocardial tissue. *Am. J. Physiol. Heart Circ. Physiol.* 310, H1388–H1401. doi: 10.1152/ajpheart.00665.2015
- Ju, Y. K., Lee, B. H., Trajanovska, S., Hao, G., Allen, D. G., Lei, M., et al. (2015). The involvement of TRPC3 channels in sinoatrial arrhythmias. *Front. Physiol.* 6:86. doi: 10.3389/fphys.2015.00086
- Lei, M., Wu, L., Terrar, D. A., and Huang, C. L. H. (2018). Modernized classification of cardiac antiarrhythmic drugs. *Circulation* 138, 1879–1896. doi: 10.1161/CIRCULATIONAHA.118.035455
- Liu, J., Dobrzynski, H., Yanni, J., Boyett, M. R., and Lei, M. (2007). Organisation of the mouse sinoatrial node: structure and expression of HCN channels. *Cardiovasc. Res.* 73, 729–738. doi: 10.1016/j.cardiores.2006.11.016
- Ni, H., Wang, Y., Crawford, W., Zhang, S., Cheng, L., Zhang, H., et al. (2017). Three-dimensional image reconstruction of distribution of Pnmt⁺ cell-derived cells in murine heart. *Sci. Data* 4, 170134.
- Nussinovitch, U., and Gepstein, L. (2015). Optogenetics for in vivo cardiac pacing and resynchronization therapies. *Nat. Biotechnol.* 33, 750–754. doi: 10.1038/nbt.3268
- Nyns, E. C. A., Kip, A., Bart, C. I., Plomp, J. J., Zeppenfeld, K., Schalij, M. J., et al. (2016). Optogenetic termination of ventricular arrhythmias in the whole heart: towards biological cardiac rhythm management. *Eur. Heart J.* 38, 2132–2136. doi: 10.1093/eurheartj/ehw574
- O'Shea, C., Holmes, A. P., Winter, J., Correia, J., Ou, X., Dong, R., et al. (2019b). Cardiac Optogenetics and Optical Mapping – Overcoming Spectral Congestion in All-Optical Cardiac Electrophysiology. *Front. Physiol.* 10, 1–14.
- O'Shea, C., Holmes, A. P., Yu, T. Y., Winter, J., Wells, S. P., Correia, J., et al. (2019a). ElectroMap: high-throughput open-source software for analysis and mapping of cardiac electrophysiology. *Sci. Rep.* 9, 1389. doi: 10.1038/s41598-018-38263-2
- Sharpe, E. J., St Clair, J. R., and Proenza, C. (2016). Methods for the isolation, culture, and functional characterization of sinoatrial node myocytes from adult mice. *J. Vis. Exp.* 116:54555. doi: 10.3791/54555
- Torrente, A. G., Barrere, C., Nargeot, J., Mangoni, M. E., Mesirca, P., Rizzetto, R., et al. (2016). L-type Cav1.3 channels regulate ryanodine receptor-dependent Ca²⁺ release during sino-atrial node pacemaker activity. *Cardiovasc. Res.* 109, 451–461. doi: 10.1093/cvr/cvw006
- Wang, Y., Lin, W. K., Crawford, W., Ni, H., Bolton, E. L., Khan, H., et al. (2017). Optogenetic control of heart rhythm by selective stimulation of cardiomyocytes derived from Pnmt⁺ cells in murine heart. *Sci. Rep.* 7, 40687. doi: 10.1038/s41598-017-18302-0
- Wen, Q., Gandhi, K., Capel, R. A., Hao, G., O'Shea, C., Neagu, G., et al. (2018). Transverse cardiac slicing and optical imaging for analysis of transmural gradients in membrane potential and Ca²⁺ transients in murine heart. *J. Physiol.* 596, 3951–3965. doi: 10.1113/JP276239

Conflict of Interest Statement: The authors declare that the research was conducted in the absence of any commercial or financial relationships that could be construed as a potential conflict of interest.

Copyright © 2019 Dong, Mu-u-min, Reith, O'Shea, He, Duan, Kou, Grassam-Rowe, Tan, Pavlovic, Ou and Lei. This is an open-access article distributed under the terms of the Creative Commons Attribution License (CC BY). The use, distribution or reproduction in other forums is permitted, provided the original author(s) and the copyright owner(s) are credited and that the original publication in this journal is cited, in accordance with accepted academic practice. No use, distribution or reproduction is permitted which does not comply with these terms.

Chapter 5

Optical mapping of transverse mouse ventricular slices

The heart is known to exhibit transmural gradients. Cardiomyocytes in the epicardial, myocardial and endocardial layers possess distinct electrical current contributions and hence distinct action potential morphologies. Changes in the distribution of action potential (AP) morphology can alter the dispersion of repolarisation, and has been observed in diseased hearts. It is important therefore we have robust methods to study transmural gradients in experimental models, including mouse hearts.

Tissue slices have been shown to be an effective platform for cardiac electrophysiological (EP) investigation in several species. Cardiac slices (also known as 'organotypic heart slices') are multicellular preparations, and hence overcome some of the drawbacks of studying isolated cardiomyocytes such as the loss of cell to cell communication and extracellular matrix components during enzymatic isolation.

Commonly, cardiac slices have been prepared longitudinally (i.e. from apex to base or in the 'long axis'), preventing study of transmural heterogeneity, and/or studied using low spatial resolution electrode techniques. The following chapter

discusses a protocol designed for harvest of transversely ('short axis') cut mouse ventricular slices. Although similar preparations have been described, these slices were then loaded with transmembrane voltage and/or intracellular calcium dyes. Slices could therefore be studied with high spatial resolution optical mapping to reveal transmural and regional gradients in the mouse ventricle.

The presented work consists of two publications detailing preparation of transverse cardiac slices and analysis of their electrophysiological behaviour using optical mapping. The first article (section 5.1) uses the described platform to study the transmural EP properties of the mouse heart. The mouse is shown to exhibit significant transmural gradients, including prolonged action potential and calcium transient durations in the endocardium compared to the epicardium, as seen in larger mammals. Conduction analysis of these slices revealed physiologically healthy conduction velocities and response to pacing in these slices. However, this analysis was limited by the use of field pacing, which cause simultaneous activation in large areas of the slices which is not due to cell to cell conduction of the electrical impulse.

The second publication (section 5.2) provides a detailed and updated protocol for preparation of mouse transverse cardiac slices. Two key advances are demonstrated. The first is dual dye loading of slices, allowing detailed investigation of voltage-calcium coupling. The second is the demonstration that slices can be paced using optical excitation (Chapter 4), which benefits from improved spatial control in comparison to field pacing techniques.

Several features of the ElectroMap software (Chapter 3) were used to analyse

data from these slice preparations. The slices often exhibited low and variable signal quality, and only via processing with ensemble averaging (section 3.3.1) of multiple stimuli did subtle transmural gradients become apparent. The conduction analysis module was utilised to quantify conduction speed across the slices as a sign on physiological health. Furthermore, activation mapping allowed the study of changes in conduction dynamics when utilising optical rather than field pacing.

5.1 Transverse cardiac slicing and optical imaging for analysis of transmural gradients in membrane potential and Ca²⁺ transients in murine heart





Publication 4. This research was originally published in The Journal of Physiology.

Transverse cardiac slicing and optical imaging for analysis of transmural gradients in membrane potential and Ca²⁺ transients in murine heart. Q Wen, K Gandhi, R A Capel, G Hao, **C O'Shea**, G Neagu, S Pearcey, D Pavlovic, D A Terrar, J Wu, P Camelliti, M Lei. J. Physiol. 596, 3951–3965. 2018

Author contributions in publication 4

I performed data analysis of activation and conduction (Figure 6). Additionally, I performed confirmatory analysis of observed action potential, calcium transient and alternans heterogeneity. By utilising the ensemble averaging in ElectroMap (Chapter 3), lowered signal to noise ratio signals were produced to confirm initial results using single beat analysis. Experiments described were carried out at Southwest Medical University or University of Oxford, and not conducted by myself.

Transverse cardiac slicing and optical imaging for analysis of transmural gradients in membrane potential and Ca^{2+} transients in murine heart

Q. Wen¹, K. Gandhi², Rebecca A. Capel³, G. Hao⁴, C. O'Shea⁵, G. Neagu³, S. Pearcey³, D. Pavlovic⁵ , Derek A. Terrar³, J. Wu¹, G. Faggian² , Patrizia Camelliti⁶  and M. Lei^{3,4} 

¹Institution of Cardiology, Union Hospital, Tongji Medical College, Huazhong University of Science and Technology, Wuhan, China

²Medical School, University of Verona, Verona, Italy

³Department of Pharmacology, University of Oxford, Oxford, UK

⁴Key Laboratory of Medical Electrophysiology of Ministry of Education, Collaborative Innovation Center for Prevention and Treatment of Cardiovascular Disease/Institute of Cardiovascular Research, Southwest Medical University, Luzhou, 6400, China

⁵Institute of Cardiovascular Sciences, University of Birmingham, Birmingham, UK

⁶School of Biosciences and Medicine, University of Surrey, Guildford, UK

Edited by: Don Bers & Jamie Vandenberg

Key points

- A robust cardiac slicing approach was developed for optical mapping of transmural gradients in transmembrane potential (V_m) and intracellular Ca^{2+} transient (CaT) of murine heart.
- Significant transmural gradients in V_m and CaT were observed in the left ventricle.
- Frequency-dependent action potentials and CaT alternans were observed in all ventricular regions with rapid pacing, with significantly greater incidence in the endocardium than epicardium.
- The observations demonstrate the feasibility of our new approach to cardiac slicing for systematic analysis of intrinsic transmural and regional gradients in V_m and CaT.

Abstract Transmural and regional gradients in membrane potential and Ca^{2+} transient in the murine heart are largely unexplored. Here, we developed and validated a robust approach which combines transverse ultra-thin cardiac slices and high resolution optical mapping to enable systematic analysis of transmural and regional gradients in transmembrane potential (V_m) and intracellular Ca^{2+} transient (CaT) across the entire murine ventricles. The voltage dye RH237 or Ca^{2+} dye Rhod-2 AM were loaded through the coronary circulation using a Langendorff perfusion system. Short-axis slices (300 μm thick) were prepared from the entire ventricles (from the apex to the base) by using a high-precision vibratome. Action potentials (APs) and CaTs

Q. Wen graduated from Tongji medical school Huazhong University of Science and Technology as a Medical Doctor in May 2015. Since graduating, he has worked at the Cardiology Department of Union Hospital, specialising in diagnosis and treatment of hypertension, CAD and heart failure. He studies the association of SNPs of IL33/ST2 signal pathway and CAD, hypertension and diabetes in the Chinese population. He translated for the 8th Central Congress Cardiology. His hobbies are reading, body building and playing basketball. **Kushal Gandhi** earned his PhD through a collaboration between the University of Verona, Italy and the University of Oxford, UK. He is now working as a postdoctoral researcher at Texas Tech University Health Sciences Center at the Permian Basin, Odessa, TX, USA. His work now focuses on the endocannabinoid system (ECS), which is dysregulated by irregular diet during pregnancy and affects future generations. ECS is vital for appetite and pain regulation, neurological development and other physiological processes in humans.



Q. Wen and K. Gandhi are joint first authors. J. Wu, G. Faggian, P. Camelliti and M. Lei are joint senior authors.

were recorded with optical mapping during steady-state baseline and rapid pacing. Significant transmural gradients in V_m and CaT were observed in the left ventricle, with longer AP duration (APD₅₀ and APD₇₅) and CaT duration (CaTD₅₀ and CaTD₇₅) in the endocardium compared with that in the epicardium. No significant regional gradients were observed along the apico-basal axis of the left ventricle. Interventricular gradients were detected with significantly shorter APD₅₀, APD₇₅ and CaTD₅₀ in the right ventricle compared with left ventricle and ventricular septum. During rapid pacing, AP and CaT alternans were observed in most ventricular regions, with significantly greater incidence in the endocardium in comparison with epicardium. In conclusion, these observations demonstrate the feasibility of our new approach to cardiac slicing for systematic analysis of intrinsic transmural and regional gradients in V_m and CaT in murine ventricular tissue.

(Received 11 April 2018; accepted after revision 12 June 2018; first published online 21 June 2018)

Corresponding author M. Lei: Department of Pharmacology, University of Oxford, Mansfield Road, OX1 3QT. Email: ming.lei@pharm.ox.ac.uk

Introduction

Because of its feasibility for genetic modification, the mouse has been the most popular animal species for modelling human disease conditions and for mechanistic research, as well as therapeutic exploration, despite distinct differences in its cardiac electrophysiological properties compared to the human heart, including marked differences in heart size, heart rates and action potential waveforms. The mouse is also the second mammalian species, after humans (Lander *et al.* 2001), in which a substantial amount of genomic information has been analysed (Waterston *et al.* 2002). Within the cardiovascular research community, the mouse has been widely used for exploring molecular, cellular and systemic mechanisms underlying inherited and acquired ventricular arrhythmic diseases (Nerbonne, 2014). As transgenic technology has advanced, mutagenesis has become much easier to carry out in mice and an increasing number of genetically modified mouse systems have been generated for the study of cardiac arrhythmias (Sabir *et al.* 2008). The models include ion channelopathies with minimal structural abnormalities, and those of structural heart disease (Choy *et al.* 2016). The former group includes catecholaminergic polymorphic ventricular tachycardia (CPVT) (Wehrens *et al.* 2003), the long (Wu *et al.* 2012) and short QT syndromes (LQTS and SQTs), and Brugada syndrome (BrS) (Papadatos *et al.* 2002; Choy *et al.* 2016). The latter group includes several types of cardiomyopathies, such as arrhythmogenic right ventricular dysplasia (ARVD) (Asano *et al.* 2004), dilated cardiomyopathy (DCM) and hypertrophic cardiomyopathy (HCM) (Choy *et al.* 2016).

Surprisingly, despite the popularity of mouse models in heart research, little is known about murine heart transmural and regional electrophysiological heterogeneities such as action potential and Ca²⁺ transient characteristics. These are vitally important for phenotypic and mechanistic research

into cardiac disease conditions, in particular cardiac arrhythmias. In this species, the transmural and regional electrophysiological heterogeneities have been largely unexplored.

Thin tissue slices, a well-established experimental preparation for electrophysiological studies of the brain, have recently emerged as a promising model for cardiac electrophysiology investigations. Thin slices, prepared from the ventricle of a number of different species (Halbach *et al.* 2006; Bussek *et al.* 2009; Camelliti *et al.* 2011; Wang *et al.* 2014), have been shown to retain structural and functional properties of the native myocardium, including tissue architecture, cell type ratio, cell distribution, cell–cell electrical and mechanical coupling, and extracellular matrix (Bussek *et al.* 2009; Camelliti *et al.* 2011). Importantly, cardiac slices exhibit similar electrophysiological characteristics to the intact heart and respond to the application of pharmacological compounds similarly to the whole heart (Camelliti *et al.* 2011; Himmel *et al.* 2012), thus providing a promising experimental model for electrophysiology, Ca²⁺ handling, and drug action investigations.

Most previous electrophysiology studies on cardiac slices have employed low spatial resolution recording methods, including patch clamp (Burnashev *et al.* 1990), sharp electrodes (Halbach *et al.* 2006; Bussek *et al.* 2009; Himmel *et al.* 2012) and low-density multi-electrode arrays (Bussek *et al.* 2009; Camelliti *et al.* 2011). Higher spatial resolution methods, such as optical mapping, provide exciting opportunities to monitor dynamic cellular electrophysiological events as they occur in real time (Wang *et al.* 2015; Kang *et al.* 2016). Furthermore, prior studies have been limited to the analysis of sub-epicardial (Wang *et al.* 2015) or sub-endocardial tangentially cut slices (Kang *et al.* 2016), or a few transmurally cut slices (Bussek *et al.* 2009), an approach inadequate for accurate capture of regional and transmural cardiac electrophysiological properties. A method

for systematic analysis of regional and transmural electrophysiological heterogeneities across the whole ventricles in mouse is currently missing.

In order to address the issues described above, in the present study we developed a feasible transverse slicing method and combined it with a high-throughput optical imaging technique as a new approach for studying cellular electrophysiology of murine heart in intact sliced ventricular tissue. These transverse slices were cut at right angles to the long axis of the heart. Our approach enables, for the first time, the use of a series of slices prepared from ventricle to measure transmembrane potential (V_m) and intracellular Ca^{2+} transient (CaT) with high temporal and spatial resolution, allowing (i) comparison of successive slices which form a stack representing the original geometry of the heart; (ii) profiling of the transmural and regional gradients in V_m and CaT in the ventricle; (iii) characterisation of transmural and regional profiles of action potential and CaT alternans.

Methods

Ethical approval

All animal experiments were performed on adult mice (CD1, 12–20 weeks old) in accordance with the United Kingdom Animals (Scientific Procedures) Act 1986 and were approved by the University of Oxford Pharmacology ethical committee (approval ref. PPL: 30–3340) and the national guidelines under which the institution operates. All mice used in this study were maintained in a pathogen-free facility at the University of Oxford. Mice were given *ad libitum* access to food and water. The authors confirm that they have taken all steps to minimise the animals' pain and suffering. Our work complies with the journal policy and regulations (Grundy, 2015).

Heart isolation

Mice were killed by cervical dislocation in accordance with Schedule 1 killing method. Hearts were rapidly excised and Langendorff-perfused with oxygenated Krebs solution (containing in mM: NaCl 119, NaHCO_3 25, sodium pyruvate 1.8, KH_2PO_4 1.2, KCl 4.7, MgCl_2 1.0, CaCl_2 1.8, and glucose 10; equilibrated with 95% O_2 /5% CO_2 , pH 7.4) at 37°C and at constant rate of 3.5–4 ml/min for 10 min. To prevent formation of blood clots in the coronary circulatory system, animals were treated with heparin (200 units) under non-recovery terminal general anaesthesia by injection of an overdose of 1.2% Avertin solution (0.5–0.8 ml i.p. (2,2,2-tribromoethanol, Sigma-Aldrich Poole, Dorset, UK) prior to killing and hearts were injected with streptokinase (400 units) via

the coronary system after organ excision according to approved procedure by the Home Office.

Dye loading

Fluorescent dyes were loaded via the coronary circulation during Langendorff perfusion, applied by injection into the aortic cannula. The voltage sensitive dye RH237 (Thermo Fisher Scientific, UK) was delivered as a 15 μl bolus of 2 mM concentration, injected into the cannula in small volume steps over a period of 5 min. The Ca^{2+} dye Rhod-2 AM (Thermo Fisher Scientific, UK) was administered as a 50 μl bolus (stock solution: 1 mg/ml in DMSO) over a 5 min period, and recirculated for 45 min in the presence of 0.5 mM probenecid. After dye loading, hearts were perfused with Krebs solution containing 10 μM blebbistatin, a myosin II inhibitor used to stop contractions and avoid movement artefacts during optical mapping recordings.

Slice preparation

Table 1 summarises the slice preparation procedure. Hearts were removed from the Langendorff set-up and dissected in cold (4°C) oxygenated (99.5% O_2) Tyrode solution (in mM: NaCl 140; KCl 4.7; glucose 10; HEPES 10; MgCl_2 1; CaCl_2 1.8; pH 7.4) containing the excitation–contraction uncoupler 2,3-butanedione monoxime (BDM, 10 mM). Atria and valves were removed using a sharp scalpel blade, leaving the ventricles intact. Ventricles were glued base-down (histoacryl tissue adhesive; Braun, Melsungen, Germany) onto a pre-made 4% agar block, previously fixed onto the vibratome specimen holder (VF-300 vibrating microtome; Precisionary Instruments Inc., Greenville, USA). Ventricles were subsequently embedded in 4% low-melt agarose and cooled on ice at 4°C. The specimen holder with agarose-embedded ventricles was mounted onto the stage of the vibratome filled with cold (4°C) oxygenated (99.5% O_2) Tyrode solution containing BDM. Short-axis slices were cut at a thickness of 100 μm , 300 μm or 500 μm , using a razor blade at a speed of 0.02 mm/s and vibration frequency of 82 Hz. After initial experiments aiming to determine the best slice thickness for dye loading, dye retention and optical mapping recordings, short-axis slices of 300 μm thickness were prepared from the entire ventricles (from the apex to the base) for the study of regional and transmural V_m and Ca^{2+} properties. As summarised in Table 1, the total cold ischaemic time during slicing is between 1.5 and 4 min. Slices were then transferred to recovery solutions for recovery in a pre-incubation chamber filled with Krebs solution containing 10 μM blebbistatin at room temperature for

Table 1. Summary of the slicing and imaging protocol

	Dye loading	Perfusion	Slicing	Recovery 1	Recovery 2	Recovery 3	Pre-imaging	Imaging
Temperature	37°C	37°C	4°C	4°C	RT	RT	37°C	37°C
Solution	Krebs	Krebs	Tyrode	Tyrode	Krebs	Krebs	Krebs	Krebs
BDM (10 mM)	No	No	Yes	Yes	No	No	No	No
Blebbistatin (10 μ M)	No	Yes	No	No	Yes	Yes	Yes	Yes
Ca ²⁺	1.8 mM	1.8 mM	1.8 mM	1.8 mM	1.8 mM	1.8 mM	1.8mM	1.8mM
O ₂	95%	95%	100%	100%	95%	95%	95%	95%
CO ₂	5%	5%	0%	0%	5%	5%	5%	5%
Duration	5–7 min	20 min	1.5–4 min	10 min	10 min	5 min	3 min	<1 min

RT, room temperature; Krebs, Krebs-Henseleit solution; Tyrode, Tyrode solution.

30 min before electrophysiological investigations. To prevent tissue from curling, slices were collected on Sylgard blocks and held in position using a nylon mesh in the pre-incubation chamber.

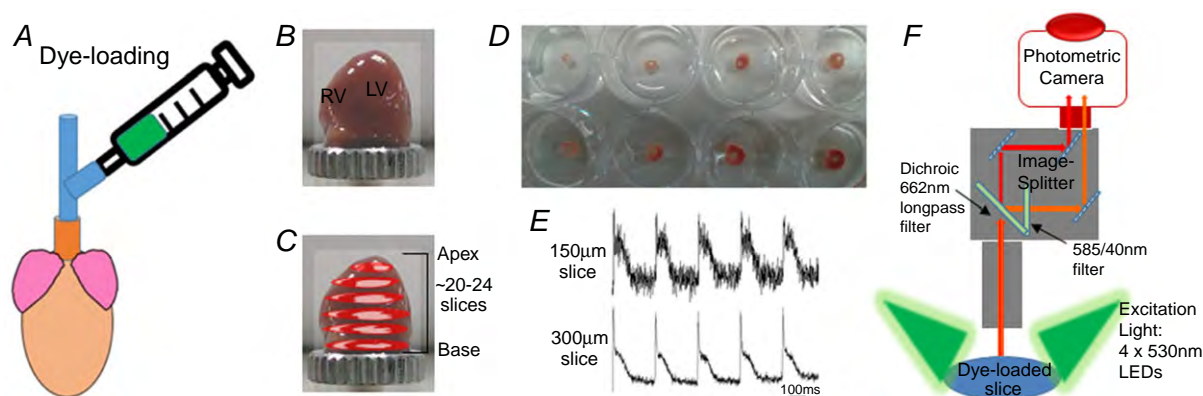
Optical mapping

Slices were electrophysiologically assessed with the optical mapping method, using a custom-designed optical mapping system equipped with an EMCCD camera (Evolve 128 Photometrics, Tucson, AZ, USA). Figure 1F shows a schematic diagram of the mapping set-up. Slices were kept in Krebs solution containing 10 μ M blebbistatin at 37°C during imaging. Four 530 nm LEDs were used for excitation of the Ca²⁺-sensitive dye Rhod-2. CaT fluorescence was collected at 585 ± 40 nm. For V_m signals, four 530 nm LEDs were used for excitation of RH237, and emission was collected using a 662 nm long pass filter. V_m and CaT measurements were taken at maximal resolution (128 \times 128 pixels; pixel area $47 \times 47 \mu$ m) at

a rate of 1000 frames/s. Slices were electrically stimulated with bipolar pulses of 2 ms duration, at voltages 1.5 times above threshold (5–10 V) and initial frequency of 2 Hz. For AP and CaT alternans investigations, slices were stimulated at frequencies of 2, 4, 8 and 16 Hz.

Data analysis

AP duration (APD) and CaT duration (CaTD) were analysed using OPTIQ (program developed by Dr Burton, University of Glasgow). AP and CaT signals were filtered using a Gaussian spatial filter (radius 2 pixels) before relevant parameters were extracted. APD was measured as the time from the upstroke to 50% and 75% repolarisation (APD50 and APD75). Similarly, the CaTD was measured as the time from the upstroke to 50% and 75% recovery (CaTD50 and CaTD75). AP and CaT alternans are defined as the electrical or calcium transient discordant in duration or in amplitude. These phenomena depend on the underlying instability mechanisms (V_m -driven or CaT-driven)

**Figure 1. Optimisation of murine cardiac slice methodology**

A, voltage (RH237) or calcium (Rhod-2 AM) dyes were loaded via coronary circulation using the Langendorff perfusion system. B, ventricles were embedded in 4% low-melt agarose and mounted onto the vibratome specimen holder. C, up to 24 transverse slices were cut from the apex to the base in ice-cold BDM Tyrode solution. D, slices were recovered at room temperature in Krebs solution containing 10 μ M blebbistatin for 30 min, before optical mapping studies. E, V_m signals in slices cut at 150 μ m and 300 μ m thickness. F, optical mapping setup with four 530 nm excitation LEDs and a 128 \times 128 EMCCD camera.

and the coupling between AP and CaT alternans cycling.

For assessment of conduction velocity (CV), the multi-vector polynomial method (Bayly *et al.* 1998) was used within bespoke analysis software, Electro-Map (O'Shea *et al.* 2017). Following Gaussian filtering (3×3 pixel area, $\sigma = 1.5$), activation maps, generated from measuring the time of the depolarisation midpoint, were spatially segmented into regions of 5×5 pixels. A polynomial surface was then fitted to local activation times to describe propagation in the area, and local CV quantified as the gradient vector of the polynomial surface. Mean CV was then calculated from the local CVs across the tissue slice.

Statistical analysis

Transmural and regional APD/CaTD distributions were analysed using a Student's paired *t* test or one-way ANOVA with *post hoc* Tukey's test and repeated measures correlation among tissue regions. Regional frequency-dependent AP/CaT alternans and arrhythmia heterogeneity were analysed using a chi-squared test. A value of $P < 0.05$ was considered statistically significant. Values are expressed as means \pm SEM.

Results

Optimisation of murine transverse ventricular slices for V_m and CaT measurements

Adult murine ventricular slices have been previously developed for electrophysiology applications (Halbach *et al.* 2006), but optimisation of the slice preparation to enable systematic analysis of V_m and CaT across the whole murine ventricles has yet to be achieved. Figure 1 illustrates the methodology implemented in this study. Critical steps included determination of an efficient dye loading method, a slice thickness able to maintain intact tissue morphology and generate optimal voltage and calcium signals, and a recovery period necessary to reach stable signals after slice preparation. As shown in Fig. 1, to achieve optimal dye loading, the voltage dye RH237 or Ca^{2+} dye Rhod-2 AM were loaded through the coronary circulation using the Langendorff perfusion system. Prevention of blood clot formation was essential for optimal dye loading and was achieved by initial injection of heparin (200 units) before killing, and subsequent injection of streptokinase (400 units) directly into the coronary system after heart excision. Ventricles were embedded in low-melting temperature agarose to provide structural support to the tissue during sectioning. Slices were cut at right angles to the long axis of the heart from the

apex to the base, and thicknesses from $100 \mu\text{m}$ to $500 \mu\text{m}$ were tested, with $300 \mu\text{m}$ found to be the best thickness to achieve optimal recordings for both V_m and CaT. Slices less than $300 \mu\text{m}$ thick showed markedly lower V_m and CaT signals (Fig. 1E), while slices thicker than $300 \mu\text{m}$ suffered from poor oxygenation. After preparation, slices were pre-incubated at room temperature in Krebs solution containing $10 \mu\text{M}$ blebbistatin for an optimal recovery time of 30 min, prior to electrophysiological assessment using a custom-designed optical mapping system (Fig. 1F). Figure 2 shows viable slices obtained with the optimised protocol, summarised in Table 1, and representative V_m and CaT signals from different regions, illustrating the robustness of this preparation for murine research. We monitored the 'rundown' of the V_m and CaT signals for up to 4 h, the average signal 'rundown' is less than 25%. Our experiments usually finished within 3 h.

Transmural and regional characteristics of V_m

After successful optimisation of the methodology, we tested the feasibility of combining murine slices with high resolution optical mapping for systematic transmural and regional profiling of V_m and CaT across the murine ventricles. Transverse slices ($300 \mu\text{m}$ thick) were prepared from the entire ventricles (from apex to base; Fig. 2A), and AP duration (APD) and CaT duration (CaTD) were mapped with high spatial and temporal resolution. Examples are shown in Fig. 2B corresponding to slice 10 shown in Fig. 2A.

Figure 3 summarises the distribution of APD at 50% repolarisation (APD50) and 75% repolarisation (APD75) across the entire murine ventricles at 2 Hz pacing frequency. Figure 3A and B show typical APD75 colour-coded maps and action potentials from a series of transverse ventricular slices, suggesting the presence of APD heterogeneities in the mouse ventricles. An important advantage of the cardiac slice model is the ability to study any region of the mouse ventricle and thus simultaneously investigate transmural, apico-basal (apex–base), and interventricular APD gradients. As shown in Fig. 3C, there are significant transmural gradients in APD50 and APD75 in the left ventricle at 2 Hz pacing frequency (Fig. 3Ca and c), with the shortest APDs occurring in the epicardium and the longest APDs occurring in the endocardium (APD50: Epi 50 ± 7 ms, Endo 58 ± 8 ms, $P < 0.01$; APD75: Epi 71 ± 8 ms, Endo 83 ± 8 ms, $P = 0.0001$, paired *t* test; $n = 5$ hearts). Differences between longest and shortest APD (transmural APD dispersion) in LV free wall were 8 ± 1 ms at APD50 and 11 ± 1 ms at APD75. Importantly transmural heterogeneities were not restricted to a particular region of the left ventricle, but were present along the entire left ventricle free wall from the apex to the base (Fig. 3Ca

and *c*), with the highest transmural APD dispersion occurring in the apical region (apex transmural dispersion: 16 ± 1 ms at APD75; $P < 0.05$, one-way ANOVA comparing apex-centre-base transmural dispersion).

In addition to transmural APD distribution, cardiac slices allowed us to investigate APD gradients across the apico-basal axis of the left ventricle free wall. As shown in Fig. 3*Ca* and *c*, there is no significant apico-basal gradient in APD50 and APD75 in either epicardium or endocardium ($P > 0.05$, one-way ANOVA with *post hoc* Tukey's test; $n = 5$ hearts).

Finally, as each slice contains left ventricle free wall, right ventricle and septum, we were able to assess inter-ventricular APD gradients. As shown in Fig. 3*Cb* and *d*, there are significant inter-ventricular differences in APD50 and APD75 at the base and centre, but not at the apex. APD was shorter in the right ventricle in comparison to the left ventricle and the septum, in the basal and centre regions ($P < 0.05$, one-way ANOVA with *post hoc* Tukey's test; $n = 5$ hearts), with inter-ventricular APD75 dispersion of 23 ± 6 ms and 13 ± 3 ms, respectively.

Transmural and regional characteristics of CaT

Analysis of transmural and regional heterogeneity in calcium handling are summarised in Fig. 4. Figure 4*A* and *B* show representative maps of CaT duration (CaTD) at 75% recovery (CaTD75) from apical, centre and basal ventricular mouse slices during electrical pacing at 2 Hz frequency (Fig. 4*A*), and typical optical CaT recordings from corresponding regions (Fig. 4*B*). As shown in Fig. 4*C*, there are significant transmural gradients in CaTD at 50% recovery (CaTD50) in apical, centre and basal regions of the left ventricle free wall at 2 Hz pacing frequency (Fig. 4*Ca*), with significantly longer CaTD50 in the endocardium compared to the epicardium (apex: 13% longer, $P < 0.01$; centre: 8%, $P < 0.05$; base: 10%, $P < 0.01$; $n = 6-8$ hearts). A significant transmural gradient in CaTD75 (Fig. 4*Cc*) was also observed in the basal and centre regions of the left ventricle ($P < 0.05$, paired *t* test; $n = 5-7$ hearts), but not in the apical region.

We further assessed the distribution of CaTD along the apico-basal axis of the left ventricle free wall. As shown in Fig. 4*Ca* and *c*, no significant apico-basal gradient in

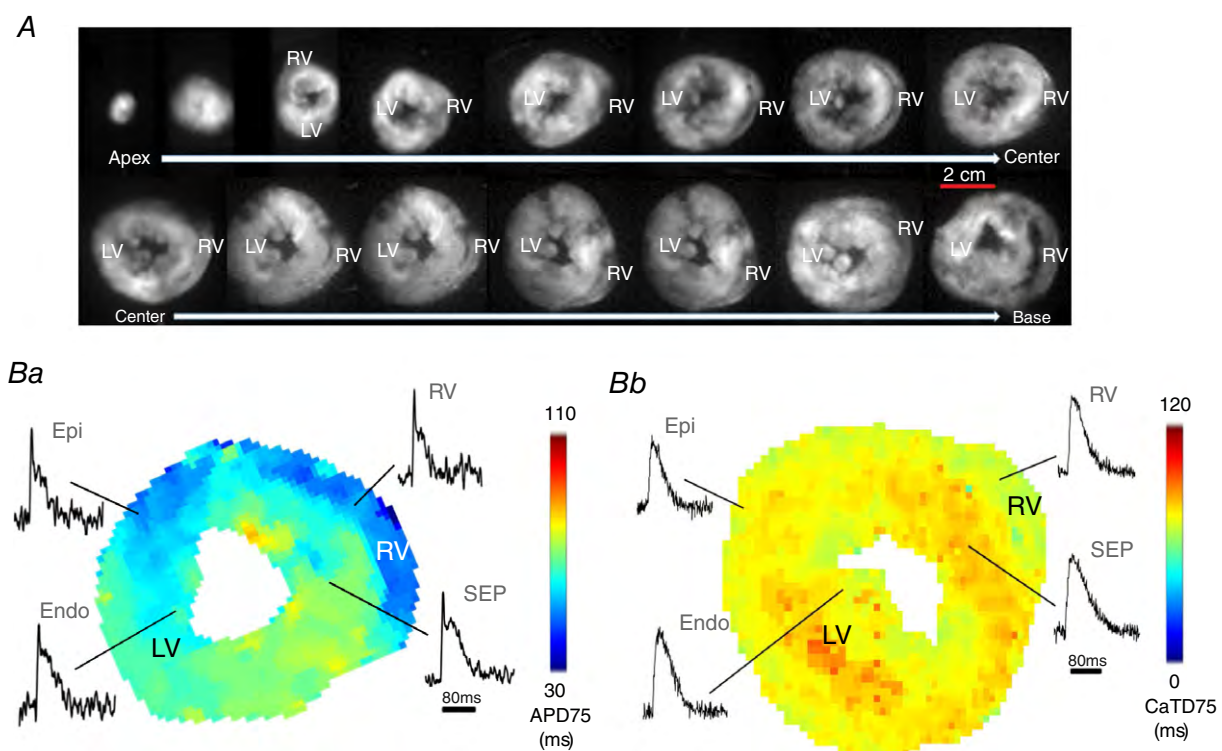


Figure 2. V_m and CaT measurements in murine ventricular slices

A, bright field images of transverse ventricular slices ($300 \mu\text{m}$ thick) prepared from both ventricles of a mouse heart (from the apex to the base). Scale bar: 2 cm. *B*, AP duration (APD; *Ba*) and CaT duration (CaTD; *Bb*) maps generated from a slice prepared from the central region of the ventricles, with raw AP and CaT signals acquired from the epicardium (Epi) and endocardium (Endo) of the left ventricle, the ventricular septum (SEP) and the right ventricle (RV). APD scale bar: 80 ms.

CaTD50 and CaTD75 was observed in the murine left ventricle ($P > 0.05$, one-way ANOVA; $n = 5-7$ hearts).

Finally, we compared CaTD measured in left ventricle free wall regions with CaTD recorded in right ventricle and ventricular septum regions for each tissue slice, to investigate interventricular CaTD gradients. As shown in Fig. 4*Cb* and *d*, there are significant regional differences in CaTD50 but not CaTD75 at the apex and base, with the shortest CaTD50 occurring in the right ventricle, and an interventricular CaTD50 dispersion of 4 ± 1 ms and 6 ± 1 ms at the apex and base, respectively ($n = 6-7$ hearts).

Transmural and regional heterogeneity of frequency-dependent AP and CaT alternans

Further experiments were carried out to assess the feasibility of using murine transverse ventricular slices and optical mapping to characterise transmural and regional

differences in frequency-dependent AP and CaT alternans and arrhythmias. Slices were paced at frequencies of 2, 4, 8 and 16 Hz, and AP and CaT were recorded at each frequency (Figs 5*A* and 7*A*). As shown in Figs 5 and 7, AP and CaT alternans and arrhythmic events often occurred at higher pacing frequencies of 8 Hz and 16 Hz, indicating a frequency-dependent relationship. At a high pacing rate of 16 Hz, alternans often converted into arrhythmia. An increase in AP alternans and arrhythmic events occurred in all regions (LV, septum and RV) during incremental pacing from 8 Hz to 16 Hz frequency (Fig. 5*B*). Transmural heterogeneities were observed in the LV free wall, with greater AP alternans and arrhythmic events in the endocardium in comparison with epicardium at both 8 Hz and 16 Hz frequencies (Fig. 5*B*; $P < 0.05$, $n = 6$ hearts). There are no significant interventricular differences observed in the incidence of AP alternans, with a similar number occurring in the left ventricle, right ventricle and septum at both 8 Hz and 16 Hz frequencies.

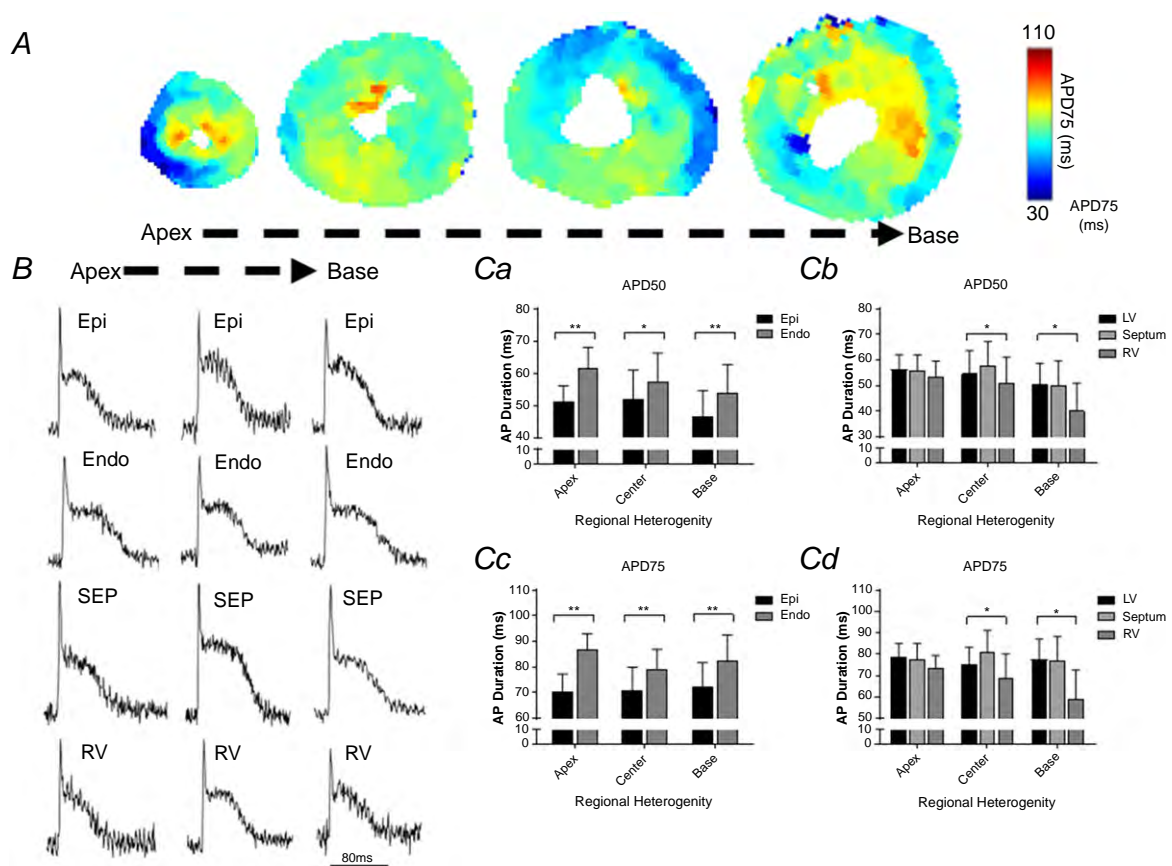


Figure 3. Transmural and regional distribution of AP duration across the murine ventricles

A, representative maps of AP duration (APD75) at 2 Hz pacing frequency (500 ms pacing cycle length) recorded from apex to base in transverse ventricular slices. B, typical optical AP recordings (unfiltered signals) obtained from different regions of the murine ventricles at 2 Hz pacing frequency. Scale bar: 80 ms. C, quantitative summary of transmural and regional APD50 (Ca and Cb) and APD75 distribution (Cc and Cd) at 2 Hz pacing ($n = 5$ hearts; ** $P < 0.01$; * $P < 0.05$). Values expressed as means \pm SEM. Epi, epicardium; Endo, endocardium; SEP, septum; RV, right ventricle; LV, left ventricle.

Figure 6 illustrates the activation maps generated within bespoke ElectroMap analysis software (O'Shea *et al.* 2017). A polynomial surface was then fitted to local activation times to describe propagation in the area, and local CV quantified as the gradient vector of the polynomial surface. Mean CV was then calculated from the local CVs across the tissue slice. As seen in Fig. 6, there is a clear slowing of conduction at higher pacing frequencies. This is apparent when CV data is analysed across all the slices (Fig. 6A-C) or across individual hearts (Fig. 6A-C). In some slices we analysed there is evidence of steep activation gradients and focal activity, which may contribute to the arrhythmias observed.

As shown in Fig. 7B, a significant increase in CaT alternans and arrhythmic events occurred in the epicardium and endocardium of the left ventricle, in the ventricular septum and in the right ventricle with increase of pacing frequency from 8 Hz to 16 Hz. Transmural heterogeneities were also observed, with lower occurrence of CaT alternans and arrhythmic events in the epicardium

in comparison with endocardium at both 8 Hz and 16 Hz frequencies (Fig. 7B; $P < 0.05$, $n = 6$ hearts).

Discussion

In the present study we developed and validated a transverse ventricular tissue slice model to enable systematic analysis of V_m and CaT across the whole murine ventricles. Our investigation of murine transverse slices, prepared from both ventricles (from apex to base) combined with high resolution optical mapping, revealed transmural and regional heterogeneities in both physiological APD and CaTD, and in the incidence of frequency-dependent AP and CaT alternans in the murine ventricles.

Optimisation of cardiac slices for V_m and CaT measurements

Cardiac slice technology has previously been employed for structural and functional studies of human biopsies

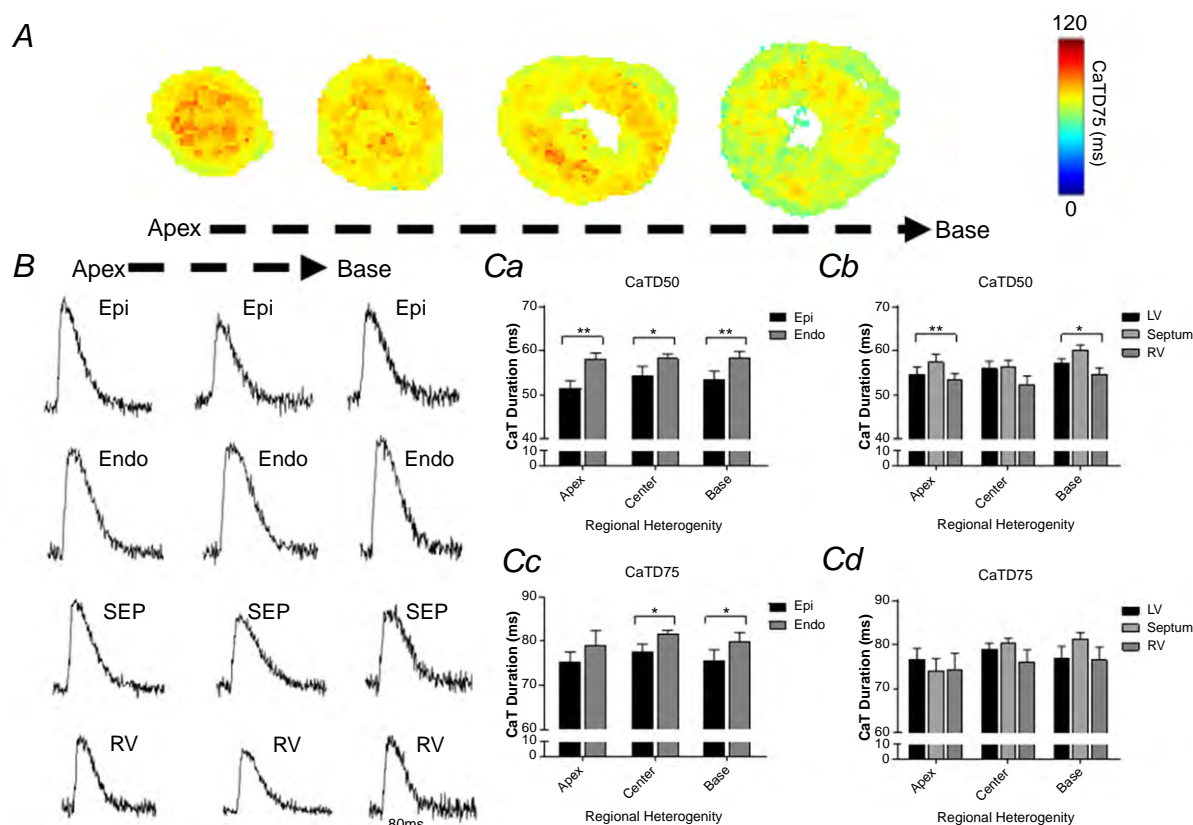


Figure 4. Transmural and regional distribution of CaT duration in the murine ventricles

A, representative maps of CaT duration (CaTD75) at 2 Hz pacing frequency (500 ms pacing cycle length) recorded from apex to base in transverse ventricular slices. B, representative optical CaT raw traces obtained from different regions of the murine ventricles at 2 Hz pacing frequency. Scale bar: 80 ms. C, quantitative summary of transmural and regional CaTD50 (Ca and Cb) and CaTD75 distribution (Cc and Cd) at 2 Hz pacing ($n = 5-8$ hearts; $**P < 0.01$; $*P < 0.05$). Values expressed as means \pm SEM. Epi, epicardium; Endo, endocardium; SEP, septum; RV, right ventricle; LV, left ventricle.

and animal hearts (Halbach *et al.* 2006; Bussek *et al.* 2009; Camelliti *et al.* 2011), but application of the preparation in optical mapping studies is only starting to emerge (Wang *et al.* 2015; Kang *et al.* 2016). This report is the first to present a detailed protocol for successful preparation of transverse ventricular slices for transmural and regional profiling of V_m and CaT with high resolution optical mapping. Important steps include dye loading via Langendorff perfusion; slice cutting perpendicular to the long axis of the heart; a slice thickness of 300 μm ; and a post-cutting recovery period of 30 min.

In contrast to prior reports of cardiac slice preparation, slices were cut at right angles to the long axis of the heart (transverse slices) and not tangentially to the epicardial

surface (Bussek *et al.* 2009; Camelliti *et al.* 2011). This allowed us to prepare a complete series of slices containing left ventricle, right ventricle and ventricular septum regions from apex to base. Given the curvature of the mouse ventricles and the different thickness of LV, RV and septum at the apex and base, preparing tangential slices containing well aligned cardiomyocytes covering the entire ventricular tissue, for the study of transmural and regional heterogeneities, was not feasible. Importantly our study demonstrates that transverse mouse slices are viable and show robust voltage and calcium signals. We identified slice thickness as a critical parameter for successful preparation of viable transverse slices. Previous studies have reported thicknesses from 150 to 500 μm (Pertsov *et al.*

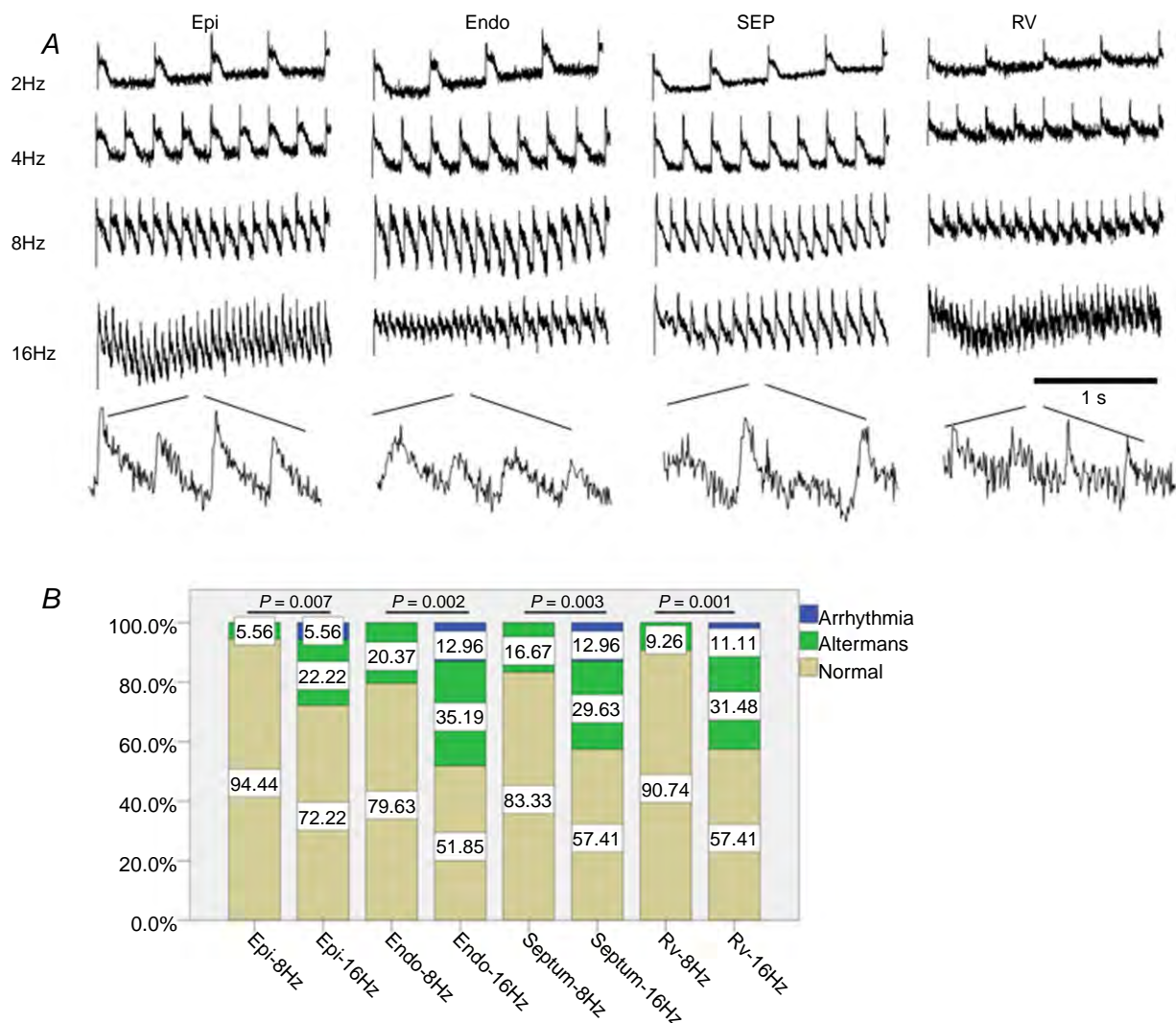


Figure 5. Regional and frequency-dependent distribution of AP alternans and arrhythmic events in murine ventricular slices

A, representative optical AP traces obtained from different regions within a ventricular slice during electrical pacing at 2, 4, 8 and 16 Hz frequency. Scale bar: 1 s. B, transmural and regional occurrence of alternans and arrhythmias at 8 Hz and 16 Hz pacing frequency. Epi, epicardium; Endo, endocardium; SEP, septum; RV, right ventricle; LV, left ventricle. $n = 6$ hearts.

1993; Halbach *et al.* 2006; Camelliti *et al.* 2011; Wang *et al.* 2015), but in this study we determined that 300 μm was the best slice thickness to guarantee cell viability and achieve optimal V_m and Ca^{2+} signals using optical mapping techniques. Transverse slices less than 300 μm showed significantly reduced V_m and CaT signals (Fig. 1E). We suggest that, with mouse ventricular myocyte dimensions estimated as 90 μm (length) \times 25 μm (width) (Toischer *et al.* 2010), overly thin slices may result in damage to the vast majority of available cells within the slice. Slices thicker than 400 μm , on the other hand, required larger electrical stimulation pulses, longer post-cutting recovery time, and suffered from poor oxygenation and limited BDM washout. BDM, if not completely washed out, is known to have residual effects on cardiac ion channels (Coulombe *et al.* 1990). Oxygen supply, in the absence of vascular perfusion, is guaranteed by diffusion in cardiac slices. However, as the maximum diffusion distance for cardiac contracting muscle is estimated to be 150 μm (Barclay, 2005), slices thicker than 300 μm will be exposed to hypoxic conditions, resulting in limited viability.

In previous studies, post-cutting recovery times ranging from 30 min (Burnashev *et al.* 1990) to 2 h (Yasuhara *et al.* 1996) were reported. For transverse mouse ventricular slices we determined an optimal recovery period to be 30 min. Slices cut in cold (4°C), oxygenated (99.5%

O_2) Tyrode solution containing BDM were placed in Krebs solution containing 10 μM blebbistatin at room temperature (equilibrated with 95% O_2 /5% CO_2) to recover. The recovery time of 30 min allowed washout of BDM and returned the slices to a more physiological temperature. Our findings are consistent with previous reports indicating recovery times for adult guinea-pig slices and neonatal rat slices of, respectively, 36 min (Wang *et al.* 2015) and 30 min (Pertsov *et al.* 1993; Davidenko *et al.* 1995).

Conduction velocity as an indicator of physiological state is shown in Fig. 6. We demonstrate that conduction velocity in our cardiac slices is comparable to conduction velocity measured in whole mouse hearts by epicardial optical mapping (Baker *et al.* 2000; Baudenbacher *et al.* 2008; Myles *et al.* 2012; Bao *et al.* 2016). As expected, higher pacing frequencies lead to reduced conduction velocities, further demonstrating physiological responsiveness of the slices (Weber *et al.* 2011).

Cardiac slices for the study of transmural and regional heterogeneity of V_m and CaT

A critical advantage of the cardiac slice model is the ability to provide access to any region of the ventricles, thus enabling exploration of regional and transmural

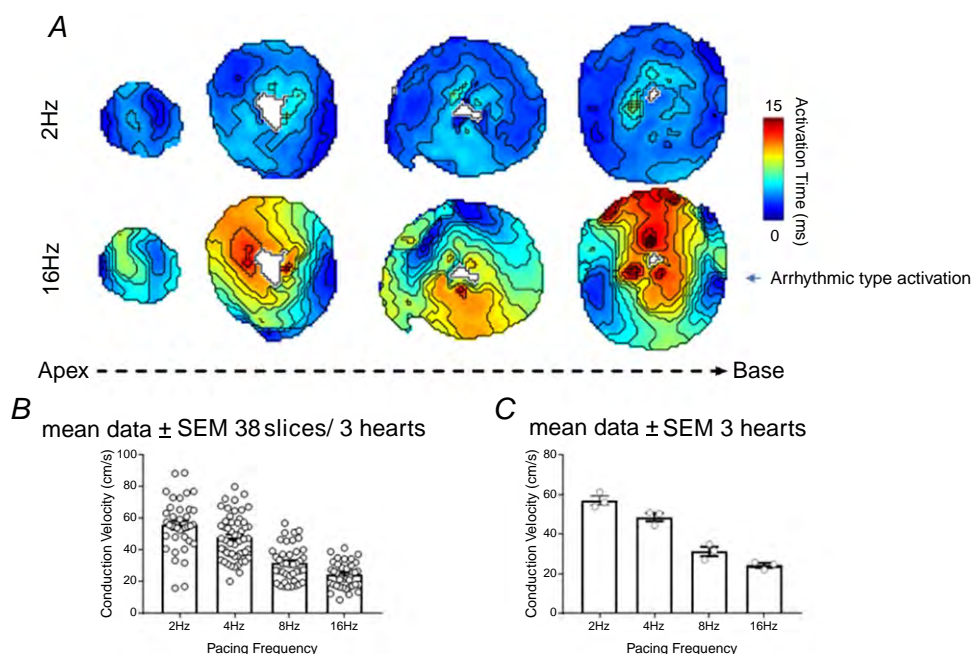


Figure 6. Analysis of conduction velocity (CV)

A, activation maps of slices (apex to base) paced at 2 Hz and 16 Hz. Conduction velocity (CV) was calculated using a multi-vector polynomial method within bespoke ElectroMap analysis software. A polynomial surface was fitted to local activation times to describe propagation in the area, and local CV quantified as the gradient vector of the polynomial surface. Mean CV was then calculated from the local CVs across the tissue slice. B, mean data for CV at a range of pacing frequencies calculated across all the slices ($n = 38$ slices/3 hearts). C, mean data for CV at a range of pacing frequencies calculated across all the hearts ($n = 3$ hearts).

differences. This is particularly important for the mouse heart, given that other *in vitro* tissue preparations, such as ventricular wedges, are not feasible for small hearts.

Action potential and calcium handling heterogeneities, and their role in the generation of arrhythmias, are well documented in hearts from larger mammals (Yan *et al.* 1998; Burton & Cobbe, 2001; Laurita *et al.* 2003; Cordeiro *et al.* 2004; Patel *et al.* 2009; Glukhov *et al.* 2010; Lou *et al.* 2011). However, experimental data on transmural and regional electrophysiological characteristics in the murine heart are still limited. In this study we have combined transverse murine cardiac slices with high resolution optical mapping for systematic transmural and regional profiling of both V_m and CaT across the murine ventricles. Our results indicate the presence of transmural

APD heterogeneities within the wall of the left ventricle (Fig. 3), with the shortest APD observed in the epicardium, in agreement with previously published results for single isolated myocytes (Brunet *et al.* 2004) and ventricular tissue (Knollmann *et al.* 2001). However, no significant apico-basal APD gradients were found in our study (Fig. 3), in contrast with previously reported findings on single isolated myocytes (Xu *et al.* 1999; Bondarenko *et al.* 2004). Transmural and apico-basal gradients in the transient outward K^+ current (I_{to}) are thought to be the main determinant of APD heterogeneities in the mouse ventricle (Xu *et al.* 1999; Brunet *et al.* 2004; Rossow *et al.* 2006).

Our results also indicate the presence of significant interventricular differences in APD, with shorter APD in the right ventricle in comparison to the left ventricle and

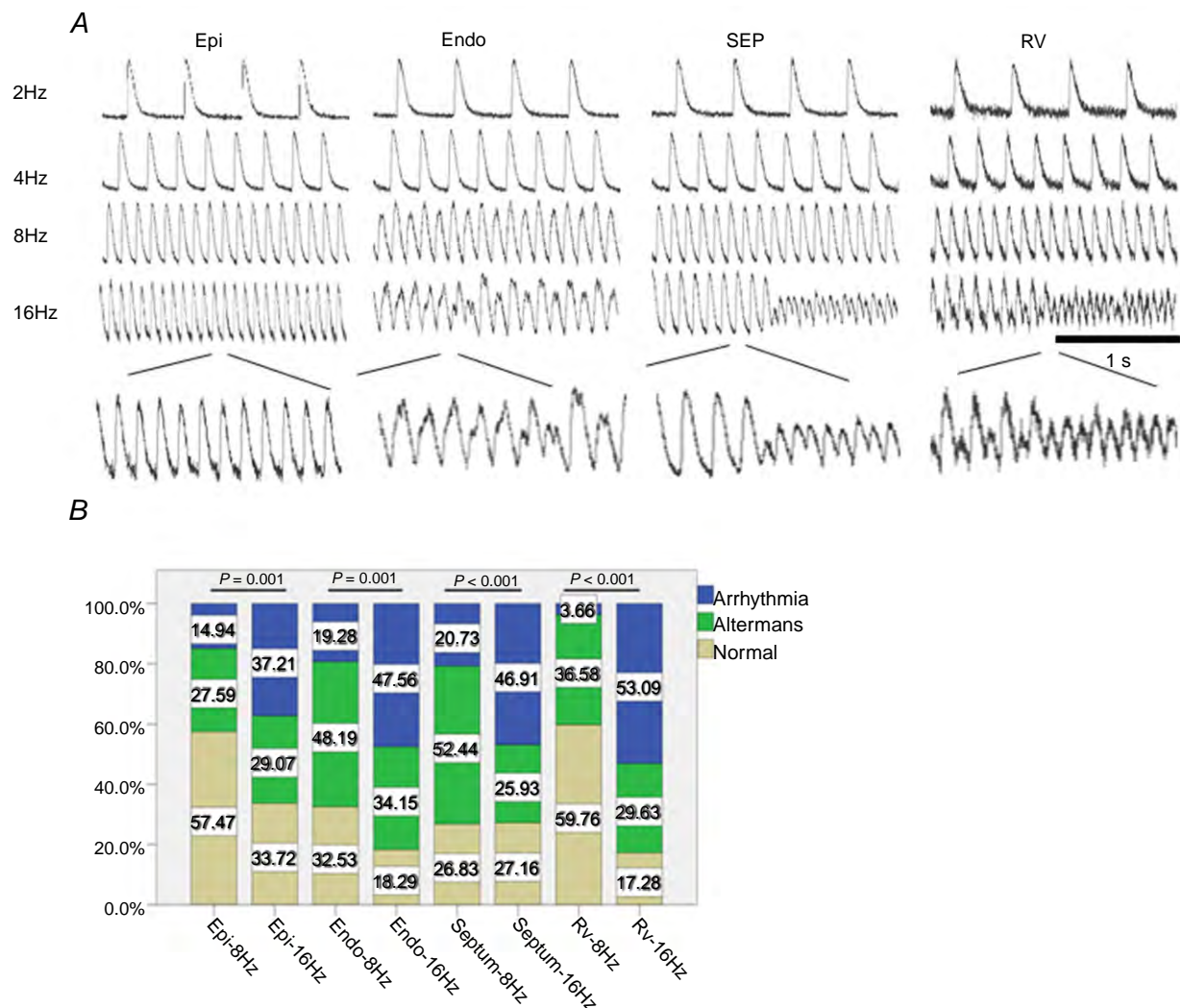


Figure 7. Regional and frequency-dependent distribution of CaT alternans and arrhythmic events in murine ventricular slices

A, representative optical CaT traces obtained from different regions within a ventricular slice during electrical pacing at 2, 4, 8 and 16 Hz frequency. Scale bar: 1 s. B, transmural and regional occurrence of alternans and arrhythmias at 8 Hz and 16 Hz pacing frequency. Epi, epicardium; Endo, endocardium; SEP, septum; RV, right ventricle; LV, left ventricle. $n = 6$ hearts.

ventricular septum (Fig. 3). This is in agreement with data from rodent studies (Watanabe *et al.* 1983; Knollmann *et al.* 2001) and larger mammals investigations (Di Diego *et al.* 1996; Volders *et al.* 1999), and it is likely to be the result of differences in repolarisation currents which are significantly higher in cells isolated from the right than the left ventricle (Brunet *et al.* 2004; Molina *et al.* 2016).

Analysis of Ca^{2+} transients revealed the presence of transmural and regional heterogeneity of calcium handling in the murine ventricles, in addition to action potential gradients. A significant transmural gradient of CaTD50 and CaTD75 was found in the LV wall, with a longer CaTD in the endocardium compared to the epicardium (Fig. 4). Similar results have been reported for hearts of other species (Figueredo *et al.* 1993; Laurita *et al.* 2003). Regional differences in the expression of calcium regulatory proteins could explain the observed transmural CaTD heterogeneity. Differences in sarcoplasmic reticulum Ca^{2+} -ATPase (SERCA2a) and ryanodine receptor type 2 (RyR2) protein expression, and sodium–calcium exchanger function, have been reported between epicardial and endocardial cells in different species including mouse (Laurita *et al.* 2003; Cordeiro *et al.* 2004; Dilly *et al.* 2006; Lou *et al.* 2011). We also observed interventricular differences in CaTD50 in our study, with a shorter CaTD50 in the right ventricle in comparison to the left ventricle and ventricular septum (Fig. 4), consistent with previously reported interventricular differences in Ca^{2+} handling and contractility in rodent hearts (Kondo *et al.* 2006; Molina *et al.* 2016).

AP and CaT alternans during rapid pacing

Cardiac alternans in the form of T-wave alternans in the ECG, corresponding to beat-to-beat alternations in ventricular repolarisation, has demonstrated clinical utility in stratifying risk for malignant arrhythmias and sudden cardiac death, providing guidance for anti-arrhythmic therapy (Verrier *et al.* 2011). At the cellular level, cardiac alternans manifests as rate-dependent beat-to-beat alternations in contraction, AP morphology and CaT amplitude (Kanaporis & Blatter, 2015). In our study, we observed alternans in AP amplitude as well as in CaT amplitude when murine slices were electrically stimulated at high pacing rates (Figs 5 and 6). Alternans in AP amplitude have been reported previously in left ventricular wedge preparations from normal and post-infarction rabbit hearts during rapid pacing (Myles *et al.* 2011). Importantly, alternans in AP amplitude were related to the development of arrhythmias during rapid pacing in the rabbit wedge, indicating that amplitude alternans may be an important mechanism for ventricular arrhythmia (Myles *et al.* 2011). As we demonstrated in Figs 5–7, arrhythmia was clearly triggered by high

pacing frequency, when we observed reduced conduction velocities and areas of steep activation gradients. The majority of the events we observed were the non-sustained ventricular tachycardia (VT) form; such non-sustained VT is likely to be caused by focal activity and steep activation gradients.

Our results indicate the presence of significant transmural differences in pacing-induced AP and CaT alternans in the mouse LV free wall, with greater incidence of alternans in the endocardium compared with the epicardium at both 8 Hz and 16 Hz pacing frequencies (Figs 5B and 7B). To the best of our knowledge, this is the first report describing transmural heterogeneities in frequency-dependent AP and CaT alternans in the murine heart. Regional differences in CaT alternans have been previously described in the canine LV during rapid pacing in studies using wedge preparations and isolated myocytes (Laurita *et al.* 2003; Cordeiro *et al.* 2007). In these published studies, larger levels of alternans were observed in cells near the endocardium compared with cells near the epicardium (Laurita *et al.* 2003; Cordeiro *et al.* 2007), consistent with the findings of our study.

In the current study, we observed similar transmural and regional distributions of AP and CaT alternans. Electrical and CaT alternans are known to be highly correlated, although it remains controversial whether the primary cause of cardiac alternans is a disturbance of intracellular Ca^{2+} signalling or electrical membrane properties. In a recent study by Kanaporis and Blatter (2015), the mechanisms of calcium cycling and action potential dynamics in cardiac alternans have been investigated in single rabbit atrial and ventricular myocytes using combined $[\text{Ca}^{2+}]_i$ and electrophysiological measurements. The findings indicate that suppression of Ca^{2+} release from the sarcoplasmic reticulum abolished APD alternans, supporting a central role for intracellular Ca^{2+} cycling in the development of cardiac alternans (Kanaporis & Blatter, 2015). Cardiac slices, simultaneously loaded with voltage- and Ca^{2+} -sensitive dyes, will allow us to examine the cellular mechanisms of cardiac alternans in a more representative multicellular model system.

Study limitations

A limitation to the study is the possibility of injury and uncoupling; partial uncoupling (reduction in conductance) could increase the differences in APDs between epicardial and endocardial regions.

Conclusions

We have developed and validated a robust experimental methodology which combines transverse ultra-thin cardiac slices and high resolution optical mapping to

enable systematic analysis of transmural and regional gradients in V_m and CaT across the entire murine ventricles.

References

- Asano Y, Takashima S, Asakura M, Shintani Y, Liao Y, Minamino T, Asanuma H, Sanada S, Kim J, Ogai A, Fukushima T, Oikawa Y, Okazaki Y, Kaneda Y, Sato M, Miyazaki J, Kitamura S, Tomoike H, Kitakaze M & Hori M (2004). Lmr1 functional retroposon causes right ventricular dysplasia in mice. *Nat Genet* **36**, 123–130.
- Baker LC, London B, Choi BR, Koren G & Salama G (2000). Enhanced dispersion of repolarization and refractoriness in transgenic mouse hearts promotes reentrant ventricular tachycardia. *Circ Res* **86**, 396–407.
- Bao Y, Willis BC, Frasier CR, Lopez-Santiago LF, Lin X, Ramos-Mondragon R, Auerbach DS, Chen C, Wang Z, Anumonwo J, Valdivia HH, Delmar M, Jalife J & Isom LL (2016). Scn2b deletion in mice results in ventricular and atrial arrhythmias. *Circ Arrhythm Electrophysiol* **9**, e003923.
- Barclay CJ (2005). Modelling diffusive O_2 supply to isolated preparations of mammalian skeletal and cardiac muscle. *J Muscle Res Cell Motil* **26**, 225–235.
- Baudenbacher F, Schober T, Pinto JR, Sidorov VY, Hilliard F, Solaro RJ, Potter JD & Knollmann BC (2008). Myofilament Ca^{2+} sensitization causes susceptibility to cardiac arrhythmia in mice. *J Clin Invest* **118**, 3893–3903.
- Bayly PV, KenKnight BH, Rogers JM, Hillsley RE, Ideker RE & Smith WM (1998). Estimation of conduction velocity vector fields from epicardial mapping data. *IEEE Trans Biomed Eng* **45**, 563–571.
- Bondarenko VE, Szigeti GP, Bett GC, Kim SJ & Rasmusson RL (2004). Computer model of action potential of mouse ventricular myocytes. *Am J Physiol Heart Circ Physiol* **287**, H1378–H1403.
- Brunet S, Aimond F, Li H, Guo W, Eldstrom J, Fedida D, Yamada KA & Nerbonne JM (2004). Heterogeneous expression of repolarizing, voltage-gated K^+ currents in adult mouse ventricles. *J Physiol* **559**, 103–120.
- Burnashev NA, Edwards FA & Verkhratsky AN (1990). Patch-clamp recordings on rat cardiac muscle slices. *Pflugers Arch* **417**, 123–125.
- Burton FL & Cobbe SM (2001). Dispersion of ventricular repolarization and refractory period. *Cardiovasc Res* **50**, 10–23.
- Bussek A, Wettwer E, Christ T, Lohmann H, Camelliti P & Ravens U (2009). Tissue slices from adult mammalian hearts as a model for pharmacological drug testing. *Cell Physiol Biochem* **24**, 527–536.
- Camelliti P, Al-Saud SA, Smolenski RT, Al-Ayoubi S, Bussek A, Wettwer E, Banner NR, Bowles CT, Yacoub MH & Terracciano CM (2011). Adult human heart slices are a multicellular system suitable for electrophysiological and pharmacological studies. *J Mol Cell Cardiol* **51**, 390–398.
- Choy L, Yeo JM, Tse V, Chan SP & Tse G (2016). Cardiac disease and arrhythmogenesis: Mechanistic insights from mouse models. *Int J Cardiol Heart Vasc* **12**, 1–10.
- Cordeiro JM, Greene L, Heilmann C, Antzelevitch D & Antzelevitch C (2004). Transmural heterogeneity of calcium activity and mechanical function in the canine left ventricle. *Am J Physiol Heart Circ Physiol* **286**, H1471–H1479.
- Cordeiro JM, Malone JE, Di Diego JM, Scornik FS, Aistrup GL, Antzelevitch C & Wasserstrom JA (2007). Cellular and subcellular alternans in the canine left ventricle. *Am J Physiol Heart Circ Physiol* **293**, H3506–H3516.
- Coulombe A, Lefevre IA, Deroubaix E, Thuringer D & Coraboeuf E (1990). Effect of 2,3-butanedione 2-monoxime on slow inward and transient outward currents in rat ventricular myocytes. *J Mol Cell Cardiol* **22**, 921–932.
- Davidenko JM, Salomonsz R, Pertsov AM, Baxter WT & Jalife J (1995). Effects of pacing on stationary reentrant activity. Theoretical and experimental study. *Circ Res* **77**, 1166–1179.
- Di Diego JM, Sun ZQ & Antzelevitch C (1996). I_{to} and action potential notch are smaller in left vs. right canine ventricular epicardium. *Am J Physiol* **271**, H548–H561.
- Dilly KW, Rossow CF, Votaw VS, Meabon JS, Cabarrus JL & Santana LF (2006). Mechanisms underlying variations in excitation-contraction coupling across the mouse left ventricular free wall. *J Physiol* **572**, 227–241.
- Figueredo VM, Brandes R, Weiner MW, Massie BM & Camacho SA (1993). Endocardial versus epicardial differences of intracellular free calcium under normal and ischemic conditions in perfused rat hearts. *Circ Res* **72**, 1082–1090.
- Grundy D (2015). Principles and standards for reporting animal experiments in *The Journal of Physiology* and *Experimental Physiology*. *J Physiol* **593**, 2547–2549.
- Glukhov AV, Fedorov VV, Lou Q, Ravikumar VK, Kalish PW, Schuessler RB, Moazami N & Efimov IR (2010). Transmural dispersion of repolarization in failing and nonfailing human ventricle. *Circ Res* **106**, 981–991.
- Halbach M, Pillekamp F, Brockmeier K, Hescheler J, Muller-Ehmsen J & Reppel M (2006). Ventricular slices of adult mouse hearts—a new multicellular in vitro model for electrophysiological studies. *Cell Physiol Biochem* **18**, 1–8.
- Himmel HM, Bussek A, Hoffmann M, Beckmann R, Lohmann H, Schmidt M & Wettwer E (2012). Field and action potential recordings in heart slices: correlation with established in vitro and in vivo models. *Br J Pharmacol* **166**, 276–296.
- Kanaporis G & Blatter LA (2015). The mechanisms of calcium cycling and action potential dynamics in cardiac alternans. *Circ Res* **116**, 846–856.
- Kang C, Qiao Y, Li G, Baechle K, Camelliti P, Rentschler S & Efimov IR (2016). Human organotypic cultured cardiac slices: new platform for high throughput preclinical human trials. *Sci Rep* **6**, 28798.
- Knollmann BC, Katchman AN & Franz MR (2001). Monophasic action potential recordings from intact mouse heart: validation, regional heterogeneity, and relation to refractoriness. *J Cardiovasc Electrophysiol* **12**, 1286–1294.
- Kondo RP, Dederko DA, Teutsch C, Chrast J, Catalucci D, Chien KR & Giles WR (2006). Comparison of contraction and calcium handling between right and left ventricular myocytes from adult mouse heart: a role for repolarization waveform. *J Physiol* **571**, 131–146.

- Lander ES, Linton LM, Birren B, Nusbaum C, Zody MC, Baldwin J, Devon K, Dewar K, Doyle M, FitzHugh W, Funke R, Gage D, Harris K, Heaford A, Howland J, Kann L, Lehoczky J, LeVine R, McEwan P, McKernan K, Meldrim J, Mesirov JP, Miranda C, Morris W, Naylor J, Raymond C, Rosetti M, Santos R, Sheridan A, Sougnez C, Stange-Thomann Y, Stojanovic N, Subramanian A, Wyman D, Rogers J, Sulston J, Ainscough R, Beck S, Bentley D, Burton J, Clee C, Carter N, Coulson A, Deadman R, Deloukas P, Dunham A, Dunham I, Durbin R, French L, Grafham D, Gregory S, Hubbard T, Humphray S, Hunt A, Jones M, Lloyd C, McMurray A, Matthews L, Mercer S, Milne S, Mullikin JC, Mungall A, Plumb R, Ross M, Shownkeen R, Sims S, Waterston RH, Wilson RK, Hillier LW, McPherson JD, Marra MA, Mardis ER, Fulton LA, Chinwalla AT, Pepin KH, Gish WR, Chisoe SL, Wendl MC, Delehaunty KD, Miner TL, Delehaunty A, Kramer JB, Cook LL, Fulton RS, Johnson DL, Minx PJ, Clifton SW, Hawkins T, Branscomb E, Predki P, Richardson P, Wenning S, Slezak T, Doggett N, Cheng JF, Olsen A, Lucas S, Elkin C, Uberbacher E, Frazier M, Gibbs RA, Muzny DM, Scherer SE, Bouck JB, Sodergren EJ, Worley KC, Rives CM, Gorrell JH, Metzker ML, Naylor SL, Kucherlapati RS, Nelson DL, Weinstock GM, Sakaki Y, Fujiyama A, Hattori M, Yada T, Toyoda A, Itoh T, Kawagoe C, Watanabe H, Totoki Y, Taylor T, Weissbach J, Heilig R, Saurin W, Artiguenave F, Brottier P, Bruls T, Pelletier E, Robert C, Wincker P, Smith DR, Doucette-Stamm L, Rubenfield M, Weinstock K, Lee HM, Dubois J, Rosenthal A, Platzer M, Nyakatura G, Taudien S, Rump A, Yang H, Yu J, Wang J, Huang G, Gu J, Hood L, Rowen L, Madan A, Qin S, Davis RW, Federspiel NA, Abola AP, Proctor MJ, Myers RM, Schmutz J, Dickson M, Grimwood J, Cox DR, Olson MV, Kaul R, Raymond C, Shimizu N, Kawasaki K, Minoshima S, Evans GA, Athanasiou M, Schultz R, Roe BA, Chen F, Pan H, Ramser J, Lehrach H, Reinhardt R, McCombie WR, de la Bastide M, Dedhia N, Blocker H, Hornischer K, Nordsiek G, Agarwala R, Aravind L, Bailey JA, Bateman A, Batzoglu S, Birney E, Bork P, Brown DG, Burge CB, Cerutti L, Chen HC, Church D, Clamp M, Copley RR, Doerks T, Eddy SR, Eichler EE, Furey TS, Galagan J, Gilbert JG, Harmon C, Hayashizaki Y, Haussler D, Hermjakob H, Hokamp K, Jang W, Johnson LS, Jones TA, Kasif S, Kasprzyk A, Kennedy S, Kent WJ, Kitts P, Koonin EV, Korf I, Kulp D, Lancet D, Lowe TM, McLysaght A, Mikkelsen T, Moran JV, Mulder N, Pollara VJ, Ponting CP, Schuler G, Schultz J, Slater G, Smit AF, Stupka E, Szustakowski J, Thierry-Mieg D, Thierry-Mieg J, Wagner L, Wallis J, Wheeler R, Williams A, Wolf YI, Wolfe KH, Yang SP, Yeh RF, Collins F, Guyer MS, Peterson J, Felsenfeld A, Wetterstrand KA, Patrinos A, Morgan MJ, de Jong P, Catanese JJ, Osoegawa K, Shizuya H, Choi S, Chen YJ & Szustakowski J (2001). Initial sequencing and analysis of the human genome. *Nature* **409**, 860–921.
- Laurita KR, Katra R, Wible B, Wan X & Koo MH (2003). Transmural heterogeneity of calcium handling in canine. *Circ Res* **92**, 668–675.
- Lou Q, Fedorov VV, Glukhov AV, Moazami N, Fast VG & Efimov IR (2011). Transmural heterogeneity and remodeling of ventricular excitation-contraction coupling in human heart failure. *Circulation* **123**, 1881–1890.
- Molina CE, Heijman J & Dobrev D (2016). Differences in left versus right ventricular electrophysiological properties in cardiac dysfunction and arrhythmogenesis. *Arrhythm Electrophysiol Rev* **5**, 14–19.
- Myles RC, Burton FL, Cobbe SM & Smith GL (2011). Alternans of action potential duration and amplitude in rabbits with left ventricular dysfunction following myocardial infarction. *J Mol Cell Cardiol* **50**, 510–521.
- Myles RC, Wang L, Kang C, Bers DM & Ripplinger CM (2012). Local beta-adrenergic stimulation overcomes source-sink mismatch to generate focal arrhythmia. *Circ Res* **110**, 1454–1464.
- Nerbonne JM (2014). Mouse models of arrhythmogenic cardiovascular disease: challenges and opportunities. *Current Opin Pharmacol* **15**, 107–114.
- O'Shea C, Holmes A, Yu TY, Winter J, Correia J, Kirchhof P, Fabritz L, Rajpoot K & Pavlovic D (2017). 188 Development of a novel software package for high-throughput processing and analysis of cardiac optical mapping data. *Heart* **103**, A128–A129.
- Papadatos GA, Wallerstein PMR, Head CEG, Ratcliff R, Brady PA, Benndorf K, Saumarez RC, Trezise AEO, Huang CLH, Vandenberg JJ, Colledge WH & Grace AA (2002). Slowed conduction and ventricular tachycardia after targeted disruption of the cardiac sodium channel gene *Scn5a*. *Proc Natl Acad Sci U S A* **99**, 6210–6215.
- Patel C, Burke JF, Patel H, Gupta P, Kowey PR, Antzelevitch C & Yan GX (2009). Is there a significant transmural gradient in repolarization time in the intact heart? Cellular basis of the T wave: a century of controversy. *Circ Arrhythm Electrophysiol* **2**, 80–88.
- Pertsov AM, Davidenko JM, Salomonsz R, Baxter WT & Jalife J (1993). Spiral waves of excitation underlie reentrant activity in isolated cardiac muscle. *Circ Res* **72**, 631–650.
- Rossow CF, Dilly KW & Santana LF (2006). Differential calcineurin/NFATc3 activity contributes to the Ito transmural gradient in the mouse heart. *Circ Res* **98**, 1306–1313.
- Sabir IN, Killeen MJ, Grace AA & Huang CL (2008). Ventricular arrhythmogenesis: insights from murine models. *Prog Biophys Mol Biol* **98**, 208–218.
- Toischer K, Rokita AG, Unsold B, Zhu W, Kararigas G, Sossalla S, Reuter SP, Becker A, Teucher N, Seidler T, Grebe C, Preuss L, Gupta SN, Schmidt K, Lehnart SE, Kruger M, Linke WA, Backs J, Regitz-Zagrosek V, Schafer K, Field LJ, Maier LS & Hasenfuss G (2010). Differential cardiac remodeling in preload versus afterload. *Circulation* **122**, 993–1003.
- Verrier RL, Klingenhoben T, Malik M, El-Sherif N, Exner DV, Hohnloser SH, Ikeda T, Martinez JP, Narayan SM, Nieminen T & Rosenbaum DS (2011). Microvolt T-wave alternans physiological basis, methods of measurement, and clinical utility – consensus guideline by International Society for Holter and Noninvasive Electrocardiology. *J Am Coll Cardiol* **58**, 1309–1324.
- Volders PG, Sipido KR, Carmeliet E, Spatjens RL, Wellens HJ & Vos MA (1999). Repolarizing K^+ currents I_{TO1} and I_{Ks} are larger in right than left canine ventricular midmyocardium. *Circulation* **99**, 206–210.

- Wang K, Lee P, Mirams GR, Sarathchandra P, Borg TK, Gavaghan DJ, Kohl P & Bollensdorff C (2015). Cardiac tissue slices: preparation, handling, and successful optical mapping. *Am J Physiol Heart Circ Physiol* **308**, H1112–H1125.
- Wang K, Terrar D, Gavaghan DJ, Mu UMR, Kohl P & Bollensdorff C (2014). Living cardiac tissue slices: an organotypic pseudo two-dimensional model for cardiac biophysics research. *Prog Biophys Mol Biol* **115**, 314–327.
- Watanabe T, Delbridge LM, Bustamante JO & McDonald TF (1983). Heterogeneity of the action potential in isolated rat ventricular myocytes and tissue. *Circ Res* **52**, 280–290.
- Waterston RH, Lindblad-Toh K, Birney E, Rogers J, Abril JF, Agarwal P, Agarwala R, Ainscough R, Alexandersson M, An P, Antonarakis SE, Attwood J, Baertsch R, Bailey J, Barlow K, Beck S, Berry E, Birren B, Bloom T, Bork P, Botcherby M, Bray N, Brent MR, Brown DG, Brown SD, Bult C, Burton J, Butler J, Campbell RD, Carninci P, Cawley S, Chiaromonte F, Chinwalla AT, Church DM, Clamp M, Clee C, Collins FS, Cook LL, Copley RR, Coulson A, Couronne O, Cuff J, Curwen V, Cutts T, Daly M, David R, Davies J, Delehaunty KD, Deri J, Dermitzakis ET, Dewey C, Dickens NJ, Diekhans M, Dodge S, Dubchak I, Dunn DM, Eddy SR, Elnitski L, Emes RD, Eswara P, Eyrae E, Felsenfeld A, Fewell GA, Flicek P, Foley K, Frankel WN, Fulton LA, Fulton RS, Furey TS, Gage D, Gibbs RA, Glusman G, Gnerre S, Goldman N, Goodstadt L, Grafham D, Graves TA, Green ED, Gregory S, Guigo R, Guyer M, Hardison RC, Haussler D, Hayashizaki Y, Hillier LW, Hinrichs A, Hlavina W, Holzer T, Hsu F, Hua A, Hubbard T, Hunt A, Jackson I, Jaffe DB, Johnson LS, Jones M, Jones TA, Joy A, Kamal M, Karlsson EK, Karolchik D, Kasprzyk A, Kawai J, Keibler E, Kells C, Kent WJ, Kirby A, Kolbe DL, Korf I, Kucherlapati RS, Kulbokas EJ, Kulp D, Landers T, Leger JP, Leonard S, Letunic I, Levine R, Li J, Li M, Lloyd C, Lucas S, Ma B, Maglott DR, Mardis ER, Matthews L, Mauceli E, Mayer JH, McCarthy M, McCombie WR, McLaren S, McLay K, McPherson JD, Meldrum J, Meredith B, Mesirov JP, Miller W, Miner TL, Mongin E, Montgomery KT, Morgan M, Mott R, Mullikin JC, Muzny DM, Nash WE, Nelson JO, Nhan MN, Nicol R, Ning Z, Nusbaum C, O'Connor MJ, Okazaki Y, Oliver K, Overton-Larty E, Pachter L, Parra G, Pepin KH, Peterson J, Pevzner P, Plumb R, Pohl CS, Poliakov A, Ponce TC, Ponting CP, Potter S, Quail M, Raymond A, Roe BA, Roskin KM, Rubin EM, Rust AG, Santos R, Sapozhnikov V, Schultz B, Schultz J, Schwartz MS, Schwartz S, Scott C, Seaman S, Searle S, Sharpe T, Sheridan A, Shownkeen R, Sims S, Singer JB, Slater G, Smit A, Smith DR, Spencer B, Stabenau A, Stange-Thomann N, Sugnet C, Suyama M, Tesler G, Thompson J, Torrents D, Trevaskis E, Tromp J, Ucla C, Ureta-Vidal A, Vinson JP, Von Niederhausern AC, Wade CM, Wall M, Weber RJ, Weiss RB, Wendl MC, West AP, Wetterstrand K, Wheeler R, Whelan S, Wierzbowski J, Willey D, Williams S, Wilson RK, Winter E, Worley KC, Wyman D, Yang S, Yang SP, Zdobnov EM, Zody MC & Lander ES (2002). Initial sequencing and comparative analysis of the mouse genome. *Nature* **420**, 520–562.
- Weber FM, Luik A, Schilling C, Seemann G, Krueger MW, Lorenz C, Schmitt C & Dossel O (2011). Conduction velocity restitution of the human atrium – an efficient measurement protocol for clinical electrophysiological studies. *IEEE Trans Biomed Eng* **58**, 2648–2655.
- Wehrens XH, Lehnart SE, Huang F, Vest JA, Reiken SR, Mohler PJ, Sun J, Guatimosim S, Song LS, Rosembly N, D'Armiento JM, Napolitano C, Memmi M, Priori SG, Lederer WJ & Marks AR (2003). FKBP12.6 deficiency and defective calcium release channel (ryanodine receptor) function linked to exercise-induced sudden cardiac death. *Cell* **113**, 829–840.
- Wu J, Zhang Y, Zhang X, Cheng L, Lammers WJEP, Grace AA, Fraser JA, Zhang H, Huang CLH & Lei M (2012). Altered sino-atrial node function and intra-atrial conduction in murine gain-of-function Scn5a+/delta KPQ hearts suggest an overlap syndrome. *Am J Physiol Heart Circ Physiol* **302**, H1510–H1523.
- Xu H, Guo W & Nerbonne JM (1999). Four kinetically distinct depolarization-activated K⁺ currents in adult mouse ventricular myocytes. *J Gen Physiol* **113**, 661–678.
- Yan GX, Shimizu W & Antzelevitch C (1998). Characteristics and distribution of M cells in arterially perfused canine left ventricular wedge preparations. *Circulation* **98**, 1921–1927.
- Yasuhara S, Takaki M, Kikuta A, Ito H & Suga H (1996). Myocardial VO₂ of mechanically unloaded contraction of rat ventricular slices measured by a new approach. *Am J Physiol Heart Circ Physiol* **270**, H1063–H1070.

Additional information

Competing interests

We confirm that none of the authors has any conflicts of interests on the submission form and in the manuscript.

Author contributions

Q.W, K.G, R.C, G.N and S.P: acquisition, analysis and/or interpretation of data for the work; G.H and C.OS: analysis and/or interpretation of data for the work, M.L and P.C: conception and design of the work, manuscript writing and revising it critically for important intellectual content; D.P, D.T, J.W and G.F: supporting the work and revising manuscript critically for important intellectual content. All authors have approved the final version of the manuscript and agree to be accountable for all aspects of the work. All persons designated as authors qualify for authorship, and all those who qualify for authorship are listed.

Funding

This study was supported by MRC (G10002647, G1002082; M.L.), BHF (PG/14/80/31106, PG/16/67/32340, PG/12/21/29473, PG/11/59/29004; M.L.), BHF CRE at Oxford (M.L.) grants.

5.2 A protocol for transverse cardiac slicing and optical mapping in murine heart.

Publication 5. This research was originally published in Frontiers in Physiology.

A protocol for transverse cardiac slicing and optical mapping in murine heart. S C He*, Q Wen*, **C O'Shea***, R Mu-u-min*, K Kun, A Grassam-Rowe, Y Liu, Z Fan, X Q Tan, X Ou, P Camelliti, D Pavlovic, M Lei. Front. Physiol. 10:755, 1-8, 2019.

*These authors share first authorship

Author contributions in publication 5

I performed all data analysis presented and contributed to writing the protocol and manuscript. Experiments described were carried out at Southwest Medical University or University of Oxford, and not conducted by myself.



A Protocol for Transverse Cardiac Slicing and Optical Mapping in Murine Heart

S. He^{1†}, Q. Wen^{2†}, C. O'Shea^{3†}, R. Mu-u-min^{4†}, K. Kou¹, A. Grassam-Rowe⁴, Y. Liu⁵, Z. Fan⁵, X. Tan¹, X. Ou^{1‡}, P. Camelliti^{6‡}, D. Pavlovic^{3‡} and M. Lei^{1,4*‡}

¹ Key Laboratory of Medical Electrophysiology of Ministry of Education and Medical Electrophysiological Key Laboratory of Sichuan Province, Institute of Cardiovascular Research, Southwest Medical University, Luzhou, China, ² Institute of Cardiology, Union Hospital, Tongji Medical College, Huazhong University of Science and Technology, Wuhan, China, ³ Institute of Cardiovascular Sciences, University of Birmingham, Birmingham, United Kingdom, ⁴ Department of Pharmacology, University of Oxford, Oxford, United Kingdom, ⁵ Department of Cardiovascular Medicine, Southwest Medical University, Luzhou, China, ⁶ School of Biosciences and Medicine, University of Surrey, Guildford, United Kingdom

OPEN ACCESS

Edited by:

Bas J. Boukens,
University of Amsterdam, Netherlands

Reviewed by:

Mathilde R. Rivaud,
Netherlands Heart Institute,
Netherlands
Franziska Schneider-Warme,
Universitäts-Herzzentrum
Freiburg-Bad Krozingen, Germany

*Correspondence:

M. Lei
ming.lei@pharm.ox.ac.uk

[†]Joint first authors

[‡]Joint senior authors

Specialty section:

This article was submitted to
Cardiac Electrophysiology,
a section of the journal
Frontiers in Physiology

Received: 08 December 2018

Accepted: 31 May 2019

Published: 25 June 2019

Citation:

He S, Wen Q, O'Shea C,
Mu-u-min R, Kou K,
Grassam-Rowe A, Liu Y, Fan Z, Tan X,
Ou X, Camelliti P, Pavlovic D and
Lei M (2019) A Protocol
for Transverse Cardiac Slicing
and Optical Mapping in Murine Heart.
Front. Physiol. 10:755.
doi: 10.3389/fphys.2019.00755

Thin living tissue slices have recently emerged as a new tissue model for cardiac electrophysiological research. Slices can be produced from human cardiac tissue, in addition to small and large mammalian hearts, representing a powerful *in vitro* model system for preclinical and translational heart research. In the present protocol, we describe a detailed mouse heart transverse slicing and optical imaging methodology. The use of this technology for high-throughput optical imaging allows study of electrophysiology of murine hearts in an organotypic pseudo two-dimensional model. The slices are cut at right angles to the long axis of the heart, permitting robust interrogation of transmembrane potential (V_m) and calcium transients (CaT) throughout the entire heart with exceptional regional precision. This approach enables the use of a series of slices prepared from the ventricles to measure V_m and CaT with high temporal and spatial resolution, allowing (i) comparison of successive slices which form a stack representing the original geometry of the heart; (ii) profiling of transmural and regional gradients in V_m and CaT in the ventricle; (iii) characterization of transmural and regional profiles of action potential and CaT alternans under stress (e.g., high frequency pacing or β -adrenergic stimulation) or pathological conditions (e.g., hypertrophy). Thus, the protocol described here provides a powerful platform for innovative research on electrical and calcium handling heterogeneity within the heart. It can be also combined with optogenetic technology to carry out optical stimulation; aiding studies of cellular V_m and CaT in a cell type specific manner.

Keywords: optical mapping, transverse cardiac slice, membrane potentials, Ca^{2+} transients, murine heart

INTRODUCTION

Thin living tissue slices are a widely used experimental preparation for electrophysiological studies of the brain (Accardi et al., 2016). Slices have recently been adopted as a promising model for the investigations of cardiac electrophysiology in different species, for example: viral delivery, culturing, and mechanical stimulation (Halbach et al., 2006; Bussek et al., 2009; Camelliti et al., 2011;

Wang et al., 2015; Kang et al., 2016; Thomas et al., 2016; Randi et al., 2017; Watson et al., 2017, 2019; Wen et al., 2018). Importantly, cardiac slices exhibit similar electrophysiological characteristics to the intact heart and respond to the application of pharmacological compounds similarly to the whole heart (Bussek et al., 2009; Camelliti et al., 2011; Wen et al., 2018). They have advantages for investigating transmural and regional characteristics of a variety of physiological parameters of the heart, thus providing a promising experimental model for heart research.

Because of feasibility for genetic modification, the mouse has been widely used for exploring molecular, cellular and systemic mechanisms underlying inherited and acquired cardiac arrhythmic diseases (Nerbonne and Kass, 2005; Huang, 2017). Despite the popularity of mouse models in cardiac arrhythmic research, cardiac transmural heterogeneities of action potential and Ca^{2+} transient characteristics, which are vitally important for phenotypic and mechanistic research in cardiac disease conditions, have only been explored recently in the mouse heart (Wen et al., 2018). We reported a robust approach for transverse cardiac slicing and optical mapping of transmembrane potential (V_m) and intracellular Ca^{2+} transient (CaT) in murine hearts, providing unprecedented and potentially high-throughput characterization of action potentials (APs) and intracellular Ca^{2+} transients *everywhere* in the mouse ventricles (Wen et al., 2018). Such an approach can be potentially adapted for large mammalian hearts and human tissue, thus representing a powerful *in vitro* model system for translational cardiovascular research (Thomas et al., 2016; Randi et al., 2017; Watson et al., 2017, 2019). Using this technique, we demonstrated the feasibility of our new approach to cardiac slicing for systematic analysis of intrinsic transmural and regional gradients in V_m and CaT in murine ventricular tissue (Wen et al., 2018).

In the present protocol, we describe a detailed feasible transverse slicing method, cutting slices at right angles to the long axis of the heart and combined it with a high-throughput optical imaging technique as a new approach for studying cellular electrophysiology of murine heart in an organotypic pseudo two-dimensional ventricular tissue model. Our method enables the use of a series of slices prepared from the ventricles to simultaneously measure V_m and CaT with high temporal and spatial resolution allowing comparison of transmural and regional profiles of APs and CaTs. This technique can potentially be combined with other molecular techniques such as *in situ* immunostaining and virus transfection to gain insight into arrhythmia mechanisms in various heart disease conditions.

MATERIALS AND EQUIPMENT

Animals

Animals used were 10–12 weeks, 20–25 g, male C57BL mice or Pnmt-Cre/ Channelrhodopsin 2 (ChR2) mice as we previously reported (Wang et al., 2017). The Pnmt-Cre/ChR2 mouse line exhibits cell-type specific expression of ChR2 by crossing B6.Cg-Gt (ROSA)26Sor^{tm27.1}(CAG-COP4H134R/tdTomato)Hze/J strain (Stock No. 012567, Jackson Labs) with a Cre transgenic

strain under the control of a *Pnmt* promoter (Wang et al., 2017). ChR2 was specifically introduced into murine cells expressing the *Phenylethanolamine n-methyltransferase* (*Pnmt*) gene, which encodes for the enzyme responsible for conversion of noradrenaline to adrenaline. The murine model led to the identification of a distinctive class of Pnmt-expressing neuroendocrine cells and their descendants (i.e., Pnmt⁺ cell derived cardiomyocytes) within the heart (Wang et al., 2017).

All procedures including animal subjects have been approved by Institutional Animals Ethics Committees at Southwest Medical University, Luzhou, China or Department of Pharmacology at University of Oxford, United Kingdom and the national guidelines under which the institution operates. All mice used in this study were maintained in a pathogen-free facility at Southwest Medical University or University of Oxford. Mice were given *ad libitum* access to food and water. The authors confirm that they have taken all steps to minimize the animals' pain and suffering.

Chemicals and Reagents

The relevant information of the chemicals and reagents are described in **Table 1**.

Instruments and Equipment

- Dumont forceps (Medical Equipment Factory of Shanghai Medical Instruments Co., Ltd., Shanghai, China).
- Mayo scissors (Medical Equipment Factory of Shanghai Medical Instruments Co., Ltd., Shanghai, China).
- Kelly hemostatic forceps (Medical Equipment Factory of Shanghai Medical Instruments Co., Ltd., Shanghai, China).
- Iris forceps (Medical Equipment Factory of Shanghai Medical Instruments Co., Ltd., Shanghai, China).
- Syringe Filter, Aquo-system, 0.45 μm /13 mm (Sangon Biotech Shanghai, China, F513143-0001).
- Langendorff perfusion system.
- Perfusion pump (Longer Precision Pump Co., Ltd., Baoding, China, BT100-2J).
- Vibration slicer (Leica VT1000s, Nussloch, Germany).
- EMCCD camera (Evolve 512, Photometrics, Tucson, AZ, United States).
- MacroLED light source (Cairn Research, Faversham, United Kingdom).
- MyoPacer EP field stimulator (Ion Optix Co., Milton, MA, United States S006152).
- Electrical stimulation chamber (custom-made by the workshop of Department of Pharmacology, University of Oxford).
- Heater Controller (custom-made by the workshop of Department of Pharmacology, University of Oxford).

Solutions

- Krebs solution (containing in mM: NaCl 119, NaHCO_3 25, NaH_2PO_4 1.0, KCl 4.7, MgCl_2 1.05, CaCl_2 1.35, and glucose 10; equilibrated with 95% O_2 /5% CO_2 , pH 7.4) at 37°C, pH = 7.35–7.4.
- HEPES buffered BDM solution (in mM: NaCl 140; KCl 4.7; glucose 10; HEPES 10; MgCl_2 1.05; CaCl_2 1.35; pH 7.4)

TABLE 1 | Reagents utilized.

Chemical and catalog references	Supplier
NaCl (SLBS2340V)	Sigma-Aldrich, St. Louis, MO, United States
NaHCO ₃ (SLBX3605)	Sigma-Aldrich
NaH ₂ PO ₄ (BCBW9042)	Sigma-Aldrich
KCl (SLBS5003)	Sigma-Aldrich
MgCl ₂ (BCBS6841V)	Sigma-Aldrich
CaCl ₂ (SLBK1794V)	Sigma-Aldrich
Glucose (SLBT4811V)	Sigma-Aldrich
HEPES (W1122DO10)	Sangon biological, Shanghai, China
2,3-butanedione monoxime (BDM) (29297)	Sigma-Aldrich
Blebbistatin (SLBV5564)	Tocris Bioscience, Minneapolis, MN, United States
Voltage-sensitive dye RH237 (1971387)	Thermo Fisher Scientific, Waltham, MA, United States
Calcium indicator Rhod-2AM (1890519)	Invitrogen, Carlsbad, CA, United States
Dimethyl sulfoxide (DMSO) (RNBT7442)	Sigma-Aldrich
Heparin Sodium (H51021209)	Chengdu Haitong Pharmaceutical Co., Ltd., Chengdu, China
Avertin (2,2,2-tribromoethanol)	Sigma-Aldrich Poole, Dorset, United Kingdom
Pluronic F127 (1899021)	Invitrogen, Carlsbad, CA, United States
Low-melt agarose (A600015.0005)	BBi Life Sciences, Shanghai, China

containing the excitation–contraction uncoupler 2,3-butanedione monoxime (BDM, 10 mM) and was stored at 4°C.

- Blebbistatin stock solution, 10 mM in DMSO.
- Voltage-sensitive dye RH237 stock solution, 1.25 mg/mL in DMSO.
- Calcium indicator Rhod-2AM stock solution, 1 mg/mL in DMSO.

Preparation of Experimental Setup(s)

- Prepare the Langendorff perfusion system. Turn on the perfusion system pump. Starting the peristaltic pump that is used for retrograde perfusion. Wash the perfusion system with 1 L deionized water with initial flow rate at 90 ml/min. Once all the deionized water has evacuated from the chamber, circulate the Krebs solution and pass it through a 0.45 μm filter. Keep Krebs solution at 37°C with a water jacket, circulated and oxygenated by bubbling O₂/CO₂ (95%/5%) gas into the solution. Adjust the flow rate to 4 ml/min.
- Prepare the optical mapping system (Figure 1), a custom-designed system equipped with an EMCCD camera. The excitation light for Ca²⁺ sensitive dye Rhod-2 and voltage sensitive dye RH237 is provided by four MacroLED lamps (525 nm, 1750 lumen, 7 mm² emitters, Cairn Research) with aspheric condensers driven using MacroLED control boxes and digitally modulated from Metamorph software. LEDs are directed onto the slices from the four corners of the bath, to produce an even, near-critical, illumination at approximately 30 mm, with equal distance from 4 corners. An ET525/50 sputter coated filter (Chroma Technology) is used to remove any out-of-band light for each LED. Samples are imaged using a custom MacroScope (Cairn Research) with an F/0.95, 25 mm C-mount camera lens, spaced to give a working distance of approximately 40 mm.

The fluorescence emission light is split with a 635 nm longpass dichroic mirror and subsequently filtered (Vm: 662 nm LP, CaT: 585/40 nm) to separate the Ca²⁺ and voltage signals based on their wavelengths using the OptoSplit apparatus (Cairn Research). Once split, the Vm and CaT signals are imaged on to the camera such that they are reproduced side-by-side on the sensor and recorded simultaneously (Vm imaged on one side of the chip, CaT on the other).

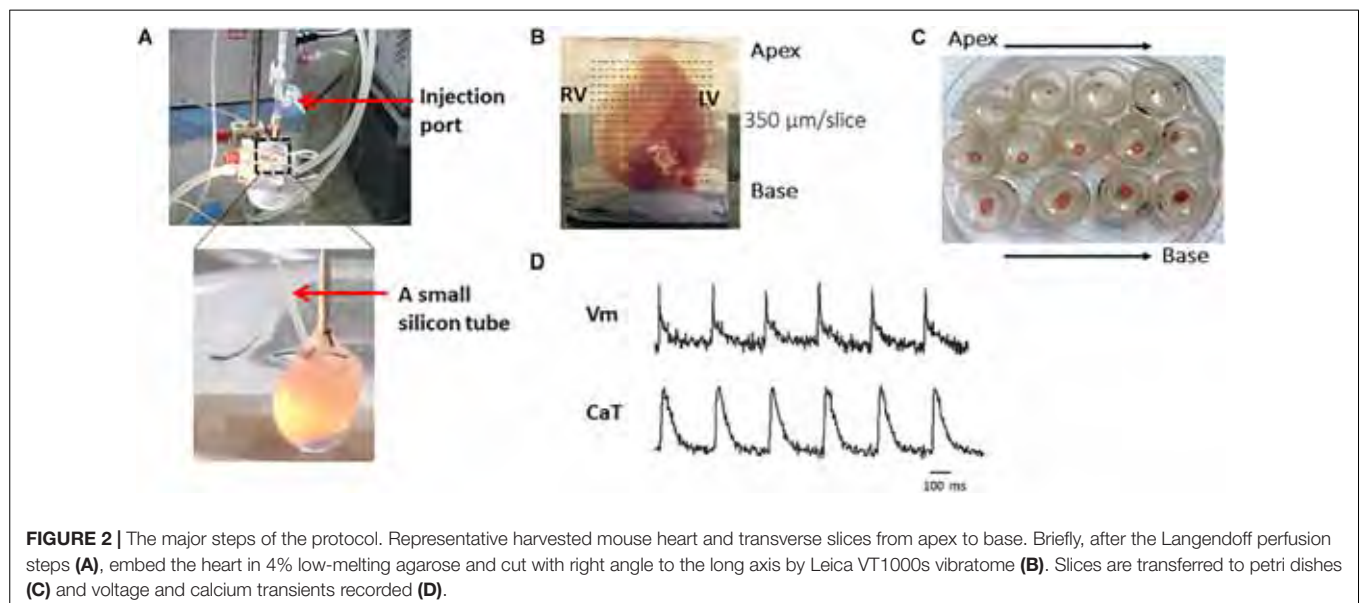
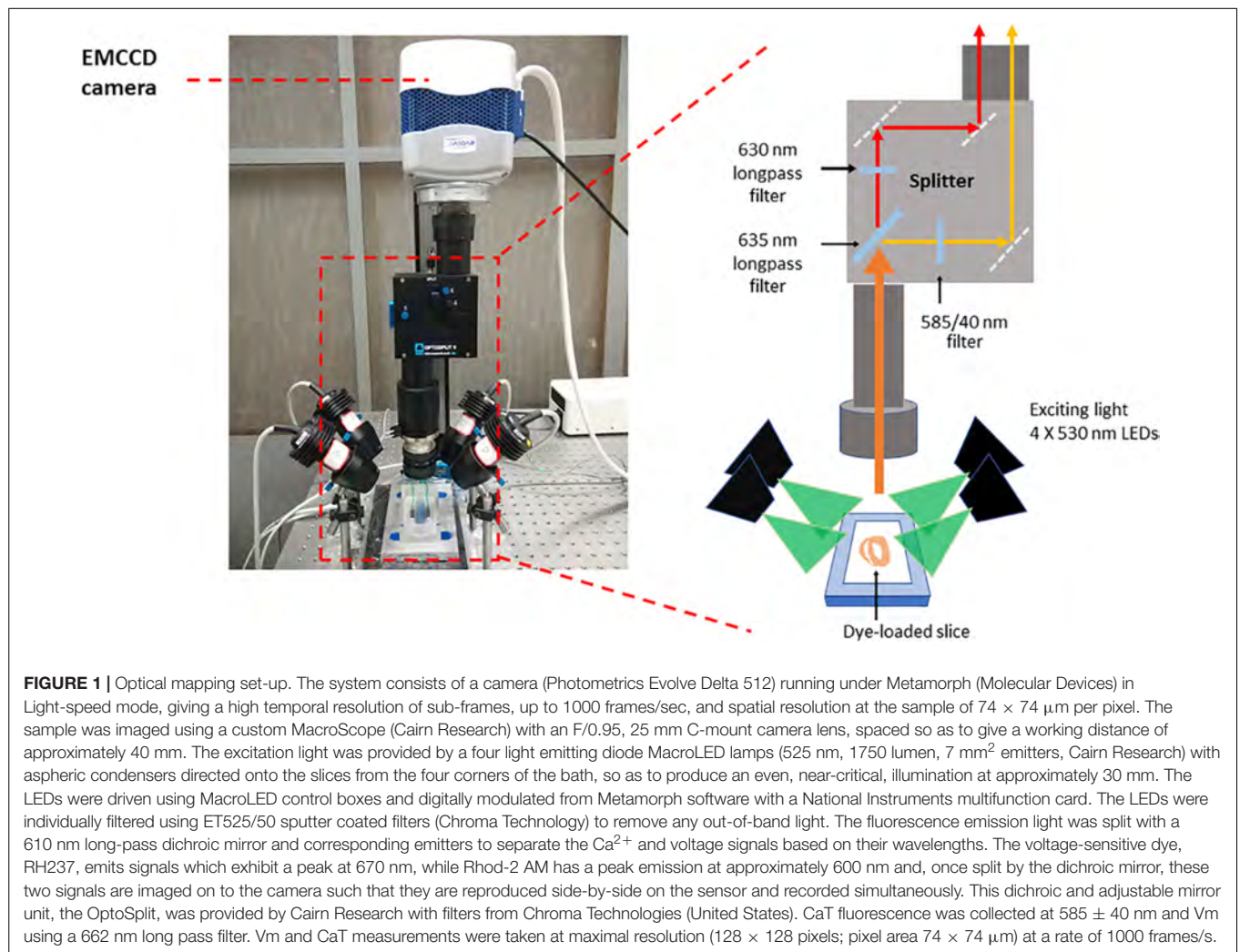
- Prepare the vibratome. Install a new blade at the holder and fill the cooling chamber with crushed ice.

PROCEDURE

Figure 2 shows the major steps of the protocol.

Harvest, Cannulation, and Perfusion of Mouse Heart (30 min)

- (1) Anesthetize the animal with 1.2% Avertin solution (0.5–0.8 ml I.P.) containing heparin (200 units I.P.), ensuring lack of pain reflex, prior to sacrifice (Complete in 10 min).
- (2) Open the chest, quickly remove the heart and keep the heart in oxygenated (95% O₂, 5% CO₂), (37 ± 1°C) Krebs solution. Using a dissecting microscope, identify the aorta and make a clean cut across the ascending aorta below the right subclavian artery. Cannulate the aorta onto a custom-made cannula and tie with 4-0 black-braided silk suture around the cannula. After cannulation, retrogradely perfuse the heart and superfuse with constant-temperature (37 ± 1°C) Krebs solution. The retrograde perfusion rate was adjusted in the range of 3.5–4.0 mL/min (Complete this step in 3 min).
- (3) Important! Insert a small silicon tube (0.7 mm diameter) into the left ventricular cavity through the left atrial



appendage in order to prevent ventricular pressure increasing due to solution congestion and to prevent acidification of the perfusate trapped in the left ventricular cavity. This is especially important after the suppression of ventricular contractions with an excitation-contraction uncoupler.

After the dyes are loaded, the steps described in Sections “Chemicals and Reagents,” “Instruments and equipment,” and “Solutions” should be performed in the dark.

Load Calcium and Voltage Sensitive Dyes and Excitation-Contraction Uncoupler (50–60 min)

- (1) Before dye loading, ensure the isolated heart is beating rhythmically without ischemia (10 min).
- (2) Mix 50 μ l calcium indicator Rhod-2 AM 1:1 with Pluronic F127 (20% solution in DMSO) and then dilute in 1 ml Krebs solution. Recirculate oxygenated (95% O₂, 5% CO₂) Krebs solution at constant-temperature ($37 \pm 1^\circ\text{C}$) and then inject Rhod-2 AM solution slowly over 7–10 min through the injection port near the cannula.
- (3) Continue to recirculate Krebs solution after finishing injection (now, the perfusate contains Rhod-2 AM and Pluronic F127) (20 min).
- (4) During this time, dilute 30 μ l voltage-sensitive dye RH237 (1.25 mg/ml stock) in 1 ml Krebs solution.
- (5) Switch to perfusion with oxygenated (95% O₂, 5% CO₂), constant-temperature ($37 \pm 1^\circ\text{C}$), Krebs solution and perfuse the heart for 2–3 min. Then inject RH237 solution slowly over 7–10 min through the injection port.
- (6) After loading the voltage dye, recirculate oxygenated Krebs solution containing 10 μ M blebbistatin [maintaining constant temperature at $37 \pm 1^\circ\text{C}$] until the heart stops beating (10–15 min).
- (7) Whilst waiting for the heart to stop beating, prepare equipment and solutions for ventricular slicer. A standard razor blade is cut into half and placed on the blade holder so that the blunt side of the blade was tight up against the holder. A circle of solidified agar is mounted on the ventricular slicer's plunger using superglue.

Ventricular Slicing, Harvest, and Recovery (60–70 min)

- (1) Take the heart off the Langendorff setup.
- (2) Carry out all dissections in ice cold HEPES buffered BDM solution. Remove atria and connective tissue from the ventricles to flatten the base.
- (3) Mount base of the heart on solidified 4% agarose of slicer's plunger using surgical glue.
- (4) Freshly prepare 4% low-melt agarose, cool on ice, and pour to cover the whole heart. Surround the plastic cap with the metal support.
- (5) After the agarose is solidified, place the ventricular slicer plunger inside the metal merged into vibratome bath until

it reaches stop point. Fill the ventricular slicer bath with ice-cold HEPES buffered BDM solution.

- (6) Cut slices transversally at a thickness of 300–350 μ m, with speed of 0.05 mm/s, amplitude of 1 mm and vibration frequency of 80 Hz (2 min per slice).
- (7) On average 14 ventricular slices are harvested. Transfer each slice (other than the first which was usually discarded) to a petri dish containing ice-cold HEPES buffered BDM solution for 10 min. Pin the slices on small pieces of thin square shape Sylgard sheets (1 \times 1 cm in diameter, 0.2 cm thickness), cover with mesh. Then transfer the slices to 1st, 2nd, and 3rd petri dishes filled with oxygenated blebbistatin Krebs solution (10 μ M) at room temperature (RT) for 10 min in each dish.
- (8) Repeat slicing procedure until the last slice is harvested.

Optical Mapping

- (1) Place each slice in oxygenated blebbistatin Krebs solution (10 μ M) in 37°C tissue bath for 2–3 min to equilibrate.
- (2) Place the slice into a custom-made stimulation chamber filled with 37°C oxygenated blebbistatin Krebs solution (10 μ M) between the two pacing electrodes. Use pin(s) and mesh to flatten the slice.
- (3) Place the slices into the optical mapping setup (**Figure 2**, details in Materials and equipment). For field pacing, stimulate with square pulses of 2 ms duration, at voltages 1.5 times above threshold (minimum voltage required to pace tissue) with 1:1 coupling.
- (4) For optical pacing, the tissues are paced through the activation of ChR2 light-sensitive channels. This is achieved by the delivery of 470 nm blue light pulses (2–10 ms pulse width) generated by OptoFlash (Cairn Research, Faversham, United Kingdom). Pulses are triggered by a 1401 digitiser and Spike 2 software (Cambridge Electronic Design). Approximate blue light intensity is measured with a 818-ST2 Wand Detector connected to a 843 R Power meter (both Newport Corporation, CA, United States) and we estimate an average irradiance in our experiments of 0.1–0.3 mW/mm² based on an approximate distance of 1–2 cm between Sylgard and liquid light guide (Oriel instruments Model No 77525).
- (5) For AP and CaT alternans investigations, stimulate slices at frequencies of 2, 4, 8 and 16 Hz. Between pacing protocols, turn off the LED lights to minimize photobleaching (and other possible side effects, including phototoxicity). When testing, turn off the oxygenation to avoid motion artifacts.
- (6) After experiment is finished, clean the perfusion system with deionized water.

Data Analysis

- (1) Recorded image files are loaded into an optical mapping analysis software ElectroMap¹ (O'Shea et al., 2019). Pre-process images with application of 3×3 pixel Gaussian spatial filter and top-hat (kernel length = 100 ms) baseline correction.

¹<https://github.com/CXO531/ElectroMap>

- (2) Measure action potential duration (APD)/Calcium transient duration (CaTD) at desired repolarization/decay percentage at each pixel across the tissue, as measured from time of maximum upstroke velocity. Voltage-calcium latency can be measured as time difference between AP and CaT peak.
- (3) For assessment of conduction velocity, render activation map by measuring activation time, for example by measuring depolarization midpoint or upstroke time (dV/dt max). Conduction velocity across the slice can then be quantified using multi-vector polynomial method with a local window size of 5×5 pixels (Bayly et al., 1998).

Exemplar Results

Figure 1 shows the optical mapping set-up. After the slices were prepared, slices were pre-incubated at room temperature in Krebs solution containing $10 \mu\text{M}$ blebbistatin for an optimal recovery time, prior to electrophysiological assessment using a custom-designed optical mapping system.

Figure 2 shows the major steps of the protocol. To achieve optimal dye loading, the voltage dye RH237 and/or Ca^{2+} dye Rhod-2 AM were loaded through the coronary circulation using the Langendorff perfusion system (**Figure 2A**). Prevention of blood clot formation was essential for optimal dye loading and was achieved by initial injection of heparin (200–300 units) before animal sacrifice. Ventricles were embedded in low-melting temperature agarose as illustrated in **Figure 2B** to provide structural support to the tissue during sectioning. Slices were cut at right angles to the long axis of the heart from the apex to the base, and thicknesses from 300–350 μm found to be the best thickness to achieve optimal recordings for both Vm and CaT (**Figure 2B**). **Figure 2C** shows viable slices obtained with the optimized protocol and representative V_m and CaT signals.

Figure 3A shows fluorescence images of voltage dye RH237 and Ca^{2+} dye Rhod-2 AM as imaged using the optical mapping setup. Using this protocol, and the optical imaging setup, we are able to dually measure parameters such as AP duration (**Figure 3B**) and CaT duration and (**Figure 3C**). The “rundown” of the Vm and CaT signals was monitored for up to 4 h, the average signal “rundown” being less than 25%. Our experiments usually finished within 3 h from the beginning of Langendorff perfusion of the heart.

Figure 4 shows an example of activation (**Figure 4A**) and APD75 (**Figure 4B**) maps reconstructed from electrical and light-paced APs in a ventricular slice from Pnmt-Cre/ChR2 mouse heart. Also shown are exemplar V_m signals from different regions of the ventricle.

DISCUSSION

The protocol described here allows high resolution mapping of V_m and CaT on thin transverse slices cut at right angles to the long axis of the heart, permitting robust interrogation of V_m and CaT throughout the entire heart with exceptional regional precision. Since the apico-basal location of each

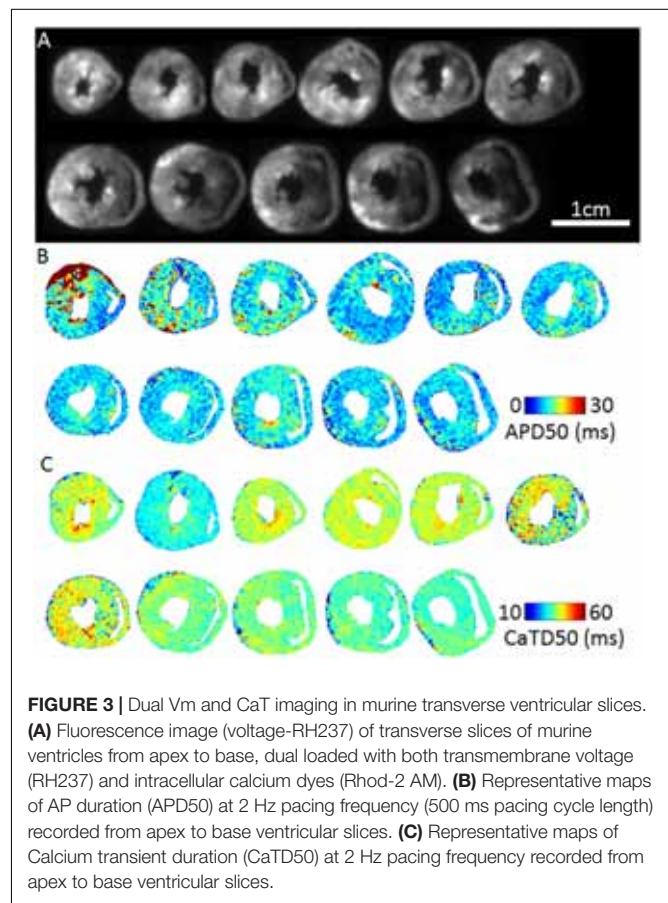
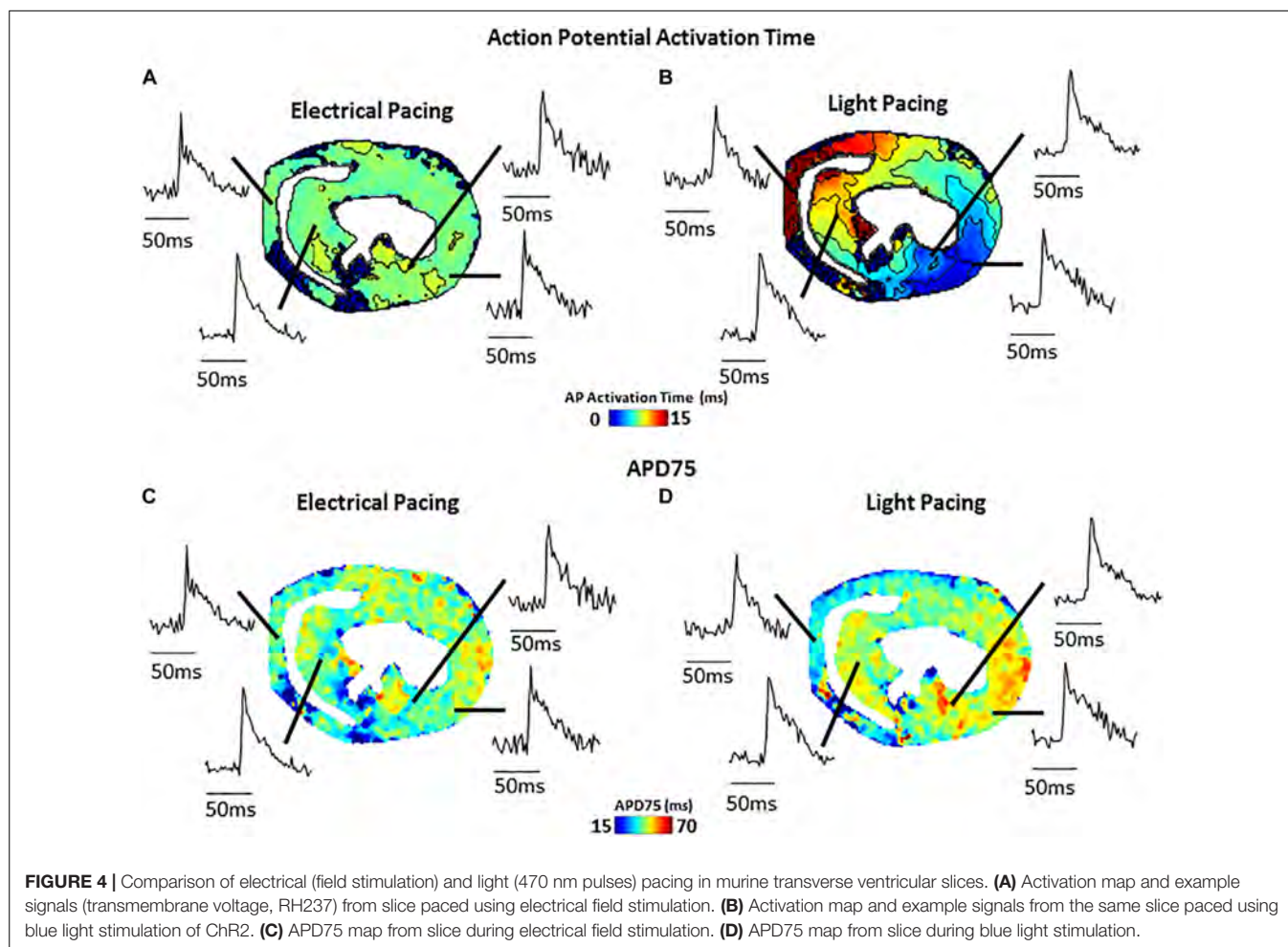


FIGURE 3 | Dual Vm and CaT imaging in murine transverse ventricular slices. **(A)** Fluorescence image (voltage-RH237) of transverse slices of murine ventricles from apex to base, dual loaded with both transmembrane voltage (RH237) and intracellular calcium dyes (Rhod-2 AM). **(B)** Representative maps of AP duration (APD50) at 2 Hz pacing frequency (500 ms pacing cycle length) recorded from apex to base ventricular slices. **(C)** Representative maps of Calcium transient duration (CaTD50) at 2 Hz pacing frequency recorded from apex to base ventricular slices.

slice is known and every slice is fully transmural, such rich data allows for characterization of regional AP and CaT properties. This includes AP and CaT durations, alternans threshold, transmural activation and conduction velocities, and correlation of AP and CaT properties such as voltage-calcium coupling latency in each slice. The main processes of the protocol include: (i) Preparing solutions and experimental setup; (ii) Harvesting, cannulation and perfusion of the mouse heart by Langendorff perfusion; (iii) Loading calcium and voltage sensitive dyes and excitation-contraction uncoupler; (iv) Ventricular Slicing; (v) Optical mapping; (vi) Image processing and analysis. The protocol was further developed since it was first published (Wen et al., 2018) in two major aspects: (i) simultaneous dual dye images allowing correlation of AP and CaT properties in each slice; (ii) implementing improved image processing and analysis such as correlation of AP and CaT properties.

Applications

Our novel approach potentially provides not only a unique technique applicable to hearts of other species (such as widely used rat and rabbit), but also other tissues such as brain, adrenal medullary tissue, gut, etc. As we demonstrate here (**Figure 4**), such slice imaging technique can be also combined with optogenetic technology to carry out



optogenetic light stimulation of specific cells. Such an approach could be further extended by use of genetically encoded reporter proteins allowing cell-type specific study of V_m and Ca^{2+} signals, as well as cell-specific activation. We believe that the approach would be of considerable interest to researchers in manifold biomedical research fields and would serve as a useful platform for further innovative biomedical research.

Advantages

Firstly, a critical advantage of our cardiac slice model is the ability to provide access to any region of the ventricles, thus enabling exploration of regional and transmural differences. This is particularly important for the mouse heart, given that other *in vitro* tissue preparations, such as ventricular wedges, are not feasible for small hearts. Secondly, this technique may prove extremely valuable for characterizing regional arrhythmogenic changes in genetic murine models of cardiovascular disease (e.g., catecholaminergic polymorphic ventricular tachycardia, hypertrophic cardiomyopathy), as well as comprehensive regional characterization of remodeling in acquired pathologies (myocardial infarction, pressure-overload heart failure). Thirdly, depending on the optics, camera

resolution, and slice size and position, it may be possible to image several or all slices from a single mouse heart simultaneously, giving a high throughput platform to electrophysiological investigations. Finally, it can also be combined with optogenetic technology to carry out optogenetic light stimulation – aiding studies requiring precise manipulation of cellular V_m and CaT.

Limitations and Adaptations

(i) Possibility of tissue injury increasing regional V_m and CaT differences. This can be overcome by optimized protocol with very slow cutting speed, embedding in supportive but oxygen permeable medium, and use of blebbistatin as uncoupler during slice preparation. (ii) Rundown of the V_m and CaT signals. The “rundown” of the V_m and CaT signals was also monitored for up to 4 h, the average signal “rundown” being less than 25%. Our experiments usually finished within 3 h. This can be overcome by efficient imaging processes, and the application of 0.5 mM Probenecid in the recovery and recording solutions to reduce the Ca^{2+} dye loss. (iii) The measurements of the parameters under electrical pacing condition was conducted by field stimulation (considering the fragile dedicated slice preparation), thus our approach may suffer from tissue activation occurring at the same

time point across the preparation. Whilst this is not what we observed regularly in our data, this approach may affect the conduction velocity (CV) measurement. A better approach with point stimulation or selective optical activation of a subset of cells (Figure 4) should be pursued.

ETHICS STATEMENT

Animals used were 10–12 weeks, 20–25 g, male B57BL mice. All procedures including animal subjects have been approved by the Institutional Animals Ethics Committees at the Southwest Medical University, Luzhou, China or the Department of Pharmacology at the University of Oxford and the national guidelines under which the institution operates. All mice used in this study were maintained in a pathogen-free facility at the Southwest Medical University or the University of Oxford. Mice were given *ad libitum* access to food and water. The authors confirm that they have taken all steps to minimize the animals' pain and suffering.

REFERENCES

- Accardi, M. V., Pugsley, M. K., Forster, R., Troncy, E., Huang, H., and Authier, S. (2016). The emerging role of in vitro electrophysiological methods in CNS safety pharmacology. *J. Pharmacol. Toxicol. Methods* 81, 47–59. doi: 10.1016/j.vascn.2016.03.008
- Bayly, P. V., KenKnight, B. H., Rogers, J. M., Hillsley, R. E., Ideker, R. E., and Smith, W. M. (1998). Estimation of conduction velocity vector fields from epicardial mapping data. *IEEE Trans. Biomed. Eng.* 45, 563–571. doi: 10.1109/10.668746
- Bussek, A., Wettwer, E., Christ, T., Lohmann, H., Camelliti, P., and Ravens, U. (2009). Tissue slices from adult mammalian hearts as a model for pharmacological drug testing. *Cell Physiol. Biochem.* 24, 527–536. doi: 10.1159/000257528
- Camelliti, P., Al-Saud, S. A., Smolenski, R. T., Al-Ayoubi, S., Bussek, A., Wettwer, E., et al. (2011). Adult human heart slices are a multicellular system suitable for electrophysiological and pharmacological studies. *J. Mol. Cell Cardiol.* 51, 390–398. doi: 10.1016/j.yjmcc.2011.06.018
- Halbach, M., Pillekamp, F., Brockmeier, K., Hescheler, J., Müller-Ehmsen, J., and Reppel, M. (2006). Ventricular slices of adult mouse hearts - a new multicellular in vitro model for electrophysiological studies. *Cell Physiol. Biochem.* 18, 1–8. doi: 10.1159/000095132
- Huang, C. L. (2017). Murine electrophysiological models of cardiac arrhythmogenesis. *Physiol. Rev.* 97, 283–409. doi: 10.1152/physrev.00007.2016
- Kang, C., Qiao, Y., Li, G., Baechle, K., Camelliti, P., Rentschler, S., et al. (2016). Human organotypic cultured cardiac slices: new platform for high throughput preclinical human trials. *Sci. Rep.* 6:28798. doi: 10.1038/srep28798
- Nerbonne, J. M., and Kass, R. S. (2005). Molecular physiology of cardiac repolarization. *Physiol. Rev.* 85, 1205–1253. doi: 10.1152/physrev.00002.2005
- O'Shea, C., Holmes, A. P., Yu, T. Y., Winter, J., Wells, S. P., Correia, J., et al. (2019). ElectroMap: high-throughput open-source software for analysis and mapping of cardiac electrophysiology. *Sci. Rep.* 9:1389–1389. doi: 10.1038/s41598-018-38263-2
- Randi, A. M., Kane, C., Perbellini, F., Bardi, I., Gorelik, J., Sikkel, M. B., et al. (2017). Investigation of cardiac fibroblasts using myocardial slices. *Cardiovasc. Res.* 114, 77–89. doi: 10.1093/cvr/cvx152

AUTHOR CONTRIBUTIONS

SH, QW, RM, XT, and XO carried out the experiments. CO'S and DP carried out the data process and data analysis. PC and ML designed the experiments. SH, QW, RM, XT, XO, and ML drafted the manuscript. PC, CO'S, and DP revised and edited the manuscript. All authors have made a substantial contribution to the manuscript.

FUNDING

This study was supported by the MRC (G10002647 and G1002082 to ML), the BHF (PG/14/80/31106, PG/16/67/32340, PG/12/21/29473, and PG/11/59/29004 to ML), (FS/17/33/32931 to PC and ML), and (PG/17/55/33087, RG/17/15/33106 to DP), the BHF CRE at Oxford (ML) grants, EPSRC (EP/L016346/1 to DP), the National Natural Science Foundation of China (Nos. 81700308 and 31871181) and the Royal Society (RSG\R1\180198 to PC).

- Thomas, R. C., Singh, A., Cowley, P. M., Myagmar, B.-E., Montgomery, M. D., Swigart, P. M., et al. (2016). A myocardial slice culture model reveals alpha-1A-adrenergic receptor signaling in the human heart. *JACC Basic Trans. Sci.* 1, 155–167. doi: 10.1016/j.jacbs.2016.03.005
- Wang, K., Lee, P., Mirams, G. R., Sarathchandra, P., Borg, T. K., Gavaghan, D. J., et al. (2015). Cardiac tissue slices: preparation, handling, and successful optical mapping. *Am. J. Physiol. Heart Circ. Physiol.* 308, H1112–H1125. doi: 10.1152/ajpheart.00556.2014
- Wang, Y., Lin, W. K., Crawford, W., Ni, H., Bolton, E. L., Khan, H., et al. (2017). Optogenetic control of heart rhythm by selective stimulation of cardiomyocytes derived from Pnmt+ cells in murine heart. *Sci. Rep.* 7:40687. doi: 10.1038/srep40687
- Watson, S. A., Scigliano, M., Bardi, I., Ascione, R., Terracciano, C. M., and Perbellini, F. (2017). Preparation of viable adult ventricular myocardial slices from large and small mammals. *Nat. Prot.* 12:2623. doi: 10.1038/nprot.2017.139
- Watson, S. A., Terracciano, C. M., and Perbellini, F. (2019). Myocardial slices: an intermediate complexity platform for translational cardiovascular research. *Cardiovasc. Drugs Ther.* 33, 239–244. doi: 10.1007/s10557-019-06853-5
- Wen, Q., Gandhi, K., Capel, R. A., Hao, G., O'Shea, C., Neagu, G., et al. (2018). Transverse cardiac slicing and optical imaging for analysis of transmural gradients in membrane potential and Ca²⁺ transients in murine heart. *J. Physiol.* 596, 3951–3965. doi: 10.1111/JP276239

Conflict of Interest Statement: The authors declare that the research was conducted in the absence of any commercial or financial relationships that could be construed as a potential conflict of interest.

Copyright © 2019 He, Wen, O'Shea, Mu-u-min, Kou, Grassam-Rowe, Liu, Fan, Tan, Ou, Camelliti, Pavlovic and Lei. This is an open-access article distributed under the terms of the Creative Commons Attribution License (CC BY). The use, distribution or reproduction in other forums is permitted, provided the original author(s) and the copyright owner(s) are credited and that the original publication in this journal is cited, in accordance with accepted academic practice. No use, distribution or reproduction is permitted which does not comply with these terms.

Chapter 6

Temporal irregularity quantification and mapping of optical action potentials using wave morphology similarity

Within the ElectroMap software we incorporated several established processing and analysis methods. However, in producing the software we also wanted to introduce novel methods for analysis of optical mapping data. Here, we introduce semi-automated analysis of temporal regularity from optically recorded action potentials. This is important as temporal alterations in action potential morphology are both predictive and consequent of arrhythmia, so robust methods to quantify temporal heterogeneity are valuable tools for optical mapping research. In this chapter, we tested both direct application of clinically used methodologies, namely the regularity index, and also adaption of existing techniques for use with optically recorded action potentials.

6.1 Temporal irregularity quantification and mapping of optical action potentials using wave morphology similarity

Publication 6.

This article was originally published in Progress in Biophysics and Molecular Biology.

Temporal irregularity quantification and mapping of optical action potentials using wave morphology similarity. **C O'Shea**, J Winter, A P Holmes, D M Johnson, J N Correia, P Kirchhof, L Fabritz, K Rajpoot, D Pavlovic. *Progress in Biophysics and Molecular Biology. Article in Press*

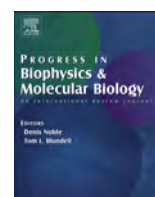
Author contributions in publication 6

I implemented and wrote the code for regularity index (RI) quantification of optical action potentials, and also designed, implemented and wrote the code for optical wave similarity (OWS) quantification. I added these features to the ElectroMap software, and analysed all data included. I performed *in silico* experiments. I performed mouse left atrial experiments. Andrew Holmes and Daniel Johnson also performed some of these experiments. Guinea pig experiments were performed by James Winter. I produced all figures and wrote the original manuscript draft, which was then edited by all authors.



Contents lists available at ScienceDirect

Progress in Biophysics and Molecular Biology

journal homepage: www.elsevier.com/locate/pbiomolbio

Temporal irregularity quantification and mapping of optical action potentials using wave morphology similarity

Christopher O'Shea ^{a,b,c}, James Winter ^a, Andrew P. Holmes ^{a,d}, Daniel M. Johnson ^a,
Joao N. Correia ^e, Paulus Kirchhof ^{a,f,g}, Larissa Fabritz ^{a,f}, Kashif Rajpoot ^{c,**,1},
Davor Pavlovic ^{a,*,1}

^a Institute of Cardiovascular Sciences, University of Birmingham, UK^b EPSRC Centre for Doctoral Training in Physical Sciences for Health, School of Chemistry, University of Birmingham, UK^c School of Computer Science, University of Birmingham, Birmingham, B15 2TT, UK^d Institute of Clinical Sciences, University of Birmingham, UK^e Institute of Microbiology and Infection, School of Biosciences, University of Birmingham, UK^f Department of Cardiology, UHB NHS Foundation Trust, Birmingham, UK^g Cardiology Specialty, SWBH NHS Trust, Birmingham, UK

ARTICLE INFO

Article history:

Received 18 September 2019

Received in revised form

8 November 2019

Accepted 20 December 2019

Available online xxx

Keywords:

Optical mapping

Wave similarity

Regularity index

Temporal stability

Optical action potential

ABSTRACT

Background: Cardiac optical mapping enables direct and high spatio-temporal resolution recording of action potential (AP) morphology. Temporal alterations in AP morphology are both predictive and consequent of arrhythmia. Here we sought to test if methods that quantify regularity of recorded waveforms could be applied to detect and quantify periods of temporal instability in optical mapping datasets in a semi-automated, user-unbiased manner.

Methods and results: We developed, tested and applied algorithms to quantify optical wave similarity (OWS) to study morphological temporal similarity of optically recorded APs. Unlike other measures (e.g. alternans ratio, beat-to-beat variability, arrhythmia scoring), the quantification of OWS is achieved without a restrictive definition of specific signal points/features and is instead derived by analysing the complete morphology from the entire AP waveform.

Using model datasets, we validated the ability of OWS to measure changes in AP morphology, and tested OWS mapping in guinea pig hearts and mouse atria. OWS successfully detected and measured alterations in temporal regularity in response to several proarrhythmic stimuli, including alterations in pacing frequency, premature contractions, alternans and ventricular fibrillation.

Conclusion: OWS mapping provides an effective measure of temporal regularity that can be applied to optical datasets to detect and quantify temporal alterations in action potential morphology. This methodology provides a new metric for arrhythmia inducibility and scoring in optical mapping datasets.

© 2019 The Authors. Published by Elsevier Ltd. This is an open access article under the CC BY license (<http://creativecommons.org/licenses/by/4.0/>).

1. Introduction

Cardiac arrhythmias, such as ventricular and atrial fibrillation (VF/AF), are characterised by complex spatiotemporal activation and repolarisation dynamics (Moe and Abildskov, 1959; Ten Tusscher et al., 2007; Pandit and Jalife, 2013). Advances in knowledge of the mechanistic drivers or origins of these events (Atienza et al., 2012; Schotten et al., 2011) could be used to develop more effective therapies, for example, leading to improvements in radiofrequency ablation procedures (Ravelli and Mase, 2014; Li et al., 2017). However, recordings of cardiac electrical activity in the time preceding and during an arrhythmia are often temporally

Abbreviations: Atrial Fibrillation, AF; Ventricular Fibrillation, VF; Action Potential, AP; Action Potential Duration, APD; Regularity Index, RI; Optical Wave Similarity, OWS; Optical Action Potential, OAP; Sympathetic Nervous Stimulation, SNS; Pacing Cycle Length, PCL; Premature Atrial Activity, PAA.

* Corresponding author. Institute of Cardiovascular Sciences University of Birmingham, Birmingham, B15 2TT, UK.

** Corresponding author.

E-mail addresses: k.m.rajpoot@bham.ac.uk (K. Rajpoot), d.pavlovic@bham.ac.uk (D. Pavlovic).

¹ These authors share senior authorship.

<https://doi.org/10.1016/j.pbiomolbio.2019.12.004>

0079-6107/© 2019 The Authors. Published by Elsevier Ltd. This is an open access article under the CC BY license (<http://creativecommons.org/licenses/by/4.0/>).

Please cite this article as: O'Shea, C et al., Temporal irregularity quantification and mapping of optical action potentials using wave morphology similarity, Progress in Biophysics and Molecular Biology, <https://doi.org/10.1016/j.pbiomolbio.2019.12.004>

disorganised and/or irregular. In the case of electrogram recordings, such signals are termed 'fractionated' and the more complex morphology reflects local differences in activation, repolarisation and/or fibrotic areas within the tissue, leading to alterations in the amplitude and temporal regularity of the recorded signal (Caldwell and Redfearn, 2012; Baher et al., 2019). In optical mapping, where action potentials (APs) are recorded using voltage sensitive fluorescent indicators, arrhythmias are associated with similar alterations in signal amplitude and temporal heterogeneity (Laughner et al., 2012). For these reasons, signal parameters such as cycle length and AP duration (APD) become inconsistent and hard to define/measure. Thus, novel temporal heterogeneity measures not reliant on defined waveform points/features consisting of repetitive periods of depolarisation and repolarisation are required.

For both electrogram and optical mapping datasets, strategies have been proposed for quantification of electrophysiological properties in the time prior to and during an arrhythmia. Beat to beat analyses have been successfully utilised in several optical mapping studies to highlight temporal instability (Wang et al., 2014; Winter et al., 2018; O'Shea et al., 2019a). These approaches however can be labour intensive, while high throughput methodologies rely on the automated identification of specific signal points, features (e.g. activation and repolarisation times) and phenomena (e.g. alternans) (O'Shea et al., 2019a; Fabritz et al., 2003). These features can become challenging to algorithmically and accurately measure when signal amplitude decreases, as is observed at fast pacing frequencies and during polymorphic arrhythmia (Laughner et al., 2012; O'Shea et al., 2019a). Furthermore, dominant frequency (Laughner et al., 2012) and phase analysis (Umapathy et al., 2010; Kirchhof et al., 1998) have been employed to map regions of the heart that may act as drivers of arrhythmia (e.g. mother rotors) and to predict termination of arrhythmia episodes. However, these methodologies either forgo 'direct' analysis of the signal waveforms or rely on manual inspection. Instead, they use mathematical techniques to transform the signal into another form, for example, into the frequency domain via the fast Fourier transformation.

In electrogram-based electrophysiological mapping, the 'regularity index (RI)' has been shown to be an effective method to quantify temporal organisation directly (Faes et al., 2002; Ravelli et al., 2005). This method, as first set out in 2002 for atrial electrograms (Faes et al., 2002), computes the similarity between local activation waves with the hypothesis that waves with a lower index are representative of tissue areas with dyssynchronous activation and repolarisation. RI and similar methods have the advantage of quantifying temporal regularity using simple signal processing methods across the entire waveform morphology (Baher et al., 2019; Faes et al., 2002). The RI approach relies on the setting of a threshold value for 'similarity'. The use of such an approach for analysis of optical signals has not been evaluated, in particular the effects of setting a similarity threshold.

In this study, we have developed and utilised RI mapping in optical mapping datasets, and further develop an analogous but updated approach for use in optical mapping datasets which we term optical wave similarity (OWS). RI and OWS metrics are compared. OWS is measured from optical mapping datasets to demonstrate its utility in detecting and quantifying temporal homogeneity/regularity of model and optical action potentials (OAPs). Temporal heterogeneity is induced by changes in pacing cycle length and sympathetic nervous stimulation (SNS) in guinea pig ventricles and isolated mouse left atria. Robust measures of temporal heterogeneity across the myocardium, recorded using optical mapping methodologies and integrated into freely available software, will potentially help researchers identify novel drivers of arrhythmogenesis (Baher et al., 2019; Winter et al., 2018; Johnson

et al., 2010).

2. Methods

2.1. Animal welfare

All animal procedures were undertaken in accordance with ethical guidelines set out by the UK Animals (Scientific Procedures) Act 1986 and Directive 2010/63/EU of the European Parliament on the protection of animals used for scientific purposes. Experiments were approved by the home office (mouse: PPL 30/2967 and PFDAAF77F, guinea pig: PPL PF75E5F7F) and the institutional review boards at University of Birmingham (mouse) and King's College London (guinea pig).

2.2. Optical mapping

All data utilised in this study were acquired previously, full details of experimental procedures can be found in the relevant publications (Winter et al., 2018; Holmes et al., 2016; Yu et al., 2014).

Briefly, *ex vivo* isolated intact guinea pig whole hearts were imaged utilising an innervated preparation (Ng et al., 2001). Hearts were loaded with voltage dye Di-8-ANEPPS (1 mg/ml in DMSO, 200–300 μ l), paced via silver bipolar electrodes and imaged at 0.5 kHz at 64×64 pixel resolution (320 μ m pixel width). Sympathetic nervous stimulation (SNS) was achieved by bi-lateral stimulation of efferent sympathetic nerves by a decapolar 5-French catheter in the spinal column. Hearts were paced at 170 ms pacing cycle length (PCL), and PCL reduced by 10 ms every 10 beats until induction of ventricular fibrillation (Winter et al., 2018).

Isolated *ex vivo* mouse hearts were loaded with Di-4-ANEPPS (0.125 mg/ml in DMSO, 1 ml), left atria isolated, pinned down in the superfusion chamber and paced using platinum bipolar electrodes and imaged at 0.987 kHz with maximal resolution of 200×2048 pixels (Holmes et al., 2016) (71 μ m pixel width). Atria were paced at 150 ms PCL, and PCL was reduced by 10 ms every 20 stimuli down to 50 ms. Some atria were also paced at 150 ms PCL for 1 min to observe instances of spontaneous activity, such as premature atrial activity (PAA).

In both sets of experiments the electromechanical un-coupler blebbistatin (15 μ M for guinea pig, 42.75 μ M for mouse atria) was used to prevent movement of the tissue and motion artefacts on the recordings.

2.3. Optical data pre-processing

Spatial filtering of the optical mapping images was performed via a 3×3 pixel Gaussian filter. Baseline correction was performed using a top-hat kernel (200 ms length for guinea pig data, 100 ms for mouse) (Yu et al., 2017). No temporal filtering was applied.

Image stacks were then segmented based on PCL. PCL segmentation of the image stack was performed based on the tissue average signal, $F_{tissue}(t)$,

$$F_{tissue}(t) = \sum_{n=1}^N f_n(t) \quad 1$$

where $f_n(t)$ is the fluorescent value of pixel n at time t . Only the N pixels which were selected following thresholding (i.e. pixels inside the red outline in Fig. 1A) were included for summation in equation (1) and all subsequent analysis. Peaks in $F_{tissue}(t)$ were then identified by setting a threshold amplitude (half of maximum $F_{tissue}(t)$)

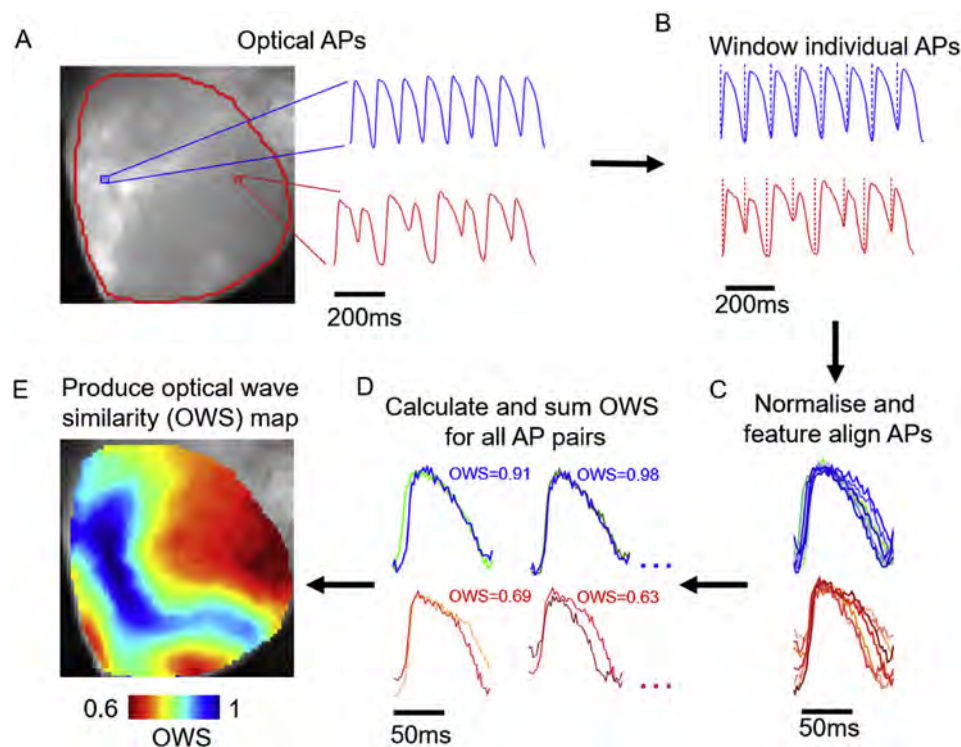


Fig. 1. Calculation of optical wave similarity (OWS) from voltage optical mapping data. A) Fluorescence image of voltage dye loaded guinea pig whole heart. Representative signals are shown from the locations marked in blue and red on the fluorescence image. B) Windowing of optical signals based on signal minima. C) Normalisation and alignment of individual optical action potentials (OAPs) in the recorded optical signal. D) Example calculations of OWS from OAP pairs. E) Constructed map of OWS following analysis steps set out in A-D.

and minimum peak distance (40 ms for both guinea pig and mouse). The PCL was then defined as the time period between one peak and the previous. The signal was then segmented when changes in PCL of 10 ms were identified. During ventricular fibrillation (VF), automatic PCL based segmentation was not used due to variable time intervals and lower signal amplitude. Instead, a custom selection of time period where the tissue averaged signal clearly demonstrated VF was performed (O'Shea et al., 2019a).

2.4. Computationally modelled action potentials

Alongside application of OWS to optically mapped datasets, mathematical models of guinea pig (Luo and Rudy, 1994) and mouse (Bondarenko, 2004) ventricular action potentials were used to validate use of OWS for AP waveforms. Temporal alterations in the action potential morphology were induced by altering the conductance of the respective repolarising potassium channels in each model for odd beats only. This induced alternans like behaviour in the models. For the guinea pig action potentials, potassium channel (I_K and I_{K1}) conductance was increased by 70%, while for the mouse potassium channel (I_{to} , I_{Kss} , I_{Ks} , I_{K1} , I_{Kur}) conductance was decreased by 45% (Clerx et al., 2016). 1000 beats were simulated in total to allow the models to reach steady-state, and the last 20 beats used for analysis (see below).

The model traces were down sampled to match the recording rates of the optical mapping systems used in this study (0.5 kHz for guinea pig, 1 kHz for mouse). To study the effects of signal quality, noise was added to the datasets by altering the AP by a value selected from a set of normally distributed pseudorandom numbers, the standard deviation of which was set as a percentage value of the action potential amplitude. Due to its pseudorandom nature, this operation was repeated 15 times for each noise level

tested. Note: For direct comparison to noise levels of experimental recording, optical noise values were retrieved in the inverse manner, i.e. the amplitude of the optical action potential (OAP) was compared to the standard deviation of the signal at diastolic baseline. These studies were performed using the myokit software (<http://myokit.org>) (Clerx et al., 2016) and MATLAB (The MathWorks).

2.5. Optical wave similarity

2.5.1. Windowing

Optical wave similarity (OWS) and regularity index (RI) were calculated via adaptation of the method set out by Faes et al. for use in bipolar electrograms (Faes et al., 2002). Following the PCL detection, signals were time windowed, Fig. 1B. Unless stated otherwise, for guinea pig action potentials, window timeframe was set at 50 ms before and 150 ms after the peak in the tissue averaged signal ($F_{tissue}(t)$, equation (1)). Due to the shortening of the diastolic interval at faster PCLs (Shattock et al., 2017), the signals were further windowed by the minimum before and after each peak before OWS calculation. The time window used for measuring the OWS between two OAPs was from the closest minima (of either OAP) before and after the peak in the signals. Due to the shorter OAP morphology and smaller tissue area of murine atria (Riley et al., 2012), a constant windowing timeframe of 20 ms before and 40 ms after the peak was utilised for these recordings and no further windowing based on signal minima was required.

2.5.2. Normalisation and signal alignment

Following PCL detection, segmentation and windowing of individual OAPs, the image stack was split into sections (up to 10 sections of 10 beats for guinea pig hearts, 7 sections of 20 beats for

mouse atria) matching the PCL protocols described above. For single beat OWS analysis, the individual OAP was compared with the subsequent OAP. Signals were aligned according to the peak times in tissue average signal, equation (1).

For the computationally modelled datasets, OWS analysis was applied to the final 20 beats of 1000 stimulations, to ensure the models had reached steady state. The model APs were aligned by the peak.

2.5.3. Calculation of wave similarity

To calculate wave similarity, we utilised the cosine similarity metric. First, the individual, windowed OAPs (A) were zero corrected (translated so the mean value was zero) and normalised as shown in equation (2),

$$A_n = \frac{A}{\sqrt{\sum_{k=1}^K A(k)^2}} \quad 2$$

where A_n is the normalised signal and K is the number of samples in the OAP after windowing, Fig. 1C. The wave similarity, s , between two successive normalised and aligned OAPs, A_1 and A_2 , was then calculated as,

$$s(A_1, A_2) = (A_1 \cdot A_2) \quad 3$$

where $A_1 \cdot A_2$ denotes the scalar dot product (Fig. 1D). The result of equation (3) is a value approaching 1 when A_1 and A_2 exhibit a similar morphology, 0 when the two OAPs are morphologically distinct (e.g. two signals of just noise), and -1 if the signals are identical but of opposite phase. For a sequence of OAPs from each pixel, the overall OWS was then calculated from all paired wave similarity values as,

$$OWS = \frac{2}{M(M-1)} \sum_{i=1}^M \sum_{j=i+1}^M s(A_i, A_j) \quad 4$$

where M is the number of OAPs in the sequence. As previously stated, when undertaking single beat OWS analysis, an individual OAP was compared with the subsequent OAP.

To calculate regularity index (RI), the method of Faes et al. originally applied to atrial electrograms was employed (Faes et al., 2002). The wave distance, d , between two normalised and aligned OAPs, A_1 and A_2 was calculated as,

$$d(A_1, A_2) = \arccos(A_1 \cdot A_2) \quad (5)$$

where \arccos is the inverse cosine function.

A threshold distance, ϵ , was then set, and RI of a train of M OAPs measured as

$$RI = \frac{2}{M(M-1)} \sum_{i=1}^M \sum_{j=i+1}^M H(\epsilon - d(A_i, A_j)) \quad (6)$$

where H is a Heaviside step function which equals 1 when $d(A_i, A_j) \leq \epsilon$ (i.e. when two OAPs are similar) and 0 when $d(A_i, A_j) > \epsilon$ (i.e. when two OAPs are dissimilar). By the definitions in equations (4) and (6), both higher OWS and RI indicate a greater temporal regularity.

2.6. Alternative metrics

To compare the results of OWS analysis with other methodologies, we also conducted APD alternans and dominant frequency analysis.

2.6.1. APD alternans (ΔAPD_{80})

APD_{80} was calculated as the interval between the maximum upstroke velocity during depolarisation (dF/dt_{max}) and the time of 80% repolarisation to baseline. APD_{80} alternans magnitude (ΔAPD_{80}) was then calculated as the absolute difference between APD_{80} of one OAP compared to the previous at each location in the image (Winter et al., 2018; O'Shea et al., 2019b). In some cases, especially at short PCLs, 80% repolarisation was not observed before the next depolarisation. These areas were excluded from analysis (see blue areas in Fig. 6Aii). The results were then averaged for each PCL.

2.6.2. Dominant frequency analysis

For dominant frequency mapping, the frequency spectrum of the signal was computed using fast Fourier transform, with a Hann window applied. Zero padding was applied to achieve a frequency resolution of 0.05 Hz, and the frequency range studied was from 0.5 to 50 Hz (Li et al., 2017).

2.7. Statistical analysis and data availability

Unless stated, data are presented as mean \pm standard error of the mean. As all interventions are paired in the same samples, group mean differences were tested via two-tailed paired student's t-test. Significance was defined as $P < 0.05$.

The pre-processing and signal segmentation described here, as well as all subsequent steps to calculate wave similarity and regularity index have been integrated into an updated version of our electrophysiological mapping software ElectroMap (O'Shea et al., 2019a) (<https://github.com/CXO531/ElectroMap>).

3. Results

3.1. Principles of wave similarity measurements

The steps for calculating OWS from optically recorded samples are illustrated in Fig. 1. The key steps in OWS analysis from optically recorded signals (Fig. 1A) are windowing (Fig. 1B), normalisation (equation (2)), feature alignment (Fig. 1C) and OWS calculation (Fig. 1D and equations (3) and (4)). These steps result in a wave similarity map such as shown in Fig. 1E. The application of OWS during arrhythmia (ventricular fibrillation, VF) is shown in Supplementary Fig. S1. The calculation of the regularity index (RI) follows the same processing steps of windowing, normalisation and alignment. However, for calculation of RI the wave distance is instead calculated (equation (5)) and collapsed to 0 or 1 based on a defined distance threshold (equation (6)). The relationship between these two measures is explored below.

3.2. Wave similarity detects temporal heterogeneity in computationally modelled and optically recorded action potentials

To initially validate whether this approach could be utilised to quantify temporal regularity, we measured OWS in model action potentials. Guinea pig and mouse model action potentials were utilised, with and without temporal alterations. Temporal alterations replicating alternans (Fig. 2A and B) were generated by altering the conductance of the respective repolarising potassium channels in each model for odd beats only, as described in the methods. In the absence of noise, OWS was reduced by the presence of alternans. For guinea pig action potentials, alternans reduced OWS from 1 to 0.68 (Fig. 2Aii), while mouse alternans reduced OWS from 1 to 0.80 (Fig. 2Bii). These differences in measured OWS values are maintained as noise levels are increased to those expected in experimental setups (noise of 8–20% as

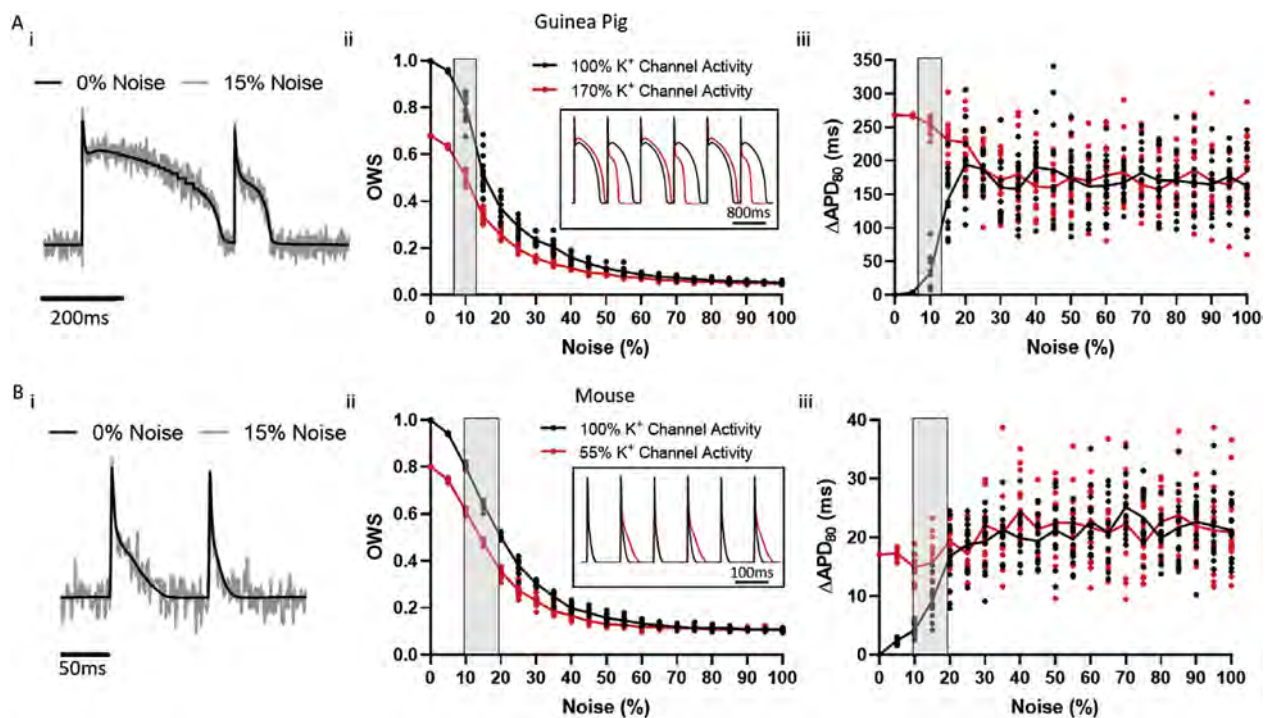


Fig. 2. Validation of the use of optical wave similarity (OWS) for measurement of modelled alternans behaviour. Ai) Example modelled guinea pig action potentials without (black) noise and with addition of 15% noise (grey). ii) OWS measurement of computationally modelled guinea pig action potentials without (black) and with (red) temporal irregularity as a function of noise. Inset shows the two modelled, normalised, signals used (with no noise). iii) ΔAPD_{80} alternans (ΔAPD_{80}) of computationally modelled guinea pig action potentials without (black) and with (red) temporal irregularity as a function of noise. Grey areas show the noise range observed in our experimental optical recordings from guinea pig whole hearts. Bi) Example modelled mouse action potentials with (15%, grey) and without (black) noise addition. ii) OWS measurement of computationally modelled mouse action potentials without (black) and with (red) temporal irregularity as a function of noise. Inset shows the two modelled, normalised, signals used (with no noise). iii) ΔAPD_{80} of computationally modelled mouse action potentials without (black) and with (red) temporal irregularity as a function of noise. Grey areas show the noise range observed in our experimental optical recordings from mouse atria.

observed in our experimental work, highlighted in grey in Fig. 2A and B). As noise is increased beyond these levels however, both the temporally regular and irregular signals exhibit similar and low OWS values, reducing to circa 0.050 and 0.11 for the guinea pig and mouse respectively.

APD alternans magnitude (ΔAPD_{80}) is increased in the model data without noise, from 0 ms to 268 ms and 17.1 ms for guinea pig and mouse action potentials respectively, Fig. 2Aiii and Biii. Increased ΔAPD_{80} in the temporally irregular signals is maintained at experimental noise levels. As noise is increased beyond these experimental values, it is no longer possible to detect the differences in APD alternans magnitude between the temporally regular and irregular signals. This convergence occurs quicker than for OWS, suggesting improved sensitivity for alternans detection compared to standard alternans quantification method. For example, at 25% noise level OWS is still significantly lower in the guinea pig temporally regular signal (0.29 ± 0.01 vs 0.20 ± 0.004 , no alternans vs alternans, $P < 0.0001$). For ΔAPD_{80} however, there is no significant difference (187.4 ± 8.4 ms vs 187.5 ± 9.7 ms, no alternans vs alternans, $P = 0.99$). Similarly, for mouse action potentials at 25% noise OWS is still lower (0.38 ± 0.01 vs 0.28 ± 0.01 , no alternans vs alternans, $P < 0.0001$), but there is no difference in ΔAPD_{80} amplitude (18.8 ± 1 ms vs 17.2 ± 0.9 ms, no alternans vs alternans, $P = 0.26$).

Dynamic decreases in PCL are known to induce greater temporal action potential variability due to the occurrence of AP alternans (Johnson et al., 2010). As an initial investigation into the use of OWS analysis in optically recorded action potentials, we therefore quantified OWS at progressively shorter PCLs in guinea pig whole hearts and mouse atria, Fig. 3. In both experimental models, OWS

decreases with decreasing PCL as expected, Fig. 3A and B. OWS analysis therefore is an effective measure of temporal homogeneity in optically mapped datasets. To test the sensitivity of OWS measure to window setting, we repeated the analysis of OWS as a function of PCL in the guinea pig heart with altering window lengths (50–1000 ms). In all cases, OWS reduced with decreasing PCL, Supplementary Fig. S2A.

3.3. Correlation of wave similarity and regularity index measures

The measurement of OWS and the electrogram derived regularity index (RI) (Faes et al., 2002) is set out by equations (4) and (6) respectively. To test the correlation between these two methods, RI analysis was applied to guinea pig whole hearts at different distance thresholds (ϵ). Fig. 4A and B demonstrate that, as expected, areas of low OWS in an individual heart concurrently demonstrate low RI when an appropriate threshold value is set (e.g. when $\epsilon = \pi/6$, $r^2 = 0.79$). However, when a small distance (high similarity) threshold is set, correlation between the measures is lost (e.g. when $\epsilon = \pi/18$, $r^2 = 0.012$). Furthermore, setting a large distance threshold such as $\epsilon = \pi/3$ is observed to reduce the dynamic range of the RI measure, as many areas are measured to have $RI = 1$ when the OWS measure suggests there are differences in temporal homogeneity (OWS values ranging from 0.77 to 0.94). Setting of the threshold value is also observed to affect mean RI measurements across whole hearts at various PCLs, Fig. 4C. Again, setting a large distance threshold of $\pi/3$ leads to many samples of $RI = 1$, reducing dynamic range. A high similarity, low distance, threshold of $\pi/18$ reduces correlation with OWS measure, ($r^2 = 0.51$ compared to $r^2 = 0.86$ when $\epsilon = \pi/6$).

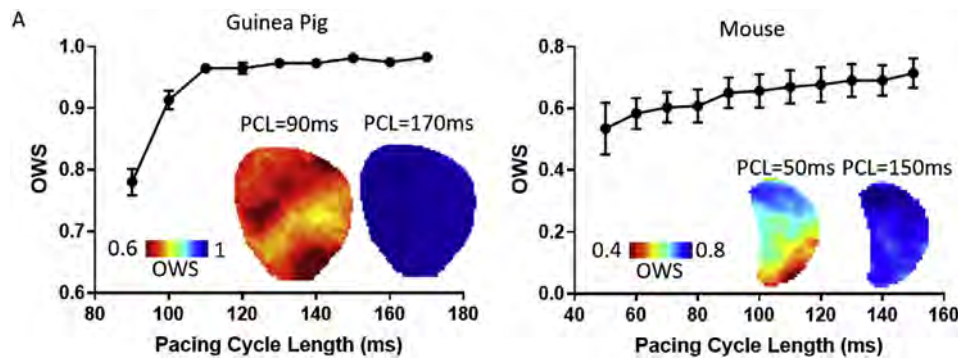


Fig. 3. Validation of the use of optical wave similarity (OWS) for measuring action potential regularity. A) OWS as a function of pacing cycle length (PCL) in optically mapped guinea pig hearts, $n = 6$. Inset shows example OWS maps at PCL = 170 ms and 90 ms respectively. B) OWS as a function of PCL in optically mapped mouse left atria, $n = 7$. Inset shows example OWS maps at PCL = 150 ms and 50 ms respectively.

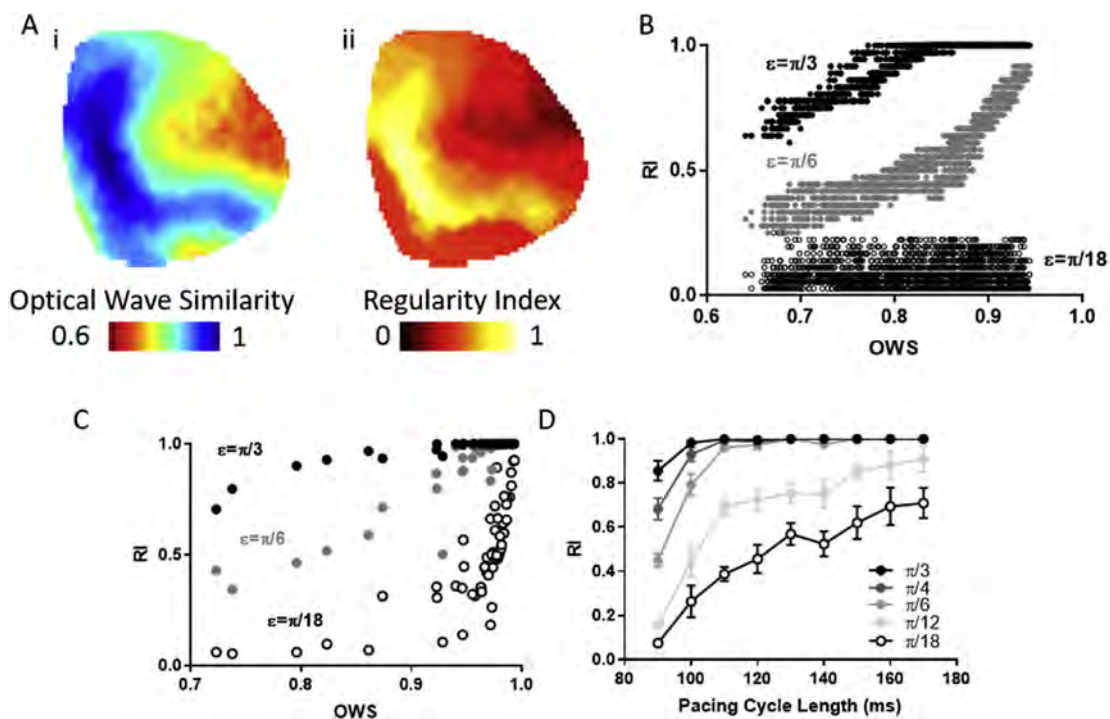


Fig. 4. Correlation of regularity index (RI) and optical wave similarity (OWS) measures in guinea pig whole hearts. A) Example OWS (i) and RI maps (ii, $\epsilon = \pi/6$) at PCL = 90 ms. B) Spatial correlation between OWS and RI measures in the guinea pig heart ($r^2 = 0.86$). C) Correlation of mean OWS and RI measures in guinea pig whole hearts across PCLs. D) RI measure as a function of distance threshold (ϵ). $n = 6$ hearts, 9 PCLs per heart.

These results demonstrate that a key aspect of RI analysis is setting of an appropriate threshold value, ϵ . We therefore measured RI in guinea pig whole hearts as a function of changing threshold as shown in Fig. 4D. As expected, and proportional to the OWS response (Fig. 3C), RI decreased with decreasing PCL. RI therefore, like OWS, appears to be an effective measure of temporal homogeneity in optically mapped datasets. However, considering that the choice of ϵ dramatically alters 'baseline' values and response to decreasing PCL we opted to utilise OWS in subsequent studies.

3.4. Beat-to-beat wave similarity detects short periods of temporal instability

Acute variations in pacing cycle length are known to induce temporal instability in the electrical behaviour of the heart (O'Shea et al., 2019a). To test OWS analysis in this context, we utilised this

parameter to analyse beat-to-beat heterogeneity in a guinea pig whole heart which underwent a sudden increase in pacing frequency from 5 Hz to 8 Hz and then returned to 5 Hz, Fig. 5A–D. OWS analysis identified a transient period of temporal heterogeneity immediately after the onset of 8 Hz pacing (Fig. 5A and B). Similarly, return to 5 Hz pacing induces a reduction in OWS from 0.99 to 0.75, but again the temporal stability of the heart recovers quickly, Fig. 5C and D. Interestingly, immediately after the cycle length change a substantive heterogeneity in OWS is observed between the apex and the base of the heart. Follow up studies will address the pathophysiological significance of this regional heterogeneity.

We also investigated how OWS performs in the setting of spontaneous electrical premature atrial activity (PAA). Mouse left atrium was exposed to 150 ms PCL and areas of the trace exhibiting PAAs were analysed, Fig. 5E. The morphology of the OAPs of the PAAs is seen to be markedly distinct, with $OWS = 0.49 \pm 0.02$ and

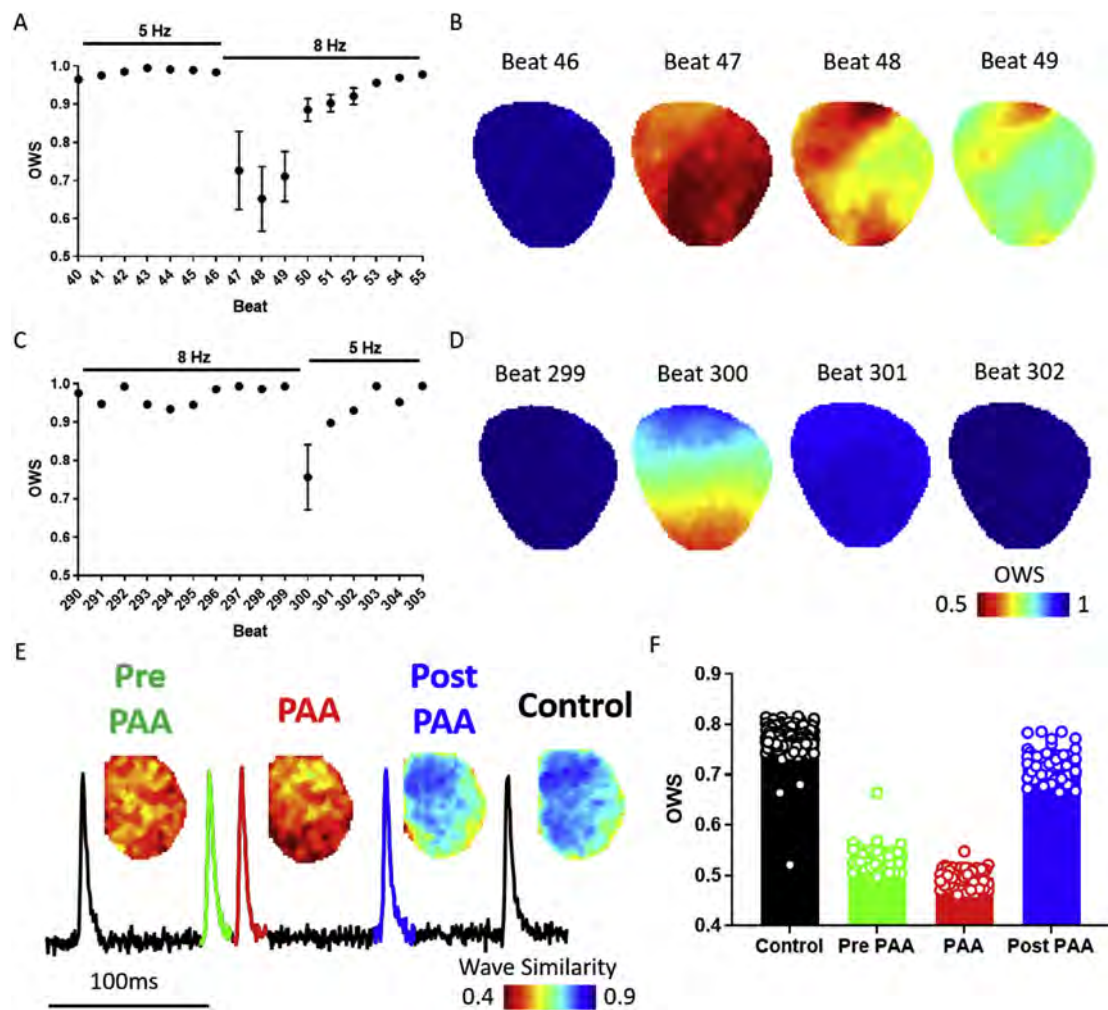


Fig. 5. Single beat optical wave similarity mapping. A) Single beat OWS as a guinea pig heart transitions from 5 Hz to 8 Hz pacing. B) OWS maps immediately before (Beat 46) and after (Beat 47–49) pacing frequency change. C) Single beat OWS as the heart transitions from 8 Hz to 5 Hz pacing. D) OWS maps immediately before (Beat 299) and after (Beat 300–302) pacing frequency change. E) Example trace of a premature atrial activity (PAA, red) and example OWS maps. F) Mean data of OWS for all beats in the experiment classified as control (black), pre-PAA (green), PAA (red) and post-PAA (blue).

0.53 ± 0.02 when compared to the APs immediately before and after the PAA. In contrast, $OWS = 0.73 \pm 0.03$ for APs following the PAA, and 0.77 ± 0.02 for all other 'control' beats, Fig. 5E and F. These results are corroborated by traditional action potential duration (APD) analysis. APD₇₀ of the 'control' beats in this study was 13.3 ± 0.02 , vs 12.9 ± 0.07 for the PAAs for example. OWS mapping therefore suggests that the PAAs are associated with potentially proarrhythmic periods of temporal instability.

3.5. Optical wave similarity detects and quantifies alternans and predicts ventricular fibrillation onset

Dynamic pacing at shorter PCLs induces alternans thereby increasing temporal heterogeneity. Previous work has demonstrated that the PCL required to initiate VF is shorter during SNS of intact guinea pig hearts, showing that SNS is protective against the onset of ventricular fibrillation by the suppression of alternans (Winter et al., 2018). To test how the OWS analysis compares to established measures of beat to beat heterogeneity, namely APD alternans, OWS and alternans magnitude were quantified in guinea pig hearts loaded with a voltage-sensitive dye during SNS and control (no SNS) conditions (preceding onset of VF), Fig. 6A–C. As previously shown, APD alternans magnitude at increased PCL was

shortened (Fig. 6Aii and C). Control hearts showed a significantly increased alternans amplitude compared to SNS at PCL of 100 ms ($\Delta APD_{80} = 9.95 \pm 1.6$ ms vs 4.07 ± 0.9 ms, control vs SNS, $P = 0.0078$). OWS analysis showed comparable changes in temporal heterogeneity. As PCL is decreased, OWS decreases (Fig. 6Ai and B) and at PCL of 100 ms $OWS = 0.91 \pm 0.02$ vs 0.98 ± 0.02 (control vs SNS, $P = 0.0106$). Similar results were seen at all but the longest window settings tested, Supplementary Fig. S2B. There were also regional differences in the onset of temporal heterogeneity, Fig. 6E–F. In control conditions at PCL = 90 ms, the left ventricular (LV) apex is observed to exhibit low OWS when compared to the right ventricle (RV), $OWS = 0.82 \pm 0.03$ vs 0.94 ± 0.01 , LV apex vs RV, $P = 0.045$). In SNS at PCL = 90 ms, the LV apex ($OWS = 0.89 \pm 0.02$) is again observed to exhibit lower OWS versus both the RV (0.96 ± 0.01 , $P = 0.0317$) and LV base (0.96 ± 0.01 , $P = 0.0362$). Therefore, OWS effectively distinguishes between physiological interventions that affect temporal homogeneity in optically recorded action potentials, demonstrating here that hearts without SNS are less temporally stable at the same PCLs. OWS also highlights regional variations in temporal stability, which may have arrhythmogenic consequences.

The hearts without SNS (control) enter VF at slower PCLs (Fig. 6) (Winter et al., 2018), demonstrating the use of OWS in a similar

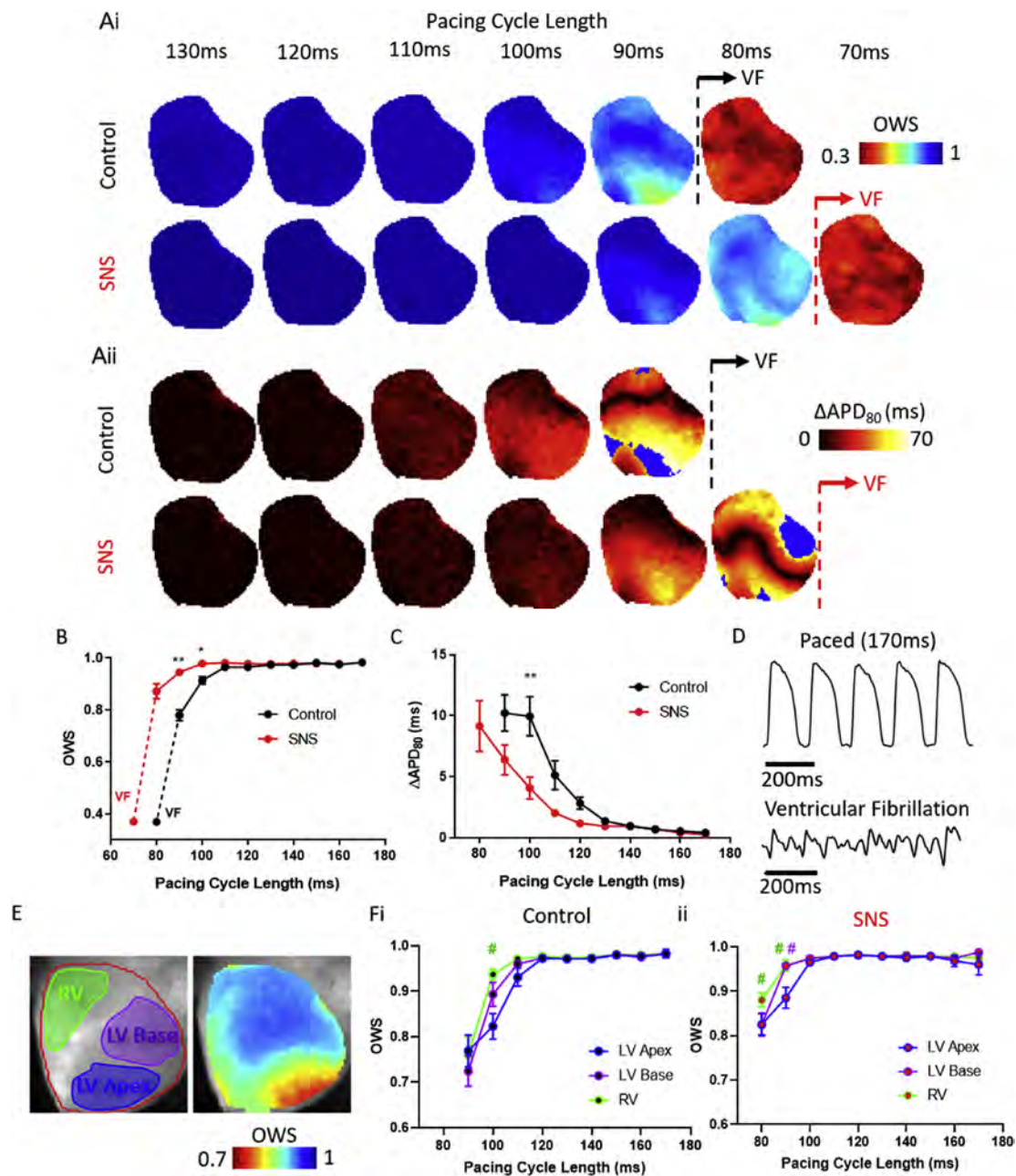


Fig. 6. Effects of sympathetic nervous stimulation on optical wave similarity (OWS) and APD alternans (ΔAPD_{80}) measures. A) Example OWS (i) and ΔAPD_{80} alternans (ii) maps from 130 to 70 ms PCL in a guinea pig heart without (control, black) and with SNS (red). The transition to ventricular fibrillation (VF) is marked by the dashed line in both conditions. Blue areas in APD alternans maps denote areas not analysed due to 80% repolarisation not being reached. B) Grouped data of mean OWS values as a function of PCL in control hearts with/without SNS, before (solid line) and during (dashed line) VF. C) Grouped data of mean ΔAPD_{80} as a function of PCL in control hearts before and during SNS, before onset of VF. D) Example single pixel optical traces recorded during 170 ms PCL stimulation and during VF induced via pacing. E) Anatomical locations of left ventricle (LV) Apex (blue), base (purple) and right ventricle (RV, green) on fluorescence image of voltage dye loaded guinea pig whole heart used for regional studies of OWS. F) Grouped data of regional OWS values as a function of PCL in control hearts with (i) and without (ii) SNS. $n = 6$ hearts, * $P < 0.05$, ** $P < 0.01$ control vs SNS, # $P < 0.05$ LV Apex vs RV (green) or LV Base (purple).

manner as APD alternans as a metric for arrhythmia inducibility. The rapid and disorganised OAPs recorded in arrhythmic data such as during VF makes traditional parameter measurements (APD, alternans, cycle lengths etc) difficult to perform (Kirchhof et al., 1998), Fig. 6D. We therefore tested whether OWS analysis could be used to quantify data during VF. Indeed, OWS is greatly decreased during VF, Fig. 6B, suggestive of large temporal heterogeneity in OAPs recorded during arrhythmia. OWS during VF was 0.37 ± 0.02 and 0.37 ± 0.01 for control and SNS respectively, and there was no difference between conditions ($P = 0.90$).

We also mapped dominant frequency in the hearts during VF. No correlation was found between the two measures (Supplementary Figs. S3A–B). Dominant frequency during VF was reduced in control hearts compared to those with SNS (14.4 ± 0.3 vs Hz 16.4 ± 0.5 Hz, $P = 0.0085$, Supplementary Fig. S3C).

4. Discussion

Here, we have developed and tested the application of OWS mapping as an approach for analysis of pro-arrhythmic and

arrhythmic activity in cardiac optical mapping datasets, Fig. 1. This approach has been inspired primarily from the development of 'regularity index' measures, originally designed for use in atrial electrograms during AF (Faes et al., 2002; Ravelli et al., 2005). Arguably, however, the results shown here demonstrate that the most promising use of OWS analysis in optical datasets may be mapping temporal stability of OAPs before the occurrence of arrhythmias, thus providing a novel index identifying period of electrical instability directly preceding arrhythmias. In Fig. 6 for example, SNS stimulation is shown to suppress temporal heterogeneity induced by decreasing PCL, Fig. 6B. These results align with alternans analysis of the datasets with the same sensitivity, with a significant difference between the control and SNS groups evident with both measures at PCL = 100 ms, Fig. 6B and C (Winter et al., 2018). Measuring APD alternans however requires the measurement of baseline signal level, activation time (for which several different methods are proposed (O'Shea et al., 2019a)), peak time and repolarisation time from the OAPs. As shown in Fig. 2, noise can therefore corrupt APD alternans measures, and restrictive definitions on activation and repolarisation times can prevent analysis of APD, Fig. 6Aii. In contrast, OWS analysis foregoes the need for quantification of these specific and inconsistently defined signal features/points (Laughner et al., 2012).

Furthermore, misidentification of these parameters may lead to false positives or false negatives and may explain the loss of significant difference between the two conditions at PCL = 90 ms, which is evident with OWS analysis. OWS analysis therefore provides a simpler and more easily reproducible processing and analysis pipeline that incorporates entire OAP signal morphology alternations. Additionally, OWS measurement, like alternans analysis, can be performed on a beat-to-beat basis to highlight acute periods of instability, Fig. 5. However, in contrast to alternans analysis, OWS is not designed to study a specific form of temporal instability, and hence can be applied to analyse nonperiodic alterations in cardiac electrophysiology, such as apparently random alterations in beat-to-beat variability that are observed in varied proarrhythmic conditions (Johnson et al., 2010).

OWS, as expected, is proportional to RI mapping results as shown in Fig. 4. RI analysis has been utilised in several important studies of temporal regularity including deciphering the difference in electrical behaviour during paroxysmal and chronic AF (Ravelli et al., 2005). Fig. 4D however shows that the selection of the threshold value ϵ impacts greatly on the measured baseline RI values (at slowest PCL), and the response to decreased PCL. OWS analysis did not involve the setting of such a cut off value, so was deemed more appropriate for these initial studies into the effectiveness of regularity-based measures in optical mapping. Furthermore, the dynamic range of measured OWS values can be reduced by threshold selection. For example, many samples demonstrate mean RI values of 1 when $\epsilon = \pi/3$, despite exhibiting a range of OWS values (0.77–0.94), Fig. 4C. RI mapping therefore may result in subtle changes in waveform morphology temporal stability, for example with small changes in PCL, not being identified.

During arrhythmia (in this case VF), OWS detects an increase in temporal heterogeneity, Fig. 6B and D. This demonstrates that it can be used as a simple marker for arrhythmia onset. However, further studies are required to extend its use to classify sub-types of arrhythmia or arrhythmia severity in optical mapping data. The same alignment and windowing strategy as used for the non-arrhythmic (minima before and after the alignment time) was used to analyse the hearts during VF. Furthermore, during VF the use of equation (1) to detect peaks and hence define alignment times is potentially flawed due to low signal amplitude and regional heterogeneity in activation rates. An important future study therefore would be optimisation of identifying active times for

arrhythmic data (Hajimolahoseini et al., 2018).

Another important consideration is how much lower OWS values report noise in the signal compared to physiological variations. From the model studies conducted, it is observed that OWS decreases with increased noise, and asymptotically approaches a low but non-zero value as noise is increased to levels far beyond those we saw in our experimental recordings, where it can be assumed that any underlying regularity is completely masked by noise. The values of OWS observed in the extreme noise model signals (circa 0.05 and 0.11 for guinea pig and mouse respectively) are much less than the values of OWS measured during VF (0.37 ± 0.02), signifying that there is still regularity in the signals. This suggests that, although noise clearly impacts OWS analysis (Fig. 2A and B), it could still be utilised as a method of subclassifying arrhythmias based on temporal stability. Further studies looking into distinct arrhythmia types are required to confirm this hypothesis, as in the present study only VF was studied, with and without SNS. Analysis resulted in the same values of OWS being recorded in both conditions, suggesting no difference in these arrhythmias in terms of temporal stability (Fig. 6B).

OWS provides a single metric designed to report temporal stability. Analysis of electrogram recordings however suggest that value is gained by utilising these measures concurrently with other measures to identify critical sources or substrates. These measures can combine OWS analysis with other time domain (Baher et al., 2019) (e.g. cycle length by barycentre estimation (Ravelli and Mase, 2014)) or frequency domain metrics (Chang et al., 2013). Therefore, rate and regularity are combined, and it has previously been shown how drivers of AF can exhibit rapid (i.e. high dominant frequency) but regular (high OWS) electrical impulses (Warren et al., 2006). The fact that (i) no correlation was observed between dominant frequency and OWS measures (Supplementary Figs. S3A–B) and (ii) dominant frequency analysis distinguished between control and SNS conditions when OWS does not (Fig. 6E and Supplementary Fig. S3C) supports the idea that these two measures contain divergent information about the electrical behaviour of cardiac tissue. It is suggested that a combined approach, in electrogram mapping, allows classification of sites not just simply by temporal regularity, but also into drivers/sources of arrhythmia and arrhythmia substrates (Ravelli and Mase, 2014). The application of such an approach for optical data therefore warrants further investigation.

As highlighted, a potential advantage of OWS over other methods is the more limited number of signal features that need to be identified, increasing ability for automated analysis. However, optical mapping experiments are conducted in several experimental models with distinct AP morphologies. Furthermore, alongside OAPs, cytosolic and sarcoplasmic reticulum calcium concentrations can be optically measured with calcium sensitive dyes (Wang et al., 2014; Jaimes et al., 2016). The recorded optical calcium transients will also exhibit a distinct wave morphology compared to OAPs. Therefore, further validation and optimisation of OWS is required with different models and fluorescent dyes. In these studies, OWS is shown to be slightly dependent on window size, although only very long window size is shown to effect results of decreasing PCL or applying SNS, Supplementary Fig. S2. More automated windowing methods, including using time or frequency domain based measured features, may improve the method.

A key aspect of this work is the incorporation of these techniques into our freely available mapping software ElectroMap ([www.github.com/CXO531/ElectroMap](https://github.com/CXO531/ElectroMap)) (O'Shea et al., 2019a). From ElectroMaps updated user interface, OWS and RI mapping can be applied with user defined alignment strategy, distance threshold and windowing options, broadening the application of these analyses to different experimental models and fluorescent sensors not

presently tested.

5. Conclusion

OWS mapping provides effective measures of temporal regularity that can be applied in optical datasets. Using these methods, physiological alternations down to single beat timescales can be quantified, and different states can be classified which are known to suppress arrhythmia. By considering the whole signal morphologies of OAPs, the definition of specific signal features is not required, and alterations in any part of the AP will contribute to the local OWS measure.

Appendix A. Supplementary data

Supplementary data to this article can be found online at <https://doi.org/10.1016/j.pbiomolbio.2019.12.004>.

Funding

This work was funded by the EPSRC studentship (Sci-Phy-4-Health Centre for Doctoral Training L016346) to D.P., K.R. and L.F., Wellcome Trust Seed Award Grant (109604/Z/15/Z) to D.P., British Heart Foundation Grants (PG/17/55/33087, RG/17/15/33106, FS/19/12/34204, FS/19/16/34169) to D.P., European Union (grant agreement No 633196 [CATCH ME] to P.K. and L.F.), British Heart Foundation (FS/13/43/30324 to P.K. and L.F.; PG/17/30/32961 to P.K. and A.H., Accelerator Award AA/18/2/34218 to the Institute of Cardiovascular Sciences), and Leducq Foundation to P.K. J.W. is supported by the British Heart Foundation (FS/16/35/31952).

Author contributions

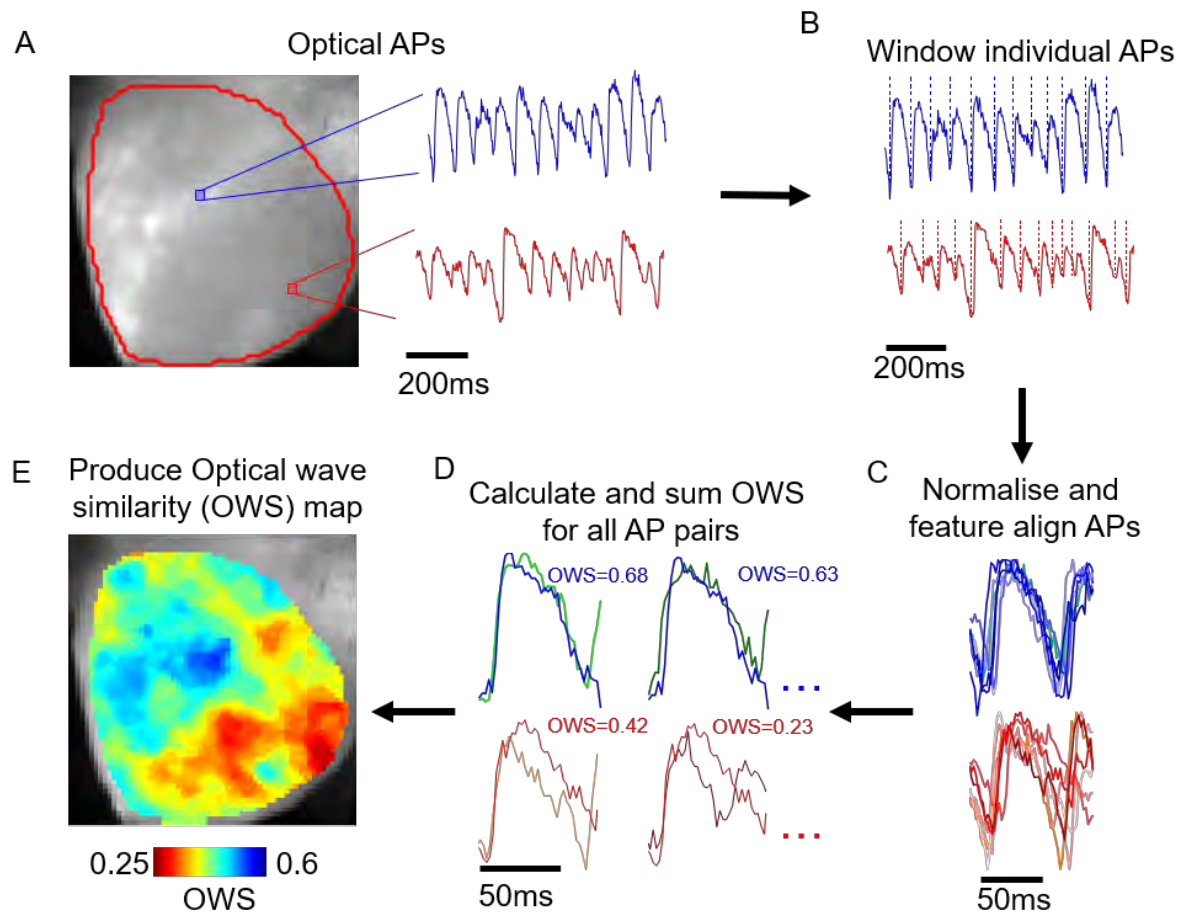
C.O., J.W., A.P.H., J.N.C., P.K., L.F., K.R. and D.P., designed the research. C.O., J.W., A.P.H. and D.M.J. conducted experiments. C.O. produced analysis algorithms, incorporated analysis into ElectroMap software and analysed data. All authors contributed to writing the manuscript.

References

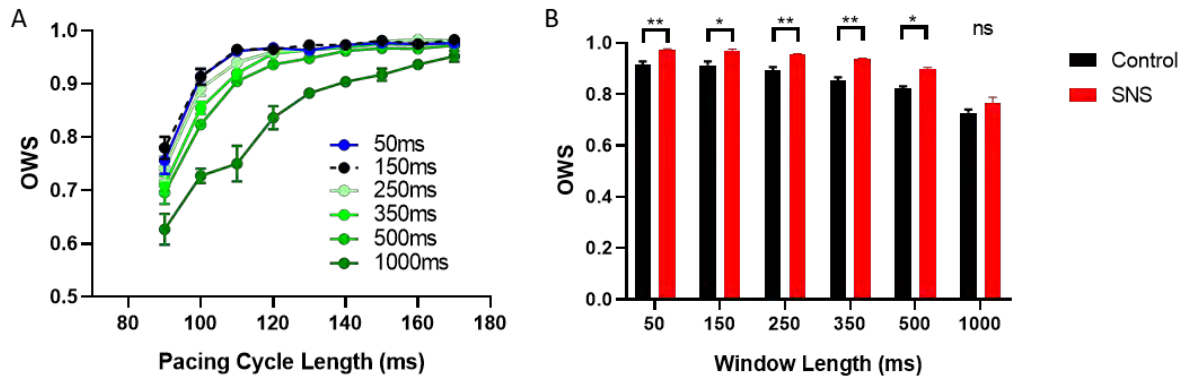
- Atienza, F., Martins, R.P., Jalife, J., 2012. Translational research in atrial fibrillation: a quest for mechanistically based diagnosis and therapy. *Circulation: Arrhythmia and Electrophysiology* 5, 1207–1215.
- Baher, A., et al., 2019. Recurrence quantification analysis of complex-fractionated electrograms differentiates active and passive sites during atrial fibrillation. *J. Cardiovasc. Electrophysiol.* <https://doi.org/10.1111/jce.14161>.
- Bondarenko, V.E., 2004. Computer model of action potential of mouse ventricular myocytes. *Aust. J. Pharm.: Heart and Circulatory Physiology* 287, H1378–H1403.
- Caldwell, J., Redfearn, D., 2012. Ablation of complex fractionated atrial electrograms in catheter ablation for AF: where have we been and where are we going? *Curr. Cardiol. Rev.* 8, 347–353.
- Chang, S.-L., et al., 2013. Electrophysiological characteristics of complex fractionated electrograms and high frequency activity in atrial fibrillation. *Int. J. Cardiol.* 168, 2289–2299.
- Clerx, M., Collins, P., de Lange, E., Volders, P.G.A., 2016. Myokit: a simple interface to cardiac cellular electrophysiology. *Prog. Biophys. Mol. Biol.* 120, 100–114.
- Fabritz, L., et al., 2003. Effect of pacing and mexiletine on dispersion of repolarisation and arrhythmias in Δ KPQ SCN5A (long QT3) mice. *Cardiovasc. Res.* 57, 1085–1093.

- Faes, L., Nollo, G., Antolini, R., Gaita, F., Ravelli, F., 2002. A method for quantifying atrial fibrillation organization based on wave-morphology similarity. *IEEE (Inst. Electr. Electron. Eng.) Trans. Biomed. Eng.* 49, 1504–1513.
- Hajimolahoseini, H., Hashemi, J., Gazor, S., Redfearn, D., 2018. Inflection point analysis: a machine learning approach for extraction of IEGM active intervals during atrial fibrillation. *Artif. Intell. Med.* 85, 7–15.
- Holmes, A.P., et al., 2016. A regional reduction in *ito* and *IKCh* in the murine posterior left atrial myocardium is associated with action potential prolongation and increased ectopic activity. *PLoS One* 11, e0154077.
- Jaimes 3rd, R., et al., 2016. A technical review of optical mapping of intracellular calcium within myocardial tissue. *ajpheart Am. J. Physiol. Heart Circ. Physiol.* 310, 00665, 2015.
- Johnson, D.M., et al., 2010. *IKs* restricts excessive beat-to-beat variability of repolarization during beta-adrenergic receptor stimulation. *J. Mol. Cell. Cardiol.* 48, 122–130.
- Kirchhof, P.F., Larissa Fabritz, C., Franz, M.R., 1998. Phase angle convergence of multiple monophasic action potential recordings precedes spontaneous termination of ventricular fibrillation. *Basic Res. Cardiol.* 93, 412–421.
- Laughner, J.I., Ng, F.S.F.S., Sulkin, M.S., Arthur, R.M., Efimov, I.R., 2012. Processing and analysis of cardiac optical mapping data obtained with potentiometric dyes. *Aust. J. Pharm.: Heart and Circulatory Physiology* 303, H753–H765.
- Li, X., et al., 2017. An interactive platform to guide catheter ablation in human persistent atrial fibrillation using dominant frequency, organization and phase mapping. *Comput. Methods Progr. Biomed.* 141, 83–92.
- Luo, C.-H., Rudy, Y., 1994. A dynamic model of the cardiac ventricular action potential simulations of ionic currents and concentration changes. *Circ. Res.* 74, 1071–1096.
- Moe, G.K., Abildskov, J.A., 1959. Atrial fibrillation as a self-sustaining arrhythmia independent of focal discharge. *Am. Heart J.* 58, 59–70.
- Ng, G.A., Brack, K.E., Coote, J.H., 2001. Effects of direct sympathetic and vagus nerve stimulation on the physiology of the whole heart - a novel model of isolated Langendorff perfused rabbit heart with intact dual autonomic innervation. *Exp. Physiol.* 86, 319–329.
- O'Shea, C., et al., 2019a. ElectroMap: high-throughput open-source software for analysis and mapping of cardiac electrophysiology. *Sci. Rep.* 9, 1–13.
- O'Shea, C., et al., 2019b. High-throughput analysis of optical mapping data using ElectroMap. *J. Vis. Exp.* 1–10. <https://doi.org/10.3791/59663>.
- Pandit, S.V., Jalife, J., 2013. Rotors and the dynamics of cardiac fibrillation. *Circ. Res.* <https://doi.org/10.1161/CIRCRESAHA.111.300158>.
- Ravelli, F., Mase, M., 2014. Computational mapping in atrial fibrillation: how the integration of signal-derived maps may guide the localization of critical sources. *Europace* 16, 714–723.
- Ravelli, F., et al., 2005. Wave similarity mapping shows the spatiotemporal distribution of fibrillatory wave complexity in the human right atrium during paroxysmal and chronic atrial fibrillation. *J. Cardiovasc. Electrophysiol.* 16, 1071–1076.
- Riley, G., Syeda, F., Kirchhof, P., Fabritz, L., 2012. An introduction to murine models of atrial fibrillation. *Front. Physiol.* 3 (AUG), 1–16.
- Schotten, U., Verheule, S., Kirchhof, P., Goette, A., 2011. Pathophysiological mechanisms of atrial fibrillation: a translational appraisal. *Physiol. Rev.* 91, 265–325.
- Shattock, M.J., et al., 2017. Restitution slope is principally determined by steady-state action potential duration. *Cardiovasc. Res.* 113, 817–828.
- Ten Tusscher, K.H.W.J., Hren, R., Panfilov, A.V., 2007. Organization of ventricular fibrillation in the human heart. *Circ. Res.* 100.
- Umapathy, K., et al., 2010. Phase mapping of cardiac fibrillation. *Circulation: Arrhythmia and Electrophysiology* 3, 105–114.
- Wang, L., et al., 2014. Optical mapping of sarcoplasmic reticulum Ca^{2+} in the intact heart: ryanodine receptor refractoriness during alternans and fibrillation. *Circ. Res.* 114, 1410–1421.
- Warren, M., et al., 2006. Mechanisms of wave fractionation at boundaries of high-frequency excitation in the posterior left atrium of the isolated sheep heart during atrial fibrillation. *Circulation* 113, 626–633.
- Winter, J., et al., 2018. Sympathetic nervous regulation of cardiac alternans in the intact heart. *Front. Physiol.* 9, 1–12.
- Yu, T.Y., et al., 2014. An automated system using spatial oversampling for optical mapping in murine atria. Development and validation with monophasic and transmembrane action potentials. *Prog. Biophys. Mol. Biol.* 115, 340–348.
- Yu, T.Y., et al., 2017. Optical mapping design for murine atrial electrophysiology. *Comput. Methods Biomech. Biomed. Eng.: Imaging & Visualization* 5, 368–378.

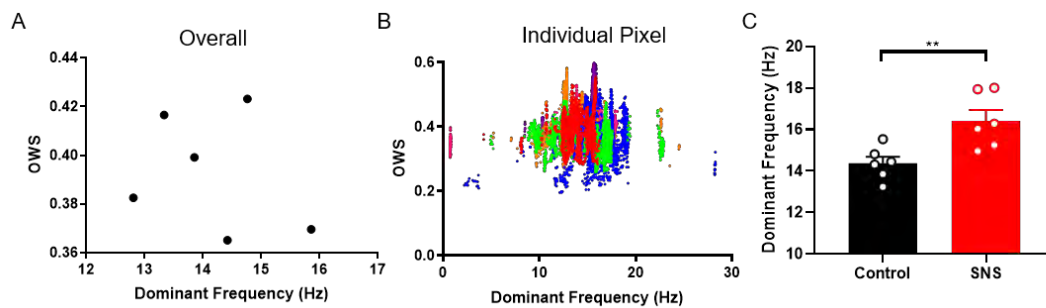
Supplementary Information



Supplementary Figure S1: Calculation of optical wave similarity (OWS) from voltage optical mapping data from a heart during ventricular fibrillation (VF). **A)** Fluorescence image of voltage dye loaded guinea pig whole heart. Representative signals are shown from the locations marked in blue and red on the fluorescence image. **B)** Windowing of optical signals based on signal minima. **C)** Normalisation and alignment of individual optical action potentials (OAPs) in the recorded optical signal. **D)** Example calculations of OWS from OAP pairs. **E)** Constructed map of OWS following analysis steps set out in A-D.



Supplementary Figure S2: Optical wave similarity (OWS) measure as a function of window size in guinea pig whole hearts. Window length refers to time after peak, and time before peak was held at 50ms. A) OWS as a function of pacing cycle length for different window sizes from 50ms (blue) to 1000ms (green). B) OWS at different window lengths with (red) and without (black) sympathetic nervous stimulation (SNS) at 100ms PCL. n=6 hearts, *p<0.05, **p<0.01 control vs SNS



Supplementary Figure S3: Correlation between optical wave similarity (OWS) and dominant frequency measures during ventricular fibrillation (VF). A) Mean OWS and dominant frequency values of each heart. B) Correlation between OWS and dominant frequency values. Each colour represents a different heart, while each point represents a different pixel. C) Dominant frequency with (red) and without (black) sympathetic nervous stimulation in hearts during VF. n=6 hearts, **p<0.01 control vs SNS

Chapter 7

Effects of high fat diet and pitx2 deficiency on left atrial electrophysiology

The following section details unpublished data on the effects of high fat diet on left atrial electrophysiology in wild type and pitx2 deficient mice. Optical mapping experiments were conducted as detailed in section 2. Experiments were conducted by myself in conjunction with Simon Wells.

Data were analysed by myself using the ElectroMap software (Chapter 3, publication 1). Inhomogeneous dye loading, imaging with a high resolution camera (pixel size = $71.4\mu\text{m}$) and the thin profile of the mouse left atria meant the isolated left atrial preparations often exhibited low signal quality. Utilising the software and applying spatial filtering and ensemble averaging however allowed effective analysis of these data. Data analysis was further aided by automated pacing frequency identification which segmented the data into pacing cycle lengths without user input. Conduction velocity module was used to quantify conduction, while action potential waveform analysis was performed using duration and time to peak analyses. High throughput single beat analysis was also performed to study beat-to-beat variations.

7.1 Introduction

Obesity is a known risk factor for atrial fibrillation (AF) [1]. The underlying mechanisms by which obesity promotes AF development are not fully understood. It has been demonstrated that the presence of pericardial fat (i.e. adipose tissue in or near the heart) is associated with AF development and recurrence of AF following ablation procedures. Importantly, the link between pericardial fat and AF is independent of other risk factors suggesting that the local fat deposits directly contribute to AF [2], [3]. Obesity and aging are both associated with an increase in pericardial adipose tissue [4]. Adipose tissue releases a range of peptides with autocrine, paracrine and endocrine effects [5], including sex steroids [6], and has been observed both outside the heart (paracardial fat), but also in the pericardial, epicardial and myocardial layers [7].

Fatty deposits, both infiltrating or surrounding the heart, can therefore cause structural remodelling directly or via paracrine effects of pro-fibrotic, pro-inflammatory or other adipocyte mediators [7]. One such mediator may be oestrogens such as oestradiol. In aged and aged-high fat diet (HFD) mice for example, a strong correlation was observed between pericardial adipose expression of aromatase (final enzyme responsible for conversion of androgens to oestrogens) and atrial arrhythmia inducibility. Effects of aging were exacerbated by HFD, and increased arrhythmia inducibility was also observed in hearts acutely perfused with 17β -oestradiol [8], suggesting a possible association between local oestrogen levels and atrial arrhythmias.

Alongside lifestyle factors such as obesity, it is well established that there is a

genetic component to AF [9]. Chromosomal gene variants close to the Paired like homeodomain-2 (PITX2) gene for example are associated with an increased risk of AF [10]. The PITX2 gene encodes for the transcription factor pitx2, the cardiac isoform of which (pitx2c) is found primarily in the left atrium (LA) and is crucial for healthy development of left-right atrial asymmetry as it regulates expression of LA ion channels [11], as well as having multiple other targets [12], [13]. Reduced levels of pitx2 promote sinoatrial like gene expression in the LA [14], depolarises resting membrane potential [15], [16], shortens action potential duration [15] and increases atrial arrhythmia inducibility [9], [14], [15].

To further elucidate the affects HFD may exert on atrial electrophysiology, cardiac optical mapping of isolated mouse LA was utilised to allow high resolution study on the effects of HFD on action potential morphology and conduction. Experiments were performed in mice at ages of 26-32 weeks, following 20 weeks of high fat diet (HFD) lifestyle. Mice at this age can be considered mature adults, and so fully developed, but with little senescence biomarkers [17]. Therefore, effects of age induced cardiac remodelling or pericardial adipose tissue are thought to be minimally confounding to the effects of the HFD lifestyle [8]. Due to the strong association of pitx2 deficiency in AF, an additional aim of this study was to investigate if mice with a heterozygous expression of a PITX2 null allele (pitx2null mice) would exhibit differential responses to HFD compared to wild type (WT) littermates.

7.2 Methods

Wild type and *pitx2* null littermate mice were fed on a high fat “SDS Western” diet (HFD) for 20 weeks. Western diet chow consisted of 21% fat and 20% protein with drinking water supplemented with 15% fructose. Diet was started between the ages of 6-12 weeks, meaning mice were aged between 26 and 32 weeks at time of experiment. Simultaneously, age-matched mice were fed on the control diet. Control diet chow consisted of 2.5% fat and 14% protein, with standard drinking water. For both control and HFD mice, food and water were available *ad libitum*. Mice were monitored weekly for weight gain or any health complications.

On completion of the diet, left atrial optical mapping experiments using transmembrane voltage dye Di-4-ANEPPS were performed as described in section 2.1. Isolated atria were paced in dark conditions for a minimum of 10 minutes at 1Hz pacing rate to allow the tissue to equilibrate in the optical mapping setup. Once motion artefacts were observed to cease via blebbistatin superfusion, LED illumination was switched on and 1minute recordings made at 0.987kHz sampling rate. Atria were paced at 120ms, 100ms and 80ms pacing cycle length for 100 stimuli at each.

For analysis, the last 20 beats of the 100 stimuli were ensemble averaged, other than in investigations of beat-to-beat variability. Images were spatially filtered with a 4x4 Gaussian filter and temporally filtered with a 3rd order Savitzky-Golay filter. Non-physiological alterations in baseline fluorescence were corrected for by use of a top-hat filter (length 100ms). These processing methods differ compared to other analyses presented in this thesis, and were chosen to match

those used in ongoing optical mapping studies of the sex steroids on atrial electrophysiology [18]. Conduction Velocity (CV), action potential duration (APD) and time to peak (TTP) were mapped across the tissue as described in section 2.1. APD_{30,50} and 70 were quantified, and APD heterogeneity was assessed as the standard deviation of APD distribution across the LA. Beat-to-beat variability of repolarisation was quantified as the mean difference of the tissue averaged APD in the n th beat (APD _{n}) and subsequent beat (APD _{$n+1$}) [19]. This measure of beat-to-beat variability restricts analysis to only consecutive beats. Hence, the coefficient of variability was also quantified as the standard deviation of the measured individual beat APD values divided by the mean APD [20]. Beat-to-beat variability and coefficient of variability was quantified from the final 20 beats of the 100 stimuli at each respective pacing cycle length.

7.3 Results

7.3.1 High fat diet increases mouse body weight of both WT and pitx2 deficient mice

There was no significant difference in body weight of animals at the start of the feeding protocol, Figure 7.1A. However, 20 weeks of HFD feeding led to a significant increase in body weight for both WT and pitx2null mice compared to controls, Figure 7.1B. HFD increased WT body weight to 48.6 ± 1.5 g versus 40.0 ± 1.8 g for WT animals on control diet ($P=0.0032$). Similarly, pitx2null mice fed on HFD had a body weight of 47.0 ± 1.3 g versus 35.5 ± 1.3 g for control diet

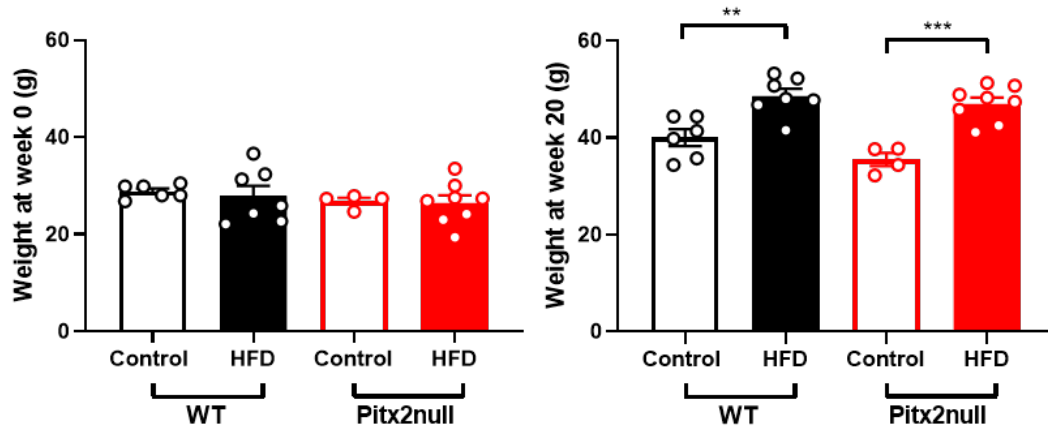


Figure 7.1: Effects of high fat diet (HFD) on body weight of wild type and pitx2null mice. A) Body weight before 20 weeks of control or high fat diet. B) Body weight after 20 weeks of control or high fat diet. $n=4-8$, ** $P<0.01$, *** $P<0.001$

($P=0.0004$). There was a non-significant trend for pitx2 deficient animals to exhibit a lower body weight, both before and after 20 weeks control/HFD diet feeding.

7.3.2 High fat diet prolongs left atrial action potential duration in both wild type and pitx2null mice

Left atrial electrophysiology was assessed by voltage optical mapping. Figure 7.2A shows APD70 distribution of WT and pitx2null mice following 20 weeks control or HFD diet. APD70 was prolonged by HFD when compared to control conditions (23.5 ± 2.2 vs 16.7 ± 2.5 ms; $P=0.0002$) in WT mice. Similarly, HFD prolonged APD70 of pitx2null mice (20.7 ± 2.0 vs 15.94 ± 2.0 ms; $p=0.0095$), Figure 7.2A-C. Both control and HFD pitx2null mice exhibited shorter APD70 than WT mice on the same diet, however these differences were not significant. HFD induced prolongation of APD was evident at all pacing cycle lengths, and

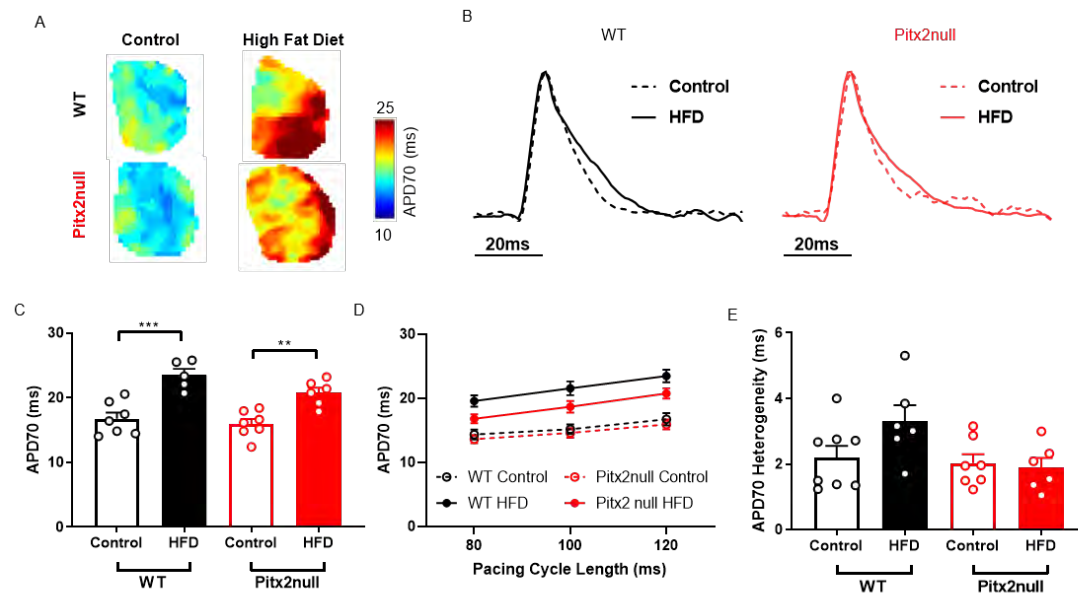


Figure 7.2: Action potential duration (APD) 70 mapping of wild type (WT) and *Pitx2* null mouse left atria, with and without high fat diet (HFD). A) Representative left atria APD70 maps from WT and *Pitx2* null mice, after 20 weeks control or high fat diet. B) Representative optical mapping recordings. C) Grouped APD70 data at 120ms pacing cycle length. D) AP70 as a function of pacing cycle length. E) Grouped APD70 heterogeneity (measured as standard deviation) data at 120ms pacing cycle length. n=5-8, **P<0.01, ***P<0.001

APD similarly shortened in all groups as pacing cycle length was reduced (increase in pacing frequency), Figure 7.2D.

As well as localised alterations, heterogeneity of action potential morphology across cardiac tissue (also referred to as dispersion of repolarisation) is known to contribute to arrhythmogenesis [21]–[23]. Heterogeneity of APD was therefore quantified as the standard deviation of the LA APD distribution. Despite HFD induced prolongation of APD, APD heterogeneity was not changed by either diet or *Pitx2* deficiency, Figure 7.2E.

To see if effects of HFD were consistent throughout repolarisation, APD30 and APD50 were also quantified. When studying these earlier phases of depolarisation, trends identified at APD70 (prolonged APD by HFD in both

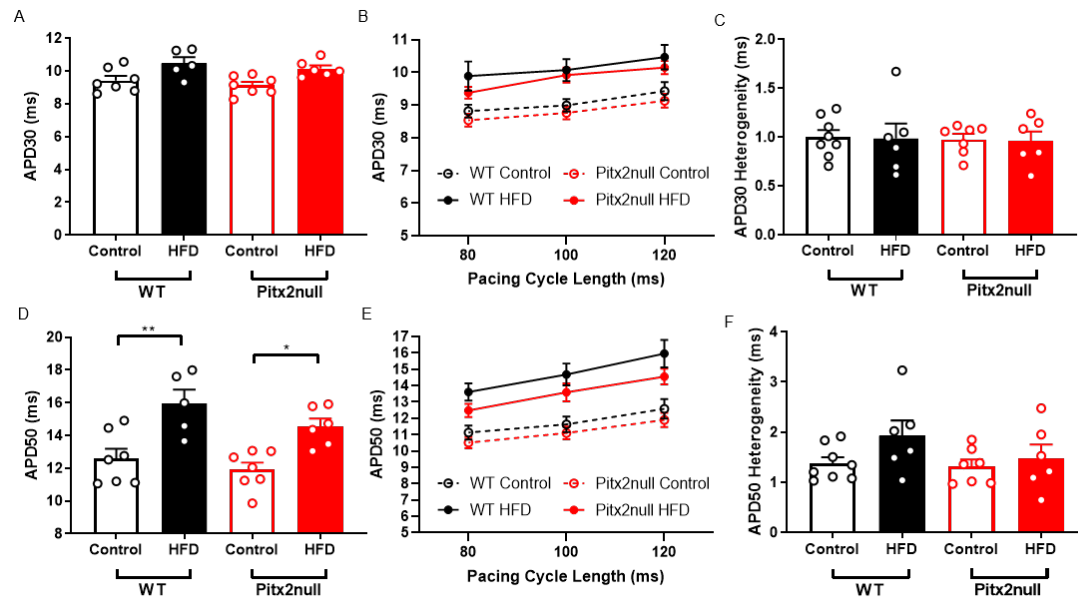


Figure 7.3: Action potential duration (APD)30 and APD50 mapping of wild type (WT) and pitx2null mouse left atria, with and without high fat diet (HFD). A) Grouped APD30 data at 120ms pacing cycle length. B) APD30 as a function of pacing cycle length. C) Grouped APD30 heterogeneity. D) Grouped APD50 data at 120ms pacing cycle length. E) APD50 as a function of pacing cycle length. F) Grouped APD50 heterogeneity. n=5-8, *P<0.05, **P<0.01

genotypes) are observed, although not significantly at the early (APD30) repolarisation phase, Figure 7.3.

7.3.3 High fat diet does not alter beat-to-beat variability of repolarisation

Increase in beat-to-beat variability at both single cell and whole tissue levels has been reported as arrhythmogenic, both concurrently and independently of AP alterations such as prolongation [19], [24]. Optical mapping images were therefore segmented into single beats and APD70 mapped, Figure 7.4A. Mean APD70 was then quantified for each individual beat, Figure 7.4B. Mean APD70 of the n^{th} beat (APD70_n) was then compared to the mean APD70 of the

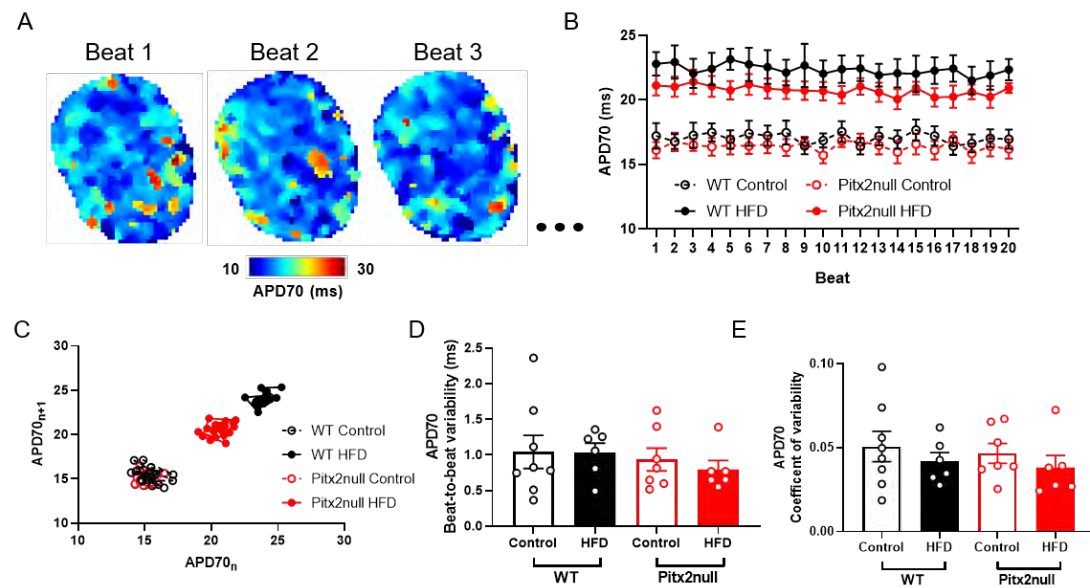


Figure 7.4: Beat-to-beat variability of wild type (WT) and *pitx2* null mouse left atria, with and without high fat diet A) Representative single beat action potential duration (APD) 70 maps. B) Grouped data of mean APD70 at single beats. C) Example Poincare plots of APD70_{n+1} as a function of APD70_n. D) Grouped data of beat-to-beat variability between groups. E) Grouped data of the coefficient of variability in APD70 between groups

subsequent, $n+1^{\text{th}}$ beat, (APD70_{n+1}) Figure 7.4C. No significant differences were observed in consecutive beat-to-beat variability in either diet or genotype. Figure 7.4D. To test overall variability, not just between consecutive beats, the coefficient of variability was also quantified. Again, no significant differences were observed, Figure 7.4E.

7.3.4 High fat diet does not alter left atrial optical time to peak or conduction velocity

As APD measurements (primarily) reflect changes in repolarisation, TTP was also quantified to study alterations in depolarisation owing to diet or genotype. No differences were observed in TTP at any pacing cycle length (Figure 7.5A-

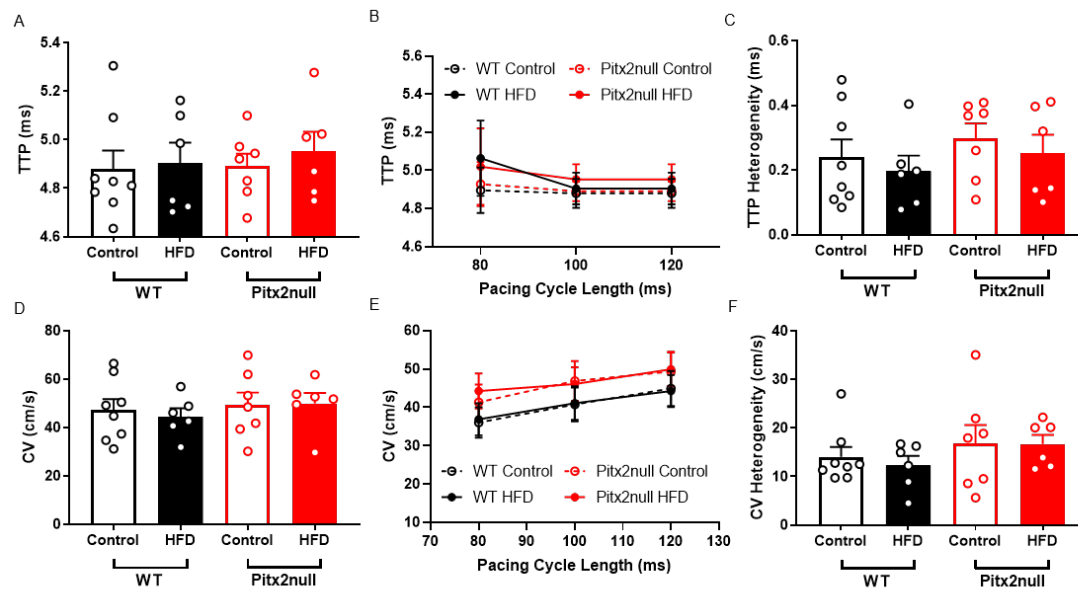


Figure 7.5: Conduction velocity (CV) and time to peak (TTP) mapping of wild type (WT) and pitx2null mouse left atria, with and without high fat diet (HFD). A) Grouped TTP data at 120ms pacing cycle length. B) TTP as a function of pacing cycle length. C) Grouped TTP heterogeneity. D) Grouped CV data at 120ms pacing cycle length. E) CV as a function of pacing cycle length. F) Grouped CV heterogeneity. n=5-8

C), and spatial heterogeneity in TTP was similar in all experimental groups. LA CV was also quantified using the polynomial multi-vector method. HFD did not alter conduction in either WT or pitx2null mice at any pacing cycle length, Figure 7.5D-F.

7.4 Discussion

In this study, cardiac optical mapping was used to investigate the effects of HFD lifestyle on LA electrophysiology in both WT and pitx2null mice. HFD prolonged APD50 and APD70 measured at multiple pacing cycle lengths. APD prolongation is a fundamental condition underlying the occurrence of both delayed (DADs) and early after depolarisations (EADs). HFD induced

prolongation of APD therefore may result in increased incidence of triggered activity in the left atrium, a known mechanism for arrhythmia initiation [25]. Furthermore, localised APD lengthening at/or near fat infiltration can increase repolarisation dispersion. The increase in heterogeneity can become even more pronounced on the background of shortening APD in other areas of the tissue, as often observed in AF [26]. Modelling studies have demonstrated that prolongation of APD (and depolarisation of the resting membrane potential) in response to adipocytes can result in complex spiral like spatio-temporal excitation patterns, with and without AF induced electrical remodelling [27]. APD prolongation may therefore be a mechanism by which obesity increases incidence of atrial arrhythmia.

Prolongation of APD suggests HFD induced electrical remodelling in the mouse LA. Structural remodelling, for example via fibrosis or fat infiltration was not directly measured in these studies. Maintained LA CV (and CV heterogeneity) in HFD mice studied here however suggests that pro-fibrotic activity is not present in the left atrium as a result of HFD, as areas of fibrosis would expect to be evident as areas of conduction slowing and therefore reduced overall CV and increased CV heterogeneity. Previous reports have shown that long-term HFD increases pericardial fat and fibrosis in sheep atria [28]. In these studies where structural remodelling was directly observed, CV slowed, and CV heterogeneity increased [28]. Direct analysis of structural remodelling in HFD fed mice is however warranted to confirm no fat inflation/fibrosis as inferred by conduction analysis.

Findings of HFD prolonging APD herein match findings observed in isolated

rabbit LA cells, where co-culturing with adipocytes induced electrophysiology remodelling and prolonged APD₉₀ induced by larger late sodium (I_{NaL}) and L-type calcium currents (I_{CaL}), among other EP changes [29]. However, there are inconsistent reports on the effects of HFD and/or peri- and epicardial fat on atrial EP. In the studies of Takahashi *et al* for example it was shown that young adult mice (3 to 4 months) fed with HFD for 2 months show reduced expression levels of connexin 40 (Cx40) in mouse atria, but not major sodium or potassium channels [30]. No atrial fibrosis or dilation was seen, but conduction slowing was observed without alterations in APD, in line with the measured expression profiles of the HFD mice. Furthermore, chronic HFD in rats leads to gap junction remodelling and down regulation of connexin proteins Cx40 and Cx43, again expecting to result in conduction changes not observed here [31]. The results obtained herein contradict these previous findings, as no conduction slowing was observed but AP morphology was altered. Takahashi *et al* used optical mapping of the intact RA, measured APD₉₀ (a repolarisation level where significance was lost in our findings) and utilised single vector CV quantification [30]. The diet content and length were also different between the two studies. These methodology differences may explain in some part the discrepancies between the two optical mapping studies.

In guinea pig atria, HFD did induce alterations in AP morphology, but with HFD inducing shortening of APD [32]. The shortening of APD was attributed to an increase in outward rapid (I_{Kr}) and slow (I_{Ks}) potassium currents, which are not expressed by mouse models [33]. In contrast, a decrease in ultra-rapid potassium (I_{Kur}) was observed (when combined with rapid atrial pacing), which is present

in the adult mouse atria and could potentially lead to an increased APD [34]. Decrease of I_{Kur} could therefore be a possible mechanism, in conjunction with changes in I_{NaL} and I_{CaL} , by which HFD induces APD prolongation in mouse left atria. In other studies of adipocyte effects on cardiomyocytes however (co-cultured for 2 to 4 hours), I_{Kur} is increased [29], showing that adipose tissue may exert differing acute and chronic responses.

A possible mechanism by which HFD induces APD prolongation may be the paracrine effects of adipose tissue synthesised oestrogens. Conventionally, oestrogens are thought to be cardioprotective, with lower incidence of cardiovascular diseases in women during reproductive age attributed to, partly, higher levels of circulating oestrogens when compared to men and post-menopausal women [35]. However, oestrogen-only therapy has been shown to elevate AF incidence in women [36], while acute oestrogen exposure in mouse hearts increases atrial arrhythmia vulnerability [8], [37]. Furthermore, it has been reported that acute oestrogen at physiological concentrations suppresses repolarising potassium currents, prolonging APD and potentially explaining the greater susceptibility of females to drug induced torsades de pointes with QT interval prolongation [38].

Depolarisation of the optical recorded APs (quantified as TTP) was not altered by either HFD. However, these results may be artefactual owing to the nature of optically recording APs [39]. Further work using electrode techniques in intact and/or isolated cardiomyocytes is therefore required to fully elucidate effects on cellular depolarisation.

Pitx2 deficiency was not observed to substantially change the response of atrial EP to HFD. In line with previous reports, both control and HFD fed pitx2null mice showed a shorter APD when compared to WT littermates, although this was not significant [15]. Interestingly, the results here suggest pitx2 deficient APD shortening may be greater when comparing between HFD fed mice than controls, suggesting a possible link between pitx2 expression and HFD induced electrophysiological changes. It has recently been shown that pitx2 deficiency leads to increased fat infiltration in cardiac tissue following myocardial infarction, showing a role for pitx2 in cardiac tissue regeneration by maintaining mitochondrial function [40]. The link between HFD, cardiac injury and pitx2 deficiency therefore warrants further studies.

7.5 Conclusion

HFD caused APD prolongation without changing conduction in mouse left atria. These effects are not substantially altered between WT mice and those with pitx2 deficiency. Further studies are required to elucidate the mechanisms by which APD is prolonged by HFD, and the role of adipocyte mediators such as oestrogen.

7.6 Chapter 7 References

- [1] W. Chua et al., “Data-driven discovery and validation of circulating blood-based biomarkers associated with prevalent atrial fibrillation,” *European Heart Journal*, pp. 1–10, 2019.
- [2] M. O. Al Chekakie et al., “Pericardial fat is independently associated with

human atrial fibrillation,” *Journal of the American College of Cardiology*, vol. 56, no. 10, pp. 784–788, 2010.

[3] C. X. Wong et al., “Pericardial fat is associated with atrial fibrillation severity and ablation outcome,” *Journal of the American College of Cardiology*, vol. 57, no. 17, pp. 1745–1751, 2011.

[4] C. J. Nalliah, P. Sanders, H. Kottkamp, and J. M. Kalman, “The role of obesity in atrial fibrillation,” *European Heart Journal*, vol. 37, no. 20, pp. 1565–1572, 2016.

[5] E. E. Kershaw and J. S. Flier, “Adipose tissue as an endocrine organ,” *Journal of Clinical Endocrinology and Metabolism*, vol. 89, no. 6, pp. 2548–2556, 2004.

[6] K. Siiteri, “Adipose tissue as a source of hormones,” *American journal of clinical nutrition*, vol. 45, pp. 277–82, 1987.

[7] J. Auer, “Fat: An emerging player in the field of atrial fibrillation,” *European Heart Journal*, vol. 38, no. 1, pp. 62–65, 2017.

[8] G. B. Bernasocchi et al., “Pericardial adipose and aromatase: A new translational target for aging, obesity and arrhythmogenesis?,” *Journal of Molecular and Cellular Cardiology*, vol. 111, no. June, pp. 96–101, 2017.

[9] F. Syeda, P. Kirchhof, and L. Fabritz, “PITX2-dependent gene regulation in atrial fibrillation and rhythm control,” *Journal of Physiology*, vol. 595, no. 12, pp. 4019–4026, 2017.

[10] P. T. Ellinor et al., “Meta-analysis identifies six new susceptibility loci for atrial fibrillation,” *Nature Genetics*, vol. 44, no. 6, pp. 670–675, 2012.

[11] P. Kirchhof et al., “PITX2c is expressed in the adult left atrium, and reducing Pitx2c expression promotes atrial fibrillation inducibility and complex changes in gene expression,” *Circulation: Cardiovascular Genetics*, vol. 4, no. 2, pp. 123–133, 2011.

[12] T. A. Hjalt and E. V. Semina, “Current molecular understanding of Axenfeld-Rieger syndrome,” *Expert Reviews in Molecular Medicine*, vol. 7, no. 25, pp. 0–17, 2005.

[13] M. C. Hill, Z. A. Kadow, L. Li, T. T. Tran, J. D. Wythe, and J. F. Martin, “A cellular atlas of Pitx2-dependent cardiac development,” *Development (Cambridge, England)*, vol. 146, no. 12, pp. 1–12, 2019.

[14] J. Wang, E. Klysis, S. Sood, R. L. Johnson, X. H. T. Wehrens, and J. F. Martin, “Pitx2 prevents susceptibility to atrial arrhythmias by inhibiting left-sided pacemaker specification,” *Proceedings of the National Academy of Sciences of the United States of America*, vol. 107, no. 21, pp. 9753–9758, 2010.

[15] F. Syeda et al., “PITX2 Modulates Atrial Membrane Potential and the Antiarrhythmic Effects of Sodium-Channel Blockers,” *Journal of the American*

College of Cardiology, vol. 68, no. 17, pp. 1881–1894, 2016. [16] A. Chinchilla et al., “PITX2 insufficiency leads to atrial electrical and structural remodeling linked to arrhythmogenesis,” *Circulation: Cardiovascular Genetics*, vol. 4, no. 3, pp. 269–279, 2011. [17] J. G. Fox, M. T. Davisson, and A. L. Smith, *The Mouse in Biomedical Research*, 2nd ed. 2007.

[18] S. Wells et al., “Acute Oestradiol Slows Conduction in Male, but not Female, Murine Left Atria,” *Heart, Lung and Circulation*, vol. 28, p. S200, 2019.

[19] M. B. Thomsen et al., “Increased short-term variability of repolarization predicts d-sotalol-induced torsades de pointes in dogs,” *Circulation*, vol. 110, no. 16, pp. 2453–2459, 2004.

[20] M. Zaniboni, A. E. Pollard, L. Yang, and K. W. Spitzer, “Beat-to-beat repolarization variability in ventricular myocytes and its suppression by electrical coupling,” *American Journal of Physiology - Heart and Circulatory Physiology*, vol. 278, no. 3, pp. 677–687, 2000.

[21] A. V. Glukhov et al., “Transmural dispersion of repolarization in failing and nonfailing human ventricle,” *Circulation Research*, vol. 106, no. 5, pp. 981–991, 2010.

[22] Y. Bao et al., “Scn2b Deletion in Mice Results in Ventricular and Atrial Arrhythmias,” *Circulation: Arrhythmia and Electrophysiology*, vol. 9, no. 12, pp. 1–15, 2016.

[23] L. Fabritz et al., “Effect of pacing and mexiletine on dispersion of repolarisation and arrhythmias in KQT3 mice,” *Cardiovascular Research*, vol. 57, no. 4, pp. 1085–1093, 2003.

[24] D. M. Johnson et al., “Diastolic spontaneous calcium release from the sarcoplasmic reticulum increases beat-to-beat variability of repolarization in canine ventricular myocytes after -adrenergic stimulation,” *Circulation Research*, vol. 112, no. 2, pp. 246–256, 2013.

[25] L. Gaztanga, F. E. Marchlinski, and Brian P. Betensky, “Mechanisms of Cardiac Arrhythmias,” *Rev Esp Cardiol*, vol. 65, no. 2, pp. 174–185, 2012.

[26] S. Nattel, B. Burstein, and D. Dobrev, “Atrial remodeling and atrial fibrillation: mechanisms and implications,” *Circulation. Arrhythmia and electrophysiology*, vol. 1, no. 1, pp. 62–73, 2008.

[27] T. De Coster, P. Claus, G. Seemann, R. Willems, K. R. Sipido, and A. V. Panfilov, “Myocyte remodeling due to fibro-fatty infiltrations influences arrhythmogenicity,” *Frontiers in Physiology*, vol. 9, no. OCT, pp. 1–13, 2018.

[28] H. S. Abed et al., “Obesity results in progressive atrial structural and electrical remodeling: Implications for atrial fibrillation,” *Heart Rhythm*, vol. 10, no. 1, pp. 90–100, 2013.

- [29] Y. K. Lin, Y. C. Chen, J. H. Chen, S. A. Chen, and Y. J. Chen, "Adipocytes modulate the electrophysiology of atrial myocytes: Implications in obesity-induced atrial fibrillation," *Basic Research in Cardiology*, vol. 107, no. 5, 2012.
- [30] K. Takahashi et al., "High-fat diet increases vulnerability to atrial arrhythmia by conduction disturbance via miR-27b," *Journal of Molecular and Cellular Cardiology*, vol. 90, pp. 38–46, 2016.
- [31] T. Meng et al., "Exposure to a chronic high-fat diet promotes atrial structure and gap junction remodeling in rats," *International Journal of Molecular Medicine*, vol. 40, no. 1, pp. 217–225, 2017.
- [32] L. Martinez-Mateu, J. Saiz, and A. S. Aromolaran, "Differential Modulation of IK and ICa,L Channels in High-Fat Diet-Induced Obese Guinea Pig Atria," *Frontiers in Physiology*, vol. 10, no. September, p. 1212, 2019.
- [33] J. Tamargo, R. Caballero, L. Núñez, R. Gómez, M. Vaquero, and E. Delpón, "Genetically engineered mice as a model for studying cardiac arrhythmias," *Frontiers in Bioscience*, vol. 12, no. 1, pp. 22–38, 2007.
- [34] V. Trépanier-Boulay, M. A. Lupien, C. St-Michel, and C. Fiset, "Postnatal development of atrial repolarization in the mouse," *Cardiovascular Research*, vol. 64, no. 1, pp. 84–93, 2004.
- [35] A. Iorga, C. M. Cunningham, S. Moazeni, G. Ruffenach, S. Umar, and M. Eghbali, "The protective role of estrogen and estrogen receptors in cardiovascular disease and the controversial use of estrogen therapy," *Biology of sex differences*, vol. 8, no. 1, p. 33, 2017.
- [36] M. V. Perez et al., "Effects of postmenopausal hormone therapy on incident atrial fibrillation: The Women's Health Initiative randomized controlled trials," *Circulation: Arrhythmia and Electrophysiology*, vol. 5, no. 6, pp. 1108–1116, 2012.
- [37] G. B. Bernasochi, W. C. Boon, L. M. Delbridge, and J. R. Bell, "The myocardium and sex steroid hormone influences," *Current Opinion in Physiology*, vol. 6, pp. 1–9, 2018.
- [38] J. Kurokawa et al., "Acute effects of oestrogen on the guinea pig and human IKr channels and drug-induced prolongation of cardiac repolarization," *Journal of Physiology*, vol. 586, no. 12, pp. 2961–2973, 2008.
- [39] C. O'Shea, D. Pavlovic, K. Rajpoot, and J. Winter, "Examination of the effects of conduction slowing on the upstroke of the optically-recorded action potentials," *Frontiers in Physiology*, vol. 10, no. 1295, pp. 1–11, 2019.
- [40] L. Li, G. Tao, M. C. Hill, M. Zhang, Y. Morikawa, and J. F. Martin, "Pitx2 maintains mitochondrial function during regeneration to prevent myocardial fat deposition," *Development*, vol. 145, no. 18, 2018.

Chapter 8

Conclusions

8.1 Thesis Outcomes

The major aim of this thesis was to develop novel processing and analysis tools for cardiac optical mapping datasets, and to use these tools to analyse data from a variety of pre-clinical models. A major outcome of this thesis therefore is the development of a robustly validated and freely available MATLAB based tool for analysis of optical mapping data, with a graphical user interface, ElectroMap (Chapter 3) [1], [2]. In developing ElectroMap analysis of key electrophysiological parameters such as action potential and calcium transient morphology, activation and repolarisation times, conduction velocity, diastolic intervals, time to peak and dominant frequency is more readily available. Furthermore, automated pacing frequency identification and segmentation permits analysis of entire experimental recording in a semi-automated manner, increasing both automation and throughput of optical mapping data analysis.

The designed software has been used in several studies. In this thesis, the software has been used to study:

- The shift of leading pacemaker site on optical pacing in mouse sinoatrial nodal preparations with cell selective expression of channelrhodopsin2, Chapter 4 [3].
- Mouse ventricular cardiac slices, revealing transmural gradient and conduction dynamics in response to pacing frequency and pacing regime (electrical field versus optical pacing) (Chapter 5) [4], [5].
- The effects of high fat diet lifestyle on left atrial electrophysiology in wild type and Pitx2 deficient mice (Chapter 7). These studies revealed high fat diet to induce action potential prolongation in the left atria. Other parameters, including temporal and spatial heterogeneity, were unchanged and Pitx2 deficiency did not significantly alter responses.

New techniques have also been explored to increase the automation of optical mapping data analysis. In Chapter 6, the development of optical wave similarity (OWS) is described for analysis of temporal heterogeneity. This methodology is built upon established indices utilised for electrograms. OWS is demonstrated, in both *in silico* and experimental datasets, to map changes in temporal stability due to pacing rate and physiological stimuli. Crucially, unlike other methodologies such as action potential duration alternans analysis, OWS analyses entire optical action potential waveforms without identification of user set signal features such as activation and repolarisation times.

8.2 Limitations

8.2.1 General limitations of optical mapping

Limitations with respect to specific study design and experimental setup are discussed throughout the thesis. However, the technique of optical mapping does have several general limitations that are pertinent its application. The requirement for motion uncouplers such as Blebbistatin reduces the physiological relevance of these experiments, including absence of metabolic deficit and the role of stretch/strain in arrhythmia [6], and it has been suggested that Blebbistatin alters baseline cardiac parameters [7]. Furthermore, it has been shown both in this thesis and by others that fluorescent dyes used in optical mapping may also alter the intrinsic electrophysiological behaviour of cardiac preparations [8], [9]. The use of motion uncouplers and potentially toxic dyes (and other issues including light delivery) has limited use of optical mapping to *ex vivo* and *in vitro* preparations, although the possibility of *in vivo* implementation has recently been demonstrated [10].

The nature of using light to probe cardiac electrophysiology can distort the morphology of optically recorded action potentials in comparison to electrode recordings. This is owing to photon scattering effects and tissue integration by individual pixels where there are asynchronous activation times [11]–[13]. For example, it has been shown in this thesis and previously how changing conduction can alter the morphology of the optically recorded upstroke [13]–[15]. Hence, action potential parameters such as time to peak measured from optical

signals are not only dependent on the individual cardiomyocyte action potential, limiting interpretation. In optical mapping setups where only one camera is used, as is the case for the experiments used here, the resultant image is a 2-dimensional projection of the 3-dimensional surface. This means that assumptions such as equal pixel sizes in the entire image are not valid. In the case of many of the examples presented here however, the geometry of the preparations (e.g. atria and tissue slices) means this limitation will not be as present as in whole heart setups. For whole heart optical mapping, there are now several reports of the use panoramic multi-camera setups to overcome these issues [16], [17].

8.2.2 Mouse models in cardiac electrophysiology research

Mouse models have been extensively used throughout this thesis. As in other areas, mouse models are widely utilised in the study of cardiac electrophysiology. In comparison to other mammalian models, mice benefit from large litters, short gestation periods, rapid maturation and ability to reduce genetic and environmental variability through inbreeding [18]. Possibly most importantly however, the methodologies to alter the genome of mice have been used and established for several years [19], [20]. This means that there are now a plethora of mouse models to study genetic variations that contribute to cardiovascular disease [21]–[25].

An important consideration however is the numerous differences in cardiac electrophysiology between mice and humans, as many physiological parameters

in mammals are known to scale with size. The mouse heart beats between 500 and 700 beats per minute for example, and there are substantial changes in all ECG parameters [26]. Furthermore, Figure 1.3 shows the human and mouse action potential, with distinct ionic currents and morphology [24]. These differences mean that the effects of genetic, physiological or pharmacological interventions on mouse electrophysiology cannot be directly translated to larger mammals and humans [26]–[28].

8.2.3 Analysis limitations and future work

A key aim of this thesis was to automate analysis where possible to increase throughput and reduce levels of user bias. However, there are several areas in which user input and judgment are still required. Although automated thresholding techniques were incorporated into the analysis software [29], it was found in most cases custom region of interest selection was still required due to inhomogeneous/poor tissue loading and the presence of motion artefacts. Currently, thresholding is based on the baseline fluorescence values, which do not necessarily correlate to signal level. Important future work therefore would be to test the efficacy of techniques using the signal time-course, and not just the baseline level, to distinguish between cardiac tissue and background [30], [31], or tissue with and without successful motion uncoupling.

Ideally, optical mapping would be able to be performed in freely beating hearts. Recent studies have demonstrated the possibility to achieve this through utilisation of computer vision techniques, and even simultaneous imaging

voltage, calcium and contraction recording [32], [33]. The use of such computational techniques would simultaneously improve the physiological relevance of optical mapping experiments and automate analysis by removing the need to remove areas of tissue that are still contracting. The incorporation of motion artefact correction techniques would therefore be an important future development, although certain experimental criteria (e.g. homogenous illumination and sufficient contrast areas) are likely to have to be met [34].

Pacing cycle length detection and segmentation and windowing was automatically applied, but settings such as peak amplitude and time interval thresholds often required tuning to recognise all pacing regimes. This was particularly the case when analysing data from different animal species, or in data which was corrupted by large levels of noise for example due to bubbles. The need for parameter tuning could potentially be reduced by altering the signal segmentation is applied on, i.e. currently the whole signal tissue average. Possibilities to improve automation here are to use pacing stimuli rather than tissue derived signals, segment based on signal derivatives such as pseudo electrocardiograms, or to use frequency domain analysis [35]–[37].

Throughout this thesis, traditional and established signal and image processing have been applied. However, in many areas of medical imaging artificial intelligence methodologies have shown efficacy for image thresholding, registration and signal classification [38], [39]. In optically recorded action potentials, relatively simple methodologies such as spectral clustering [40] have shown use for phenotyping cardiomyocytes from embryonic stem cells [41]. The use of artificial intelligence methods therefore is a potential avenue to further

automate processing and analysis of optical mapping datasets. This includes non-selective analysis of the entire waveform rather than specific and inconsistently defined signal points, as explored with optical wave similarity (Chapter 6).

8.3 Conclusion

The original aims of this thesis were

- To develop processing and analysis tools for optical mapping datasets
- To develop novel analysis approaches to increase automation of optical mapping data analysis
- To use developed tools and techniques for the analysis of unique pre-clinical models using optical mapping

Optical mapping is undoubtedly an extremely powerful technique for cardiac electrophysiological research. However, limitations with respect to processing and analysis of these often large and complex datasets persist. In this thesis, a MATLAB based software tool and novel methodologies were developed for processing and analysis datasets. Additionally, novel analysis approaches have been developed to automate analysis of temporal stability in optically recorded signals. These tools have been made freely available to other researchers.

Furthermore, developed tools and have applied to several powerful pre-clinical models, garnering important insights for cardiac electrophysiology. These include

optogenetic control of sinoatrial preparations, transmural heterogeneity in mouse ventricles, and the effects of high fat diet and Pitx2 deficiency on left atrial EP.

8.4 Chapter 8 References

- [1] C. O'Shea et al., "ElectroMap: High-throughput open-source software for analysis and mapping of cardiac electrophysiology," *Scientific Reports*, vol. 9, no. 1389, pp. 1–13, 2019.
- [2] C. O'Shea et al., "High-Throughput Analysis of Optical Mapping Data Using ElectroMap," *Journal of Visualized Experiments*, no. 148, pp. 1–10, 2019.
- [3] R. Dong et al., "A Protocol for Dual Calcium-Voltage Optical Mapping in Murine Sinoatrial Preparation With Optogenetic Pacing," *Frontiers in Physiology*, vol. 10, no. 954, pp. 1–11, 2019.
- [4] S. He et al., "A Protocol for Transverse Cardiac Slicing and Optical Mapping in Murine Heart," *Frontiers in Physiology*, vol. 10, no. 775, pp. 1–8, 2019.
- [5] Q. Wen et al., "Transverse cardiac slicing and optical imaging for analysis of transmural gradients in membrane potential and Ca²⁺ transients in murine heart," *The Journal of Physiology*, vol. 596, no. 17, pp. 3951–3965, 2018.
- [6] D. M. Johnson and G. Antoons, "Arrhythmogenic mechanisms in heart failure: Linking -adrenergic stimulation, stretch, and calcium," *Frontiers in Physiology*, vol. 9, no. October, pp. 1–23, 2018.
- [7] K. E. Brack, R. Narang, J. Winter, and G. Andr, "The mechanical uncoupler blebbistatin is associated with significant electrophysiological effects in the isolated rabbit heart," vol. 5, pp. 1009–1027, 2013.
- [8] A. P. Larsen, K. J. Sciuto, A. P. Moreno, and S. Poelzing, "The voltage-sensitive dye di-4-ANEPPS slows conduction velocity in isolated guinea pig hearts.," *Heart rhythm: the official journal of the Heart Rhythm Society*, vol. 9, no. 9, pp. 1493–500, 2012.
- [9] J. Winter, C. O'Shea, D. Pavlovic, L. Fabritz, and P. Kirchhof, "151 Direct evidence that sympathetic nervous activation accelerates ventricular conduction velocity, but inhibition of responses by DI-8-ANEPPS," *Heart*, vol. 104, no. Suppl 6, p. A107 LP-A108, Jun. 2018.
- [10] P. Lee et al., "In-Vivo Ratiometric Optical Mapping Enables High-Resolution Cardiac Electrophysiology in Pig Models," *Cardiovascular Research*, 2019.
- [11] M. J. Bishop, D. J. Gavaghan, N. A. Trayanova, and B. Rodriguez, "Photon

Scattering Effects in Optical Mapping of Propagation and Arrhythmogenesis in the Heart,” *Journal of Electrocardiology*, vol. 40, no. 6, pp. 75–80, 2007.

[12] R. D. Walton, R. M. Smith, B. G. Mitrea, E. White, O. Bernus, and A. M. Pertsov, “Extracting surface activation time from the optically recorded action potential in three-dimensional myocardium,” *Biophysical Journal*, vol. 102, no. 1, pp. 30–38, 2012.

[13] C. O’Shea, D. Pavlovic, K. Rajpoot, and J. Winter, “Examination of the effects of conduction slowing on the upstroke of the optically-recorded action potentials,” *Frontiers in Physiology*, vol. 10, no. 1295, pp. 1–11, 2019.

[14] M. Entz, S. A. George, M. J. Zeitz, T. Raisch, J. W. Smyth, and S. Poelzing, “Heart rate and extracellular sodium and potassium modulation of gap junction mediated conduction in Guinea pigs,” *Frontiers in Physiology*, vol. 7, no. 16, pp. 1–10, 2016.

[15] C. J. Hyatt et al., “Synthesis of voltage-sensitive fluorescence signals from three-dimensional myocardial activation patterns,” *Biophysical Journal*, vol. 85, no. 4, pp. 2673–2683, 2003.

[16] P. Lee et al., “Low-Cost Optical Mapping Systems for Panoramic Imaging of Complex Arrhythmias and Drug-Action in Translational Heart Models,” *Scientific Reports*, vol. 7, no. August 2016, p. 43217, 2017.

[17] C. Gloschat et al., “RHYTHM: An Open Source Imaging Toolkit for Cardiac Panoramic Optical Mapping,” *Scientific Reports*, vol. 8, no. 2921, pp. 1–12, 2018.

[18] J. G. Fox, M. T. Davisson, and A. L. Smith, *The Mouse in Biomedical Research*, 2nd ed. 2007.

[19] R. Jaenisch and B. Mintz, “Simian virus 40 DNA sequences in DNA of healthy adult mice derived from preimplantation blastocysts injected with viral DNA,” *Proceedings of the National Academy of Sciences of the United States of America*, vol. 71, no. 4, pp. 1250–1254, 1974.

[20] M. G. S. Consortium, “Initial sequencing and comparative analysis of the mouse genome,” *Nature*, vol. 420, no. 6915, pp. 520–562, 2002.

[21] W. Li, L. Yin, C. Shen, K. Hu, J. Ge, and A. Sun, “SCN5A Variants: Association With Cardiac Disorders,” *Frontiers in Physiology*, vol. 9, no. October, pp. 1–13, 2018.

[22] G. Riley, F. Syeda, P. Kirchhof, and L. Fabritz, “An introduction to murine models of atrial fibrillation,” *Frontiers in Physiology*, vol. 3 AUG, no. August, pp. 1–16, 2012.

[23] C. L.-H. Huang, “Murine Electrophysiological Models of Cardiac Arrhythmogenesis,” *Physiological Reviews*, vol. 97, no. 1, 2017.

[24] J. M. Nerbonne, “Studying cardiac arrhythmias in the mouse - A reasonable

model for probing mechanisms?," Trends in Cardiovascular Medicine, vol. 14, no. 3, pp. 83–93, 2004.

[25] P. A. Doevendans, M. J. Daemen, E. D. De Muinck, and J. F. Smits, "Cardiovascular phenotyping in mice," Cardiovascular Research, vol. 39, no. 1, pp. 34–49, 1998.

[26] S. Kaese and S. Verheule, "Cardiac electrophysiology in mice: A matter of size," Frontiers in Physiology, vol. 3 SEP, no. September, pp. 1–19, 2012.

[27] S. Clauss et al., "Animal models of arrhythmia: classic electrophysiology to genetically modified large animals," Nature Reviews Cardiology, 2019.

[28] L. Wang et al., "Different paths, same destination: divergent action potential responses produce conserved cardiac fight-or-flight response in mouse and rabbit hearts," Journal of Physiology, vol. 15, pp. 3867–3883, 2019.

[29] N. Otsu, "A Threshold Selection Method from Gray-Level Histograms," IEEE Transactions on Systems, Man, and Cybernetics, vol. 9, no. 1, pp. 62–66, 1979.

[30] J. Kittler and J. Illingworth, "On Threshold Selection Using Clustering Criteria.," IEEE Transactions on Systems, Man and Cybernetics, vol. SMC-15, no. 5, pp. 652–655, 1985.

[31] C. M. Jarque and A. K. Bera, "A Test for Normality of Observations and Regression Residuals," International Statistical Review / Revue Internationale de Statistique, vol. 55, no. 2, p. 163, 1987.

[32] J. Christoph et al., "Electromechanical vortex filaments during cardiac fibrillation," Nature, vol. 555, no. 7698, pp. 667–672, 2018.

[33] J. Christoph, J. Schröder-Schetelig, and S. Luther, "Electromechanical optical mapping," Progress in Biophysics and Molecular Biology, vol. 130, pp. 150–169, 2017.

[34] J. Christoph and S. Luther, "Marker-Free Tracking for Motion Artifact Compensation and Deformation Measurements in Optical Mapping Videos of Contracting Hearts," Frontiers in Physiology, vol. 9, no. November, 2018.

[35] M. Matson, N. Carlsson, T. Beke-Somfai, and B. Nordén, "Spectral properties and orientation of voltage-sensitive dyes in lipid membranes," Langmuir, vol. 28, no. 29, pp. 10808–10817, 2012.

[36] I. Uzelac and F. H. Fenton, "Robust framework for quantitative analysis of optical mapping signals without filtering," Computing in Cardiology, vol. 42, pp. 461–464, 2015.

[37] Y. Zhao, "From cardiac optical imaging data to body surface ECG," 2014.

[38] C. D. Cantwell et al., "Rethinking multiscale cardiac electrophysiology with machine learning and predictive modelling," Computers in Biology and Medicine, 2019.

vol. 104, pp. 339–351, 2019.

[39] C. Krittanawong et al., “Deep learning for cardiovascular medicine: a practical primer,” *European Heart Journal*, 2019.

[40] A. Y. Ng, M. I. Jordan, and Y. Weiss, “On Spectral Clustering: Analysis and an Algorithm,” *Advances in Neural Information Processing Systems*, pp. 849–856, 2001.

[41] R. Zhu, M. A. Millrod, E. T. Zambidis, and L. Tung, “Variability of Action Potentials Within and among Cardiac Cell Clusters Derived from Human Embryonic Stem Cells,” *Scientific Reports*, vol. 6, no. November 2015, pp. 1–12, 2016.

Appendix A

Supplementary Information for ElectroMap: High-throughput open-source software for analysis and mapping of cardiac electrophysiology, Chapter 3

A.1 Supplementary Material

This appendix provides the supplementary material provided for publication 1, *ElectroMap: High-throughput open-source software for analysis and mapping of cardiac electrophysiology* (Chapter 3). Figure A1-A10 correspond to supplementay Figures I-V in publication 1.

A.1.1 Detailed Methods

Software Development and Availability

All software, processing algorithms and model datasets were developed and implemented in MATLAB R2017a (Mathworks, USA), see Figure 3.1A for graphical user interface (GUI). GUI was designed using MATLAB's GUIDE functionality, and the software can be run either within MATLAB (assuming required toolboxes are present) or from a standalone executable file (e.g. .exe

on a Windows PC, .dmg for Mac OS). Use of the executable file will require download of the freely available MATLAB Runtime (<https://uk.mathworks.com/products/compiler/matlab-runtime.html>). Total download size is 1.3GB. To run the software within MATLAB, the Image Processing, Signal Processing, Statistics and Machine Learning and the Curve Fitting toolbox are required. The total download size of MATLAB code (.m) files < 3MB.

Software source code can be retrieved at <https://github.com/CXO531/ElectroMap> while executable versions are hosted at <https://drive.google.com/open?id=1nJyI07w9Wlt5zWcit0aEylbtg31tANxl>. The software was developed and optimised for use on windows machines and this is the recommended operating system for the software. However, the software has also been tested and successfully used on MAC machines.

Optical Mapping

Mouse (MF1 n=8, 129/Sv n=1) optical mapping experiments were conducted as previously reported [1]–[3]. Animals were anaesthetised using inhaled 4% isoflurane in O₂. Whole hearts were then isolated, mounted on Langendorff apparatus and perfused via the ascending aorta. A standard bicarbonate buffered Krebs–Henseleit solution at 37°C was used containing in mM: NaCl 118; KCl 3.52; MgSO₄ 0.83; KH₂PO₄ 1.18; NaHCO₃ 24.9; Glucose 11.0; CaCl₂ 1.8. Fluorescent dye in DMSO (Voltage: DI-4-ANEPPS (0.125mg/ml), Calcium: Rhod-2-AM (1mg/ml)) was then loaded for 5-10 minutes. The left atrium was

then isolated, and the posterior atrial surface exposed. The atria were superfused under normoxic (95%O₂/5%CO₂) or hypoxic (95%N₂/5%CO₂) conditions with Krebs solution containing contraction uncoupler blebbistatin (10 μ M) and paced with bipolar platinum electrodes at 2 times diastolic threshold. Fluorescent dyes were excited by four LEDs at 530nm, and filtered fluorescence (>630nm for DI-4-ANEPPS; 565-605nm for Rhod-2-AM) captured using ORCA flash 4.0 camera (1kHz sampling rate, 200x2048 pixels, 71 μ m/pixel).

Optical mapping experiments in guinea pigs (n=6) were conducted as previously reported [4], [5]. Adult male guinea pigs were anaesthetised with sodium pentobarbitone (160mg/Kg, i.p.) along with concomitant heparin. Hearts were perfused in Langendorff mode through the descending aorta (perfusion pressure 65-75mmHg, 37°C). Buffer solutions contained in mM: NaCl 114.0; KCl 4.0; CaCl 1.4; NaHCO₃ 24.0; NaH₂PO₄ 1.1; glucose 11.0 and sodium pyruvate 1.0. Solutions were filtered using an in-line cellulose filter (5 μ m pore diameter)). Hearts were uncoupled with blebbistatin (15 μ M) and stained with Di-8-ANEPPS (1mg/ml in DMSO; 200-300 μ L). Dyes were injected slowly into the perfusion line over a 5 to 10-minute period. Excitation light was at 530nm, with emission light collected at >610nm. Hearts were imaged through an Olympus MVX10 stereomicroscope and signals recorded on Evolve Delta 512x512 pixel EMCCD cameras (500Hz sampling rate, 64x64 pixels, 320 μ m/pixel).

Optical mapping experiments of human atria were conducted as previously reported [6]. The left atrial appendage was removed using an endoscopic stapling device (Endo Gia stapler, Tyco Healthcare Group). The tissue sample was transported to the optical mapping setup in 100mL cooled superfusion fluid

(Na⁺, 155.5 mmol/L; K⁺, 4.7 mmol/L; Ca²⁺, 1.45 mmol/L; Mg²⁺, 0.6 mmol/L; Cl⁻, 136.6 mmol/L; HCO₃⁻, 27 mmol/L; PO₄³⁻, 0.4 mmol/L; glucose, 11.1 mmol/L; and heparin, 1000 IE). In the optical mapping setup the preparation was submerged in a tissue bath. The superfusion fluid was kept at a temperature of 36.5°C to 37.5°C and oxygenised with a mixture of 95% O₂ and 5% CO₂ to maintain a pH of 7.4. The preparations was stimulated at 100 beats per minute at twice diastolic threshold with a pulse width of 2ms using an epicardial electrode. The preparation was equilibrated for \geq 30 minutes. Di-4-ANEPPS (Tebu Bio) was used as a membrane potential-sensitive fluorescent dye and Blebbistatin to remove motion artifacts. A MiCAM Ultima camera (SciMedia USA Ltd) was used to record epicardial images of an area of 1 cm² with a resolution of 100 x 100 pixels and a sample time of 0.5ms. Images were stored using MiCAM Ultima Experiment Manager. The occurrence of small motion artifacts precluded analysis of the repolarisation across the atrial preparation.

A.1.2 Processing and Analysis Parameters

The software allows a choice of spatial filtering, temporal filtering, and baseline correction methods. However, in the analysed data presented in this work, a 4x4 pixel Gaussian spatial filter was applied to the raw signal which was subsequently filtered using a 3rd order Savitzky-Golay temporal filter. Linear top-hat filtering was used to correct for non-physiological changes in baseline fluorescence.

Results were exported from ElectroMap's interface in a variety of formats depending on specific analysis performed. To study both mean values but

additionally tissue heterogeneity for conduction velocity and calcium decay constant, all calculated values within the maps were exported as comma separated value files, as were the results of angular distributions of CV and the activation curves. The corresponding maps were exported as TIFF files. For extended beat-to-beat analyses, summary data (mean, standard deviation) for each individual beat was exported in a single comma separated value file as it was calculated automatically in ElectroMap once the whole file analysis had begun. Corresponding maps at each individual beat were also exported as a single GIF file and additionally AVI video files.

Activation and duration mapping

For the quantification of conduction velocity, it is necessary first to define time of activation for each pixel in an image to create the activation map. Equally, activation time requires measurement to quantify both action potential and calcium transient duration. For the methods for this that are employable in ElectroMap, see Figure 3.10. For conduction velocity analysis, unless otherwise stated, the midpoint of depolarisation was used to produce the activation maps. APD and CaT measurements were taken from upstroke (i.e. dF/dt_{max}) to 50% repolarisation/decay, unless otherwise stated.

Conduction Velocity Measurement

A stand-alone conduction velocity module was developed and integrated within ElectroMap, including two established methodologies for CV calculation, 'multi-

vector' and 'single vector' methods (figure 3A and B) while a novel activation curve method (figure 3C and D) is introduced.

The polynomial 'multi-vector' method to quantify CV_{local} is the polynomial surface method developed by Bayly et al, originally proposed for use in epicardial electrode mapping [7]. For local regions of $n \times n$ pixels, a polynomial surface, $T(x,y)$, is fitted using least squares fitting that describes the relationship between activation time, t , and spatial position (x,y) , where $T(x,y)$ is of the form,

$$T(x,y) = ax^2 + by^2 + cxy + dx + ey + f. \quad (A.1)$$

The local conduction velocity can then be calculated as

$$CV_{local} = \frac{T_x}{T_x^2 + T_y^2} \mathbf{i} + \frac{T_y}{T_x^2 + T_y^2} \mathbf{j} \quad (A.2)$$

where $T_x = \partial x / \partial T$ and $T_y = \partial y / \partial T$ are the 'conduction gradients' in the x and y direction respectively, and \mathbf{i} and \mathbf{j} are unit vector directions. This procedure therefore computes both a magnitude and direction of conduction in each local region.

The 'single vector' method will measure the time delay (t) in activation between two points, and then use the distance between the points (r) to estimate conduction velocity. The single vector velocity, CV_{single} , between two points separated by distance r will then be calculated as:

$$CV_{\text{single}} = r/\Delta t \quad (\text{A.3})$$

Additionally, we have developed and implemented a novel ‘activation-curve’ method for conduction analysis. Here, the percentage of tissue activation is plotted as a function of time as demonstrated in Figure 3.2D. Hence, at time t , the value of the activation curve as a percentage, $\text{Act}(t)$ will be:

$$\text{Act}(t) = 100 * 1/N. \sum_{n=1}^N \delta_n(t) \quad (\text{A.4})$$

in a tissue image series made up of N pixels, where $\delta_n(t)$ becomes 1 at time of activation (and 0 otherwise). Equation 3.3 can similarly be used to plot a repolarisation curve, where $\delta_n(t)$ is redefined to become 1 at time of repolarisation. From this activation curve, it is possible to define an activation constant, such as time to reach 50% (act50) or 90% (act90) activation. Comparison between activation constants of each tissue can then allow objective comparison of changes in conduction kinetics.

Calcium decay constant (τ)

τ was calculated by fitting of a mono-exponential decay model of the form:

$$F(t) = F_0 \exp(-t/\tau) + C \quad (\text{A.5})$$

where the fluorescence level at time t depends on the peak fluorescence, F_0 , and

the subsequent decay (C is a constant). For the calculation of τ present in Figure 6, equation 4 was fitted from 30% to 90% (τ_{30-90}) decay from peak cytosolic Ca^{2+} . However, we also investigated the effects on decay constant mapping of fitting to other stages of Ca^{2+} decay, such as from 10% to baseline ($\tau_{10\text{-BL}}$, Figure 3.13E).

Cardiac alternans module

Cardiac alternans were defined by four different measures, duration alternans, peak alternans, load alternans and release alternans (Figure 3.16). Peak alternans (ALT_{peak}) between subsequent calcium transients was defined as the percentage increase in peak value of the larger peak (peak_l) compared to the smaller peak (peak_s):

$$\text{ALT}_{\text{peak}} = 100 * (\text{peak}_l / \text{peak}_s) \quad (\text{A.6})$$

Duration alternans (ΔAPD or ΔCaT) were measured as the time difference between the duration of one action potential/calcium transient and the next. For example, in the case of two consequent calcium transients of duration CaT_1 and CaT_2 :

$$\Delta\text{CaT} = |\text{CaT}_1 - \text{CaT}_2| \quad (\text{A.7})$$

The effects of cytosolic Ca^{2+} load and overall amplitude (in contrast to just peak

value) were investigated by comparing the load alternans amplitude to the release alternans amplitude, as in Wang *et al*, 2014 (where similar measures were applied to study sarcoplasmic reticulum Ca^{2+} handling) [8]. If L is defined as the peak amplitude of the large beats (i.e. where the amplitude is greater than the previous beat), S the amplitude of the small beats, and D the diastolic load of the small beats the release alternans ($\text{ALT}_{\text{release}}$) are defined as:

$$\text{ALT}_{\text{release}} = 1 - (S/L) \quad (\text{A.8})$$

Conversely, we define load alternans (ALT_{load}) as:

$$\text{ALT}_{\text{load}} = D/L \quad (\text{A.9})$$

Dominant frequency and phase mapping

Dominant frequency analysis is achieved by calculating the frequency spectrum of the input signal by fast Fourier transform. Dominant frequency was then defined as the frequency with the most power in the resulting frequency spectrum in the range of 4-10Hz. Zero padding was applied to deliver a power spectrum with a frequency resolution of 0.05Hz [9], [10]. Settings such as frequency range and resolution are controlled within ElectroMap's interface. Phase mapping is performed by calculating the Hilbert transform of the signal, from which the instantaneous phase ranging from $-\pi$ to π can be calculated at a given time point [10], [11].

A.1.3 Production of model murine datasets

The datasets were produced by creating a MATLAB function that for a given time, t , will return the fluorescence value $F(t)$. This function acts by simply approximating the murine optical action potential (i.e. that recorded by a potentiometric dye) in a piecewise manner. Depolarisation of the action potential was modelled using a simplified Gaussian function:

$$F(t) = F_0 \exp(-(t - t_p)^2); \quad 0 \leq t \leq t_p \quad (\text{A.10})$$

where t_p is the time to peak, i.e. time between depolarisation starting and peak transmembrane voltage and F_0 is the maximum fluorescence/voltage value. The repolarisation was then modelled in two parts:

$$F(t) = m * (t - t_p) + F_0; \quad t_p < t \leq (t_p + \text{apd20}) \quad (\text{A.11})$$

where m is the line gradient that connects the peak fluorescence at t_p to a later time ($t_p + \text{apd20}$) where the fluorescence is 80% of its peak value (as dictated by the user, apd20). Hence the early repolarisation is modelled as a straight line. From this point, it is then modelled as an exponential decay:

$$F(t) = A \exp(-Bt); \quad t > t_p + \text{apd20} \quad (\text{A.12})$$

where A and B are constants found by fitting an exponential decay to user defined

values for the times of 30%,50%,70% and 90% repolarisation occur (i.e. apd30, apd50, apd70, apd90). Random noise was added to $F(t)$ by selecting a value from a set of normally distributed pseudorandom numbers, the standard deviation of which is set as a percentage value of the action potential amplitude. An example of using this model function is shown in Figure 3.12A, as well as the effect of different noise levels on simulated action potential morphology (Figure 3.12B).

2D images of a murine atria have then been modelled using this function. The pseudocode for this is shown below, where factors such as overall velocity, the presence of a conduction block and sampling rate are used to work out an 'effective time' for each pixel in each frame. This model has several limitations owing to its simplicity both in approximation of the murine action potential (a morphological approximation) and conduction across the atria. Therefore, it is currently limited to the simple validations presented here.

Model Pseudocode

For each frame

Compute frame time, $T = \text{Frame_number} * (1/\text{sampling_rate})$

For each pixel

If pixel not within area of conduction block

Find effective distance,

$$D = (x^2 + (A*y)^2)^{1/2}$$

where x and y are coordinate distance from wave origin (centre of image) and A is a constant that controls the degree of anisotropy in conduction. For example, A=1 represents isotropic conduction, A=2 represents 2 times slower conduction along y direction compared to x.

End

If pixel inside area of conduction block

Find effective distance

$$D = D1 + D2.$$

where D1 = effective distance before reaching conduction block and D2 = effective distance within conduction block. Hence

$$D1 = (x1^2 + (A*y1)^2)^{1/2}$$

where x1 and y1 are coordinate distance from origin to area of conduction and

$$D2 = C * (x2^2 + (A*y2)^2)^{1/2}$$

where x2 and y2 are coordinate distance from edge of conduction block region along line connecting pixel with origin. C is a constant that represents the conduction block factor, i.e. C=2 represents 50% velocity within block region compared to rest of tissue.

End

Compute effective time, $t = T - D/V$

where V is the velocity of wave propagation.

Compute $F(t)$ using function described above and save $F(t)$ for each pixel within each frame.

Addition of noise

End

A.1.4 Supplemental Figures

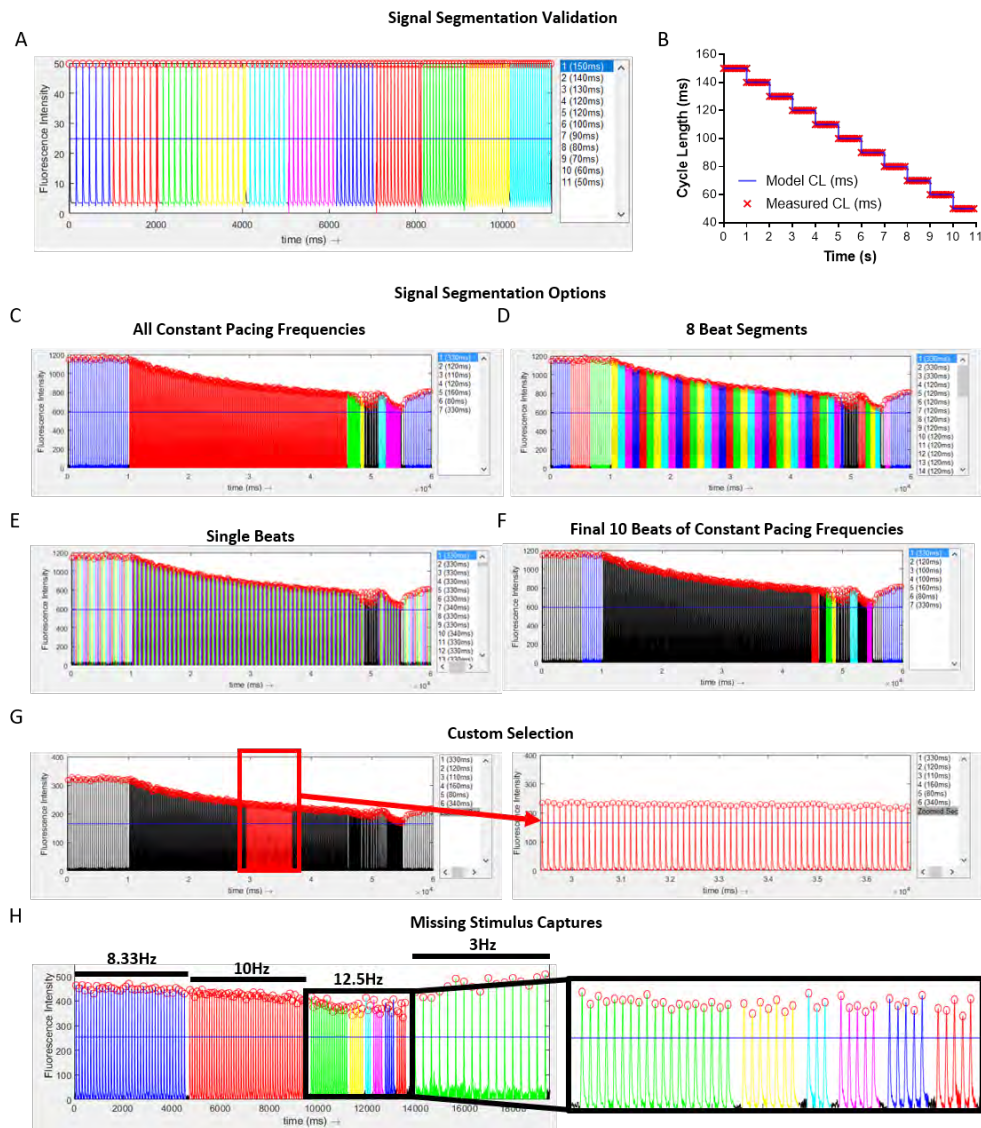


Figure A.1: Automatic, pacing frequency, based signal segmentation options and validation. A and B) We validated our pacing frequency-based segmentation by created a model dataset where the cycle length was reduced by 10ms every 1s from 150ms to 50ms (A). B) The measured CL in ElectroMap exactly matched that of the model throughout. C-G) ElectroMap automatically detects changes in pacing frequency in real experimental data, as demonstrated in (C). The signal can then be further segmented into segments of a desired number of beats, such as 8 shown here in (D). This can be done down to a single beat level (E). Equally, only the final few beats at a given pacing frequency can be analysed to allow sufficient frequency adaption, such as the final beats in (F). G) Along with automatic segmentation, custom region selection is achievable by selecting the desired time from the signal. H) Example of automatic segmentation with missing stimulus captures induced by 12.5Hz pacing.

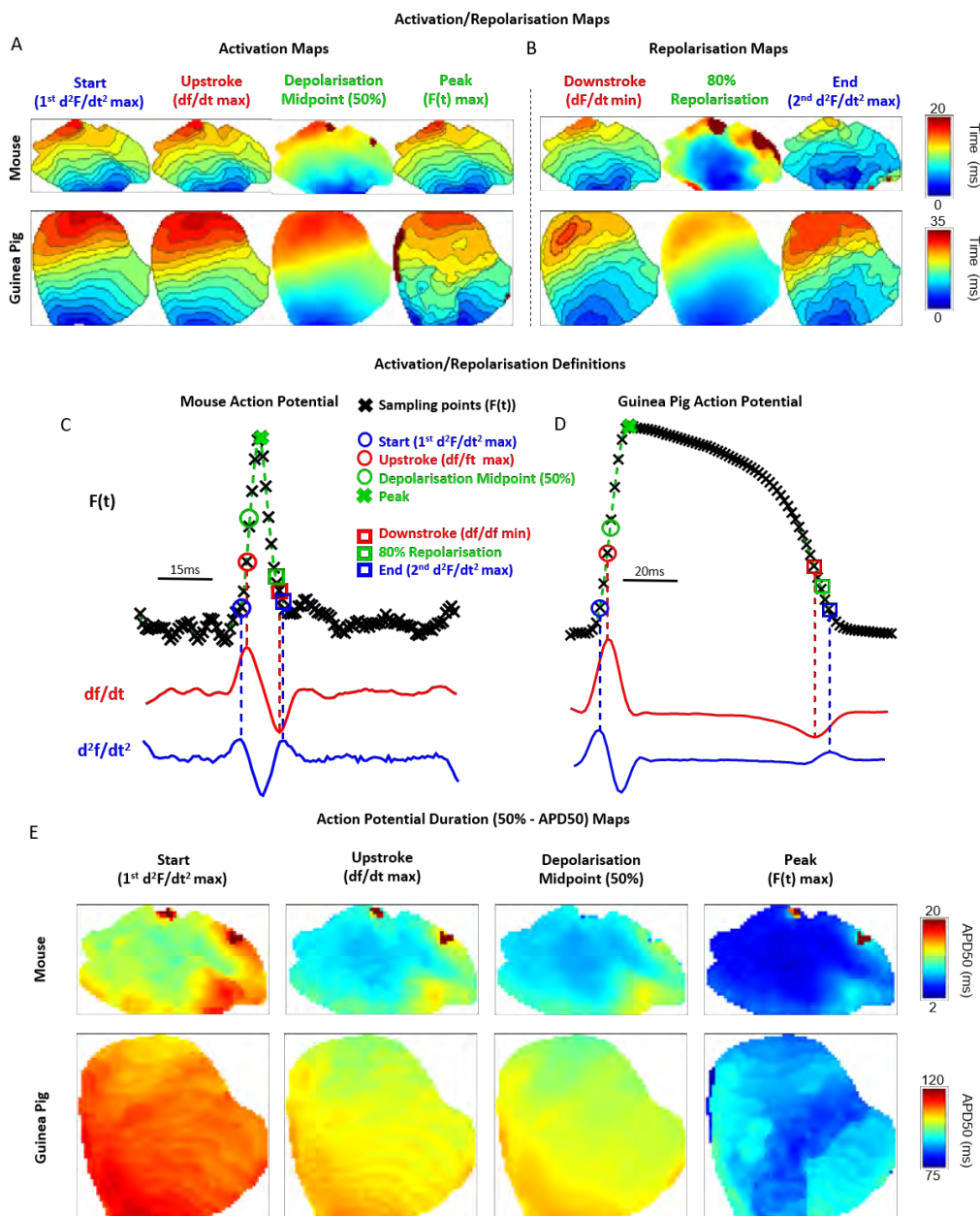


Figure A.2: Activation and repolarisation definitions. A) Example activation maps from both mouse atrium and guinea pig whole heart using the four different activation definitions employable using ElectroMap. Isochronal line shown at 1ms (murine data sampling rate) and 2ms (guinea pig data sampling rate) intervals in maps where interpolation is not applied. B) Example repolarisation maps from both mouse atrium and guinea pig heart using the three different repolarisation definitions in ElectroMap. C) Optically measured murine action potential (black, $F(t)$) with its first (red, dF/dt) and second (blue d^2F/dt^2) derivative shown below. Highlighted are the four measured activation points and three measured repolarisation points used to construct the upper activation and repolarisation maps in A and B. D) As C, but from the Guinea Pig action potential to construct the lower activation/repolarisation maps in A and B. E) Example APD50 maps from Mouse and Guinea Pig tissue using the four different activation measures in defining start of the action potential for calculation of APD50.

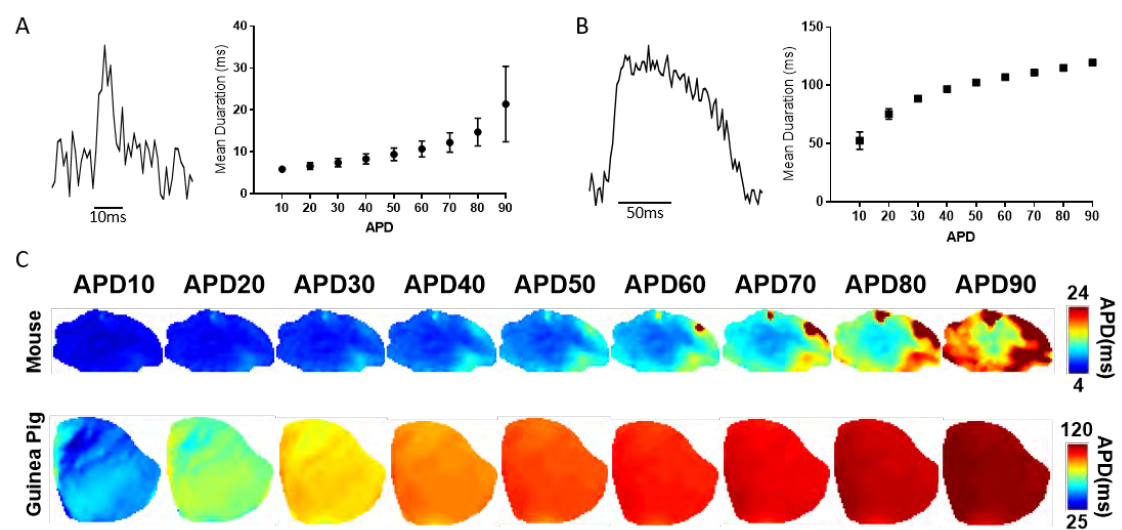


Figure A.3: Action potential duration (APD) mapping. A) Example raw trace from a single pixel (left panel) and mean APD measurements as a function of user chosen repolarisation percentage in mouse atrium (right panel). B) Example raw trace from a single pixel (left panel) and mean APD measurements as a function of repolarisation percentage in guinea pig whole heart (right panel). Data shown as mean standard deviation. C) APD maps from murine atria and guinea pig whole heart.

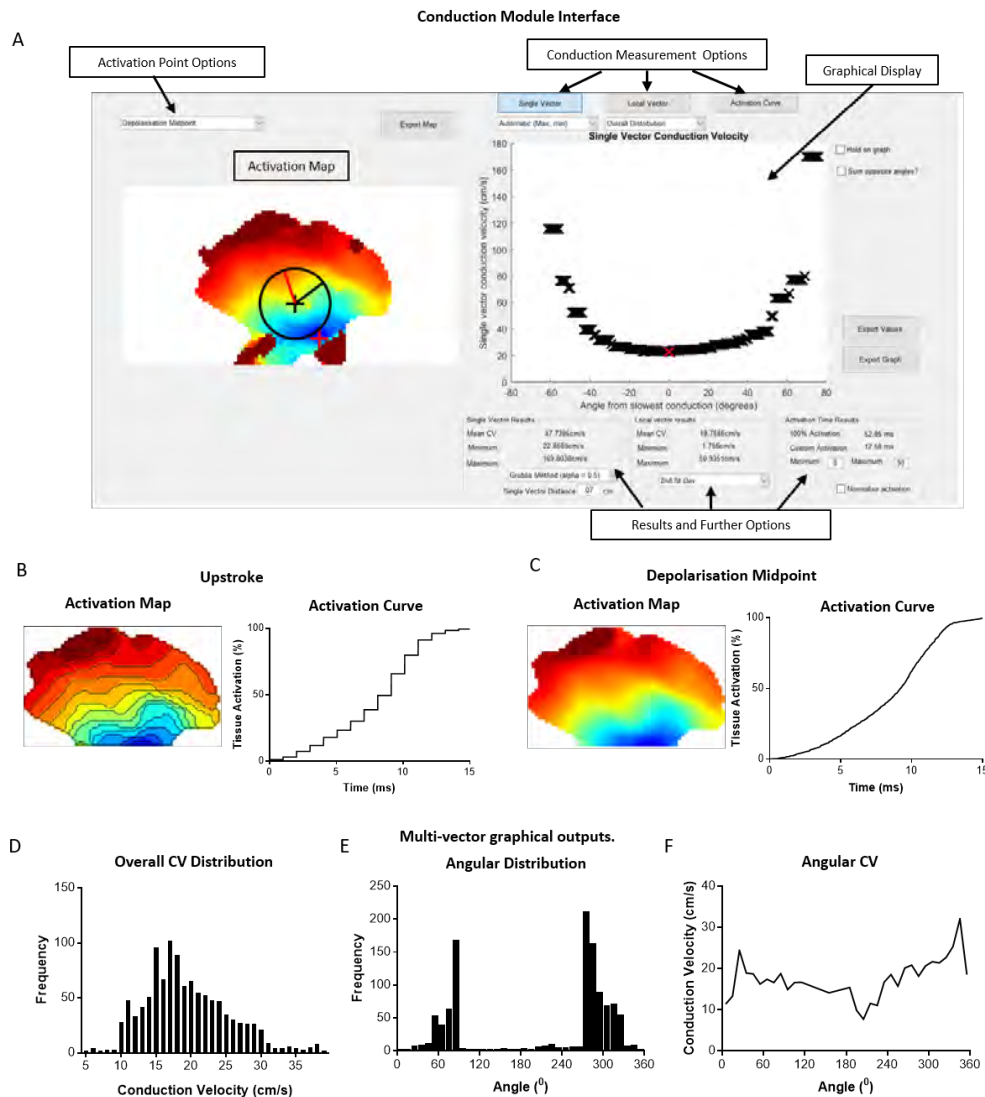


Figure A.4: Conduction velocity (CV) module. A) Conduction module user interface, including options for CV quantification method and activation/repolarisation definition. Here the module is shown to apply the automatic single vector method, where the user defines a distance and starting position. Possible single vector velocities are then measured at all angles in 10 degree increments from the starting position, and the results displayed in the graphical inset which plots velocity as a function of angle. This highlights the wide variation in single vector CV that can be measured from one position depending on direction. B-C) Activation maps and curves produced using two activation definitions, upstroke (B) and depolarisation midpoint (C). Maximum upstroke velocity measurement will always occur at sampling time, hence the step-wise nature of the activation curve which can make it difficult to accurately define activation constants. This is in contrast to the smooth activation curve calculated from depolarisation midpoint, as linear interpolation circumvents sampling rate limitations. D-F) Examples of the graphical plots available to the user when using the multi-vector methods. CV magnitude (E) and angular distribution (F) can be visualised as a measure of conduction heterogeneity. Equally, CV as a function of local vector angle (G) can give detailed insights into conduction pathways and mechanical structure within tissue.

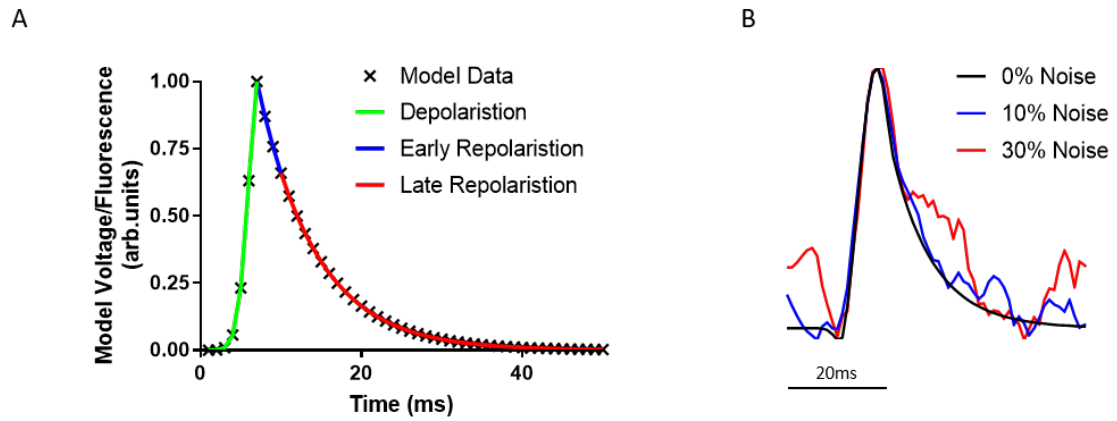


Figure A.5: Model murine action potential example. An example of the use of the action potential function described, black points show $F(t)$ for $t=1:50\text{ms}$ at 1ms intervals (i.e. sampling frequency = 1kHz). Three phases of the action potential are defined as depolarisation (green), early repolarisation (blue) and late repolarisation (red) and modelled by equations 3.9, 3.10 and 3.11 respectively. For activation analysis presented, only the depolarisation phase is relevant.

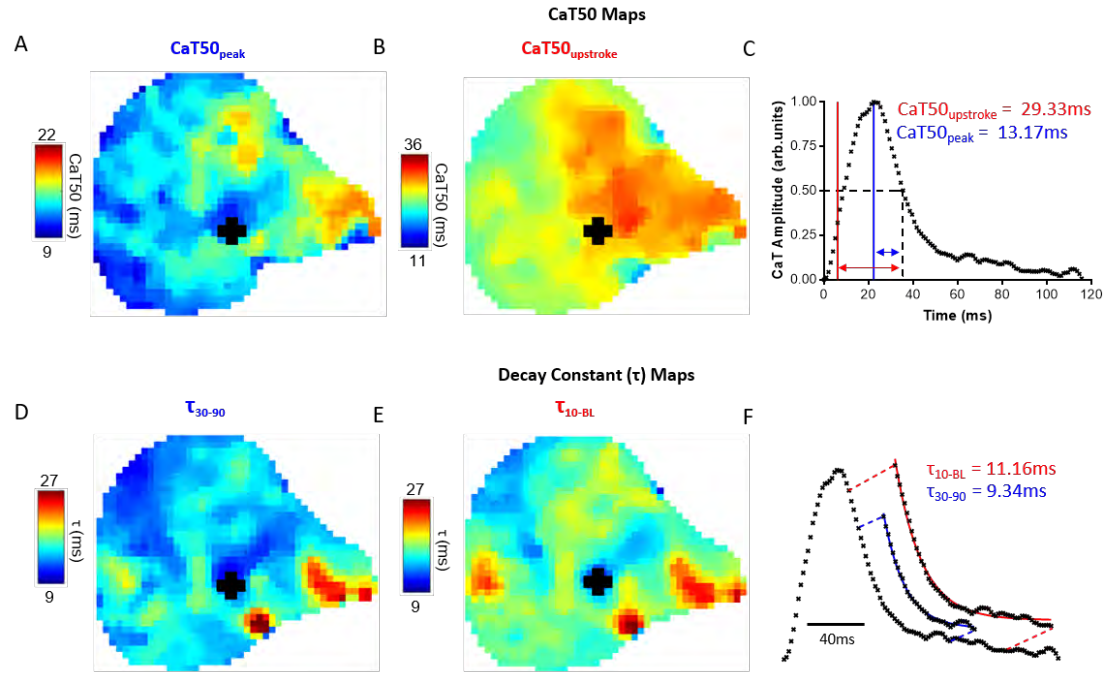


Figure A.6: Calcium mapping. A) $\text{CaT50}_{\text{peak}}$ map from murine atrium as measured from time of Ca^{2+} peak to 50% decay ($\text{CaT50}_{\text{peak}}$). B) $\text{CaT50}_{\text{upstroke}}$ map from same murine atrium as measured from time of maximum upstroke velocity ($\text{CaT50}_{\text{upstroke}}$, as figure 6A). C) Example of measurement of $\text{CaT50}_{\text{peak}}$ and $\text{CaT50}_{\text{upstroke}}$ from highlighted region of interest (as figure 6A). D) Map of decay constant, τ , from same atrium. Map shows calculation of τ by fitting of exponential decay as in equation to points between 30% and 90% decay from peak (τ_{30-90} , as figure 6D). E) τ map from same atrium, but instead applying exponential decay to points between 10% decay and baseline (τ_{10-BL}). F) Example of measurement of τ_{30-90} and τ_{10-BL} from highlighted region on interest (as figure 3.6D).

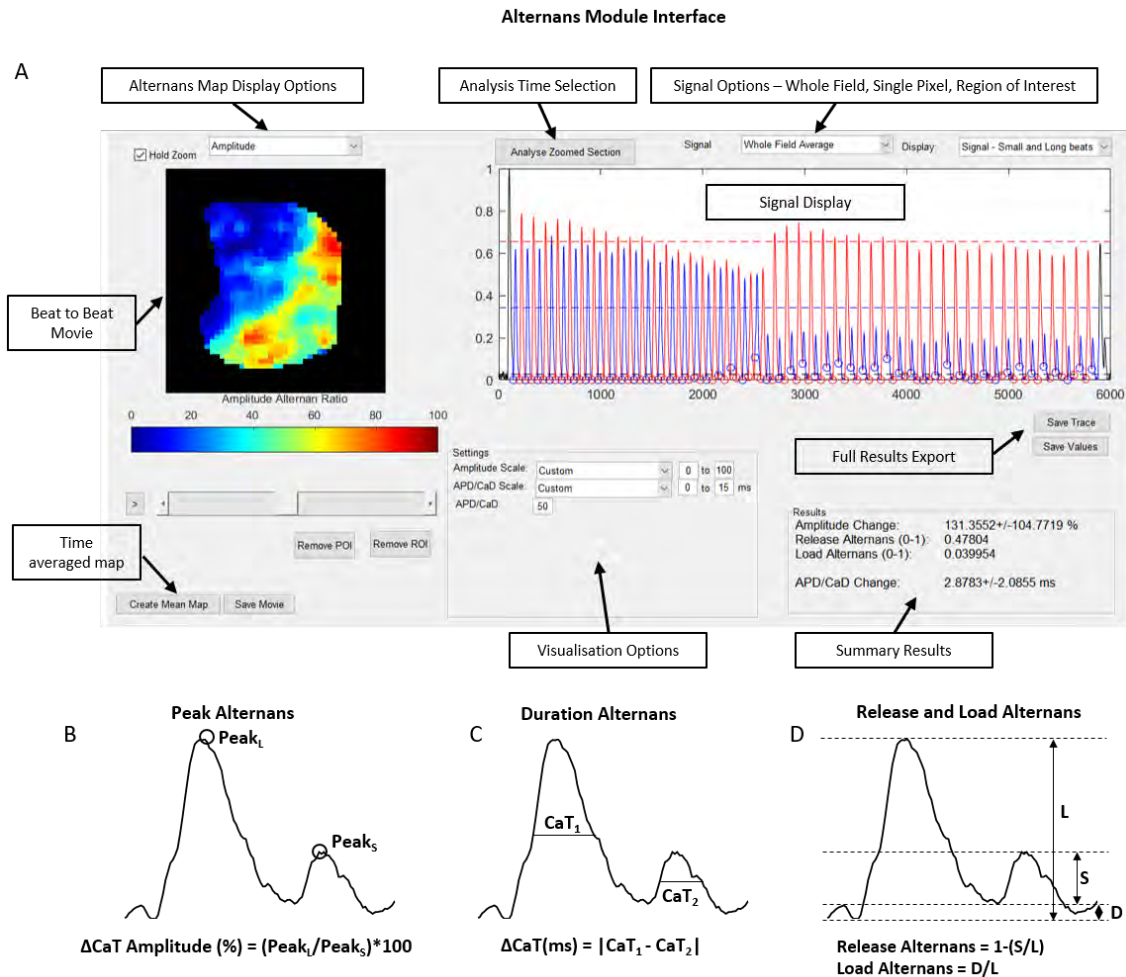


Figure A.7: Alternans module. A) Alternans module user interface, including beat to beat display of alternans behaviour across the tissue. Analysis can be performed across whole experiment or on user defined time interval. Equally, graphical display allows analysis of whole field average or a selected region (or single pixel) of interest. All results can easily be exported in the form of .avi/.gif for video files, a number of file formats for time-averaged images and .csv files for signal analysis. B-D) Illustrations of alternans measures used in ElectroMap applied to example Calcium signal.

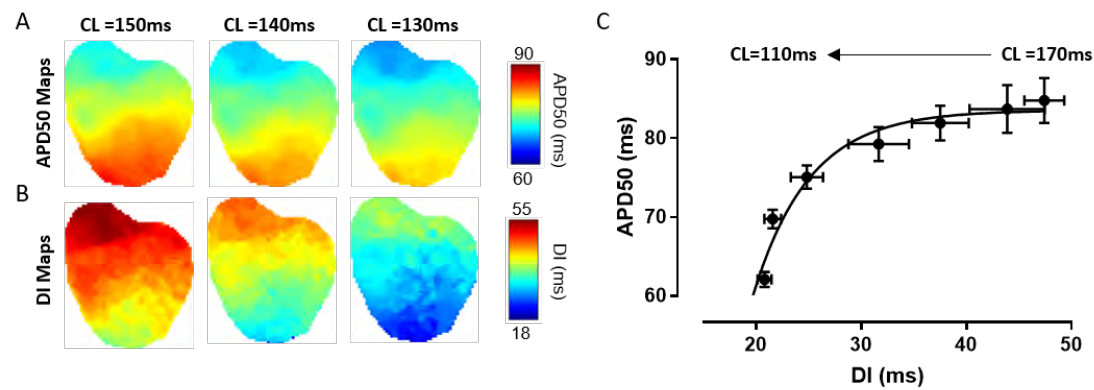


Figure A.8: Diastolic interval (DI) mapping. A) Example APD50 maps from guinea pig heart at decreasing cycle lengths (CL). As CL decreases (pacing frequency increases), APD50 decreases across the heart. B) Similarly, diastolic interval (DI) decreases with CL. Notably, areas of longer APD50 within the tissue concurrently show, as expected, shortened DI at all CLs. C) Mean APD50 as a function of mean DI shows that both decrease more rapidly at shorter CLs. Data shown in mean \pm standard error. $n=5$.

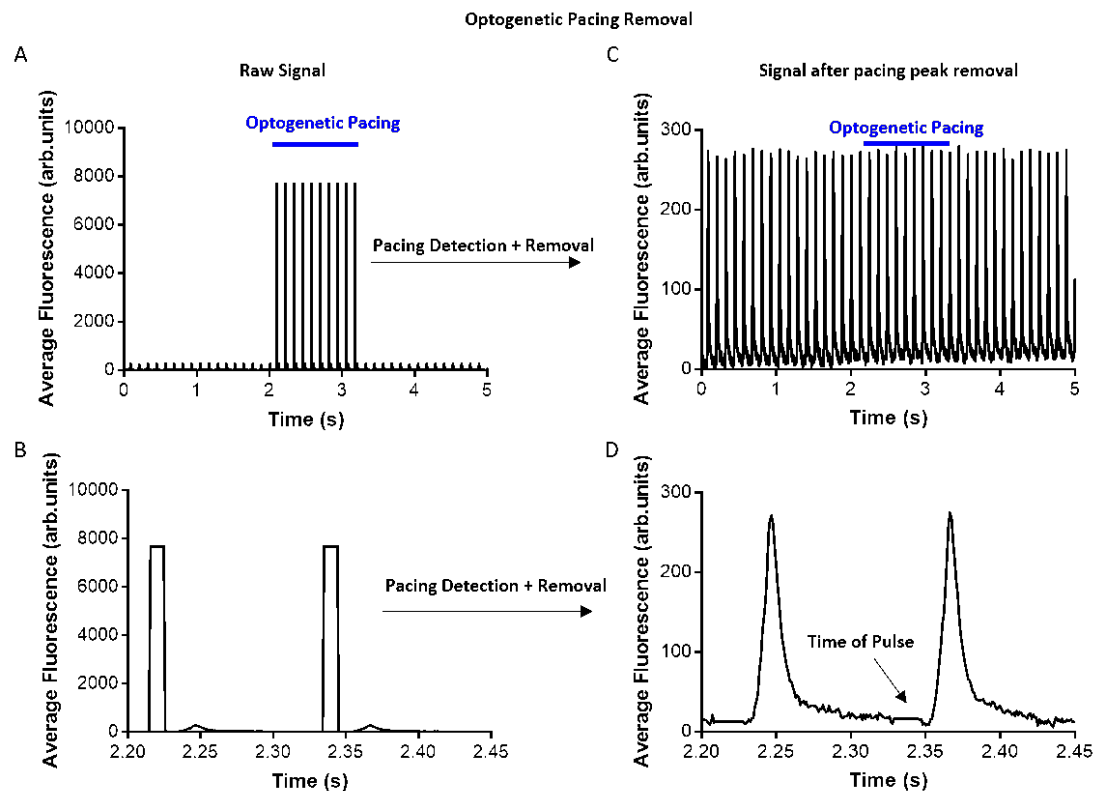


Figure A.9: Optogenetic pacing peak removal. A-B) Pseudo-Optogenetic pacing beats were added to a pre-existing dataset between 2 and 3s, as shown by the average signal. C-D) These were then automatically identified and removed using ElectroMap's 'remove frames' function.

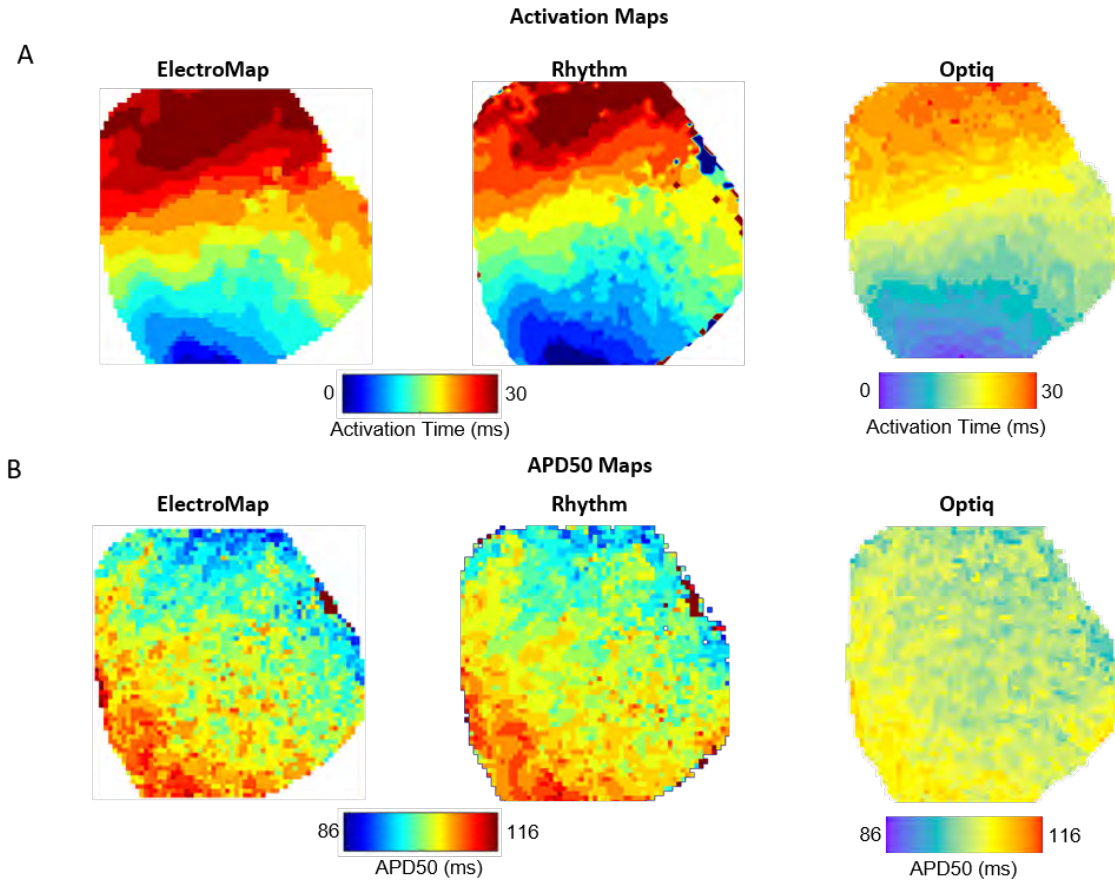


Figure A.10: Software comparison. A) Activation Map created from whole guinea pig heart using i) ElectroMap, ii) Rhythm and iii) Optiq (Cairn Research, UK). In all three cases, maximum upstroke velocity (dF/dt_{max}) was used to define time of activation. A 3x3 pixel linear ('boxcar') filter was applied to all 3 images. Other than this, no other filtering (e.g. temporal) was applied to allow direct comparison between the software. B) Whole heart APD50 maps using the same software. APD50 measured from time of maximum upstroke. The resulting mean APD50 (\pm standarddeviation) was calculated as : ElectroMap : 102 ± 5 ms, Rhythm : 103 ± 7 ms, Optiq : 102 ± 3 ms.

A.2 Supplemental References

- [1] T. Y. Yu et al., “An automated system using spatial oversampling for optical mapping in murine atria. Development and validation with monophasic and transmembrane action potentials,” *Progress in Biophysics and Molecular Biology*, vol. 115, no. 2–3, pp. 340–348, 2014.
- [2] A. P. Holmes et al., “A Regional Reduction in Ito and IKACH in the Murine Posterior Left Atrial Myocardium Is Associated with Action Potential Prolongation and Increased Ectopic Activity,” *Plos One*, vol. 11, no. 5, p. e0154077, 2016.
- [3] F. Syeda et al., “PITX2 Modulates Atrial Membrane Potential and the Antiarrhythmic Effects of Sodium-Channel Blockers,” *Journal of the American College of Cardiology*, vol. 68, no. 17, pp. 1881–1894, 2016.
- [4] M. J. Shattock et al., “Restitution slope is principally determined by steady-state action potential duration,” *Cardiovascular Research*, vol. 113, no. 7, pp. 817–828, 2017.
- [5] J. Winter, M. Bishop, C. Wilder, C. O’Shea, D. Pavlovic, and M. J. Shattock, “Sympathetic nervous regulation of cardiac alternans in the intact heart,” *Frontiers in Physiology*, vol. 9, no. January, pp. 1–12, 2018.
- [6] S. P. J. Krul et al., “Treatment of Atrial and Ventricular Arrhythmias Through Autonomic Modulation,” *JACC: Clinical Electrophysiology*, vol. 1, no. 6, pp. 496–508, 2015.
- [7] P. V Bayly et al., “Estimation of Conduction Velocity Vector Fields from Epicardial Mapping Data,” vol. 45, no. 5, pp. 563–571, 1998.
- [8] R. C. Myles, L. Wang, C. Kang, D. M. Bers, and C. M. Ripplinger, “Local-adrenergic stimulation overcomes source-sink mismatch to generate focal arrhythmia,” *Circulation Research*, vol. 110, no. 11, pp. 1454–1464, 2012.
- [9] J. I. Laughner, F. S. Ng, M. S. Sulkin, R. M. Arthur, and I. R. Efimov, “Processing and analysis of cardiac optical mapping data obtained with potentiometric dyes,” *AJP: Heart and Circulatory Physiology*, vol. 303, no. 7, pp. H753–H765, 2012.
- [10] X. Li et al., “An interactive platform to guide catheter ablation in human persistent atrial fibrillation using dominant frequency, organization and phase mapping,” *Computer Methods and Programs in Biomedicine*, vol. 141, pp. 83–92, 2017.
- [11] K. Umapathy et al., “Phase Mapping of Cardiac Fibrillation,” *Circulation: Arrhythmia and Electrophysiology*, vol. 3, no. 1, pp. 105–114, 2010.